

**Non-Dipole and Dipole Electron  
Energy Loss Spectroscopy**

By

James T. Francis, B.Sc. (Hons.-Major), McMaster University

A Thesis

Submitted to the School of Graduate Studies

in Partial Fulfillment of the Requirements

for the Degree of

Doctor of Philosophy

McMaster University

January, 1995

Copyright by James Francis 1995

**Non-Dipole and Dipole  
Core Electronic Excitation**

**DOCTOR OF PHILOSOPHY (1995)**  
**(Chemistry)**

**McMASTER UNIVERSITY**  
**Hamilton, Ontario**

**TITLE:** Non-Dipole and Dipole Core Electronic Excitation

**AUTHOR:** James T. Francis, B.Sc. (Hons.-Major), McMaster University

**SUPERVISOR:** Professor Adam P. Hitchcock, Ph.D., F.C.I.C.

**NUMBER OF PAGES:** xvii, 203

## Abstract

In contrast to photoabsorption techniques, which are subject to electric dipole selection rules, electron energy loss spectroscopy (EELS) can provide a more complete investigation of atomic and molecular electronic structure. This is due to the added capability of accessing dipole and/or spin forbidden electronic transitions under conditions of significant momentum transfer.

This work documents the design, construction and performance of a new, high resolution, variable scattering angle, variable impact energy electron spectrometer (McVAHRES) which has been used to investigate electronic transitions in gas phase atoms and molecules under both dipole and non-dipole conditions. The home-built instrument features a complex electron optics system and a sophisticated, computer-interfaced electronics system which allows a high degree of flexibility with regards to control and acquisition. This permits a wide range of experimental conditions.

New spectroscopic studies include the observation of spin-forbidden, C 1s core excited triplet states in C<sub>2</sub>H<sub>4</sub>, C<sub>2</sub>H<sub>2</sub>, and C<sub>6</sub>H<sub>6</sub>. The momentum transfer dependence of the (C 1s<sup>-1</sup>, π\*) <sup>3</sup>Π state of CO was also investigated. These results are compared to the results of theoretical calculations. Generalised Oscillator Strengths (GOS) as a function of momentum transfer were derived for the S 2p edge of SF<sub>6</sub>. This work greatly expands previous results reported in the literature. Finally, an interesting feature was observed in the S 2p spectrum of SF<sub>6</sub>, which displays quadrupolar momentum transfer behaviour.

## **Acknowledgements**

I would like to express my deepest appreciation to Prof. Adam Hitchcock for the unfailing interest, encouragement and personal support he has provided me with so generously over the course of this project. The limitless enthusiasm he has shown during our time together has, and will continue to be, a source of inspiration.

Without the selfless generosity and super-human patience shown to me by Dr. Tolek Tyliczszak over the last four years, the success of this work would not have been realised. Words cannot express my gratitude for the assistance and personal support he has given me.

Thanks are also due to my fellow students, Cassia Turci, Stephen Urquhart, Dr. Alex Wen and John Graham, for their camaraderie and invaluable assistance. The invaluable assistance of Dr. Phillip Aebi, Dr. David Kilcoyne, Dr. David Venus, Dr. Alec Bain and Dr. David Santry is deeply appreciated as is the personal support they showed me during difficult times. It has been a pleasure working with you all.

The talented and professional work performed by the McMaster Instrument Machine Shop was crucial to the success of this work. Thanks Gino, Cleaford and Michael for your superb efforts. The financial assistance for this project provided by NSERC is also greatly appreciated.

Special thanks are due to my father, late mother and my fiance Debbie for their unlimited support, patience and enthusiasm. I dedicate this thesis to them.

## Table of Contents

	Page
<b>Preliminaries</b>	
Descriptive Note . . . . .	ii
Abstract . . . . .	iii
Acknowledgements . . . . .	iv
Table of Contents . . . . .	v
List of Figures . . . . .	ix
List of Tables . . . . .	xiv
List of Abbreviations . . . . .	xvi
<b>Chapter 1 Introduction</b>	
1.1 Overview . . . . .	1
1.2 Simulation of Photoabsorption by Electron Impact . . . . .	4
1.3 Valence vs. Inner Shells . . . . .	9
1.4 EELS Under Conditions of Increasing Momentum Transfer . . . . .	11
1.4.1 Multipole Excitations and GOS studies . . . . .	12
1.4.2 Spin Exchange and Triplet States . . . . .	13
1.4.3 Bethe Surfaces . . . . .	14
1.5 Design of an EEL Spectrometer to Investigate Spin and Dipole - Forbidden Transitions . . . . .	15
1.6 Practical Applications . . . . .	17
1.7 Outline of Thesis Chapters . . . . .	18
<b>Chapter 2 Theory of Electron Energy Loss Spectroscopy</b>	
2.1 Theory of Electron Energy Loss Spectroscopy . . . . .	21
2.2 Analogies with Photoabsorption . . . . .	23
2.3 Bethe-Born Theory . . . . .	24
2.4 The Generalised Oscillator Strength . . . . .	30
2.5 Non-Dipole Transitions . . . . .	33
2.6 Summary and Translation from Theory to Experiment . . . . .	35
<b>Chapter 3 Instrument Design and Performance</b>	
3.1 Introduction . . . . .	37

Chapter 3	Instrument Design and Performance	Page
3.2	Design	
3.2.1	Mechanical Design and Materials Considerations . . . . .	39
3.2.2	Vacuum . . . . .	41
3.2.3	Rotation Mechanism . . . . .	43
3.2.4	Electron Optics Design . . . . .	46
3.2.4.1	Electron Gun . . . . .	50
3.2.4.2	Monochromator Exit Lens . . . . .	53
3.2.4.3	Analyser Entrance Lens . . . . .	57
3.2.4.4	Analyser/Monochromator Hemispherical Deflectors . . . . .	60
3.2.5	Detection . . . . .	65
3.2.6	Electronics	
3.2.6.1	Design and Construction . . . . .	66
3.2.6.2	Description of Electronics Operation . . . . .	71
3.2.7	Software	
3.2.7.1	Control . . . . .	75
3.2.7.2	Acquisition . . . . .	75
3.2.7.3	Optimisation Procedures . . . . .	78
3.3	Evaluation of Performance . . . . .	79
3.3.1	Demonstration of Control Flexibility . . . . .	80
3.3.2	Optimisation . . . . .	80
3.3.3	Lens Characterisation . . . . .	82
3.3.4	Performance Tests . . . . .	88
3.3.4.1	Resolution . . . . .	88
3.3.4.2	Variable $E_0$ . . . . .	90
3.3.4.3	Variable Scattering Angle . . . . .	90
3.3.4.4	Constant Momentum Transfer . . . . .	92
Summary	. . . . .	92
Chapter 4(a) Studies of C 1s $\rightarrow$ $\pi^*$ triplet states of carbon monoxide, benzene, ethylene and acetylene		
1.	Introduction . . . . .	96
2.	Experimental . . . . .	97
3.	Calculations . . . . .	98
4.	Results and Discussion . . . . .	98
5.	Summary . . . . .	101

Chapter 4 (b) Experimental and theoretical studies of the (C 1s → π*) <sup>3</sup> Π state of CO: Momentum transfer dependence and vi- brational structure		Page
I.	Introduction . . . . .	103
II.	Experiment . . . . .	103
III.	Calculations . . . . .	104
IV.	Results and Discussion	
A.	Momentum Transfer dependence of the triplet-singlet intensity ratio . . . . .	104
B.	Vibrational structure of the (C 1s <sup>-1</sup> , π*) singlet and triplet states . . . . .	106
V.	Summary . . . . .	108
Chapter 5 Experimental Methodology for the Determination of Generalised Oscillator Strengths		
5.1	Introduction . . . . .	110
5.2	Spectral Acquisition Strategy . . . . .	111
5.2.1	Consideration of the First Born Approximation . . . . .	111
5.2.2	Acquisition Procedures . . . . .	114
5.2.2.1	Acquisition Method 1: Scanning Full Energy Loss Spectra at a Series of Angles . . . . .	114
5.2.2.2	Acquisition Method 2: Scan Few Fixed Energy Points at Several Angles . . . . .	116
5.2.3	Correction Factors for Spectral Normalisation . . . . .	118
5.2.3.1	Gas Pressure . . . . .	119
5.2.3.2	Incident Beam Current . . . . .	119
5.2.3.3	Geometrical Overlap Correction . . . . .	122
5.3	Data Processing for Quantitative GOS Determination . . . . .	134
5.3.1	Procedures for Extracting Inelastic Peak Areas . . . . .	134
5.3.2	Calculation of the GOS as a Function of K <sup>2</sup> . . . . .	138
5.3.3	Treatment of Errors . . . . .	140
5.4	Further Examples . . . . .	141
5.4.1	Relative GOS for the C 1s → π* transition in CO . . . . .	142
5.4.2	Pseudo-Bethe Surface for the C 1s Region of CO . . . . .	142
Summary	. . . . .	146



Chapter 6	Non-Dipole S 2p and S 2s States and Generalised Oscillator Strengths for the S 2p States of SF <sub>6</sub>	Page
6.1	Introduction . . . . .	147
6.2	Non-Dipole S 2p, S 2s and F 1s States of SF <sub>6</sub> . . . . .	148
	6.2.1 Experimental Details . . . . .	152
	6.2.2 Results and Discussion	
	6.2.2.1 Orbital and State Descriptions . . . . .	153
	6.2.2.2 S 2p: Spectral Presentation and Analysis . . . . .	154
	6.2.2.3 S 2s: Spectral Presentation and Analysis . . . . .	163
	6.2.2.4 F 1s Spectra: Presentation and Analysis . . . . .	166
6.3	Generalised Oscillator Strengths for the S 2p States of SF <sub>6</sub> . . . . .	169
	6.3.1 Experimental Details . . . . .	170
	6.3.2 Validity of the First Born Approximation . . . . .	171
	6.3.3 Data Processing for Quantitative GOS Determination . . . . .	171
	6.3.4 Absolute GOS and Error Treatment . . . . .	172
	6.3.5 GOS curves for the 5 S 2p Features and the Continua . . . . .	175
	Summary . . . . .	180
Chapter 7	Concluding Remarks . . . . .	181
Appendix A	Derivation of Geometrical Overlap Correction Factor . . . . .	185
Appendix B	Brief Description of Algorithms . . . . .	187
References	. . . . .	192

## List of Figures

Chapter 1	Page
Fig.1.1 Schematic representation of the photoabsorption process. . .	5
 Chapter 2	
Fig. 2.1 Vectorial representation of momentum conservation. . .	22
Fig. 2.2 Simple two-electron state picture. . . . .	27
 Chapter 3	
Fig. 3.1 Aerial (top) and cross-sectional views of McVAHRES. . .	40
Fig. 3.2 Schematic of McVAHRES vacuum system. . . . .	42
Fig. 3.3 Schematic of computer-interfaced rotation mechanism. . .	44
Fig. 3.4 Comparison of scattering angle indicated by rotation mechanism to that determined experimentally using simple geometry. . .	45
Fig. 3.5 Calibration of the zero degree scattering angle using the (1s <sup>-1</sup> , 2s) and (1s <sup>-1</sup> , 2p) transition intensities for He. . .	47
Fig. 3.6 Thick lens parameters. . . . .	48
Fig. 3.7 (a,b and c) Input array for electron gun showing results of trajectory calculations. . . . .	52
Fig. 3.8 (a and b) Input array for monochromator exit lens showing results of trajectory calculations. . . . .	54
Fig. 3.9 Illustration of how virtual apertures can be created by imaging two appropriately spaced real apertures. . . . .	56
Fig. 3.10 Input array for analyser entrance lens showing results of trajectory calculations. . . . .	59

Chapter 3	Page
Fig. 3.11 Hemispherical electrostatic analyser. . . . .	62
Fig. 3.12 "S" geometry for tandem hemispherical analyser arrangement. . . . .	64
Fig. 3.13 Simplified schematic of McVAHRES electronics arrangement. . . . .	67
Fig. 3.14 Detailed schematic of McVAHRES electronics arrangement. . . . .	68
Fig. 3.15 Schematic of individual components comprising an individual voltage module, with output voltage $V_{out}$ . . . . .	72
Fig. 3.16 Graphical representation of power supply networking to control/acquisition computer. . . . .	74
Fig. 3.17 Example of a calibration file. . . . .	76
Fig. 3.18 Flow chart representation of the acquisition program. . . . .	77
Fig. 3.19 Demonstration of control flexibility using CO. . . . .	81
Fig. 3.20 Graphical representation of a 2-D optimisation of a single parameter. . . . .	83
Fig. 3.21 Characteristic lens voltage ratios as a function of the overall acceleration ratio $V_3/V_1$ compiled from experimental calibration files for the monochromator exit lens. . . . .	84
Fig. 3.22 Characteristic lens voltage ratios as a function of the overall deceleration ratio $V_1/V_7$ compiled from experimental calibration files for the analyser entrance lens. . . . .	85
Fig. 3.23 Demonstration of the resolution capability using He. . . . .	89
Fig. 3.24 Illustration of variable angle capability of McVAHRES in the valence regime using He. . . . .	91

Chapter 4 (a)		Page
Fig. 1	Electron energy loss spectra of CO in the region of the C 1s $\rightarrow$ $\pi^*$ transitions recorded at 2° scattering angle with 0.21 eV resolution and impact energies of ~376, ~391, and ~1806 eV, corresponding to the indicated $E_r$ , the residual electron energy after inelastic scattering. . . . .	97
Fig. 2	Electron energy loss spectra of benzene, ethylene, and acetylene in the region of the C 1s $\rightarrow$ $\pi^*$ transitions recorded with ~465 eV impact energy. . . . .	98
Fig. 3	Plot of the experimental and calculated singlet-triplet splitting ( $E(1s, \pi^*) ^1\Pi - E(1s, \pi^*) ^3\Pi = \Delta(1-3)$ ) versus experimental, absolute and INDO/S calculated relative oscillator strengths ( $\times 10^{-2}$ ) for electric dipole excitation to the $^1\Pi$ state. . . . .	100
Chapter 4 (b)		
Fig. 1	Electron energy loss spectra of CO in the region of (C 1s <sup>-1</sup> , $\pi^*$ ) $^3\Pi$ and $^1\Pi$ states recorded at residual energies of 90, 105, and 1520 eV and scattering angles of 4°, 4°, and 2°, respectively. . . . .	104
Fig. 2	Electron energy loss spectra of CO recorded using 140 eV residual energy and the indicated scattering angles. . . . .	105
Fig. 3	Momentum transfer dependence of the (C 1s <sup>-1</sup> , $\pi^*$ ) triplet/singlet intensity ratio derived from both variable impact energy and variable angle measurements. . . . .	105
Fig. 4	Curve fit analysis of the vibrational band structure of the X $^1\Sigma^+ \rightarrow$ (C 1s <sup>-1</sup> , $\pi^*$ ) $^3\Pi$ and X $^1\Sigma^+ \rightarrow$ (C 1s <sup>-1</sup> , $\pi^*$ ) $^1\Pi$ transitions recorded at 140 eV residual energy, 8° scattering angle and 0.18 fwhm resolution. . . . .	106
Fig. 5	Calculated anharmonic potential curves for the (C 1s <sup>-1</sup> , $\pi^*$ ) $^3\Pi$ and $^1\Pi$ states compared to those estimated from the experimental results using an harmonic approximation. . . . .	108

Chapter 5	Page
Fig. 5.1	Experimental test of the validity of the Born approximation for a set of scattering conditions using the S 2p edge of SF <sub>6</sub> . . . . . 113
Fig. 5.2	Comparison of the energy spectrum sampling for acquisition methods one and two. . . . . 117
Fig. 5.3	Illustration of the geometrical change in the interaction region with scattering angle. . . . . 123
Fig. 5.4 (a)	Normalised relative GOS for the He 1s → 2p dipole-allowed electronic transition at 21.22 eV derived from McVAHRES. . . . . 126
Fig. 5.4 (b)	Normalised relative GOS curve for the He 1s → 2s dipole-forbidden transition at 20.6 eV derived from McVAHRES using the mathematical overlap correction factor in comparison to literature results. . . . . 127
Fig. 5.5	Graphical evaluation of the mathematical approach to overlap correction using the normalised relative GOS for the N 1s → π* electronic transition in N <sub>2</sub> , in comparison to the results of Camilloni et al. . . . . 128
Fig. 5.6	Illustration of the magnitudes of the background signal intensity relative to the uncorrected signal intensity for the S 2p edge of SF <sub>6</sub> , at scattering angles of 2.2° and 14.1°. . . . . 132
Fig. 5.7	GOS for the N 1s → π* transition at 400 eV in N <sub>2</sub> derived from McVAHRES using the non-jet background subtraction method and area determination procedures discussed in the text. . . . . 133
Fig. 5.8	Graphical representation of the steps involved in preparing raw energy spectra for curve fitting and area determination. . . . . 136
Fig. 5.9	Demonstration of the MGAUSS fitting algorithm using SF <sub>6</sub> . . . . . 137
Fig. 5.10	Comparison of the GOS curves determined using acquisition method one vs. acquisition method two . . . . . 143

Chapter 5	Page
Fig. 5.11	First-time determination of the relative GOS function for the C 1s $\rightarrow$ $\pi^*$ transition in CO at 287.4 eV using the procedures outlined in this chapter. . . . . 144
Fig. 5.12	Bethe surface for a portion of the C 1s edge of CO. . . . . 145
Chapter 6	
Fig. 6.1	Graphical representation of a double well potential. . . . . 150
Fig. 6.2	S 2p spectra of SF <sub>6</sub> recorded with 1400 eV impact energy, the indicated scattering angles ( $q$ ) and 0.5 eV instrumental resolution. . . . . 156
Fig. 6.3	Comparison of S 2p spectra of SF <sub>6</sub> in the region of the 181 eV feature, recorded at 1400 eV and 100 eV impact energy and $K^2$ values of 12.9, 11.5 and 26.2 a.u. <sup>-2</sup> . . . . . 161
Fig. 6.4	S 2s EELS spectra of SF <sub>6</sub> recorded with 1500 eV energy and the indicated angles. . . . . 164
Fig. 6.5	F 1s EELS spectra of SF <sub>6</sub> recorded with 1500 eV impact energy ( $\theta \approx 10^\circ$ ) and 3500 eV impact energy ( $\theta \approx 2^\circ$ ). . . . . 168
Fig. 6.6	GOS curves for the <sup>1</sup> T <sub>1u</sub> (a <sub>1g</sub> ), <sup>1</sup> T <sub>1u</sub> (t <sub>2g</sub> ) and <sup>1</sup> T <sub>1u</sub> (e <sub>g</sub> ) dipole-coupled S 2p excited states derived from the experimental data as described in the text. . . . . 176
Fig. 6.7	GOS curves for the <sup>1</sup> T <sub>2g</sub> (t <sub>1u</sub> ) (177 eV) and <sup>1</sup> E <sub>g</sub> (t <sub>1u</sub> ) (181 eV) quadrupole-coupled S 2p excited states. . . . . 177
Fig. 6.8	Integrated areas for the two arctangent components used to represent the low energy (180.3 - 190.3 eV) and higher energy (192.7 - 202.7 eV) portions of the S 2p continuum. . . . . 178
Appendix A	
Fig. 1	Derivation of the geometrical overlap correction factor. . . . . 185

## List of Tables

			Page
Chapter 3			
Table 3.1	Resolution objectives for McVAHRES. . . . .		38
Table 3.2	Typical scanning modes in electron spectroscopy. . . . .		70
Table 3.3 (a)	Theoretical vs. experimental voltage ratios for mono- chromator exit lens. . . . .		87
Table 3.3 (b)	Experimental vs. theoretical voltage ratios for ana- lyser entrance lens. . . . .		87
Chapter 4 (a)			
Table 1	Energies and singlet-triplet splittings of C 1s $\rightarrow$ $\pi^*$ transitions in CO, C <sub>6</sub> H <sub>6</sub> , C <sub>2</sub> H <sub>4</sub> and C <sub>2</sub> H <sub>2</sub> derived from experimental measurements and INDO/S cal- culations. . . . .		99
Table 2	Oscillator strengths and singlet-triplet splittings for 1s $\rightarrow$ $\pi^*$ transitions. . . . .		99
Chapter 4 (b)			
Table 1	Experimental and theoretical results for potential curves and vibrational parameters. . . . .		107
Table 2	Mulliken population analysis of charge and charge transfer calculated using the SCF orbitals for R = 1.160 Å. . . . .		108
Chapter 5			
Table 5.1	Comparison of overlap-corrected experimental He elastic cross-sections with literature values. . . . .		129

Chapter 6		Page
Table 6.1	S 2p, 2s and F 1s core excited states of SF <sub>6</sub> .	155
Table 6.2	Energies (eV), term values and assignments of features in the S 2p energy-loss spectrum of SF <sub>6</sub> .	155
Table 6.3	Energies (eV), term values and assignments of features in the S 2s energy-loss spectrum of SF <sub>6</sub> .	165
Table 6.4	Energies (eV), term values and assignments of features in the F 1s energy-loss spectrum of SF <sub>6</sub> .	165
Table 6.5	Comparison of term values for S 2p, S 2s and F 1s core excitations.	167
Table 6.6	Energies, widths and line shapes for the curve fit analysis of the S 2p spectra.	167
Table 6.7	Optical oscillator strengths.	174



### List of Abbreviations and Symbols

ADC	Analog-to-Digital Convertor
$\alpha$	maximum aperture half angle
a.u.	atomic units
CI	Configuration Interaction
DAC	Digital-to-Analog Convertor
DES	De-excitation Electron Spectroscopy
$\Delta(1,3)$	singlet-triplet splitting energy
$E_0$	Impact Energy
EELS	Electron Energy Loss Spectroscopy
EHMO	Extended Hückel Molecular Orbital
EICVOM	Equivalent Ionic Core Virtual Orbital Model
ESCA	Electron Spectroscopy for Chemical Analysis
eV	electron-volt
FWHM	Full Width at Half Maximum (resolution)
GOS	Generalised Oscillator Strength
HAM/3	Hydrogenic Atoms in Molecules (version 3)
h $\nu$	(Planck's constant) x (frequency); i.e. a measure of photon energy
INDO	Intermediate Neglect of Differential Overlap
ISEELS	Inner Shell Electron Energy Loss Spectroscopy

<b>K</b>	momentum transfer
<b><math>k_0</math></b>	momentum of incident electron
<b><math>k_1</math></b>	momentum of scattered electron
<b>LCAO-MO</b>	Linear Combination of Atomic Orbitals - Molecular Orbital
<b>McFALRES</b>	McMaster Fixed Angle Low Resolution Electron Spectrometer
<b>McVAHRES</b>	McMaster Variable Angle High Resolution Electron Spectrometer
<b>NEXAFS</b>	Near Edge X-ray Absorption Fine Structure
<b>OOS</b>	Optical Oscillator Strength
<b><math>\Omega(\theta, \phi)</math></b>	solid angle of scattered electron
<b>PASCA</b>	Photoabsorption Spectroscopy for Chemical Analysis
<b><math>R_{\text{pass}}</math></b>	circular orbit of radius $R_{\text{pass}}$ in hemispherical deflectors
<b>SCF</b>	Self-Consistent Field
<b><math>\sigma_{\text{elastic}}</math></b>	integrated elastic scattering cross section
<b><math>\sigma_{\text{inelastic}}</math></b>	integrated inelastic scattering cross section
<b>UV, VUV</b>	Ultraviolet, Vacuum Ultraviolet
<b><math>V_{\text{pass}}</math></b>	potential of electrons in hemispherical deflectors traversing radius $R_{\text{pass}}$
<b>VSEELS</b>	Valence Shell Electron Energy Loss Spectroscopy
<b>XAS</b>	X-ray Absorption Spectroscopy
<b>XPS</b>	X-ray Photoelectron Spectroscopy
<b><math>\xi</math></b>	Slater-type orbital exponent

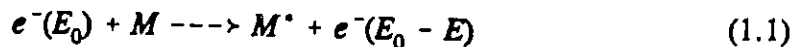
# Chapter 1

## INTRODUCTION

### 1.1 Overview

When electrons are scattered by atoms or molecules, they may impart both energy and momentum to the target species. Such a scattering process is deemed inelastic (as opposed to elastic, where there is no change in the energy of the scattered electron). Under appropriate conditions, the energy and momentum transferred by the incident electron can excite electronic transitions in the target. By probing the energy and angular distribution of the inelastically scattered electrons, one has access to detailed spectroscopic information about the nature of the excited states induced in the target. This in turn can yield information about the geometric and electronic structure of the target. These principles form the basis of a wide variety of electron scattering techniques. This work focusses on gas phase Electron Energy Loss Spectroscopy (EELS).

The basic EEL process can be represented compactly below as:



where  $e^-$  is the colliding electron with incident energy  $E_0$  and residual energy  $(E_0 - E)$  after collision with the target species  $M$ .  $M$  represents the initial state of the target before

interaction with the colliding electron.  $M^*$  represents the target after a transition has occurred to an excited final state as a result of interaction with the incident electron. The final excited state of the target lies above the initial state in energy by an amount equal to  $E$ , where  $E$  is the energy loss. In principle, energy losses in amounts up to  $E_0$  can occur for every accessible transition in the target.

When the incident electron is highly energetic (i.e. large  $E_0$  in equation 1.1) and is scattered through a small angle, the momentum transferred to the target from the colliding electron is very small. Under such conditions, the interaction between the colliding electron and the target is essentially identical to the absorption of light by the target (a process known as photoabsorption). A great deal of research has been done using the EELS method under conditions simulating photoabsorption. Such work has provided information on chemical bonding and the electronic and geometric structure of molecules. The photoabsorption process is governed by a set of rules (known as selection rules) which restricts the number of possible transitions that can occur in the target. In EELS under conditions where  $E_0$  approaches the energy loss ( $E$  in equation 1.1) and/or the scattering angles become large ( $> 10^\circ$ ), the momentum transferred to the target from the incident electron during the collision becomes significant. This can result in a relaxation of the photoabsorption-based selection rules. In this manner, electronic transitions in the target can be induced that would not otherwise be observed under conditions simulating photoabsorption. Such excitation processes are termed "optically forbidden" (as opposed to optically allowed in the case of photoabsorption). EELS can thus make a more complete investigation of atomic and molecular excitation processes relative to

photoabsorption techniques. In order to investigate optically allowed and forbidden transitions via the EELS technique, a new electron spectrometer has been built. This thesis documents its design and construction and presents the results of new spectroscopic studies performed on this instrument.

In 1914 Frank and Hertz performed their classic experiment with mercury atoms in which they demonstrated for the first time that excitations induced by inelastic electron scattering were quantized in energy [FH14]. In the late 1950's and early 1960's the advent of improved vacuum technology led to significant maturation of the field of inelastic electron scattering and its application to studies of valence electronic spectroscopy of atoms and molecules. In the 1970's and 1980's EELS was extended to inner-shell electronic excitation, mainly under conditions simulating photoabsorption. In the past 15 years there has been considerable growth in the field of electron impact phenomena because of its relevance to areas such as plasma physics, radiation chemistry and atmospheric processes. This work extends the knowledge accumulated in this field by providing additional information about atomic and molecular electronic structure through investigations of optically forbidden transitions, in addition to transitions allowed optically. The breakdown of the theoretical machinery which links EELS and photoabsorption is illustrated under conditions of increasing momentum transfer. Such work also serves as a valuable gauge to test the accuracy of high level quantum mechanical calculations.

## 1.2 Simulation of Photoabsorption by Electron Impact

The photoabsorption process corresponding to equation 1.1 can be represented by equation 1.2:



where the photon energy  $E$  is analogous to the energy loss of the incident electron that produces the excited state  $M^*$ . This is separated in energy from the initial state  $M$  by an amount equal to  $E$ . Such a process is termed *resonant*, which means that the transition will only occur when the photon energy ( $h\nu$ ) is equal to  $E$ , the energy of the transition. In photoabsorption spectroscopy, the energy of a beam of photons impinging upon a sample is scanned (see Fig. 1.1). Each transition that comes into resonance is reflected by attenuation of the beam (i.e. a photon is absorbed). The strength of the attenuation at a particular photon energy is a characteristic property of the atom or molecule, and thus absorption spectroscopy is a powerful investigative tool.

In addition to energy considerations, a set of selection rules must be satisfied in order for a transition to occur, or in other words, for the transition to be *allowed*. In the case of photoabsorption (and EELS under photoabsorption conditions), allowed transitions are those for which the dipole transition matrix element is non-vanishing. For example, an electronic, atomic transition where the electron starts in an  $s$  orbital ( $l=0$ ) and undergoes a transition to a  $p$  orbital ( $l=1$ ) is formally allowed optically. (Strictly speaking, spectroscopic transitions occur between *states*. A state is described by a mathematical construct known as a wavefunction that contains all information that is

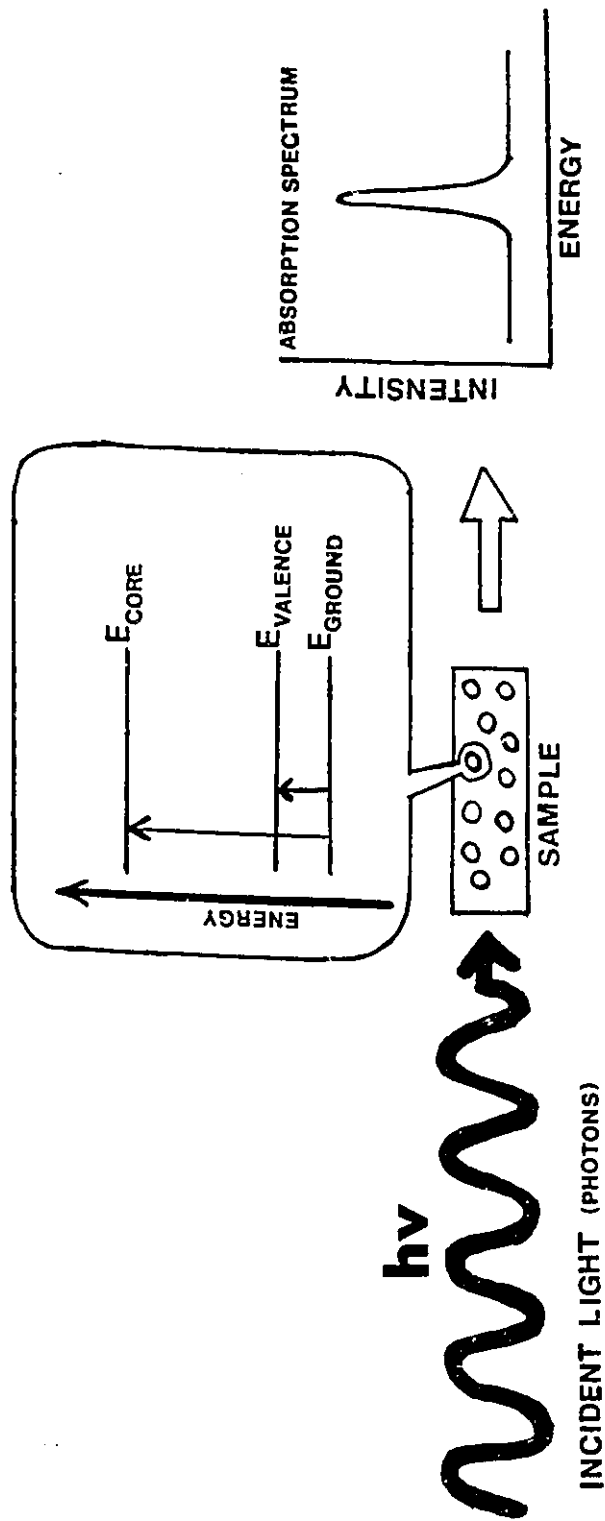


Fig. 1.1 Simple schematic representation of the photoabsorption process. A beam of photons with energy  $h\nu$  intersects the sample region. If the photons have the right energy, they may be absorbed and a transition can occur between two energy levels in the sample atoms (or molecules). The absorption process causes an attenuation in the incident beam which can be used to produce an absorption spectrum (i.e. a plot of transition intensity versus energy).

possible to know about the location and motion of the particle(s) it describes, such as the electrons in an atom or molecule. Chemists, however, often refer to transitions between initial and final *orbitals*. An orbital is a one-electron wavefunction that describes the distribution of an electron in an atom or molecule. Orbitals are often rendered visually as 3-D surfaces which makes the orbital description in spectroscopy useful in terms of providing a qualitative picture of the nature of a transition). In the case of (non-diatomic) molecules where the angular momentum information is lost, the selection rules result from orbital symmetry considerations. For photon (and photon-like EELS) induced transitions, it turns out that the initial and final states of the target are coupled by an entity known as a dipole transition moment, which reflects the reorganisation of the molecular electronic charge distribution during a transition. The dipole transition moment defines the correct symmetry to satisfy the selection rules necessary for a transition to occur. As such, optical selection rules are often referred to as *dipole* selection rules, and the corresponding transitions are deemed *electric dipole allowed*.

Atomic (and diatomic) transitions where the overall change in angular momentum is 0 or 2 are known as *quadrupole* transitions. Accordingly, in complex molecules the initial and final states are coupled by a quadrupolar transition moment. Such transitions are forbidden optically, due to the fact that the electromagnetic field of the photons induces only dipole transition moments. There are also higher order transitions, connected by octupole, etc. transition moments that are also optically forbidden.

Energetically speaking, transitions involving outer shell (valence) electrons in molecules and multi-electron atoms correspond to photon energies in the range of 5 to 50



eV. This region of the electromagnetic spectrum corresponds to the ultraviolet (UV) and vacuum ultraviolet (VUV). In the case of transitions from inner shells, the photon energies range from 50 eV to 1000 eV which corresponds to the soft X-ray region of the electromagnetic spectrum.

In 1930, Bethe [B30] made use of the Born approximation to illustrate that a quantitative relationship exists between photoabsorption and the scattering of fast electrons (implying small momentum transfer). Modern, detailed treatments of these ideas have been given by Inokuti [IIT71] and Kim [K72]. Under such conditions, it is thus possible to imagine the resonant photon energy as being analogous to the electron energy loss,  $E$  and the resulting electronic transitions are governed by dipole selection rules. Electron impact processes are, however, *non-resonant*; nevertheless their ability to excite dipole allowed transitions can be described in terms of a "virtual photon" model [W74]. In essence, the fast electron presents a white light continuum of "pseudophotons" to the target, which are absorbed with a frequency dependent probability that can be related to the optical oscillator strength (OOS). The OOS is related to the probability of an electronic transition occurring and is reflected in its spectral intensity. This analogy allows *quantitative* simulation of photoabsorption measurements through electron energy loss techniques. The availability of a photon-like source covering a continuous energy range from the UV to soft X ray (corresponding to energy losses of ca. 5 to 1000 eV), coupled with the fact that it may be packaged in a single, lab-based experimental apparatus has made EELS a valuable alternative to photoabsorption spectroscopy.

Until recently, EELS enjoyed distinct advantages over photon techniques due in

part to a lack of sufficiently intense tunable (continuum) light sources in the UV and soft X ray regions of the electromagnetic spectrum, and the fact the resolution in EELS remains constant over all energy losses when deceleration is used. However, advances in insertion device and monochromator technology for production of tunable synchrotron radiation (an intense, coherent light source covering the VUV and X-ray regions of the electromagnetic spectrum) have seriously narrowed this advantage. For example, the DRAGON type monochromators, which use spherical optical elements, can achieve  $< 50$  meV resolution in the soft X-ray region [CS90]. Synchrotron facilities are enormously expensive and at present sparsely located, which limits their usefulness to the average researcher. In spite of the high performance offered by modern synchrotron radiation sources, the resolution provided by electron energy loss techniques still remains competitive above 200 eV. Moreover, the non-resonant nature of EELS renders it immune to line saturation effects, a phenomenon in photon-based spectroscopies where transitions having natural linewidths smaller than the instrumental resolution may result in spurious intensities [IIT71]. Most important in the context of this work, however, is the fact that under conditions of significant momentum transfer EELS offers the unique capability of relaxing the selection rules for electronic excitation making it possible to stimulate dipole and/or spin forbidden processes in gas phase atoms and molecules, solids and surfaces.

### 1.3 Valence vs. Inner Shell Excitation

Beginning in the 1960's, early EELS studies such as the pioneering work by Gieger [G64] and Lassetre *et al.* [LS74] on atoms and small molecules were concerned with valence electronic transitions in the target. In the context of this thesis, this corresponds to energy losses ranging from ca. 5 - 50 eV. These studies laid the groundwork for deriving optical oscillator strength values from electron impact spectroscopy. More recent contributions to the valence literature report using angle-resolved valence shell EELS (often denoted as VSEELS) to investigate the momentum transfer dependence of valence electronic transitions, such as the work of Ying *et al.* on SF<sub>6</sub> and chlorofluorocarbons [YD&93, YM&93, YL94] and the high impact energy work by Barbieri and Bonham [BB92] investigating the Lyman-Birge-Hopfield band in N<sub>2</sub>. The attractive feature about VSEELS, from an experimental point of view, is that the cross-sections associated with excitation of valence transitions via electron impact are intrinsically larger than those corresponding to excitations from inner shells (energy losses of ca. 50 eV or more). Indeed, the cross-section for inner shell processes decreases as the inverse cube of the energy loss, and as a result all practical inner shell studies have an upper limit of about 1000 eV.

In larger molecules, however, such as aromatic hydrocarbons, there can exist a large number of possible electronic transitions between the occupied and unoccupied valence manifolds over a narrow energy range. As a result, several features may overlap one another making the valence EEL spectrum difficult to interpret. In contrast, transitions from an atomic or molecular core level usually allows unambiguous

identification of the initial orbital due to the fact that the spectral features associated with different types of core levels are well separated in energy. In addition, due to the high degree of localization of the orbitals associated with core level electrons, the shapes and energies associated with core level excitation and ionization bands do not show dramatic changes as one moves from the gaseous to the solid state [RBD91]. Thus, techniques such as inner-shell EELS (ISEELS), XPS (X-ray Photoelectron Spectroscopy) or ESCA (Electron Spectroscopy for Chemical Analysis), PASCA (Photoabsorption Spectroscopy for Chemical Analysis) and Auger spectroscopy have been extensively applied to the investigation of both solids and gases [RBD91]. Focusing on gas phase species, ISEELS is a valuable means of deriving information about electronic and geometric structure as reflected in the unoccupied orbitals. Along these lines ISEELS (under conditions simulating photoabsorption) of molecules has recently gained considerable interest as guide to the assignment of NEXAFS (Near Edge X-ray Absorption Fine Structure) spectra of surfaces [H90] and is presently finding increasing use in the characterization of a wide variety of materials including semiconductors, catalysts, polymers, etc. In this laboratory, Wen has studied various metal-ligand complexes in the gas phase by ISEELS which provided insight into the ligand-ligand interaction via the central metal atom [W92] and Urquhart, Hitchcock and Rightor have used ISEELS as a complement to transmission electron microscopy to investigate various monomeric organic species as models for core-excitation of PET (polyethylene terephthalate) [HU&92]. These studies are referenced in a complete and up-to-date bibliography compiled by Hitchcock and Mancini [HM94] which covers all inner shell excitation studies on atoms and

molecules by EELS, photoabsorption and theory/computation reported in the literature. The magnitude of this compilation attests to the past and present thriving interest in the fields of soft X-ray photoabsorption and inner shell excitation using EELS.

#### 1.4 EELS Under Conditions of Increasing Momentum Transfer

The Bethe-Born theory describes the response of a target species to fast electron impact in terms of a momentum transfer dependent, generalised oscillator strength (GOS). Under appropriate scattering conditions (i.e. within the first Born approximation which is usually satisfied whenever  $E_0$  is several times the energy loss), that part of the GOS expression representing the target electrons can be expanded in a form which includes contributions from dipole and higher order multipole transition matrix elements weighted by increasing powers of the momentum transfer,  $K$ . It is important to note that within the first Born approximation, the properties of the incident electron appear in the GOS as a mere kinematic correction factor and is determined completely by the experimental scattering geometry. In the limit of zero momentum transfer, the GOS reduces to the optical oscillator strength (OOS), which thus allows one to simulate photoabsorption using EELS. By increasing the momentum transfer, however, the contribution to the GOS from quadrupole, octupole and higher order non-dipole transition matrix elements becomes significant. In this manner, one can use EELS to access transitions that are forbidden optically based on consideration of angular momentum selection rules and the symmetries of the initial and final states.

Experimentally, momentum transfer studies on *valence* transitions, such as the

dipole forbidden  $1^1S \rightarrow 2^1S$  and dipole allowed  $1^1S \rightarrow 2^1P$  transitions in He [LSD64, SL64] have been performed some time ago. More recent contributions include studies on chlorofluorocarbons and  $N_2$  [YM&93, YL94, BB92]. By comparison, the momentum transfer dependence of inner shell transitions has been studied only recently, owing to the increased experimental challenges due to the decreased excitation cross sections.

#### 1.4.1 Multipole Excitations and GOS studies

Momentum transfer experiments where the impact energy is fixed and the scattering angle is varied can be classed as 'variable scattering angle or angle resolved' studies. Under these conditions, the first Born approximation is satisfied (by sufficiently large  $E_0$ ) and the GOS concept still applies. Determination of the GOS for a particular electronic transition (or range of transitions) as a function of momentum transfer ( $K$  or  $K^2$ , usually in a.u.) generates the so-called GOS profile. Examination of the shape of a GOS profile offers insight into the qualitative nature of the transition of interest. In particular, the GOS profiles for dipole allowed transitions display a decrease in magnitude at increasing momentum transfer, whereas transitions with a significant quadrupole component display the opposite effect. Thus, GOS profiles can aid in spectral assignments. One of the first uses of GOS profiles was in the determination of absolute OOS values from EEL results [LS71, BBS91]. The absolute GOS is evaluated at a series of momentum transfer values, typically using a sum rule (discussed in chapter 2). Extrapolation to zero momentum transfer provides the OOS in the optical limit.

Very little research has been done on inner shell GOS determinations as a function

of momentum transfer to date, but the literature is increasing. Camilloni *et al.* have derived the GOS profiles for inner shell transitions in N<sub>2</sub>, NO and N<sub>2</sub>O [CF&87]. De Souza *et al.* have documented inner shell GOS profiles of CO<sub>2</sub> and C<sub>2</sub>H<sub>2</sub> and have made comparisons to calculations. [BBS91, MB&94]. Ying *et al.* have reported GOS profiles of dipole allowed and dipole forbidden features in the S 2p spectrum of SF<sub>6</sub> [YML93]. Most recently, the GOS profiles of features in the C 1s and Cl 2p spectra of some chlorofluoromethanes have been reported by Ying *et al.* [YL94b].

#### 1.4.2 Spin Exchange and Triplet States

There is also the consideration of spin angular momentum. Formally, for low Z species (i.e. within the L-S coupling scheme), optical transitions accompanied by a change of spin are forbidden and thus a singlet initial state will result in a singlet final state after undergoing an electronic transition. It is possible to relax this selection rule and produce triplet excited states, under certain conditions. In condensed phases, triplet states can be generated optically via an intersystem crossing mechanism from a singlet excited state [T78]. It is also possible to induce spin forbidden transitions using EEL techniques, although via a distinctly different physical method. When the energy of the incident electron ( $E_0$ ) approaches the energy of a particular induced electronic transition in the target, the first Born approximation is no longer valid. As will be shown in chapter 2, such scattering conditions also correspond to a significant momentum transfer. The role of the incident electron in the interaction can thus no longer be treated as simply a kinematic correction factor applied to the transition matrix element describing the target

electrons. Rather, under such scattering conditions one must consider a system where the incident and target electrons can lose their identity in the resulting slow collision, thereby exchanging. As a result, it is possible to induce electronic transitions using EELS where the total spin angular momentum is not conserved.

The first inner shell forbidden transition was reported by Shaw *et al.* in 1982 [SK&82]. They observed the spin forbidden, singlet-to-triplet N 1s  $\rightarrow$   $\pi$ 2p transition in N<sub>2</sub> at an impact energy less than 600 eV (compared to the 400 eV energy loss). Since then, singlet-triplet 1s  $\rightarrow$   $\pi^*$  transitions have been observed in CO, COS and CS<sub>2</sub> [UT83, HK86, HK87]. In the case of CO, the impact energies were as low as 8 eV above the excitation threshold [HK86]. This type of scattering experiment where spin forbidden transitions are induced can be classed as a 'variable impact energy' study, as the necessary momentum transfer is generated via lowering  $E_0$ . It is important to note that although the first Born approximation no longer applies here, one can still define an effective momentum transfer based upon the experimental scattering geometry.

### 1.4.3 Bethe Surfaces

One of the most challenging and interesting experiments that requires both variable impact energy and variable scattering angle instrumental capability is the construction of the so-called Bethe surface [IIT71]. Energy loss spectra are acquired at a series of constant momentum transfers, and a 3-D representation is constructed using the energy loss, momentum transfer and GOS as the coordinates. An informative treatment is given by Inokuti who discusses the Bethe surface of the H atom in detail [IIT71]. Other



examples in the literature include the Bethe surfaces of Lahmam-Bennani and others [LD&80, LDW79] for the N 1s edge of NH<sub>3</sub> and the C 1s edge of CO<sub>2</sub>. An original example is presented in chapter 5 for the discrete and near continuum C 1s energy loss spectrum of CO. Wellenstein *et al.* [WS&75] have shown that information related to the charge and momentum densities of atoms and molecules can be determined from such surfaces.

### 1.5 Design of an EEL Spectrometer to Investigate Spin and Dipole Forbidden Transitions

In order to carry out the spectroscopic studies outlined above under a wide range of experimental scattering conditions an appropriate electron energy loss spectrometer had to be designed and built. This task represents a major portion of my work and is presented in chapter three.

A typical EELS spectrometer for dipole regime work consists of a thermionic electron source for beam production (usually monochromated in modern instruments), a collision region, a multi-element analyser lens and analyser (hemispherical deflectors are the most common) and a serial detector. At present, more and more instruments are utilising parallel detection, however. The scattering geometry and impact energy are usually fixed. The typical operational mode involves collecting electrons that have been scattered upon collision with the sample gas in the collision region at a fixed detection angle. The electrons are usually retarded to a constant final energy (and thus fixed resolution) prior to analysis. The energy loss spectrum is scanned by adding the desired energy loss either to the impact energy (i.e. before the collision region) or after the

collision region. Examples of such instruments include that used by Hitchcock [H90] and the high resolution Super Spec instrument of Daviel, Brion and Hitchcock [DBH84]. The resolution available from such instruments at present can exceed 0.05 eV FWHM, which is considered excellent in the field of inner shell excitation spectroscopy.

To access experimentally the forbidden core excitation processes described in the previous section, special considerations must be given in the design of the spectrometer in addition to the basic components outlined above. In particular, the optics system must accommodate a range of acceleration and deceleration ratios such that the impact energy can be varied continuously from a few hundred eV to a few keV. In addition, the electron energy analyser components must be rotatable about the zero degree scattering angle in order to accommodate variable scattering angle experiments. High resolution, of the order of 100 meV or less is also a necessity. Chapter three describes the design considerations and the computer modelling approach used for the electron optics which ultimately resulted in a suitable instrument design that in practice effectively meets each of these requirements. In addition, the instrument features a state-of-the-art, fully computer-interfaced electronics system that lends an enormous degree of stability and flexibility, with regards to control and acquisition. Customised software developed to capitalise upon the extensive interfacing has allowed a large degree of automation. The results of characterisation studies reveal that the best resolution is of the order of 0.05 eV FWHM for valence shell work and 0.150 eV typically for inner shell work. The range of scattering angles accessible varies continuously from  $-10^\circ$  to  $+100^\circ$ . Impact energies may be varied from 100 eV to 2 keV, continuously. This combination of variable angle, high

resolution and variable impact energy into one versatile unit is reflected in the name chosen for the new instrument: McVAHRES (McMaster Variable Angle High Resolution Electron Spectrometer).

In comparison with other contemporary instruments in the field of forbidden electronic excitation by EELS, McVAHRES is somewhat unique in that it can accommodate both spin forbidden (variable  $E_0$ ) and dipole forbidden (variable angle), valence and inner shell experiments. Typically, most instruments excel in only a subset of these areas. For example, the instrument used by Ying *et al.* at Waterloo [YD&93, YL94, YL94b, YM&93, YML93] uses fixed, high impact energies (2.5 keV), has a comparatively limited angular range and modest resolution (0.8 eV FWHM). The instruments of Bonham and Camilloni *et al.* [BB92, CF&87] have large angular ranges, but modest resolution ( $> 0.5$  eV FWHM). Finally, the instrument used by Harrison and King in their triplet work can accommodate extremely low impact energies [HK86, HK87]. It has low resolution (0.8 eV FWHM), is fixed at a  $90^\circ$  scattering geometry and thus lacks continuously variable scattering angle.

### 1.7 Practical Applications

The determination of absolute transition probabilities (oscillator strengths) via the EELS method for both valence and inner shell excitations of atoms and molecules is of great importance to a variety of fields [CCB91, CC&92]. These include: atmospheric chemistry, astrophysics, laser development, lithography and radiation physics. For example, the absolute oscillator strength data derived for Ne has been used to re-evaluate

the abundances of Ne in B stars [AM73]. In addition, information about energy levels and absolute oscillator strengths of neon-like systems are aiding in the development of soft X-ray lasers [E90].

Momentum transfer studies on chlorofluorocarbons are of great interest. This is primarily due to the participation of these species in the depletion of the ozone layer. These types of EELS studies can identify the nature of specific electronic transitions [YL94, YL94b, YM&93]. Such information can help determine how the molecules dissociate, which may subsequently lead to ozone-depleting reactions. The study of dipole forbidden transitions at large momentum transfer, in addition to those which are dipole allowed provides a more complete understanding of the electronic structure of atoms and molecules than can be had from photoabsorption techniques.

Spin exchange experiments in which triplet excited states are generated yield singlet-triplet splitting energies. This information is valuable as a means of evaluating the accuracy of theoretical calculations and models.

### 1.8 Outline of Thesis Chapters

Chapter two outlines the theory and basic principles behind electron energy loss spectroscopy. In addition, the Bethe-Born theory is examined in some detail.

In chapter three, the design and construction of the McVAHRES instrument is presented along with an evaluation of its performance. Details of the sophisticated electronics and operating software, which were also designed and built in-house, are discussed.

Chapter four presents the results of variable impact energy studies carried out on CO and some unsaturated hydrocarbons [FE&94, FKH94] using McVAHRES. The breakdown of the Bethe-Born theory at low impact energies is also illustrated.

The development of a rigorous methodology for the acquisition of data and subsequent procedures for deriving generalised oscillator strengths are presented in detail in chapter five.

The GOS profiles of the  $a_{1g}$ ,  $t_{1u}$ ,  $t_{2g}$  and  $e_g$  features in the S 2p spectrum of SF<sub>6</sub> were determined using McVAHRES. Due to the performance of the instrument, the momentum transfer range was extended to greater than 19 a.u.<sup>-2</sup>, compared to less than 6 a.u.<sup>-2</sup> in the study by Ying *et al.* [YML93]. In addition, due to superior resolution, the GOS profile of a feature at 181 eV in the S 2p spectrum is documented. These results are presented in chapter 6.

As an introduction to ISEELS techniques, experiments were conducted in the early stages of this project under dipole conditions using an older EEL spectrometer (known as McFALRES, for Fixed-Angle, Low Resolution, Electron Spectrometer) [H90]. This work, intended to explore specific connections between core excitation spectra, electronic structure and bonding, is presented in references FH92 and FH94. In the first of these two studies, specific core excitation features in the C 1s and O 1s EEL spectra of phenol, p-hydroquinone and p-benzoquinone are identified which are indicative of either a benzenoid or quinoid structure [FH92]. In the second study, along the same lines, spectral features in the C 1s and O 1s spectrum of the three isomeric cyclohexanediones and cyclohexanone are identified as being characteristic of either a keto or enol tautomeric

structure [FH94]. The value of semi-empirical calculations (HAM/3 and EHMO) within the equivalent core analogy in aiding the spectral interpretation of core excitation spectra is also demonstrated in this work.

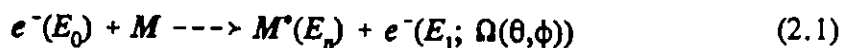
In conclusion, this work documents a high resolution, variable impact energy, variable scattering angle electron energy loss spectrometer which has been designed and built to carry out quantitative studies of dipole allowed as well as spin and dipole forbidden electronic transitions that accompany conditions of increasing momentum transfer. Its performance is demonstrated by the results of variable impact energy experiments carried out on CO and some unsaturated hydrocarbons, and variable scattering angle experiments performed on CO, N<sub>2</sub> and SF<sub>6</sub>.

## Chapter 2

### THEORY OF ELECTRON ENERGY LOSS SPECTROSCOPY

#### 2.1 Theory of Electron Energy Loss Spectroscopy

In electron energy loss spectroscopy (EELS), a 'monoenergetic' beam of electrons of incident energy  $E_0$  is produced via acceleration from an electron source through a potential difference. (In practice of course, the beam is not monoenergetic and always has a finite energy spread based on the FWHM of the profile of the electron energy distribution in the beam. For an unmonochromated source, the minimum intrinsic energy spread of the beam is typically 0.5 eV, while for monochromated beams, the energy spread may be  $< 0.1$  eV). These electrons elastically and inelastically scatter upon collision with an atom or molecule  $M$  in a field free region. This process can be represented by the following simple expression:

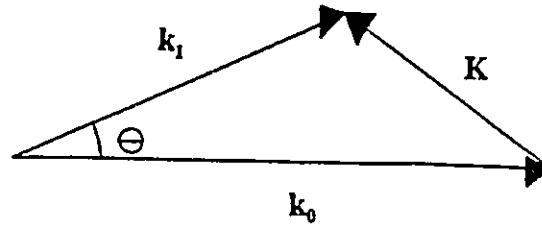


where  $M$  is the target species,  $e^-(E_0)$  is the incident electron with energy  $E_0$ ,  $M^*(E_n)$  is the target species after excitation to an excited state with energy  $E_n$  relative to the ground state and  $e^-(E_1; \Omega(\theta, \phi))$  is the outgoing electron with residual energy  $E_1$  having been scattered through angle  $\Omega(\theta, \phi)$  with respect to the incident beam during the collision. For gas phase electron energy loss experiments, the target species usually has no preferential

orientation in space, and thus the azimuthal angle dependence ( $\phi$ ) can effectively be ignored. It should also be noted that excitation to state  $n$  implies the set of all degenerate substates at energy  $E_n$ .

By conservation of energy  $E_n = E_0 - E_1$ , and thus EELS provides a direct measure of electronic transitions. For valence shell excitation,  $E_n$  is  $< 50$  eV, while for inner shell excitation,  $E_n$  ranges from 50 eV ca. 2000 eV. There is also conservation of momentum. Within a scattering model, this can be represented vectorially below in figure 2.1:

Fig. 2.1



where  $k_0$  is the wavevector of the incident electron with momentum  $|k_0|$ ,  $k_1$  is the wavevector of the outgoing electron scattered through an angle  $\theta$  with momentum  $|k_1|$  and  $K$  is the resultant momentum transfer.  $K$  can be expressed in terms of  $k_0$  and  $k_1$  using the simple cosine relation:

$$K^2 = |K|^2 = |k_0 - k_1|^2 = k_0^2 + k_1^2 - 2k_0k_1\cos\theta \quad (2.2)$$

Strictly speaking, for true conservation of energy and momentum the recoil energy



imparted to the target atom or molecule by the incident electron must be included. However, because of the large mass disparity between the electron and target, the contribution to the total momentum of the system from target recoil can effectively be ignored.

In practice, an electron energy loss experiment involves measuring the intensity of the current scattered through a solid angle  $\Omega$  at a particular energy loss  $E_n$ , which is proportional to the differential cross section. The differential cross section is denoted as:

$$\frac{d\sigma_n}{d\Omega(E_n, \theta)} \quad \text{for discrete states}$$

$$\frac{d^2\sigma}{dE d\Omega(E_n, \theta)} \quad \text{for excitation to continuum states in energy range } dE$$

## 2.2 Analogies with Photoabsorption

Under conditions of fast electron impact and small scattering angles, there exists a quantitative relationship between the differential cross section and the photoabsorption cross section. Such conditions in EELS are often referred to as corresponding to the dipole regime, as the electronic transitions excited in the target are dominated by those obeying dipole selection rules. It is possible to rationalise this relation using the semi-classical, virtual photon model [W74]. Electronic excitations in the target are generally produced by distant collisions; meaning distant relative to the dimension of the target. (This relative collision distance is known as the *impact parameter*). As such, the electric field experienced by the target is sharply pulsed in time. For sufficiently fast electrons,

the electric field approaches a delta function in time. The Fourier transform of such an electric field function contains all frequency components (with equal weighting) and thus resembles a beam of white light. The probability of absorbing a 'pseudo photon' from this spectrum depends upon the intrinsic photoabsorption characteristics of the target. It must be noted however, that unlike photoabsorption, the electron impact process is inherently *non-resonant*. This has important consequences, in that intense features in electron energy loss spectra do not display line saturation, which is a common phenomenon in photoabsorption due to the resonant nature of photoexcitation [CCB91].

### 2.3 Bethe-Born Theory

In the case of fast collisions (fast relative to the mean orbital velocity of the electrons in the shell associated with a particular inelastic process), the effect of an incident electron upon an atom or molecule can be treated as a small first order perturbation. Using this elementary picture, Bohr first developed the general structure of modern collision cross section expressions using his theory of the stopping power of materials for fast particle bombardment [B13, B15]. This theory was based upon an impulse approximation which treats the collision as a sudden transfer of energy and momentum to the target electrons. However, Bohr's collision cross section formulations proved inadequate for certain dynamical details, due mainly to the fact that quantum mechanics was still in its infancy at the time.

For a quantitative treatment of small angle, inelastic scattering of fast electrons, the use of quantum mechanical scattering theory is necessary. Such a theory was initially

derived by Hans Bethe in 1930 [B30] based upon the first Born approximation [FBA], which assumes that the interaction between the fast incident electron and target is weak [M58, A71]. This derivation was later extended by Fano [F54] and later reviewed with more physical insight by Inokuti [IIT71].

It is customary to treat first the case of electron scattering from the H atom and then generalise to the case of multielectron atoms and molecules. Within the first Born approximation the incident electron, which can be treated as a plane wave, is negligibly distorted by the collision process. As such, the differential cross section for inelastic scattering of an electron into an angle  $\theta$  while exciting a hydrogen atom to the  $n^{\text{th}}$  discrete state is given by (in Hartree atomic units) [W74]:

$$\frac{d\sigma_n}{d\Omega(\theta)} = (4\pi)^{-2} \left(\frac{k_1}{k_0}\right) \left| \int U_{0n}(r_2) \exp[i(k_0 - k_1) \cdot r_1] d\tau \right|^2 \quad (2.3)$$

where:

$$U_{0n}(r_2) = 2 \langle \Psi_n(r_2) | \frac{1}{r_1} - \frac{1}{r_{12}} | \Psi_0(r_2) \rangle \quad (2.4)$$

and  $\Psi_0(r_2)$  is the ground state wavefunction,  $\Psi_n(r_2)$  is the excited state wavefunction,  $r_1, r_2$  are the coordinates of the incident and target electrons and  $k_0, k_1$  are the wavevectors of the incident and scattered electrons.  $\hbar K^2$  is the momentum transfer, which is related to  $k_0$  and  $k_1$  by equation 2.2.

Expression 2.3 can be generalised to a multielectron atom target of nuclear charge  $Z_m$  by including the interaction with all of the target electrons, i.e.

$$U_{0n} = 2 \langle \Psi_n | \frac{Z_n}{r_1} - \sum_{s=1}^N (r_1 - r_s)^{-1} | \Psi_0 \rangle \quad (2.5)$$

where  $r_1$  is the position vector of the incident electron relative to the nucleus and the integration is over all the atomic electrons with coordinates  $r_s$ .

Making use of the Bethe integral [B30], given by:

$$\int [\exp(i\mathbf{K} \cdot \mathbf{r}_1) / |\mathbf{r}_1 - \mathbf{r}_s|] d\mathbf{r} = \left(\frac{4\pi}{K^2}\right) \exp(i\mathbf{K} \cdot \mathbf{r}_s) \quad (2.6)$$

followed by substitution of 2.5 into 2.3 leads to the following expression:

$$\frac{d\sigma_n}{d\Omega(\theta)} = 4 \left(\frac{k_1}{k_0}\right) K^{-4} \left| \langle \Psi_n | \sum_{s=1}^N \exp(i\mathbf{K} \cdot \mathbf{r}_s) | \Psi_0 \rangle \right|^2 \quad (2.7)$$

which can be rewritten as:

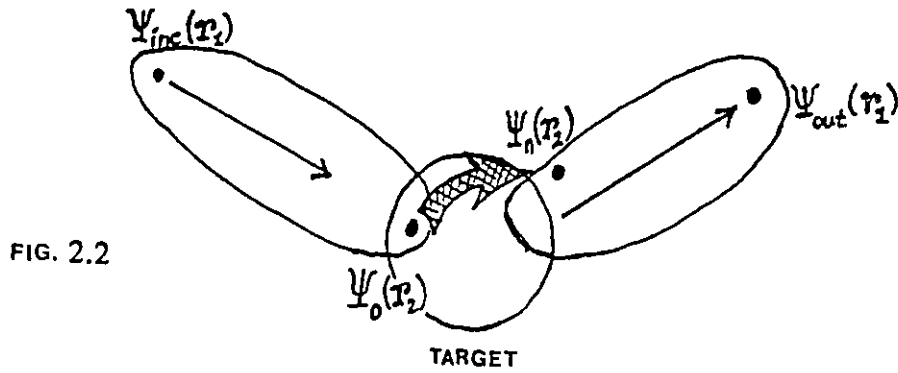
$$\frac{d\sigma_n}{d\Omega(\theta)} = 4 \left(\frac{k_1}{k_0}\right) K^{-4} \left| \epsilon_{0n}(K) \right|^2 \quad (2.8)$$

where

$$\epsilon_{0n}(K) = \langle \Psi_n | \sum_{s=1}^N \exp(i\mathbf{K} \cdot \mathbf{r}_s) | \Psi_0 \rangle \quad (2.9)$$

Equation 2.7 represents the differential cross section for small angle inelastic scattering from complex atoms.

It is instructive at this point to consider the origin of the  $\exp(i\mathbf{K} \cdot \mathbf{r})$  term in the matrix element in equation 2.9. This can be derived using a simple two-electron state picture shown below in figure 2.2 for a fast incident electron and one of the  $N$  electrons in the target atom (whose coordinates are  $\mathbf{r}_1$ ) described by coordinate  $\mathbf{r}_2$ .



The initial two-electron state describes the incoming fast electron 1 by  $\Psi_{inc}(\mathbf{r}_1)$  and the ground state electron 2 by  $\Psi_0(\mathbf{r}_2)$ . The final two-electron state describes the outgoing scattered electron 1 by  $\Psi_{out}(\mathbf{r}_1)$  and the excited electron 2 in the target by  $\Psi_n(\mathbf{r}_2)$ . Thus, assuming a weak interaction,  $\epsilon_{0n}(\mathbf{K})$  can be expressed as:

$$\epsilon_{0n}(\mathbf{K}) = \langle \Psi_n(\mathbf{r}_2) \cdot \Psi_{out}(\mathbf{r}_1) | H_{int} | \Psi_{inc}(\mathbf{r}_1) \cdot \Psi_0(\mathbf{r}_2) \rangle \quad (2.10)$$

where  $H_{int}$  is the Coulombic interaction operator, given by:

$$H_{int} = \frac{1}{|\mathbf{r}_1 - \mathbf{r}_2|} \quad (2.11)$$

Within the first Born approximation, the incoming and outgoing scattered electron can be

expressed as single plane waves, i.e.:

$$\Psi_{inc}(\mathbf{r}_1) \rightarrow \exp(i\mathbf{k}_0 \cdot \mathbf{r}_1) \quad (2.12)$$

$$\Psi_{out}(\mathbf{r}_1) \rightarrow \exp(i\mathbf{k}_1 \cdot \mathbf{r}_1) \quad (2.13)$$

Substitution of 2.12 and 2.13 into 2.10 yields the following more explicit form:

$$\epsilon_{0n}(\mathbf{K}) = \int d\mathbf{r}_1 \int d\mathbf{r}_2 \Psi_n^*(\mathbf{r}_2) \exp(-i\mathbf{k}_1 \cdot \mathbf{r}_1) \left( \frac{1}{|\mathbf{r}_1 - \mathbf{r}_2|} \right) \exp(i\mathbf{k}_0 \cdot \mathbf{r}_1) \Psi_0(\mathbf{r}_2) \quad (2.14)$$

or equivalently,

$$\epsilon_{0n}(\mathbf{K}) = \int d\mathbf{r}_1 \int d\mathbf{r}_2 \Psi_n^*(\mathbf{r}_2) \left( \frac{1}{|\mathbf{r}_1 - \mathbf{r}_2|} \right) \exp(i[\mathbf{k}_0 - \mathbf{k}_1] \cdot \mathbf{r}_1) \Psi_0(\mathbf{r}_2) \quad (2.15)$$

Letting  $\mathbf{K} = \mathbf{k}_0 - \mathbf{k}_1$  and  $\mathbf{r}_1 = \mathbf{r}_2 - \mathbf{r}$ , substitution into 2.15 yields:

$$\int d\mathbf{r}_2 \Psi_n^*(\mathbf{r}_2) \left[ \int d\mathbf{r} \left( \frac{1}{r} \right) \exp(i\mathbf{K} \cdot \mathbf{r}) \right] \exp(i\mathbf{K} \cdot \mathbf{r}_2) \Psi_0(\mathbf{r}_2) \quad (2.16)$$

Recognising that 2.16 can be simplified using a Fourier transform, one obtains the final expression:

$$\epsilon_{0n} = \text{const} \langle \Psi_n(\mathbf{r}_2) | \exp(i\mathbf{K} \cdot \mathbf{r}_2) | \Psi_0(\mathbf{r}_2) \rangle \quad (2.17)$$

which depends *only* upon the electron in the target with coordinate  $\mathbf{r}_2$ . Letting  $\mathbf{r}_2 = \mathbf{r}_i$  in 2.17 and summing over all  $N$  electrons in the target leads directly to the operator in expression 2.7 for a multielectron atom.

To extend this treatment to include electron-molecule scattering, one uses the appropriate molecular wavefunction. Within the Born-Oppenheimer approximation, the

molecular wavefunctions can be represented as a product of nuclear and electronic functions, i.e.:

$$\Psi_{e,v,r} = \Psi_e(r; Q_0) \cdot \Psi_{v,r}(Q) \quad (2.18)$$

where  $\Psi_{e,v,r}$  is the total rovibronic wavefunction encompassing the electronic, vibrational and rotational motions,  $r$  and  $Q$  are the electronic and nuclear coordinates and  $Q_0$  is the average ground state nuclear configuration. Substitution of 2.18 into 2.9 yields:

$$\epsilon_{0n} = \langle \Psi_{e_n} | \sum_{s=1}^N \exp(iK \cdot r_s) | \Psi_{e_0} \rangle \cdot \langle \Psi_{v_n, r_n} | \Psi_{v_0, r_0} \rangle \quad (2.19)$$

where  $\langle \Psi_{v_n, r_n} | \Psi_{v_0, r_0} \rangle$  is the Franck-Condon factor representing the overlap of the initial and final state vibrational wavefunctions. It has been observed experimentally that the Franck-Condon-weighted vibrational intensities derived from valence shell electron energy loss spectra are in agreement with optical values, even under conditions where the first Born approximation fails [LS&68].

It is of interest to note that the cross section expressions 2.3 and 2.7 consist of two factors of different nature. The factor  $4(k_1/k_0)K^4$  in 2.7 depends upon the energy loss and experimentally defined scattering conditions. It is representative of the incident electron *only*. Inokuti has shown [IIT71] that by expressing the cross section in terms of  $dK$  rather than  $d\Omega(\theta)$  via a suitable transformation, the analogous factor describing the incident electron can be expressed as the Rutherford cross section [IIT71] for scattering of a charged particle by a free and initially stationary electron. The remainder of expression 2.7 describes the response of the target to a transfer of momentum, and it reflects the

dynamics of the atom. In the fields of nuclear and particle physics, this factor is commonly referred to as the inelastic-scattering form factor. It is intrinsically different than the factor encompassing the incident electron due to the fact that the electrons responsible for internal excitation in the target are initially bound rather than free and are in motion about the nucleus. Thus, the factor describing the target is in the form of a matrix element. It gives the conditional probability of an excitation in the atom from the ground state to a particular excited state  $n$  effected by a transfer of momentum in the amount of  $\hbar\mathbf{K}$  [F63].

#### 2.4 The Generalised Oscillator Strength

Rather than using the cross section expressions developed in the previous section to describe electron impact excitation (within the first Born approximation), a related quantity, the generalised oscillator strength (GOS) is employed. It was first introduced by Bethe [B30] and has the general form:

$$f_n(\mathbf{K}) = \left(\frac{E_n}{2K^2}\right) |\epsilon_{0n}(\mathbf{K})|^2 \quad (2.20)$$

Combination of expression 2.20 and 2.8 yields an effective generalised oscillator strength of the form:

$$f_n'(\mathbf{K}) = \left(\frac{E_n k_0}{2 k_1 K^2}\right) \frac{d\sigma_n}{d\Omega} \quad (2.21)$$

which can be determined entirely from experimental parameters, independent of the validity of the first Born approximation. Such a framework is necessary in situations



where the first Born approximation is no longer valid. This will be discussed in section 2.5 of this chapter and also in chapter 4 for near-threshold ( $E_0$  approaching  $E_n$ ) electron impact excitation.

The GOS is a generalisation of the optical oscillator strength (OOS):

$$f_n = \left(\frac{E_n}{2}\right) \epsilon_{10n}^2 \quad (2.22)$$

where  $\epsilon_{10n}$  is the matrix element for the electric dipole transition from the ground state  $|0\rangle$  to the excited state  $|n\rangle$ . It can be shown that in the limit of zero momentum transfer, the GOS converges to the OOS using the following power series expansion:

$$\exp(i\mathbf{K} \cdot \mathbf{r}) = 1 + (i\mathbf{K} \cdot \mathbf{r}) + \frac{(i\mathbf{K} \cdot \mathbf{r})^2}{2} + \dots + \frac{(i\mathbf{K} \cdot \mathbf{r})^n}{n!} \quad (2.23)$$

Substitution of 2.23 into the matrix element in 2.7, and noting that if  $\Psi_0$  and  $\Psi_n$  are orthogonal, one obtains:

$$\epsilon_{0n}(\mathbf{K}) = \epsilon_1(i\mathbf{K}) + \epsilon_2(i\mathbf{K})^2 + \epsilon_3(i\mathbf{K})^3 + \dots \quad (2.24)$$

where :

$$\epsilon_p = \langle \Psi_n | r^p | \Psi_0 \rangle \left(\frac{1}{p!}\right) \quad (2.25)$$

Substitution into 2.20 and grouping terms yields the final form:

$$f_n(\mathbf{K}) = \left(\frac{E_n}{2}\right) [ \epsilon_1^2 + (\epsilon_2^2 - 2\epsilon_1\epsilon_3) \mathbf{K}^2 + \dots ] \quad (2.26)$$

where  $\epsilon_1$  is the dipole matrix element (i.e.  $p = 1$  in equation 2.25),  $\epsilon_2$  is the quadrupole

matrix element ( $p = 2$  in 2.25),  $\epsilon_3$  is the octupole matrix element and so on. It can thus be seen that, in the limit of zero momentum transfer, equation 2.26 reduces to the form of the OOS, or equivalently:

$$\lim_{K \rightarrow 0} f_n(\mathbf{K}) = f_n \quad (2.27)$$

Experimentally then, a large  $E_0$  and small scattering angle  $\theta$  results in a small momentum transfer, which can be seen from figure 2.1. In turn, this small momentum transfer leads to equation 2.27 from 2.26. Thus, such experimental scattering conditions are often said to correspond to the dipole (optical) regime.

This limiting behaviour in the limit of zero momentum transfer can be used to absolutely normalise GOS functions derived from a series of measurements made at several values of  $K^2$  via extrapolation to  $K^2 = 0$  and matching to the OOS. This approach has been used by Lassetre and others [LS71, HSL71], and is used in the GOS work performed using McVAHRES, discussed in chapters 5 and 6. Alternatively, it is possible to derive absolute GOS values for small momentum transfer conditions using the Thomas-Rieche-Kuhn sum rule [FC68]. It states that the total integrated oscillator strength over the discrete and continuum states in the energy loss spectrum is equal to the total number of electrons in the target involved. A similar rule [B30] accommodates finite (and constant) momentum transfer scattering conditions as well. Recently, using extremely small scattering angles and very high impact energies (relative to  $E_p$ ), Chan *et al.* have obtained accurate optical oscillator strengths for transitions in noble gases [CCB91, CC&92]. Such results have proven valuable in the field of astronomy and atmospheric

photochemistry.

In general, in addition to providing information about dipole forbidden states, McVAHRES can also yield valuable information about dipole allowed transitions.

### 2.5 Non-Dipole Transitions

Experimentally, it is possible to increase the momentum transfer to the target via variation of the scattering angle and/or variation of the impact energy of the incident electron. This corresponds to variation of  $k_0$  and/or  $\theta$  to increase  $K$  in the simple vector diagram shown in figure 2.1. It can be seen from equation 2.26 that, as the momentum transfer becomes significant, so does the contribution to the GOS from higher order multipole matrix elements. Therefore, under conditions of significant momentum transfer electron impact methods can access electronic transitions that are forbidden optically. Non-dipole valence transitions have been known for some years now, such as the quadrupole-allowed He  $1s \rightarrow 2s$  transition at 20.6 eV [LSD64, SL64]. However, dipole forbidden, *inner* shell transitions are rare by comparison. Considering the transition matrix elements in equation 2.26, even at relatively large momentum transfer, the contribution to the GOS for inner shell excitation is dominated by dipole transitions. This is due to the very small spatial extent of the core orbitals, which results in the  $r^1$ -weighted dipole transition moment being much greater than the  $r^2$ -weighted quadrupole moment, and so on for the higher order transition moments. As an example, non-dipole O  $1s$  transitions would be negligible until  $K > 20 \text{ a.u.}^{-1}$  [H90]. Thus, the motivation for the work presented in this thesis was to develop an instrument capable of providing

sufficiently large momentum transfer conditions to investigate non-dipole, inner shell excitations while maintaining the flexibility to conduct experiments under dipole conditions as well.

For conditions where  $E_0$  is fixed and equal to several times  $E_n$ , variation of the scattering angle (and thus  $K^2$  from figure 2.1) enhances the probability of observing transitions that are forbidden optically based on considerations of angular momentum. Examples include the He  $1s \rightarrow 2s$  transition cited above and the  $SF_6$  work discussed in chapter 6. However, as  $E_0$  approaches  $E_n$  (the so-called near threshold experiment), another type of forbidden transition becomes significant. Under these conditions, the first Born approximation is no longer valid, and the interaction between the incident electron and the target can no longer be considered in terms of a first order perturbation. Indeed, for incident electron energies that approach the energy of excitation of an electron in the target, the electrons effectively lose their identity in the resulting slow collision. The probability that they may exchange thus becomes significant. If the electrons have opposite spin, the resulting electronically excited state will have total spin angular momentum  $S = 1$ , which implies a triplet state. Experimentally, this is manifested in the appearance of a triplet partner to the singlet feature whose energy of excitation is approached by  $E_0$ . One of the first examples of such an inner shell excited triplet state was the  $^3\Pi$  feature observed by Shaw et. al. in the N  $1s$  spectrum of  $N_2$  [SK&82]. Chapter four discusses triplet states of CO and some saturated hydrocarbons observed using McVAHRES.

## 2.6 Summary and Translation from Theory to Experiment

This chapter has outlined the connection between EELS and photoabsorption that exists under conditions of large impact energies and small scattering angles. Under such conditions, EELS spectra are dominated by dipole allowed transitions. References FH92 and FH94 present the results of studies performed under such experimental conditions which illustrate the value of dipole regime EELS in providing information about chemical bonding and electronic structure. In addition, it was noted that EELS under conditions of extremely small momentum transfer can provide accurate OOS values that are of use in such fields as astronomy and atmospheric photochemistry.

The Bethe-Born theory was introduced in this chapter, in addition to the concept of the generalised oscillator strength which effectively describes the target's response to collision with an electron. Under experimental conditions where the scattering angle increases and the impact energy is several times  $E_0$ , it is possible to derive the GOS as a function of  $K^2$ . Extrapolation of the relative GOS to  $K^2 = 0$  allows absolute normalisation using OOS values. Alternatively, sum rules can be used to derive absolute GOS values. Chapter 6 presents GOS studies performed on  $SF_6$  using McVAHRES.

It was also shown that as the momentum transfer is increased under Bethe-Born conditions (experimentally corresponding to large  $E_0$  and large scattering angles), the contribution to the GOS from dipole forbidden transitions increases. Chapter 6 describes a non-dipole feature observed under such conditions in the S 2p spectrum of  $SF_6$ .

It was discussed how the momentum transfer can be made significant when the impact energy approaches the energy of excitation. Such conditions are conducive to

incident/target electron exchange, which results in the observation of triplet excited states. Chapter 4 presents the results of triplet state studies performed under low impact energy conditions for CO and some unsaturated hydrocarbons. Under such conditions, it was noted that the Bethe-Born theory no longer applies and the GOS concept is no longer valid. It is still possible to define a momentum transfer, however. To this end, chapter 4 presents a momentum transfer study of a core-excited triplet state of CO, obtained experimentally by varying the scattering angle at low impact energy.

## Chapter 3

### INSTRUMENT DESIGN AND PERFORMANCE

#### 3.1 Introduction

The vast majority of studies performed using electron energy loss spectroscopy have been conducted under conditions which simulate photoabsorption (as described in chapter 2). The typical minimal electron spectrometer for such dipole regime studies consisted of an unmonochromated electron gun impinging on a collision region, with the scattered electrons being collected and analysed at a fixed scattering angle using a simple lens and hemispherical deflector with serial detection. Examples of such instruments include that used by G. Wight [W74] in the early 1970's at UBC and the McMaster ISEELS instrument [H90]. The typical energy resolution offered by these instruments is about 0.7 eV FWHM.

The purpose of this work was to design and build an instrument that could operate under non-dipole conditions and thus investigate inner-shell (and valence) electronic transitions that are inaccessible using photoabsorption techniques. From the Bethe-Born treatment of momentum transfer and theory of slow collisions discussed in chapter two, it can be seen that dipole and spin forbidden transitions can be induced experimentally by varying the scattering angle or impact energy. The instrument discussed in this chapter incorporates both of these capabilities, through a rotatable analyser (120° scattering angle

range) and advanced electron optics that allow low impact energy ( $< 100$  eV above the energy of the transition) operating conditions.

More specifically, the optics were designed to operate with particular resolution requirements in mind, which are summarised below in Table 3.1.

Table 3.1. Resolution objectives for McVAHRES

Spectrum Type	Energy loss range (eV)	Desired resolution
High res. valence and core	10 - 500	$< 50$ meV
High res. core	50 - 500	$< 100$ meV
Low res. core	50 - 2000	$< 500$ meV

In addition, the optics were designed to accommodate a range of impact energies from 200 eV to 2 keV. In order to further maximise the flexibility of this instrument, in regards to the number of distinctly different types of experiments that could be performed, the power supplies associated with the optics system were computer-interfaced, as was the rotation control.

Overall, this instrument is unique in that it combines high resolution, variable angle and variable impact energy into one versatile package. Indeed, its name, McVAHRES, has been chosen to reflect this: the McMaster Variable Angle High Resolution Electron Spectrometer.



## 3.2 Design

### 3.2.1 Mechanical Design and Materials Considerations

Cross-sectional and aerial views of the complete instrument are presented in figure 3.1. Since stray magnetic fields are detrimental to the performance of electron spectrometers in general, only non-magnetic materials were used throughout the construction of the instrument. The vacuum chamber consists of two 1" thick, 33" diameter Al plates enclosing the ends of a 3/16" thick, 32" diameter, #316 stainless steel cylinder. The inside vacuum surfaces of the Al plates are polished. Two 0.5" thick, #316 stainless steel rings welded to the inside of both ends of the cylinder form the vacuum-tight surface against the Al plates, with Viton O-rings in between. The analyser entrance and monochromator lenses, as well as the analyser and monochromator hemispheres, are precision machined from Al with inner surfaces polished and coated with baked colloidal graphite which are subsequently polished. This reduces patch fields, contact potentials and electron scattering from the lens surfaces. Sapphire ball insulators between individual lens elements also provides rigid location, thus maintaining alignment. A large gap between the inner and outer hemispheres minimises the influence of patch fields (due to a low filling factor) and allows for the installation of a parallel detection unit in the future. Owing to the high operating temperatures of the electron gun (1500-3000° K), it was therefore machined from non-magnetic, #316 stainless steel. Ceramic Alumina spacers and rods are used to isolate the various elements. Commercial tungsten filaments are used (Agar, model 1401).

All internal wiring utilizes bare copper wire, AWG 22 gauge or smaller, encased

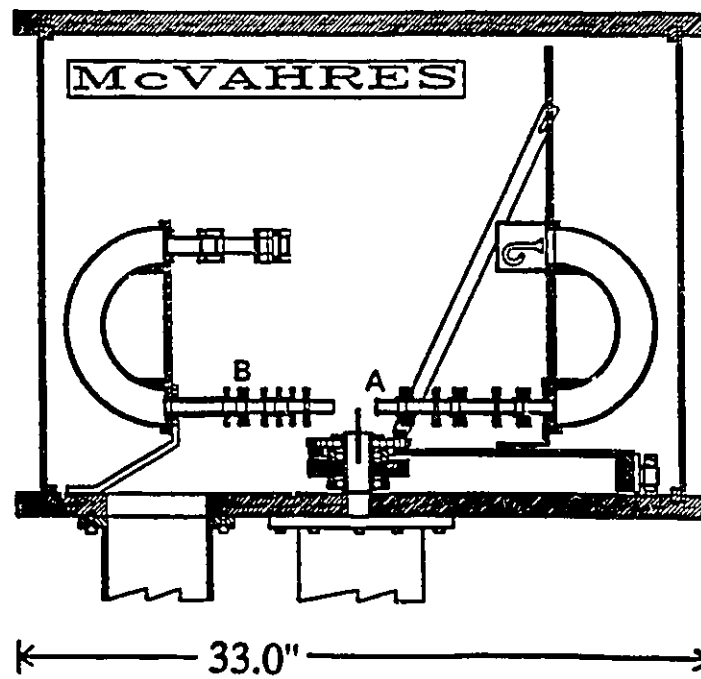
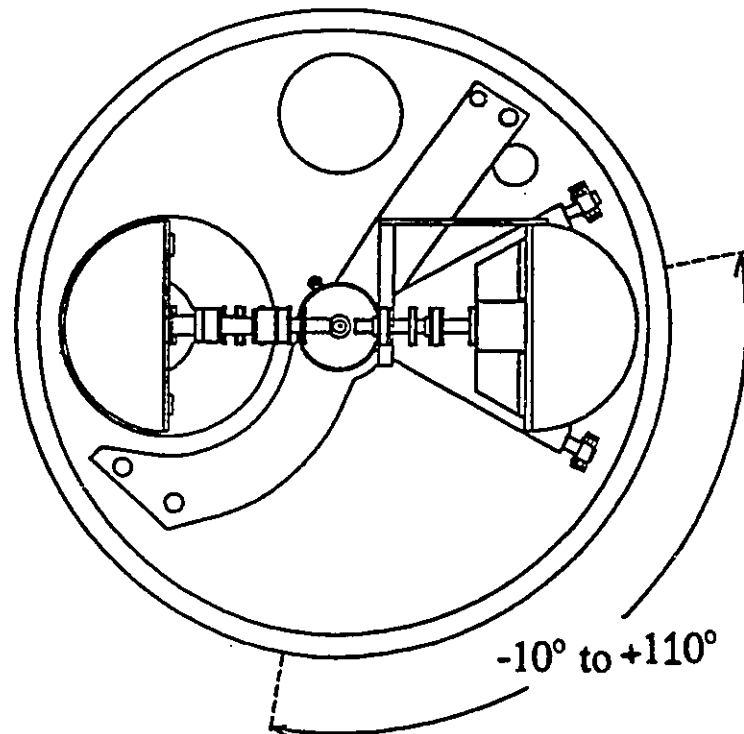


Fig. 3.1 Aerial (top) and cross-sectional views of McVAHRES

in teflon tubing. Ten Oxford ten-pin, vacuum-isolated connectors are used to interface the internal wiring with external cables. These connectors are isolated from the base Al plate via teflon casings.

### 3.2.2 Vacuum

A block diagram of the complete vacuum system and sample line is presented in figure 3.2. The base plate of the vacuum chamber has two pump ports. The main port is fitted with a Balzers TPH 510 Turbo Molecular Pump ( 500 l/s N<sub>2</sub> ) backed by an Alcatel rotary pump which provides a typical base pressure of ca.  $5 \times 10^{-7}$  Torr without baking. The second, smaller port allows for differential pumping in the future.

Gaseous samples are introduced either through a capillary array gas jet inlet centered in the collision region, which provides a 100:1 aspect ratio, or through a 1/8" copper tube which allows entrance into the chamber at the perimeter of the base plate (i.e. far from the collision region). A three-way, Whitey ball-valve distributes the sample gas through one of the two channels described above. The sample flow rate is controlled by a Granville-Phillips Series 203 leak valve. The low pressure side of the turbo is monitored using a thermocouple gauge. The pressure on the high vacuum side is monitored using a nude gauge fitted with W filaments. Both gauges are connected to a Varian Ratiomatic (Model 843) ion gauge controller. A relay circuit was incorporated into the Varian controller that opens or closes a 15 Amp, 120 volt, solid state relay switch at a user-defined pressure trip-point. The pressure trip point is selected via a ten-turn potentiometer. All high voltage power supplies are protected from high-voltage

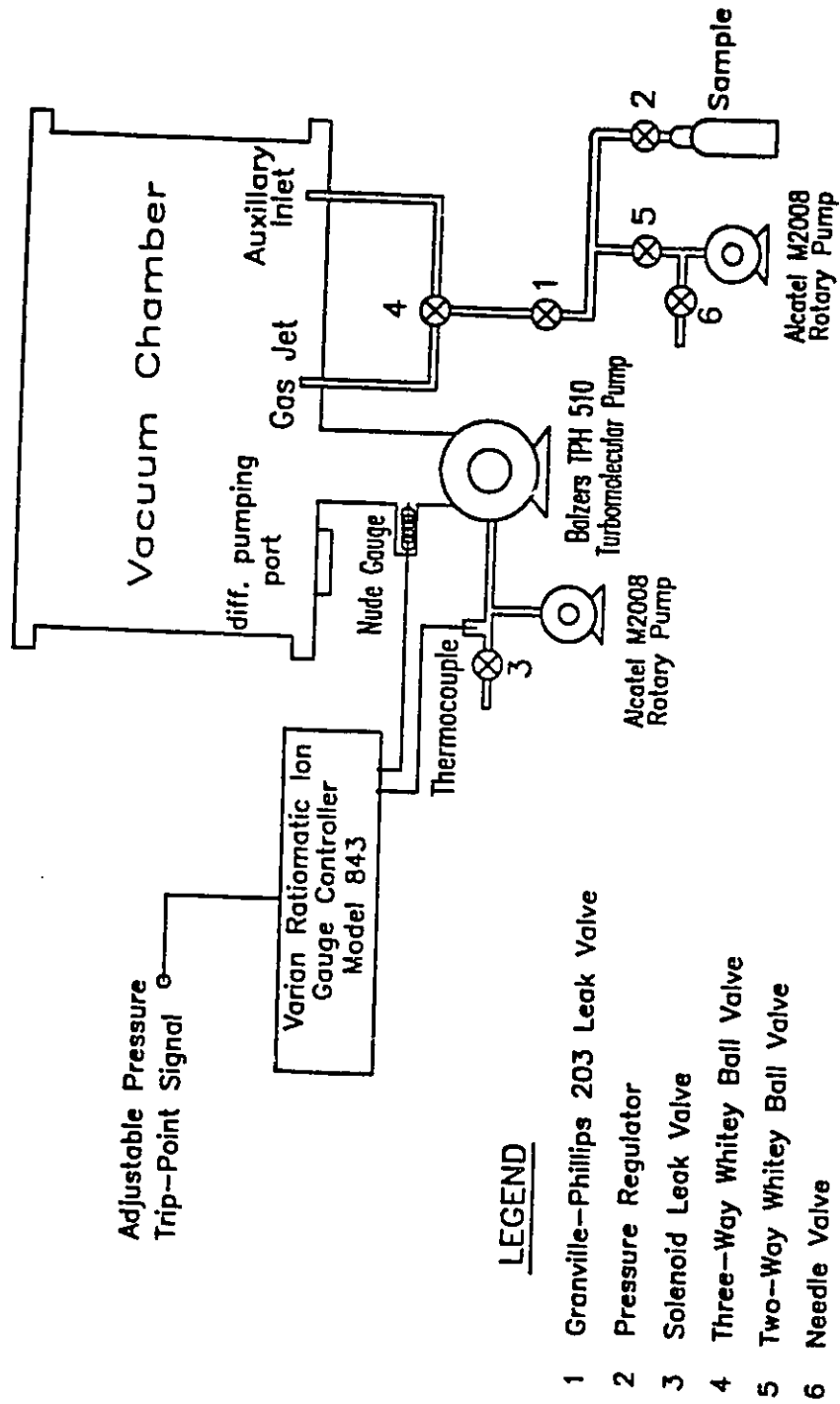


Fig. 3.2 Schematic of McVAHRES vacuum system

breakdown by this circuit in the event of sudden rise in pressure past the trip point. The relay also maintains a power-off state in the event of a line voltage power failure, such that when the line voltage is restored, no surges will affect the sensitive electronics.

### 3.2.3 Rotation Mechanism

A schematic of the rotation mechanism is presented in figure 3.3. A 3/8" thick, Al rotation platform is supported by a double bearing mounted shaft at its centre, (which is in turn supported on the base of the chamber by a 3/4" thick Al beam), and two stainless steel, 1" diameter wheels at its perimeter. This design provides excellent overall stability and smooth rotation. The rotation platform incorporates a 4" diameter gear at its centre which is coupled to a 1" diameter drive gear mounted on a 0.5" diameter, 24" long vacuum feedthrough, which serves as the drive shaft. The drive shaft is coupled to a reduction gear (360:1) at its base which is driven by an inexpensive stepper motor, the controller of which is in turn computer interfaced. There is 5° of backlash that must be accounted for whenever the rotation direction is changed. In spite of this, however, the complete interfaced rotation mechanism provides an angular precision of  $> 0.1^\circ$  for same direction scanning and an accuracy better than 1% for scattering angles up to 90°. The angular range is 120 degrees. An angular position calibration curve is shown in Figure 3.4, which plots the scattering angle indicated by the control algorithm against the actual angle determined by careful measurements and simple geometry. The error associated with the geometrical measurements is estimated to be  $\pm 0.05^\circ$ , and thus the dominant error arises from inaccuracy in the rotation mechanism. As an additional internal check, it is

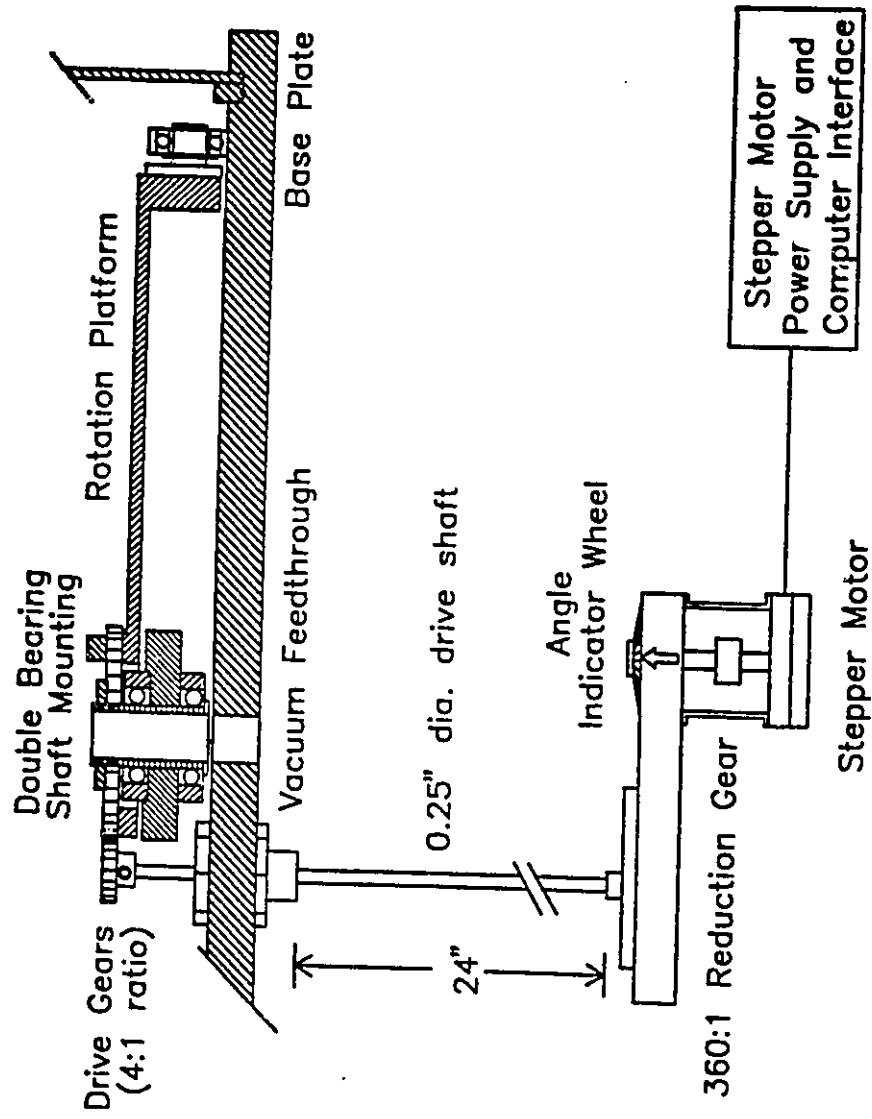


Fig. 3.3 Schematic of computer-interfaced rotation mechanism

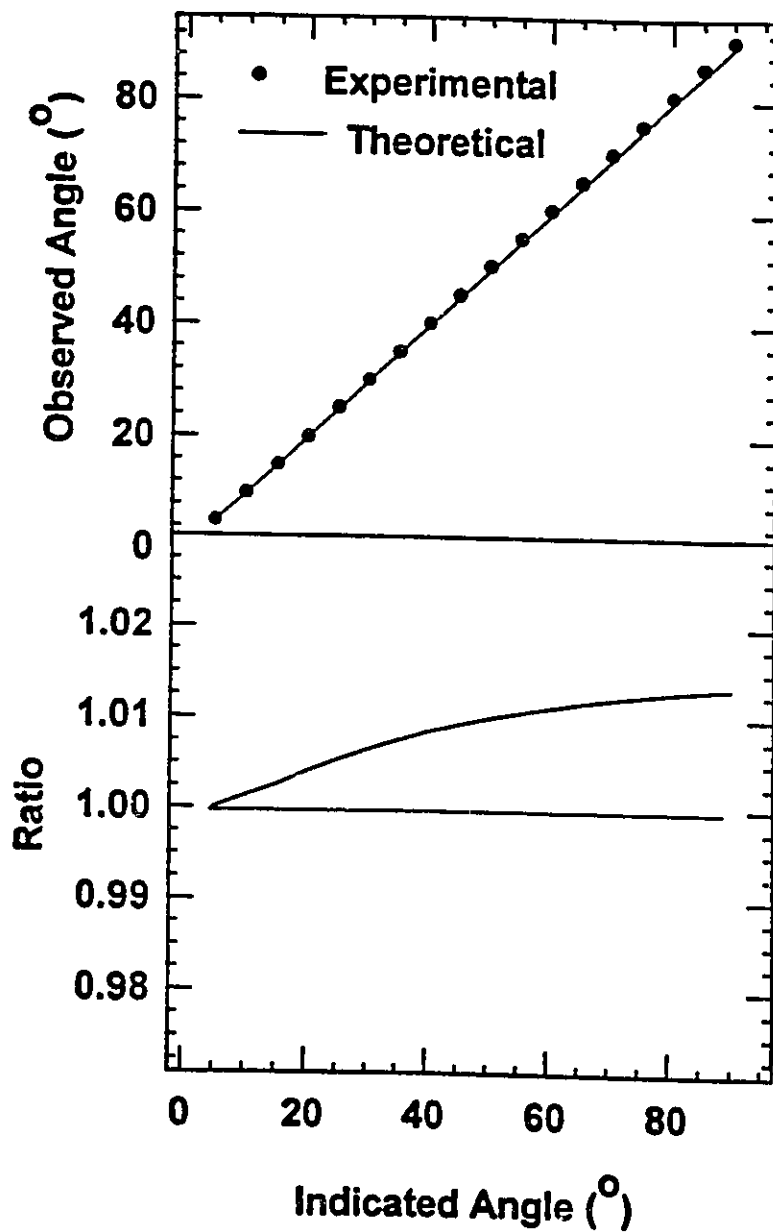


Fig. 3.4 Comparison of scattering angle indicated by rotation mechanism to that determined experimentally using simple geometry.

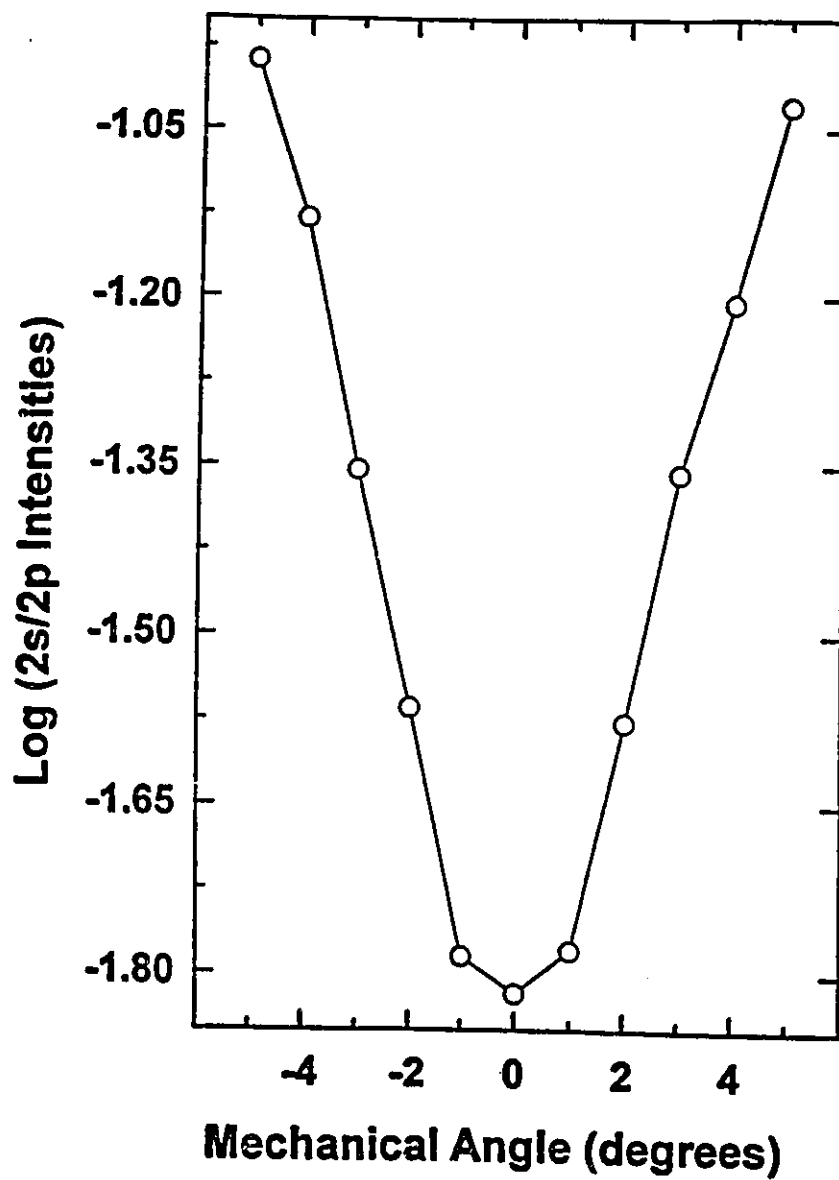


Fig. 3.5 Calibration of the zero degree scattering angle using  $(1s^{-1}, 2s)$  and  $(1s^{-1}, 2p)$  transition intensities for He.



possible to calibrate the experimental zero angle using the ratio of the integrated  $1s \rightarrow 2s$  and  $1s \rightarrow 2p$  transition intensities for He. The  $2^1S$  and  $2^1P$  features are measured in a single energy loss scan for a range of angles about the mechanical zero angle. A plot of the intensity ratios versus scattering angle yields a well-defined minimum corresponding to the true experimental zero scattering angle, as illustrated in Fig. 3.5.

### 3.2.4 Electron Optics Design

In general, an electrostatic lens consists of two or more electrodes of a given symmetry (in the case of this work, cylindrical symmetry) between which potentials are applied. The resulting electrostatic fields produced by a particular potential distribution determines the focusing properties of the lens for electrons passing through it. In the paraxial approximation, often referred to as Gaussian optics [HR76], the behaviour of an electrostatic lens is essentially identical to a Newtonian thick lens. The basic principles of electron design have been discussed in detail by Kuyatt [K67], Harting and Read [HR76] and Tanaka and Huebner [TH76] and will not be repeated here. Figure 3.6 illustrates the imaging by a thick lens of a point object, given a set of defining parameters called cardinal points ( $F_1, F_2, f_1, f_2$ ) that determine the focal properties of a lens system. Multi-element lenses are required to maintain useful focal properties over a wide range of acceleration/deceleration ratios. As the number of lens elements in the optical system increases, so does the complexity of the system of equations needed to predict its performance. Since the instrument was going to require a non-trivial optics system in order to be capable of performing a variety of different experiments, a computer

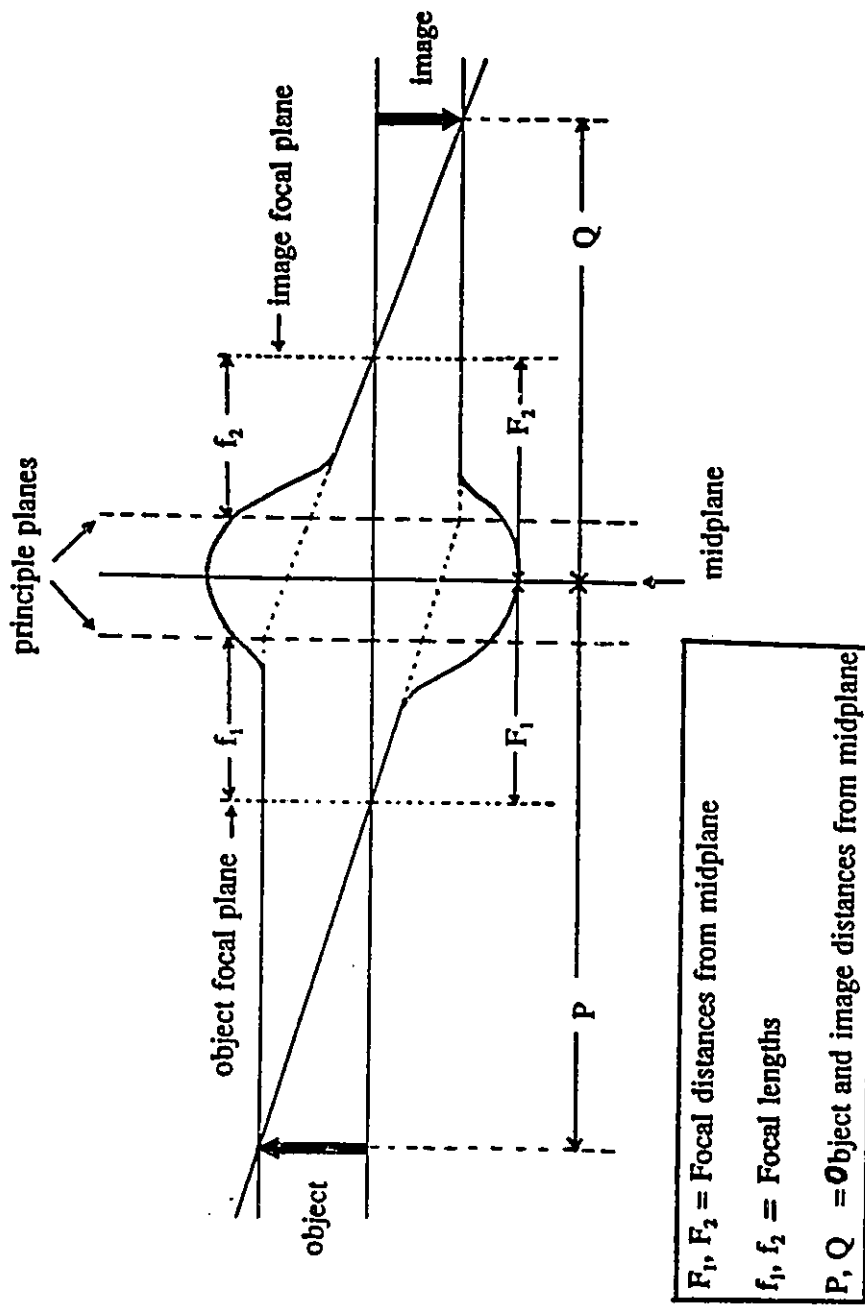


Fig. 3.6 Lens parameters. Within the paraxial approximation, the behaviour of electrostatic lenses can be treated by the Newtonian thick lens equations.

modelling approach was adopted in order to produce the working design.

The algorithm used in this work [DD77] is an electrostatic field modelling program, designed to model the electrostatic fields and forces created by a collection of shaped electrodes, given certain symmetry assumptions (in this case, cylindrical symmetry). The desired lens design is entered as a 2-D array of electrode and non-electrode points. Using a finite difference technique called over-relaxation, the algorithm provides a best-estimate of the voltages for those points within the array that depict non-electrode regions. Once the trial array is computed for a given set of test voltages, the trajectories of electrons (or ions) with user-defined initial starting coordinates and energies can be calculated. A graphical interface allows the user to view in detail the electrode array and associated electron trajectories (see figures 3.7(a), (b) and (c), 3.8 (a) and (b) and 3.10 ). The starting coordinates and energies of the electron trajectories are dictated by the required impact energy or energy loss and the desired resolution for a particular lens system. A printable log file is provided, containing information such as the initial and final electron energies, crossover points, entrance and exit angles etc., in addition to the graphical output. This information was used in the evaluation of a particular electrode array and its associated potentials, based upon two criterion. Focussing properties were judged by the radius and convergence angles of a group of trajectories, whose starting angles and energies were incremented from initial values, at a desired image point. The resolution could be estimated by noting how many trajectories successfully traversed the potential array within a defined initial energy window. The voltage values derived from the above modelling procedure also dictated the voltage ranges required in designing the

power supplies. In the following section, the model design parameters for the electron gun, monochromator exit lens and analyser entrance lens are discussed in further detail.

#### 3.2.4.1 Electron Gun

The desired properties of the electron gun included sufficient current output at low electron final energies (ca. 10  $\mu\text{A}$  at the gun exit with energies as low as 10 eV) with an image size of the order of 1 mm in diameter at a distance of 6" from the object (electron source). The image point in this case corresponds to the entrance of the monochromator. Thermionic emission from a DC-heated tungsten filament in a hairpin formation was the chosen electron source. At temperatures of the order of 3000 K, electrons are 'boiled off' at the tip of the tungsten filament with energies of ca. 0.5 eV. This type of source offers the advantages of stability, high emission and freedom from gas poisoning which is a problem associated with indirectly-heated oxide cathodes. The popular triode (cathode, grid and anode) arrangement, in the Pierce geometry [P49] was used for electron extraction and beam formation. It has been shown [S48] that the maximum current fluxes passing through the anode of such an arrangement can be of the order of  $10^4 \mu\text{A}/\text{cm}^2$ , depending upon the anode voltage and spacing relative to the cathode. The overall gun design (see figure 3.7(a) ) is a modified version of a low energy gun designed by M. Tronc [T82]. It utilizes a two-stage operation which involves extracting the electrons produced by the filament hairpin using the Pierce triode geometry and subsequently accelerating them to the second stage (a two element lens) which then decelerates and focuses the beam at the entrance of the monochromator at the desired pass energy. It was

found that without the second stage, the beam was very divergent at the monochromator entrance, resulting in decreased transmission, especially at low pass energies.

Figure 3.7(a) illustrates trajectory calculations for the simulated electron gun electrode pattern using a set of potentials corresponding to a final energy of 35 eV. The starting coordinates correspond to the tip of the filament hairpin and the initial energy was set at 0.5 eV. The starting angle was zero degrees with respect to the horizontal axis of symmetry, and was incremented by 1 degree for each successive trajectory for a total of 40 trajectories. This initial set of conditions was thus taken as an approximation to the emission pattern of the filament hairpin, and is graphically presented in figure 3.7(b) as an expanded view of the resulting algorithm output. These simulated conditions produce a well-focused beam at the exit aperture with a final electron energy of 35 eV which is illustrated in figure 3.7(c). It was found through successive trials covering a range of final electron energies (as low as 5 eV) that a set of potentials could be found which would produce the desired focal behaviour. This particular electrode pattern was thus chosen as a suitable electron gun design. Practical implementation involved reproducing as closely as possible the simulated electrode pattern, within the constraints imposed by materials selection, ease of fabrication, choice of insulating materials, etc. Using #316 stainless steel and  $\text{Al}_2\text{O}_3$  ceramic spacers, a good approximation to the simulated electron gun pattern was constructed. To remove any residual magnetic fields that may become enhanced during the machining process, all metal components were annealed (under a nitrogen atmosphere to prevent oxidation of the metal surfaces, which could produce insulating oxides and nitrides that would charge) to in excess of 1000°C. The alloy

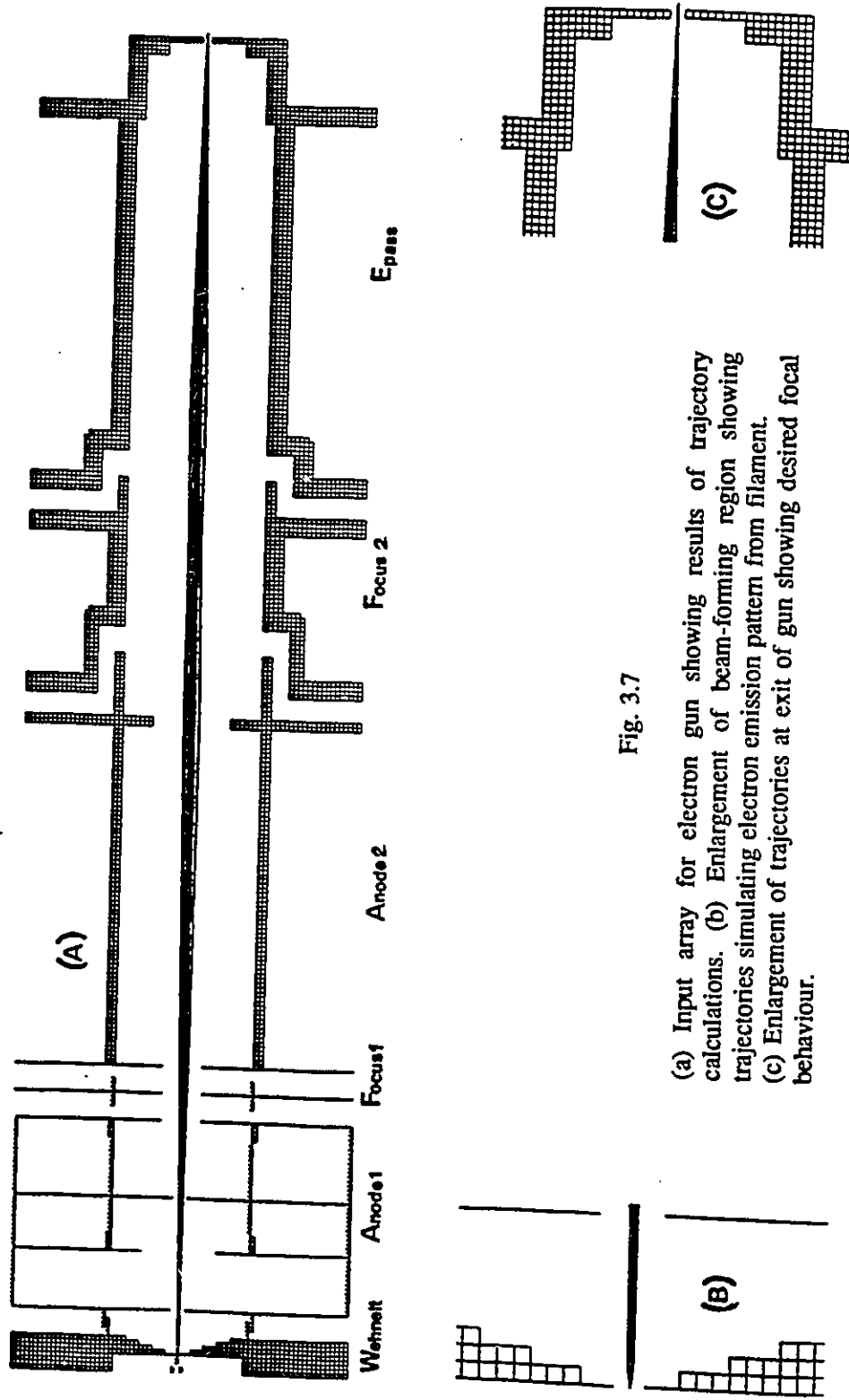


Fig. 3.7

(a) Input array for electron gun showing results of trajectory calculations. (b) Enlargement of beam-forming region showing trajectories simulating electron emission pattern from filament. (c) Enlargement of trajectories at exit of gun showing desired focal behaviour.

assumes a b.c.c. structure which has characteristic non-magnetic properties. A spring steel mounting plate was used for the filament, as it was found in practice that rigid mounting of the filament base at room temperature resulted in cracking of the filament base at operating temperatures (in excess of 2500° C) due to thermal expansion of the metal.

#### 3.2.4.2 Monochromator Exit Lens

The purpose of this lens was to accelerate the low energy (typically 10 - 25 eV) electrons exiting the monochromator hemispheres (within a certain range of exit angles; of the order of .05 rad) up to the impact energy (up to 2000 eV). In addition, the desired image size was of the order of 1 mm in diameter, at a distance from the object (monochromator exit plane) of 20 cm (corresponding to the collision region ). Space limitations restricted the overall lens stack length to 20 cm. Since the accelerating ratio of this lens system was going to exceed 100 under certain experimental conditions, a multi-element lens design would be necessary. It has been shown that single stage lenses (i.e. two or three elements) will produce unacceptable aberrations if subjected to large acceleration ratios [HR76, CNK74].

The design chosen was a modified version of a five-element lens modelled by Heddle [HP84] which is depicted in figure 3.8(a) as the model input array. This design allows the acceleration of the low energy electrons to the final impact energy to take place in two stages, thus maintaining focal properties over a wide range of acceleration ratios. The lengths of the individual elements are related as:  $L_1 = L_5 = 4L_2 = 4L_4 = 4/3L_3$ .

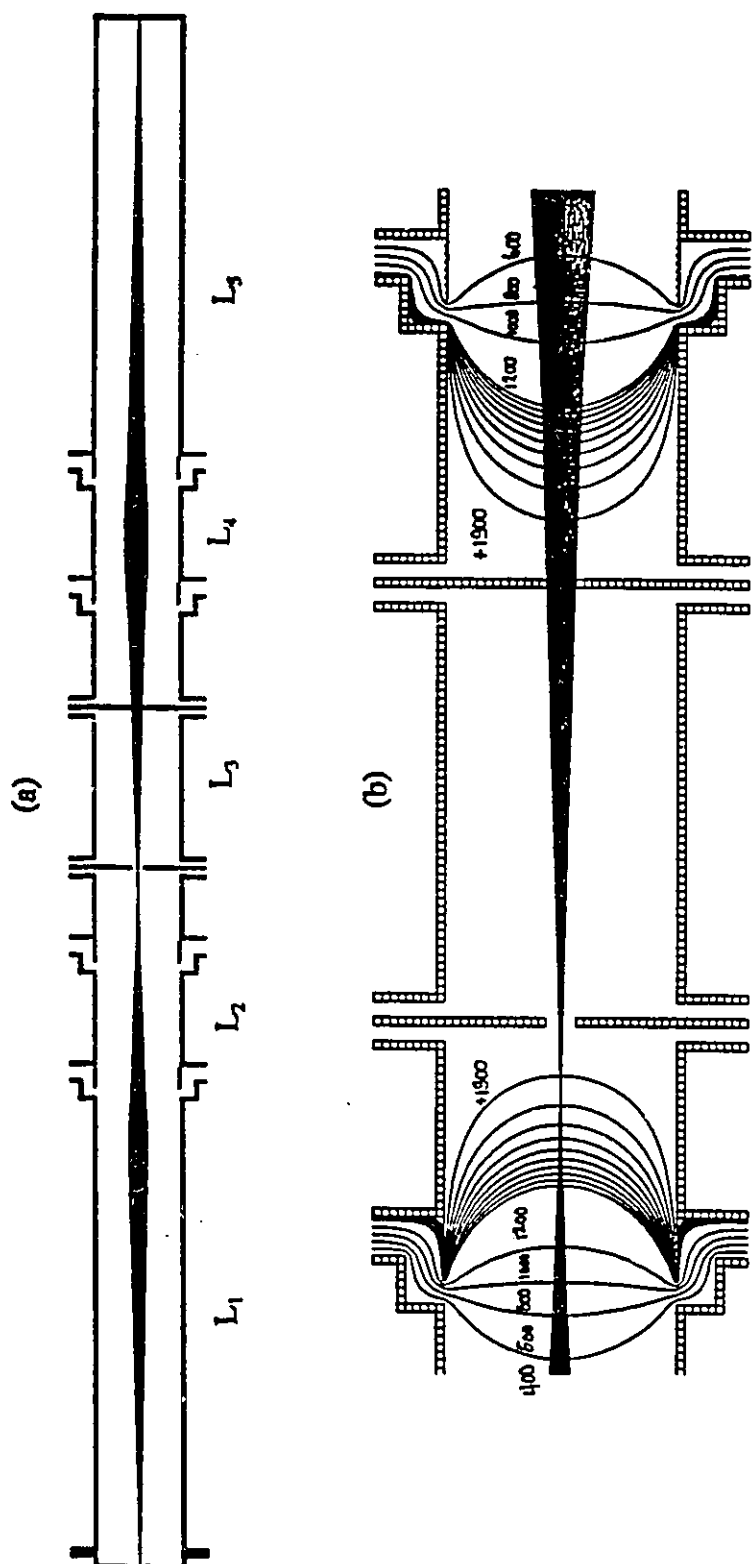


Fig. 3.8

(a) Input array for monochromator exit lens showing results of trajectory calculations. (b) Enlargement showing behaviour of trajectories in the region of the two real apertures. Contours represent the potential gradient in this region.



The gap/diameter ratio is 0.1, and thus for a 1 cm lens diameter, the elements are separated by 0.1 cm which is satisfactory for potential differences of 1 kV in a vacuum of  $10^{-6}$  Torr. By placing two real apertures (1 mm diameter) separated by 1.4" centered in  $L_3$ , virtual apertures are created as images at the entrance and exit of the lens system [S81, DBH84]. This is illustrated in figure 3.9 for a simple two-lens system that approximates the design outlined above. Virtual apertures reduce sensitivity to patch fields and provide the correct field at the exit plane of the monochromator [RC&74]. Such properties of virtual apertures are especially important with regards to maximum beam current transmission, as low pass energy, monochromated electron sources suffer from the disadvantage of reduced current intensities relative to unmonochromated sources.

Figure 3.8(a) illustrates trajectory calculations for a set of lens potentials corresponding to an overall acceleration ratio of 43 and a final impact energy of 1500 eV. The electron starting coordinates correspond to the centre of the virtual entrance plane, with initial energies of 35 eV. A range of starting angles from 0 to 1.5 degrees was used (with respect to the horizontal lens axis). This set of potentials produced a well-focused beam at the virtual exit plane. Slight adjustment of the starting lens element potentials places the image at a distance from the starting plane corresponding to the collision region of the spectrometer. Figure 3.8(b) illustrates the behaviour of the trajectories in the region of the real apertures in  $L_3$ . The first aperture appears to limit the beam angle, while the second determines the radial extent of the beam. Selected voltage contours are also plotted to illustrate the potential gradient in this region. It was found with this arrangement of electrodes that the desired focal behaviour could be achieved for a range of acceleration

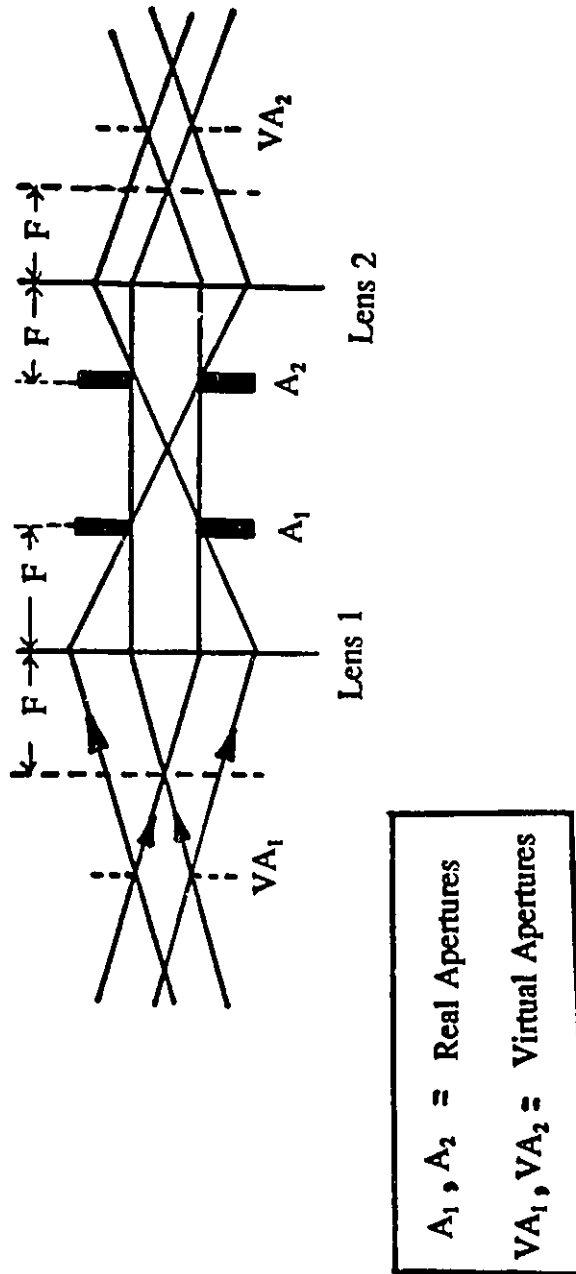


Fig. 3.9 Illustration of how virtual apertures can be created by imaging two appropriately spaced real apertures.

ratios (5 to  $> 100$  ). As in the case of the electron gun, the resolution of this lens for a particular set of potentials could be estimated by noting how many trajectories traversed the electrode array successfully within a particular range of starting energies (typically, several meV about the mean starting energy). Sets of potentials were derived with this configuration which would, in theory, provide 150 meV resolution at 25 eV initial energy (core loss regime) and 50 meV at 5 eV initial energy (valence regime). Based on the above criterion, this particular design was deemed suitable. Using hard aluminum, teflon tubing and sapphire ball insulators, a good approximation of the simulated electrode pattern was constructed. The two real apertures in  $L_3$  were made of #316 (non-magnetic) stainless steel which were coated with baked colloidal graphite. The inner surfaces of the lens elements were also coated with baked colloidal graphite and subsequently polished, to eliminate patch fields and contact potentials, which can adversely affect the electron trajectories. In order to better facilitate cleaning of the real apertures in  $L_3$  (due to a build up of cracked hydrocarbons around the aperture holes which charge and degrade the spectrometer performance), the lens was designed to be assembled in two stacks on either side of  $L_3$ . Thus, while one aperture was being cleaned, the remainder of the stack could remain rigidly intact, preventing loss of insulators and other smaller pieces.

#### 3.2.4.3 Analyser Entrance Lens

The purpose of the analyser lens is to accept scattered electrons (which have sustained a particular energy loss from the initial impact energy) within a given angular range (acceptance angle of ca. 2 degrees), decelerate them to the pass energy of the

analyser and focus them at the analyser entrance plane. Due to constraints in the size of the vacuum chamber, the distance from object (at the collision region) to final image (analyser entrance plane) was 20 cm (maximum). As in the case of the monochromator exit lens, a multi-element lens design would be required to accommodate deceleration ratios in excess of 100 under certain experimental conditions (i.e for large impact energy/high resolution work) without introducing aberration effects. Unlike the electron gun and monochromator exit lens, the analyser entrance lens was designed completely 'in house', and is thus unique to this spectrometer. After testing the focal properties of four, five and six element trial lens geometries, a design utilizing seven elements was found to be suitable and is presented in figure 3.10 as the model input array. A gap/diameter ratio of 0.1 was chosen, thus providing a 0.1 cm spacing between adjacent lens elements which would allow potential differences of up to 1 kV at  $10^{-6}$  Torr. The basic design incorporates three single stage lenses (three elements each) placed in series in such a manner that the object of one lens forms the image for the adjacent lens. Real exit and entrance apertures were chosen for this lens. Since variable detection angle was an important requirement of this instrument, it appeared to be easier to define the analyser viewing cone size and ensure the constancy of its geometry over a range of scattering angles if real apertures were used. The expected scattered electron current intensities would be small relative to that of the incident beam, and thus it was thought that little performance would be compromised if real rather than virtual apertures were used, provided attention was paid to fringing field effects at the analyser entrance plane.

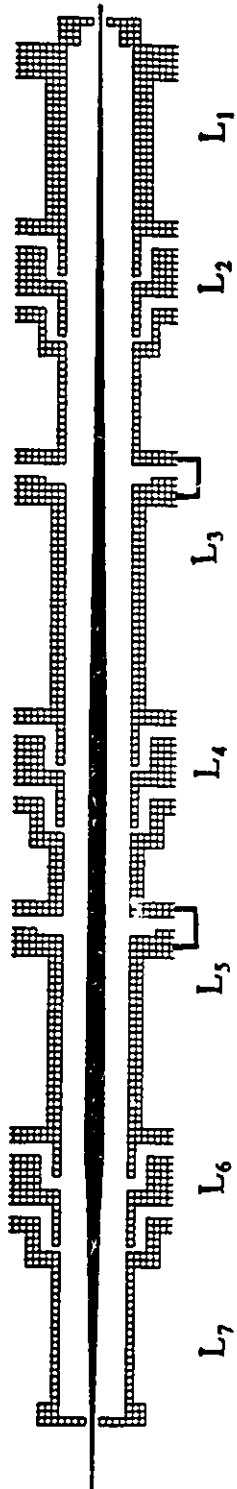


Fig. 3.10 Input array for analyser entrance lens showing results of trajectory calculations.

Figure 3.10 displays trajectory calculations for a set of potentials corresponding to electrons with initial energies of 1213 eV (corresponding to an energy loss equivalent to the C 1s  $\rightarrow \pi^*$  transition in CO from an initial impact energy of 1500 eV) and final energies of 35 eV. The starting angles ranged from 0 to 1.5 degrees with respect to the horizontal axis of the lens. As can be seen from this figure, the deceleration occurs incrementally over the three stages of the lens, resulting in a well-focused beam at the exit plane of the analyser lens. It was found through successive trials covering a wide range of deceleration ratios (and thus energy losses) that the desired focal behaviour could be obtained. For each set of trajectory calculations, the resolution was estimated in a similar manner to that described above for the electron gun and monochromator lens systems. Based on these results, this lens appeared to be a reasonable choice. As in the case of the monochromator exit lens, a good approximation to the simulated electrode pattern was constructed, using hard Al, teflon tubing and sapphire ball insulators. The inner surfaces of the lens were coated with baked colloidal graphite and subsequently polished.

#### 3.2.4.4 Analyser/Monochromator Hemispherical Deflectors

It has been shown by Heddle [H71] that hemispherical electrostatic analysers provide superior performance for electron scattering studies that are differential in both energy and angle, on the basis of étendue (entrance area, transmitted solid angle). The characteristic focussing properties of the hemispherical energy analyser are well-known, and will only be discussed briefly here. The first treatment was provided by Purcell [P38]

and later expanded by Kuyatt [K67].

Figure 3.11 depicts a cross-sectional view of a concentric hemispherical analyser system. The electrostatic field between the hemispheres varies as the inverse square of the radius. The electric field arises due to the application of a potential difference  $V$  between the two hemispheres, equal to  $(V_1 - V_2)$ ; where  $V_1$ ,  $V_2$  are the potentials of the inner and outer hemispheres, respectively.  $V$  can be expressed as:

$$V = V_{pass} \left( \frac{R_2}{R_1} - \frac{R_1}{R_2} \right) \quad (1)$$

where  $V_{pass}$  is the potential along radius  $R_{pass}$ ;  $R_1$  and  $R_2$  are the radii of the inner and outer hemispheres, respectively. Electrons entering the analyser with energy  $eV_{pass}$  will traverse a circular path of radius  $R_{pass}$ . If circular apertures of radius  $r_a$  are placed in the entrance and exit planes of the analyser with their centres on  $R_{pass}$ , then the energy resolution of the analyser can be expressed as (for first order focusing):

$$\frac{\Delta E}{E_{pass}} = \frac{r_a}{R_{pass}} + \alpha^2 \quad (2)$$

$\alpha$  is the maximum aperture half angle, and  $\Delta E$  represents the full width at half-maximum (FWHM) of the energy distribution of electrons transmitted by the analyser. Using values of 9.25 cm and 0.1 cm for  $R_{pass}$  and  $r_a$  and neglecting the  $\alpha^2$  term, the theoretical resolution of the hemispherical selectors used in this instrument is:

$$\frac{\Delta E}{E_{pass}} = 0.005 \quad (3)$$

The sphericity of the inner and outer hemispheres is an important consideration

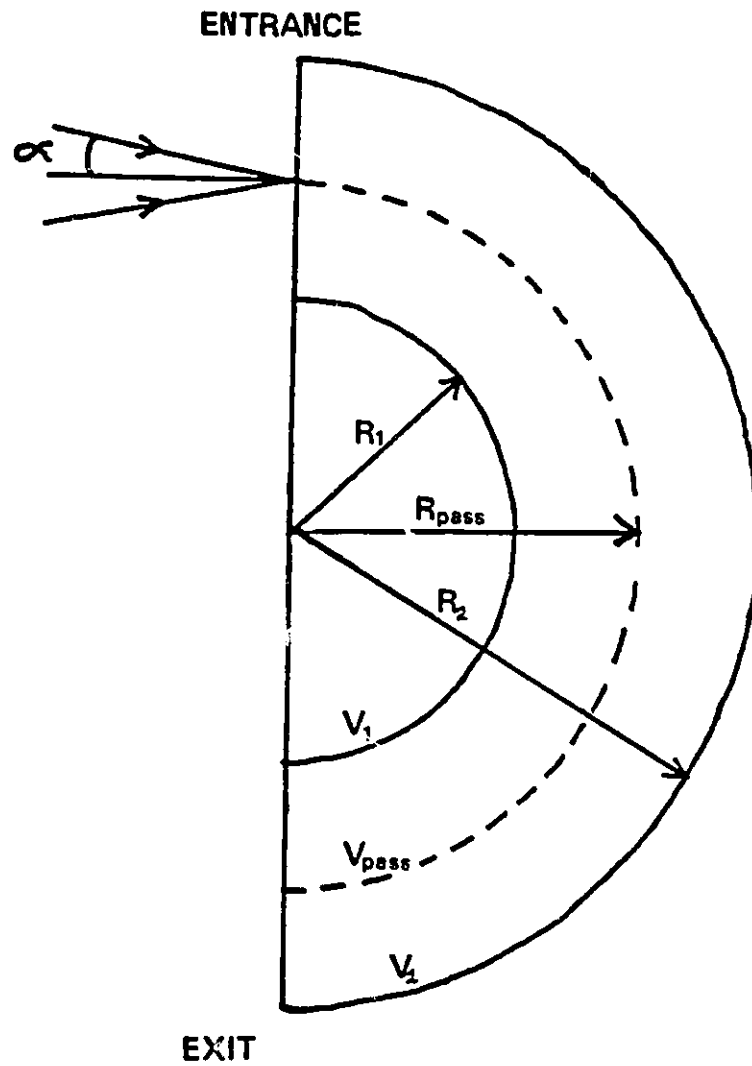


Fig. 3.11

Hemispherical electrostatic analyser. Dashed line indicates the mid-gap trajectory traversed by electrons with energy  $eV_{pass}$ .  $\alpha$  represents the acceptance angle.



when attempting to perform high resolution ( $<0.1$  eV FWHM) work. The first hemispheres in this instrument consisted of #306 non-magnetic stainless steel mixing bowls that had been rounded out on a lathe, resulting in a slightly elliptical deflector geometry. Upon replacing them with precision-machined aluminum inner and outer hemispheres of the same radial dimensions, the transmission and overall resolution improved by a factor of 10 or more, especially at pass energies less than 15 eV.

In order to allow measurements at the 0 degree scattering angle without the introduction of large background signals due to scattered electrons from the main beam, a 1.5 cm long, 0.3 mm wide slot was milled in the analyser outer hemisphere to act as a beam dump without adversely perturbing the  $1/r^2$  field. In this manner, the main beam continues through the slot largely unhindered, with the result that only those scattered electrons which have sustained an energy loss will successfully traverse the analyser hemispheres.

Provision has been made for the addition of a second set of hemispheres in tandem with the existing analyser, in an 'S' geometry (depicted in figure 3.12). Mann and Linder have demonstrated that the dispersion of a tandem analyser arrangement, each with radius  $R_{\text{pass}}$ , is essentially the same as that of a single analyser of radius  $2R_{\text{pass}}$  [ML94]. It would thus be theoretically possible to improve the resolution by a factor of two while using the same pass energies as the present single analyser. A treatment of the focal properties of the tandem analyser arrangement and necessary fringing field correction for the boundary region between the two analysers is given by A. Baraldi et. al [BDK92, BD94]. A very similar approach could be used in the present spectrometer in the future.

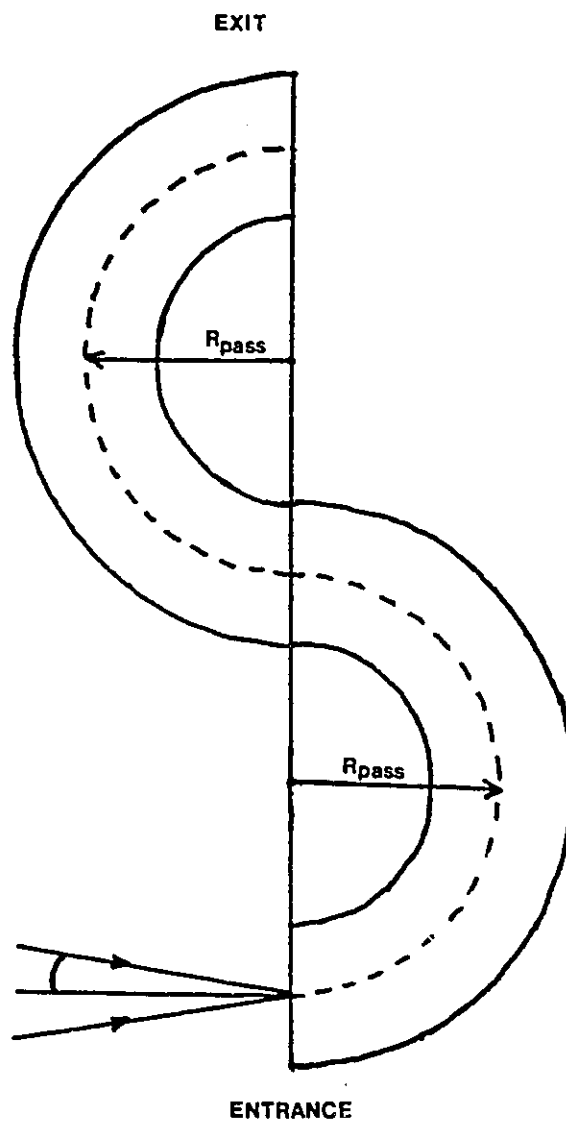


Fig. 3.12

"S" geometry for tandem hemispherical analyser arrangement. The total mid-gap trajectory path length is  $2R_{pass}$ .  $\alpha$  represents the acceptance angle.

### 3.2.5 Detection

In the present spectrometer configuration, a standard pulse counting arrangement was used. A channel electron multiplier (CEM) detector, the cone of which was mounted 1 mm behind the exit aperture of the analyser, produced amplified pulses from single electrons. These pulses were capacitatively decoupled from the detector high voltage and processed by a combination pre-amplifier and discriminator circuit (designed in-house by Tolmar Instruments [TK94]) prevented signal loss through a long coaxial cable and conditioned the signal for digital processing. The circuit also features an analog output to accommodate signal intensities outside the range of the pulse counting mode. The pulses are counted by an 8253 triple counter/timer chip mounted on a standard PC card, configured to operate two event counters and one timer, which determines the dwell time. Timing is provided by a separate quartz oscillator chip.

A state-of-the-art, 116-channel parallel detection unit (ISL model MD100), which incorporates the pre-amp and discrimination circuitry directly on the detector head, unit will be installed in the future. The real aperture will be removed at the exit plane of the analyser, allowing full energy dispersion of selected scattered electrons across the active detector window (ca. 2.5 cm). This will enhance the resolution, and substantially reduce acquisition times, as 116 energy points covering up to several eV (depending on the pass energy of the analyser system) can be acquired in a single snap shot. As an example, taking the quantity  $E_{\text{pass}}/R_{\text{pass}}$  from equation (2) as a measure of the analyser dispersion (in eV/mm), for  $E_{\text{pass}} = 25$  eV the dispersion at the analyser exit plane is 0.270 eV/mm. If the active detector area is ca. 1 cm, this represents a 2.70 eV energy range that can

be acquired in parallel in 116 points. The new detector will be tested with a single analyser at the outset, and then subsequently mounted on the tandem arrangement described in section 3.2.4.4. A. Baraldi et al [BD94] have modelled the behaviour of a multichannel detection system and it is envisaged that a similar arrangement will be used in this spectrometer.

### 3.2.6 Electronics

#### 3.2.6.1 Design and Construction

The majority of the electronics were designed by Tolmar [TK94] and constructed in house. Attractive features include: ultra-low ripple ( $< 1$  mV at the power supply output), floatable to  $> 2.5$  kV, fast response (msec) and optically isolated digital-to-analog interfacing. 95% of all spectrometer voltages are thus under computer control, which allows enormous flexibility with regard to scan modes, greatly reduced "tune-up" periods and most importantly, allows the use of optimization routines which change several voltages nearly simultaneously to maximize a given parameter.

A simplified block diagram of the electronics system is shown in figure 3.13 (a more detailed representation can be found in fig. 3.14). In this arrangement, the collision region (gas jet) is at earth while the cathode is at the negative of the impact energy. This is advantageous in that there is greater flexibility and fewer safety precautions with regards to sample introduction. The entire monochromator system (including the electron gun, hemispheres and exit lens) floats above the entrance of the analyser by an amount determined by the scan voltage. The scan voltage is provided by a modified Fluke 415B

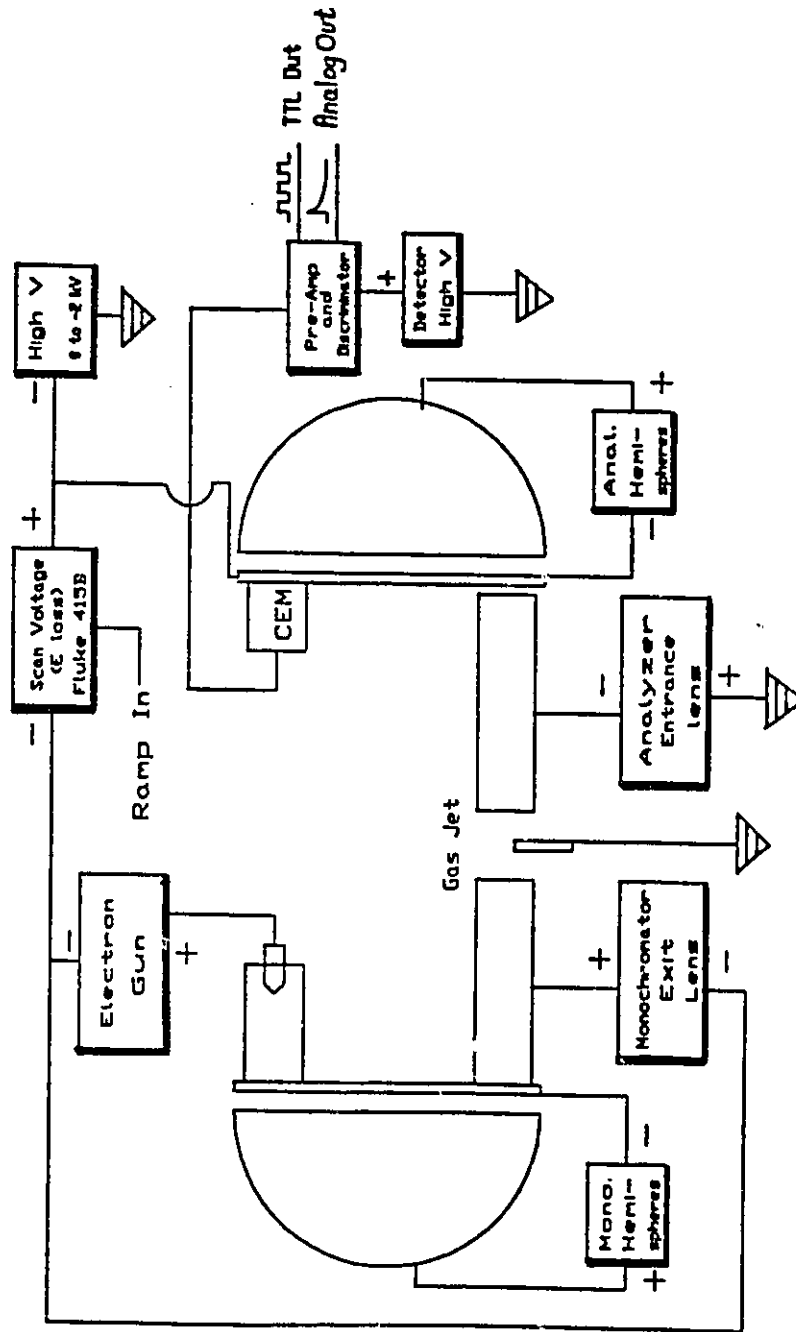


Fig. 3.13 Simplified schematic of McVAHRES electronics arrangement.

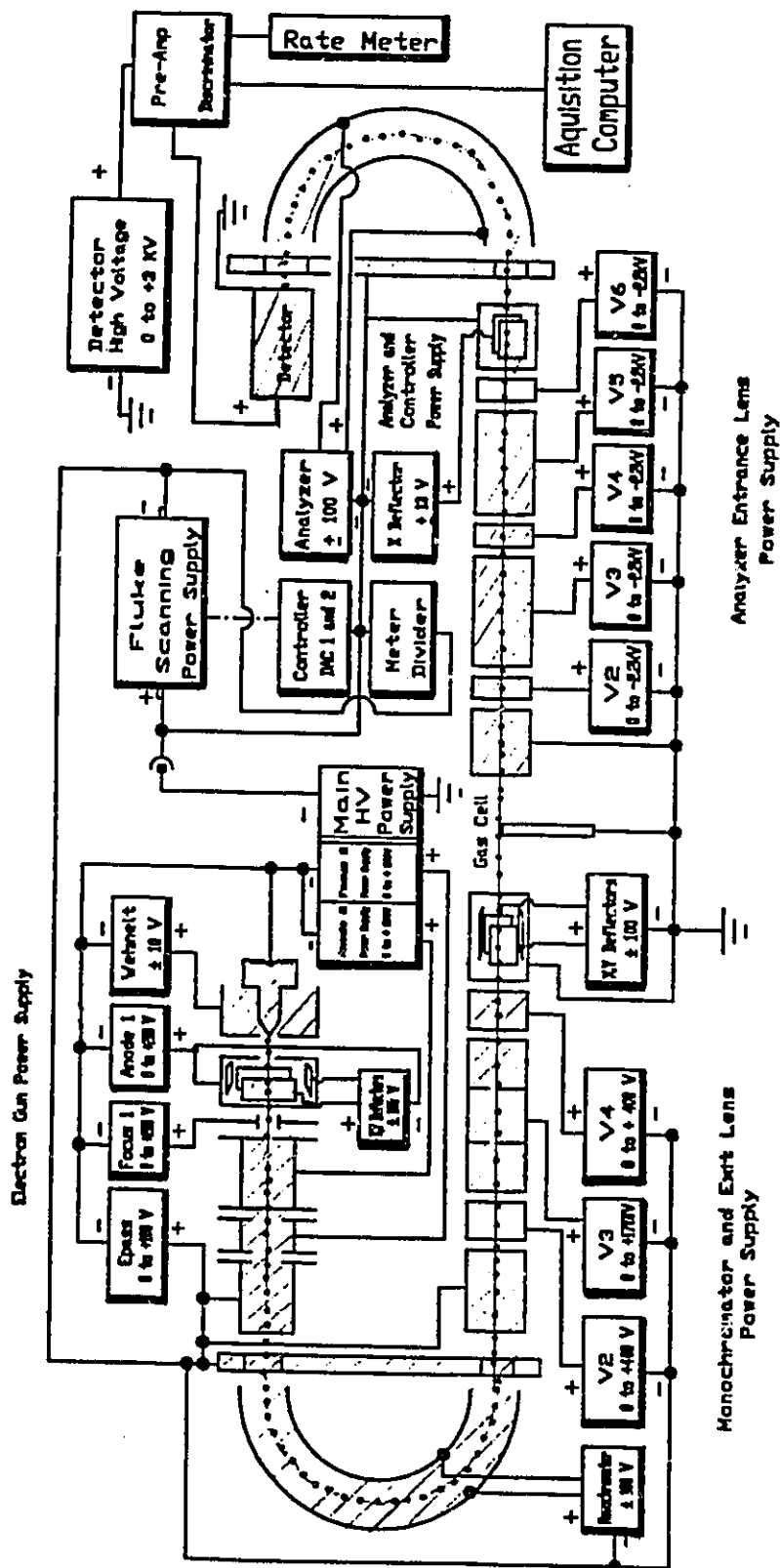


Fig. 3.14 Detailed schematic of McVAHRES electronics arrangement. The shaded regions define the various optical elements, and the dotted line shows the path of an electron through the entire system. The shadowed boxes represent the individual voltage modules.

which produces an output (within a user-defined voltage range between 0 and 1 kV) linearly proportional to a computer controlled program voltage (0 to 10 volts). To scan an energy loss spectrum, the analyser and its associated lens voltages are adjusted so as to maximize the signal on the elastic peak (0 energy loss and thus 0 scan V). The desired energy loss is then applied to the common of the monochromator system by the Fluke 415B. In this mode of operation, the scattered electrons accepted by the analyser and its associated lens have a constant residual energy. This mode of operation, along with other typical scan modes used in energy loss spectroscopy, are summarized below in Table 3.2. Thus, the focussing properties of the analyser and lens remain constant as the energy loss spectrum is scanned. This minimizes any distortion of the spectrum due to chromatic aberration, which may occur in the loss mode when the analyser lens and/or plate is scanned (at constant  $E_0$ ) to obtain a spectrum. This is due to the fact that the loss scan mode can result in changes in the focal point at the analyser entrance with scanning, thus effectively changing the transmission function of the analyser. Since the impact energy changes in the constant residual energy scan mode, however, there will be a small change in the momentum transfer as the spectrum is scanned. As an example, one can use a 165 eV to 205 eV energy scan (i.e. the 2p edge of  $SF_6$ ) at an impact energy of 700 eV and a scattering angle of  $20^\circ$ . These conditions are considered borderline with respect to satisfying the first Born approximation (see chapter 2) and the maximum effect would occur under such conditions. Using the principles developed in chapter 2, it can be seen that the momentum transfer changes  $0.28 \text{ a.u.}^{-2}$  over the course of the scan, which represents about 4% of the momentum transfer at 165 eV ( $6.2 \text{ a.u.}^{-2}$ ). In such cases, the

momentum transfer for each point energy must be evaluated when comparing spectral features. When the impact energy is large relative to the energy loss, the loss and constant residual energy scan modes offer essentially the same information spectroscopically; that is, a plot of the scattered current intensity through a solid angle  $\Omega$  as a function of energy loss. Which of these two modes is used depends on such parameters as the electron optics, physical spectrometer design, etc.

Although not yet implemented, the excitation mode offers distinctly different spectroscopic information. For example, King *et al.* [KMR77] have identified core-excited negative ion resonances by looking at the excitation function for the (C  $1s^{-1}$ ,  $\pi^*$ ) state of CO and the (N  $1s^{-1}$ ,  $\pi^*$ ) state of  $N_2$ . By modifying the scanning algorithm only (discussed in section 3.2.7.2) to scan the analyser simultaneously with the impact energy, this instrument is capable of such experiments as well.

Table 3.2. Typical Scanning Modes in Electron Spectroscopy

Mode	$E_0^1$	$E_f^2$	$(E_0 - E_f)$
Constant Residual Energy	scan	constant	varies with $E_0$
Energy Loss	constant	scan	varies with $E_f$
Excitation	scan	scan	constant

(1)  $E_0$  is the impact energy.

(2)  $E_f$  is the energy of the electrons after sustaining an energy loss relative to  $E_0$ .



### 3.2.6.2 Description of Electronics Operation

In general, each individual voltage is supplied from a voltage module, a simple schematic of which is presented in figure 3.15. A voltage module consists of a computer and manually controlled, opto-isolated 12 bit DAC with 0 to 10V (or -10V to 10V) output which controls a voltage amplifier (if the required voltage is in the range -500V to 500V) or a switching high voltage power supply (for values  $> 500V$ ).

In total, there are 21 voltages used for this instrument. The voltage modules are grouped in crates. Each crate has a motherboard with buffered computer interface and up to 7 voltage module digital interface cards can be connected to it. In addition, each crate has a rotary opto-encoder; the output of which can be switched to each voltage module for manual control. Each crate is fitted with a switchable digital panel meter (meters) for monitoring output voltages.

Each digital interface card and thus voltage module can be individually addressed via an address decoding circuit. The basis of the interface card design is three up-down LS569 counters. The outputs of these counters are opto-isolated and connected to an AD522 DAC. The LS569 counters can be loaded by the computer, or their states can be changed by a stream of pulses from an opto-encoder (manual control). The current status of the counter outputs can be read by the computer. The isolated side of the card has a stable voltage reference and the DAC output is conditioned to produce 0 to +10V (for unipolar operation) or -10V to +10V (for bipolar operation).

If the required voltage is in the -500V to 500V range, a multiconfigurational high voltage amplifier card is used. The desired range and polarity is chosen individually by

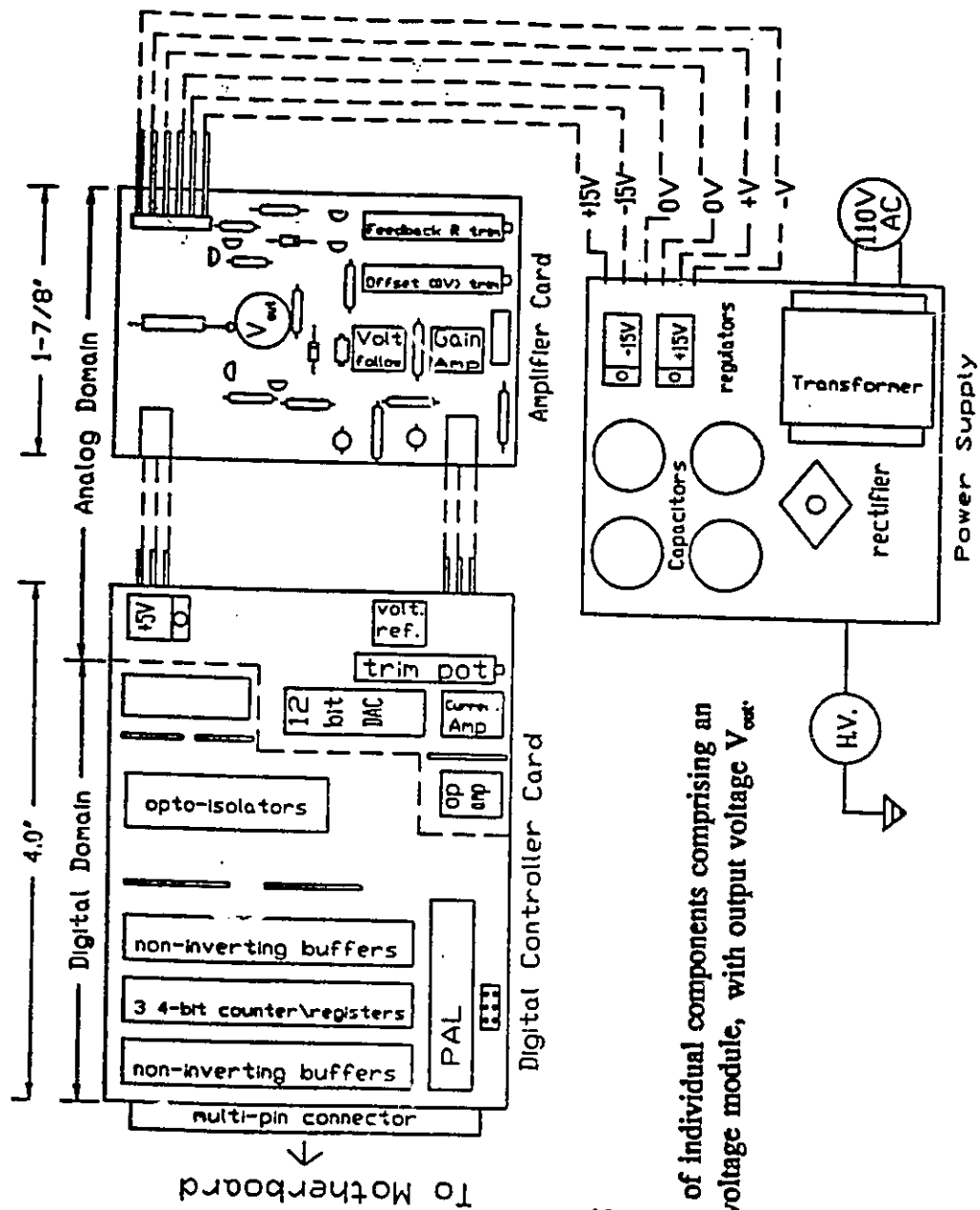


Fig. 3.15

Schematic of individual components comprising an individual voltage module, with output voltage V<sub>out</sub>.

setting appropriate jumpers and feedback resistors. Each card has two amplifiers to provide two voltages  $V_1$  and  $V_2$  where  $V_1 = -V_2$  (i.e. for deflectors) or  $V_1 = -AV_2$  (i.e. for hemispherical analysers;  $A$  is a constant determined by the electrostatics and radii of the hemispheres). In cases where the required voltage is higher than 500V, an in-house designed, switching power supply is used, which can be configured to provide up to 6 kV. The last component of the voltage module consists of a power supply providing  $\pm 15$  volts (regulated) and voltage (voltages) 10V higher than required voltage range. Power supplies are floatable to at least 2.5 kV DC above earth. This is made possible via Hammond transformers with isolated secondaries.

In practice, the working voltages provided by the arrangement above (high voltage amplifiers) are very stable and have residual AC ripple within 1 mV, measured at the output of the amplifier card.

Figure 3.16 illustrates a simple schematic of the power supply networking. The computer interface of each crate is connected to a 24 bit digital I/O card (8255 chip). This card also has a 8253 triple counter/timer chip. Two of these are used in series for pulse counting either from the channeltron or a voltage to frequency converter and the third is used for timing (via a separate quartz oscillator used as a clock). The address for each interface card consists of two parts for computer control: the first part defines the crate and the second part defines the card's position on the motherboard. Under manual control, a multi-pole switch determines which card on the motherboard will receive clocked pulses from the bi-directional opto-encoder wheel. Up to four separate crates can be supported with this design, for a total of 28 computer-controlled voltages.

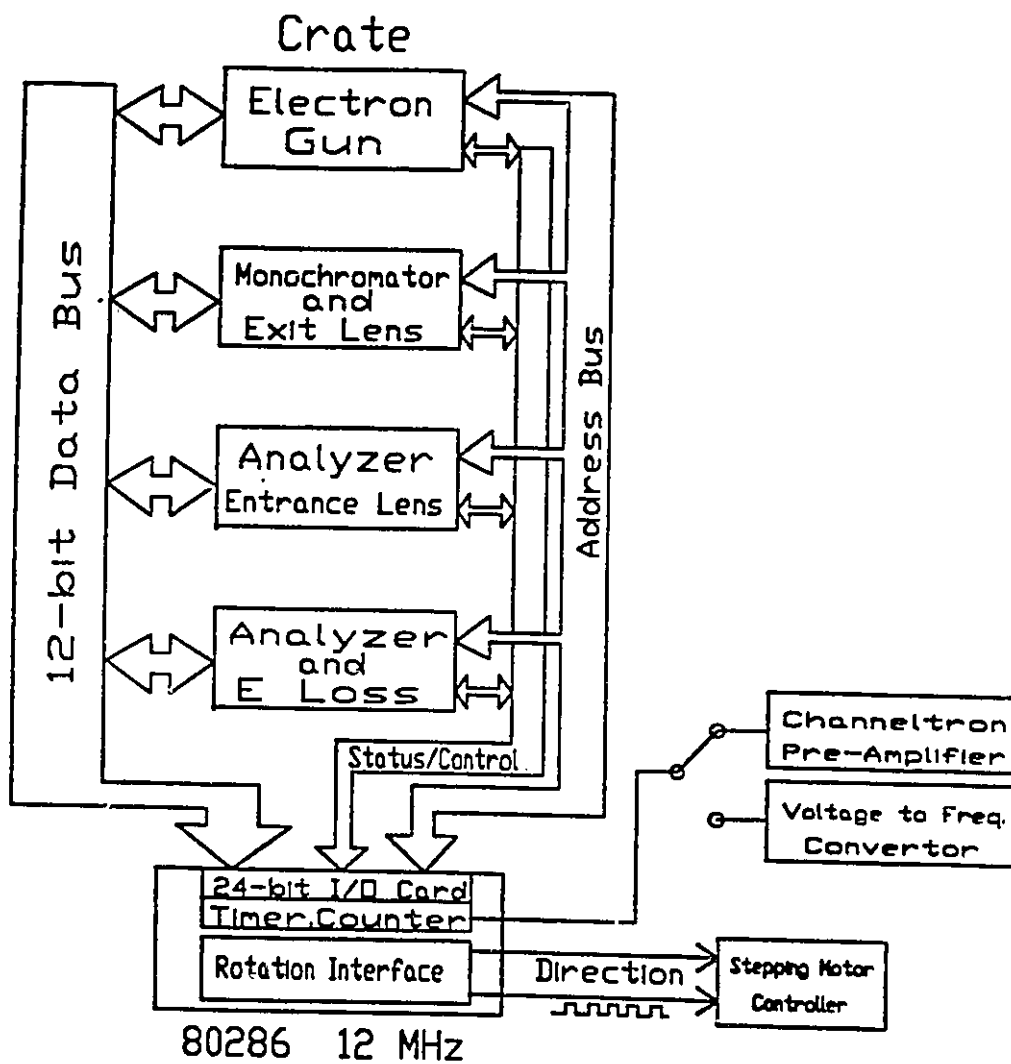


Fig. 3.16

Graphical representation of power supply networking to control/acquisition computer.

### 3.2.7 Software

#### 3.2.7.1 Control

The complete set of DAC values and thus spectrometer voltages, which may represent favourable conditions for recording a particular energy loss spectrum for example, can be read by the computer and stored as a calibration file, which also includes the parameters of the energy loss scan. This greatly simplifies the tune-up process, as all previous voltages and scan information can be re-set in one simple operation by re-loading all the DACS with the saved values. An example of a calibration file is presented in figure 3.17. In addition, any one of the 21 interfaced voltages can be scanned over a user-defined range with a variable step size. At present, up to two voltage parameters can be scanned at once, and it will be relatively simple to modify the scan algorithm in the future to allow three or more parameters to be scanned simultaneously.

The rotation mechanism stepper motor is controlled simply by toggling two bits; one bit opens and closes a relay circuit that in turn specifies the direction of rotation. The other bit is toggled in a loop, thereby producing a stream of well-defined pulses with variable pulse width and frequency. These pulses in turn increment the stepper motor.

#### 3.2.7.2 Acquisition

The acquisition algorithm is presented in the form of a flow diagram in figure 3.18. This algorithm allows the accession of many signal-averaged energy spectra, the number of which can be determined either by a pre-selected fixed number of scans, or by an average counts per point criterion. The latter is especially useful for series of

A	B	C	D	E	F
# of cards=21					
En.offset	2	1	2759	-.973000E-02	.386760E+02
En.scan	2	2	2663	-.228571E-03	.147141E-01
An.pass	2	4	2203	.488750E-01	.150001E+00
AN-X-defl	2	3	1995	-.525158E-01	.102632E+03
AN-lens1	4	1	910	.548421E+00	-.121421E+02
AN-lens2	4	2	835	.546947E+00	-.118947E+02
AN-lens3	4	3	410	.544158E+00	-.631584E+01
AN-lens4	4	4	35	.542842E+00	-.107842E+02
AN-lens5	4	5	6	.547211E+00	-.682105E+01
Wehnelt	3	3	1731	.486897E-02	-.100269E+02
Anode	3	4	1144	.489414E-01	-.241408E-01
Focus	3	5	435	.626931E-01	.206937E-01
Gun X-defl	3	6	1152	-.487586E-01	.998759E+02
Gun Y-defl	3	7	1955	-.487586E-01	.999759E+02
E-G.pass	3	1	399	.488211E-01	.257893E+00
Hono	1	1	273	.750579E-01	.184215E+00
M2	1	2	229	.646105E-01	.337895E+01
M3	1	3	904	.645316E-01	.353685E+01
M4	1	4	336	.428947E+00	.510528E+01
X-defl	1	5	2102	.512821E-01	-.105128E+03
Y-defl.	1	6	2260	.512821E-01	-.105128E+03
				-.100357E-02	.197144E-01

No of cards to scan: 1 scan 1

Fig. 3.17 Example of a calibration file. Column A names the individual voltage modules by their corresponding optical elements. Column B is the crate number where a particular voltage module is located. Column C indicates the position of the voltage module on the motherboard in a particular crate. Column D contains the numbers to be written to the DACs of the voltage modules. Columns E and F contain the calibration coefficients that convert the DAC numbers to voltages via the relation  $V_i = (\text{DAC}_i \text{ no.}) \times \epsilon_i + F_i$  for module i.

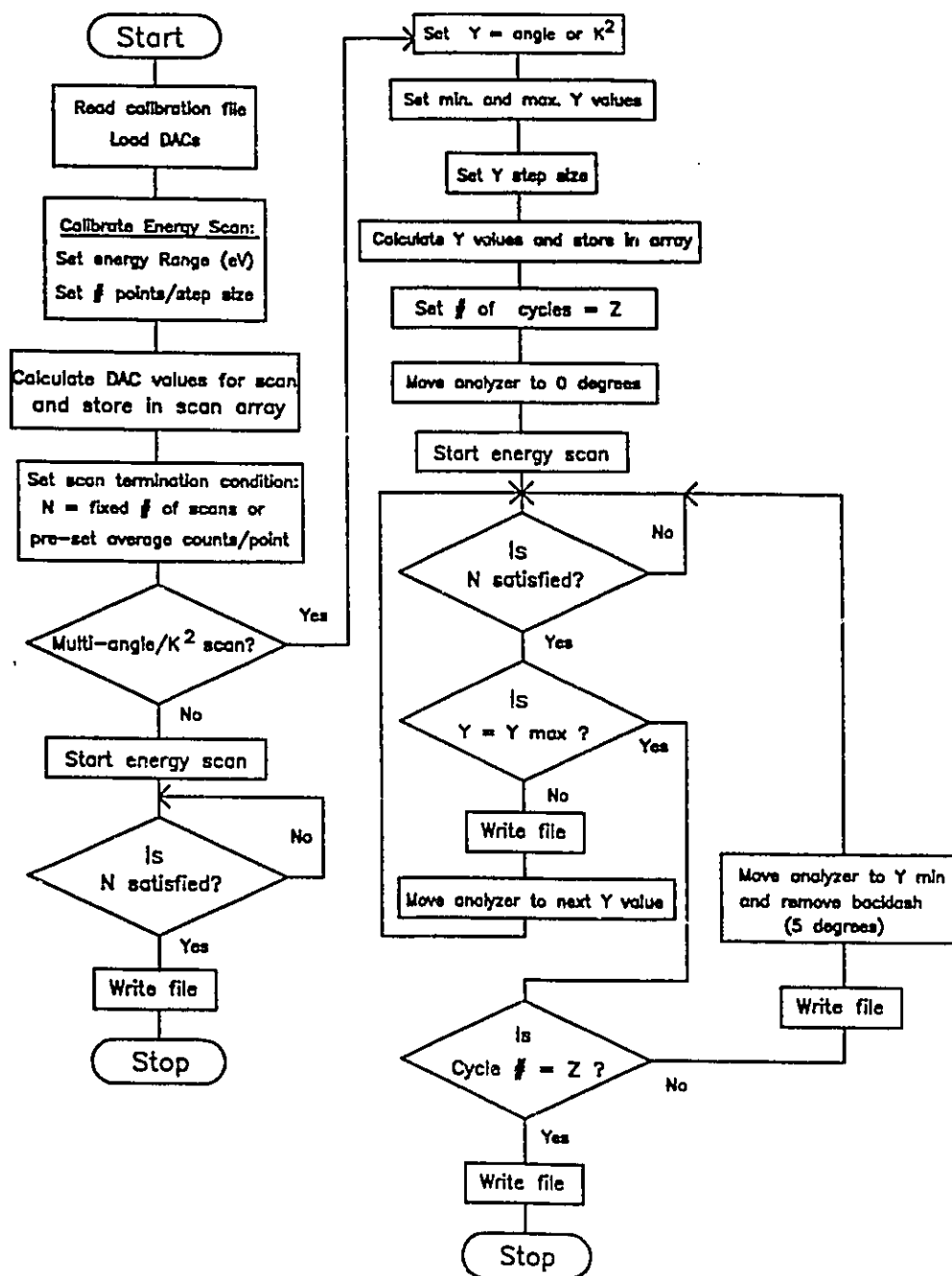


Fig. 3.18 Flow chart representation of the acquisition program.

spectra acquired at increasingly large angles. Transition cross-sections typically decrease at larger scattering angles, and thus one needs longer acquisition times in order to build up comparable statistics relative to spectra acquired at small angles. Using the multi-angle scan option, the program will acquire energy loss spectra at each of a series of user-selected angles. One can either specify the angular range directly, or by specifying a linear momentum transfer range, the algorithm will compute the required scattering angles. It is possible to cycle over the range of angles repeatedly, with a small number of energy scans being taken at each angle. By signal averaging in this manner, as opposed to taking a large number of energy scans at each angle in a single cycle over the angular range, the effects of decaying beam current and degradation of the spectrometer performance in general can be more effectively averaged out. This method has been proven reliable and will be discussed more fully in chapter 5.

At present, the beam current is monitored at the entrance to the analyser lens (see figure 3.1, point A) and at the exit of the monochromator (figure 3.1, point B) using simple analog meters. These values are recorded manually at several intervals throughout the scan period, and are later used in spectral normalisation procedures. This is not considered to be the optimum approach, and in the future automated current monitoring will be implemented using an ADC. This signal could be used as part of a feedback routine that would re-optimize the lens voltages as the current degraded over time.

### 3.2.7.3 Optimization Procedures.

Having computer-interfaced all essential spectrometer voltages, an iterative



optimisation algorithm was designed and incorporated as a subroutine of the main acquisition algorithm to allow a degree of "automated tuning". The operator can randomly select a subset of, or all twenty-one computer-interfaced voltages and by running the optimisation routine, can maximize a given parameter (eg. beam current or a specific aperture, counts per second on a particular electronic transition, etc.) as a function of the selected voltages. In addition, the parameter being optimised can be a ratio (i.e. signal/background), which is useful for optimising individual spectral features. A variable dwell time is provided, as a longer time per iteration is usually required for optimising parameters that are sensitive to rapid changes in the local electric fields in the spectrometer. This includes low-cross section transitions and very high beam current.

The algorithm is based on the Direction Set (or Powell's) method in multidimensions [PF&88] and belongs to a class of schemes called successive line minimisations. Although this is actually a minimisation routine, it is only a simple matter to negate the sign of the optimised parameter or subtract it from unity to convert the problem into a maximisation routine. The practical hardware implementation utilises the pulse counting electronics and a voltage-to-frequency convertor which transduces quantities such as beam current into conditioned pulses. Detector signals can be handled directly, using the pulse output of the pre-amp/discriminator circuit.

### 3.3 Evaluation of Performance

This section presents results obtained after commissioning the instrument which effectively demonstrate that its actual performance in practice is consistent with the

original design motives.

### 3.3.1 Demonstration of Control Flexibility

In practice, the computer-interfaced power supply network has proven particularly useful for scanning different edges (i.e. energy loss regions) which may be separated by several hundred eV and can require some degree of manual spectrometer tuning at each edge as the energy loss increases. This point is illustrated in figure 3.19. After determining three sets of voltages which provide decent spectra for energy loss regions corresponding to the valence, C 1s and O 1s edges of CO and subsequently saving them as separate calibration files, it was then possible to read the files in succession. In this manner, one can effectively repeatedly scan spectra under optimized conditions at three edges covering an energy loss range of over 500 eV without manual intervention.

The decrease in signal which occurs as the energy loss increases from the valence to core loss regimes in figure 3.19 is due to the decrease in the excitation cross-section with increasing energy. In general, larger incident beam currents are therefore required to obtain adequate signal rates for core loss transitions relative to valence shell spectra. As a result, space charge effects and diminished intensities lead to decreased resolution at increasing energy loss.

### 3.3.2 Optimisation

In practice, the optimisation procedure has proven to be very valuable, especially for maximising incident beam current at low monochromator pass energies. It is used

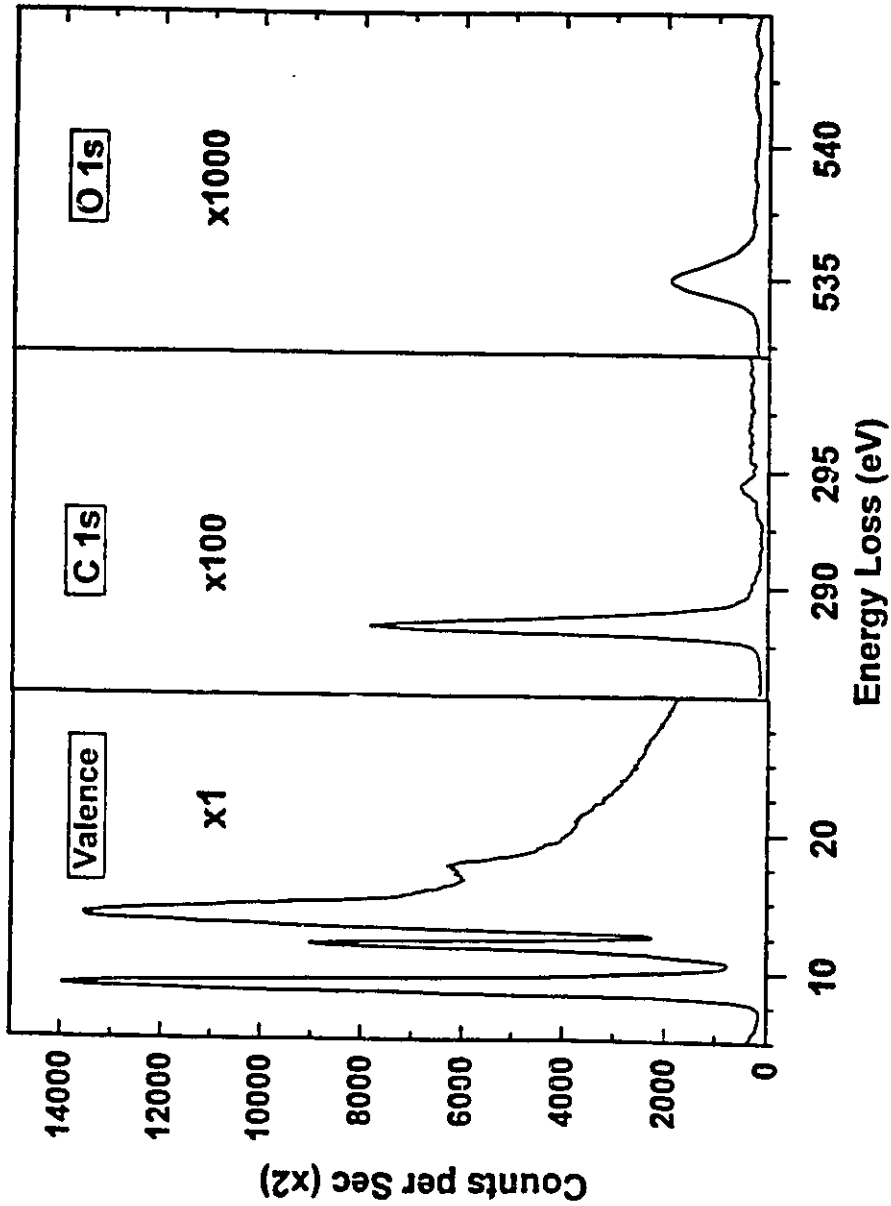


Fig. 3.19

Demonstration of control flexibility using CO. The three edges, spanning an energy loss range of over 500 eV, were scanned in a single sequence by successively reading in three calibration files and acquiring. Due to the decrease in the excitation with increasing energy, the filament current was increased at each higher energy edge (-2.05 A, -2.12 A and -2.23 A respectively for the valence, C1s and O1s edges).

routinely after installing new electron gun filaments. Since each filament has minute variations in the hairpin position that are difficult to account for with the present mounting design, re-tuning of the spectrometer is thus required as the optimum voltage settings are a sensitive function of the filament position. Computer optimisation significantly reduces the time spent manually retuning. In this respect, it is thus particularly beneficial for new instrument operators who do not yet have the experience necessary to properly tune the instrument manually.

Figure 3.20 illustrates graphically a two variable optimisation of a single parameter. After an initial optimisation to find a set of voltages that produced a maximum incident beam current, the first anode and first focus elements of the electron gun were scanned simultaneously about the global current maximum to produce a three-dimensional voltage surface. A point on the surface was chosen where the current was essentially a minimum and the optimisation procedure was modified to save the coordinates of each iteration into a file. These iteration coordinates are overplotted on the potential surface. As can be seen in figure 3.20, the routine finds its way up the steepest ascent, explores the various local maxima and finally arrives at the global current maximum. In practice, a nine parameter optimisation (corresponding to electron gun, monochromator and exit lens) which would be difficult to visualise here graphically, is used to maximise the incident beam current.

### 3.3.3 Lens Characterisation

Figures 3.21 and 3.22 illustrate characteristic experimental lens voltage ratios

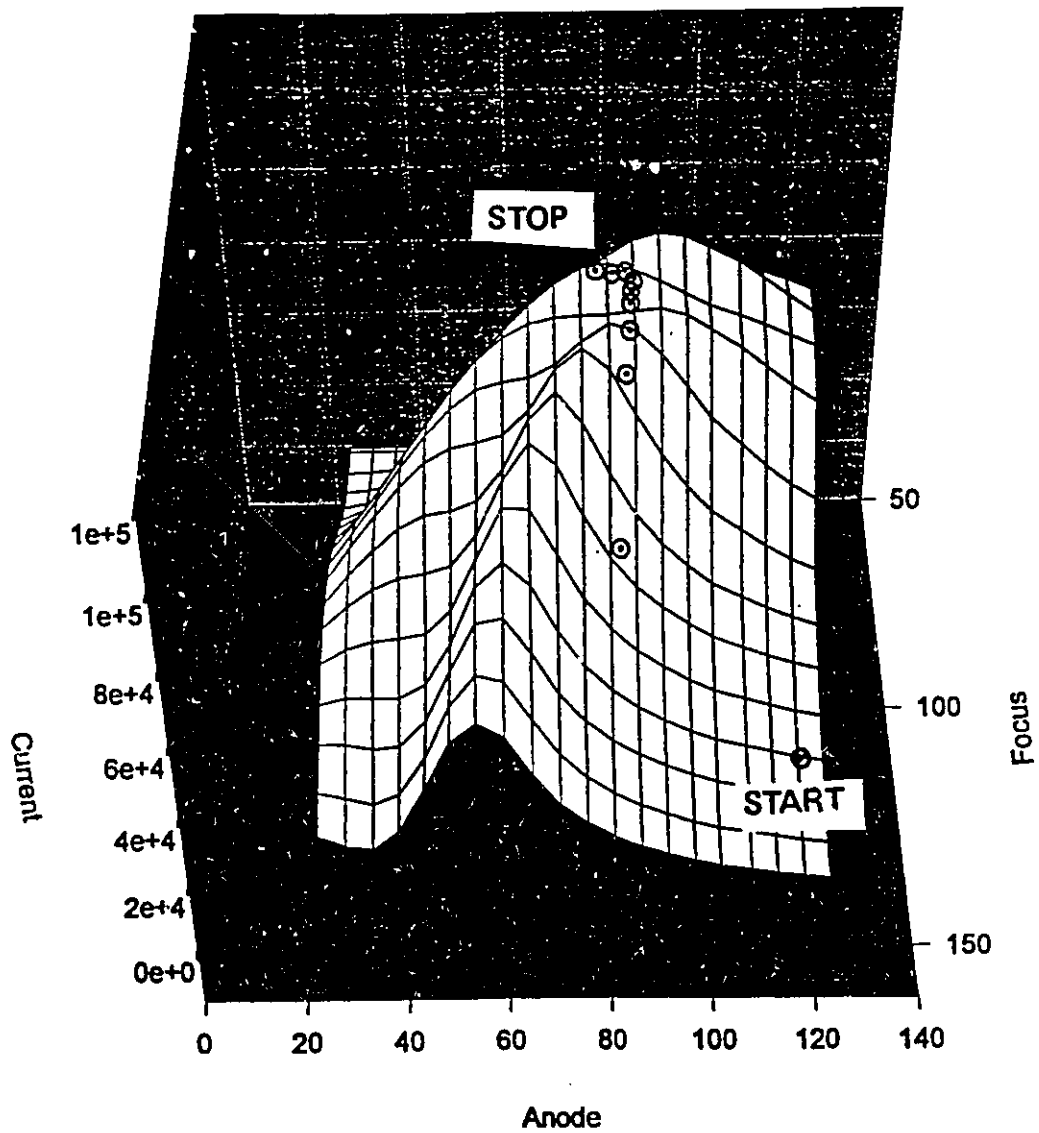


Fig. 3.20

Graphical representation of a 2-D optimisation of a single parameter. The beam current at the collision cell was optimised as a function of the first anode and first focus voltages of the electron gun ( $A_1$  and  $F_1$  in figure 3.7(a)). The iterations of the optimisation routine are overlotted as circled points on the 3-D current/voltage surface.

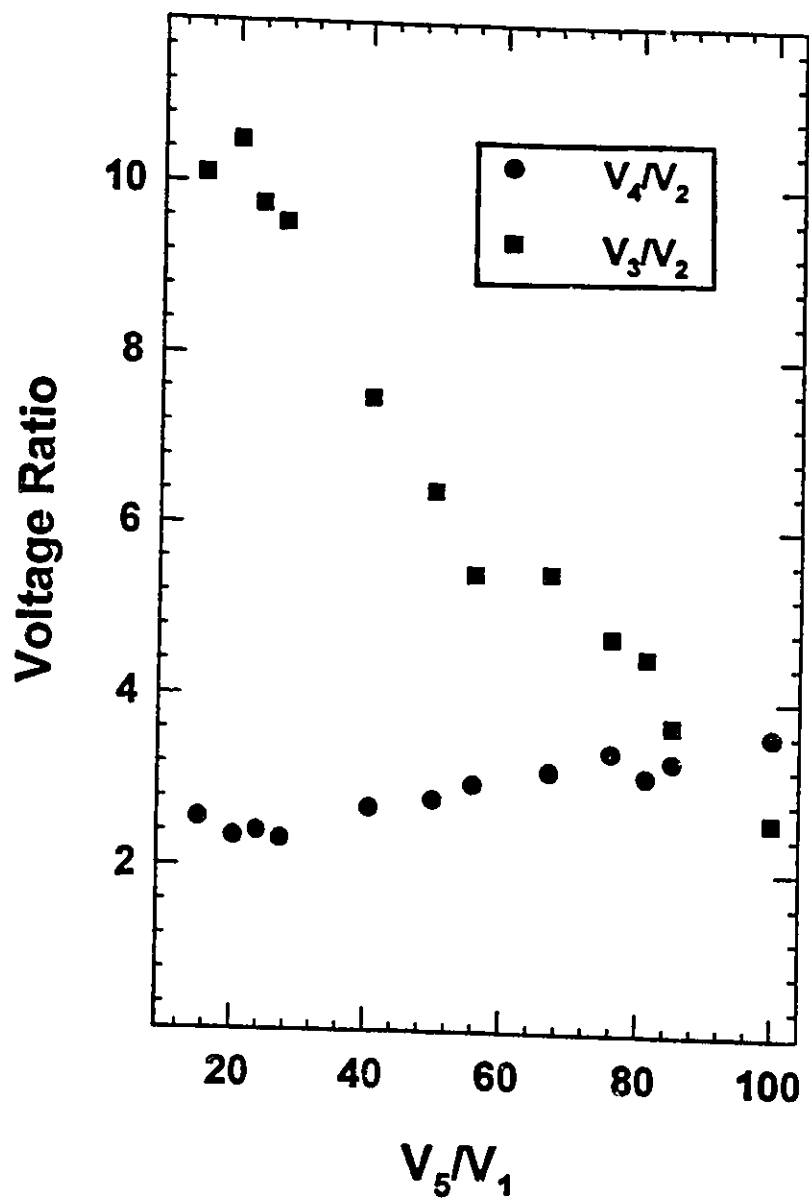


Fig. 3.21

Characteristic lens voltage ratios as a function of the overall acceleration ratio  $V_5/V_1$  compiled from experimental calibration files for the monochromator exit lens.

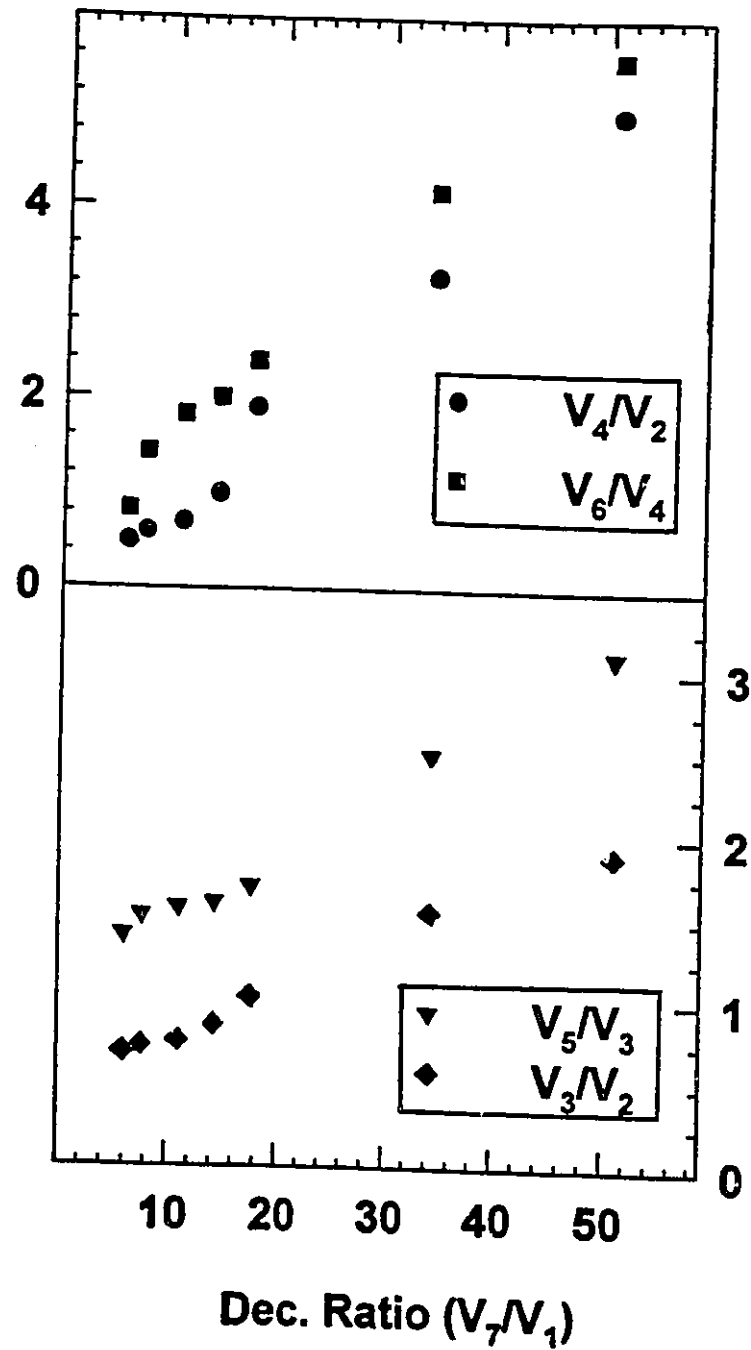


Fig. 3.22  
 Characteristic lens voltage ratios as a function of the overall deceleration ratio  $V_7/V_1$  compiled from experimental calibration files for the analyser entrance lens.

derived from several calibration files used in practice for the monochromator and analyser lenses, respectively. Tables 3.3 (a) and 3.3 (b) below compares lens ratios predicted from the theoretical simulations discussed in section 3.2.4 with those observed in practice.

It can be seen from Table 3.3 (a) for the monochromator exit lens that although there is some agreement between theory and experiment for the voltage ratio  $V_4/V_2$ , there is a rather large discrepancy between theory and experiment for the voltage ratio  $V_3/V_2$ . This is the case for all three acceleration ratios,  $V_5/V_1 = 15, 50$  and  $100$ . One possible explanation is residual magnetic fields (a few mG) that exist experimentally and are difficult to model. In addition, it is difficult to model all combinations of lens voltage ratios that provide reasonable focal behaviour; whereas experimentally, it is much easier using the optimisation routine to find a set of voltages that provide the optimum behaviour. These arguments also apply to the analyser entrance lens. While there is some agreement between experiment and theory for a deceleration ratio ( $V_7/V_1$ ) of  $5$ , there are rather large discrepancies in the voltage ratios for a deceleration ratio of  $50$ .

Overall, the agreement between the theoretical lens voltage values and those which were found to be optimal in practice is poor. However, it should be noted that the theoretical voltage values provided reasonable starting points for initial testing of the instrument. In most cases it was possible to get an electron beam from the monochromator to the collision cell using theoretical values. This beam can then be subjected to the optimisation procedure after which an optimised set of voltages will be found to maximise the beam current.



Table 3.3 (a) Theoretical vs. Experimental Voltage Ratios for Monochromator Exit Lens.

Accel. Ratio $V_5/V_1^*$	$V_4/V_2$		$V_3/V_2$	
	Experiment	Theory	Experiment	Theory
15	2.6	1.7	10.1	0.3
50	2.8	2.9	6.4	1.4
100	3.6	2.5	2.6	0.7

\* Voltages correspond to the lens elements labelled in figure 3.8 (a)

Table 3.3 (b) Experimental vs. Theoretical Voltage Ratios for Analyser Entrance Lens

Decel. Ratio $V_7/V_1^{**}$	$V_4/V_2$		$V_6/V_4$		$V_5/V_3$		$V_3/V_2$	
	Expt.	Theory	Expt.	Theory	Expt.	Theory	Expt.	Theory
5	1.4	1.3	0.8	0.4	1.5	2.5	0.8	0.6
50	5.0	2.9	5.6	0.3	3.0	13.2	1.8	0.5

\*\* Lens voltages correspond to the elements labelled in figure 3.10.

### 3.3.4 Performance Tests

This section presents some selected results obtained with McVAHRES that demonstrate its capabilities. In addition, chapters 4, 5 and 6 document extensively the results of experiments performed using this instrument, which also effectively demonstrate the high resolution, variable  $E_0$  and variable scattering angle aspects of the instrument.

#### 3.3.4.1 Resolution

Figures 3.23 and figure 4, chapter 4 (b) illustrate the energy resolution available with this instrument in the valence and core excitation regimes, for He and CO, respectively. Figure 3.23 corresponds to a FWHM of 0.090 eV for the  $(1s^{-1}, 2p) ^1P$  state of He at 21.22 eV, while figure 4, chapter 4 (b) corresponds to a FWHM of 0.18 eV for the  $(C 1s^{-1}, \pi^*) ^1\Pi$  state at 287.4 eV. The difference in the resolution between the valence and inner shell regimes has been discussed in section 3.3.1. While this does not represent the highest resolution available in the field, it is considered more than reasonable for the type of experiments the instrument was designed to perform (discussed in chapters 4 and 6). Indeed, the actual resolution achieved in practice in both the valence and inner shell regimes compares favourably with the design objectives outlined in the introduction. The addition of the second analyser hemisphere and parallel detection unit (discussed in section 3.2.5) in the future should offer significant improvement in resolution.

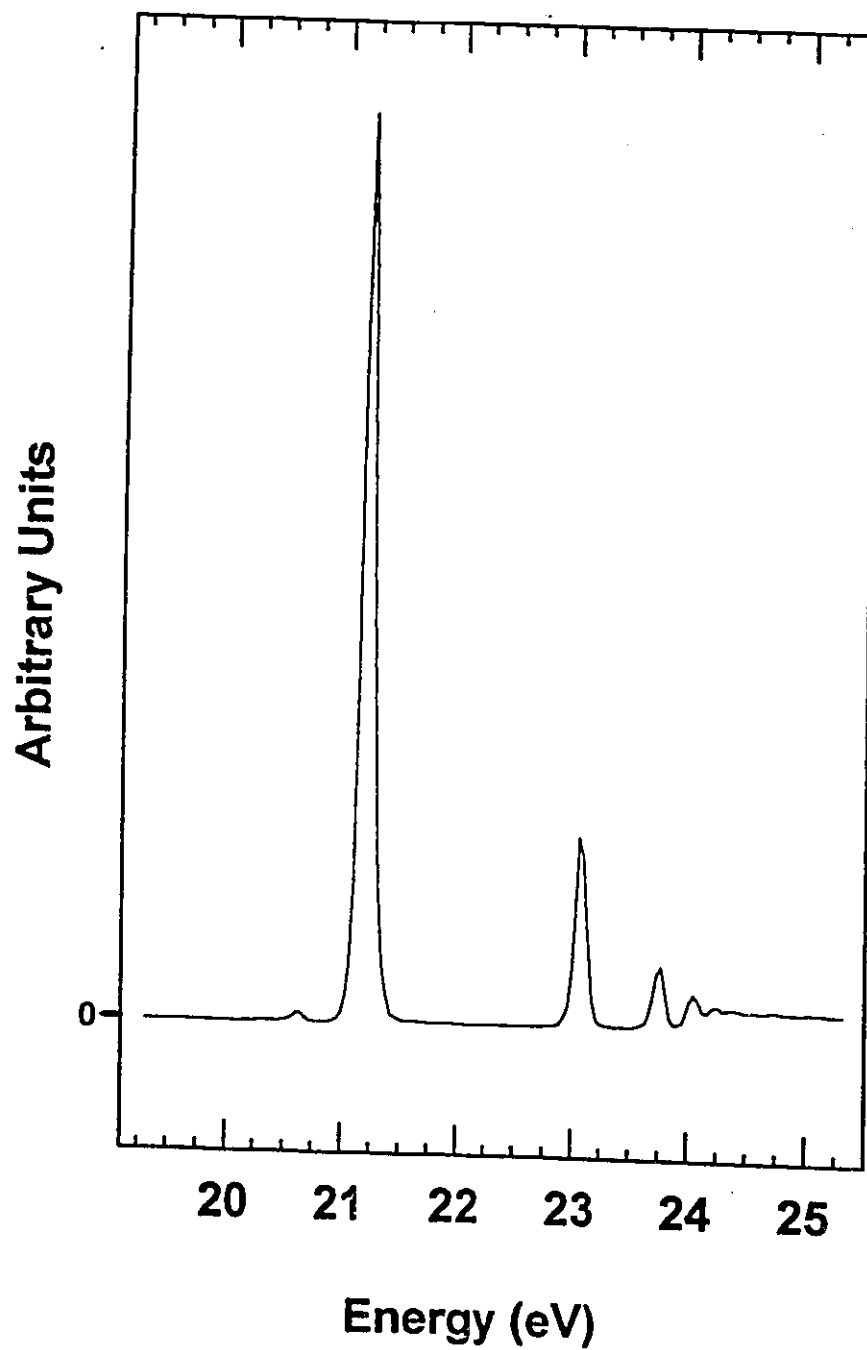


Fig. 3.23  
Demonstration of resolution capability using He. The FWHM of the  $(1s^{-1}, 2p) {}^12P$  feature at 21.22 eV is 0.090 eV.

#### 3.3.4.2 Variable $E_0$

Figure 1, chapter 4 (b) demonstrates the variable impact energy capability of the instrument using the ( $C\ 1s^{-1}, \pi^*$ )  $^3\Pi$  state of CO at 286.0 eV, which is only unambiguously detectable at impact energies below about 430 eV. As discussed more fully in chapter 4, the transition probability of this triplet state of CO is enhanced as the impact energy approaches the energy of excitation. Low impact energy, inner shell experiments such as these are particularly difficult due to the fact that sufficient beam (> 100 nA) is required for adequate signal intensity while simultaneously maintaining low monochromator pass energies for reasonable resolution (ca. 200 meV). As a result, space charging effects and patch fields become significant and can degrade spectrometer performance over a period of several hours.

In the valence regime, much lower incident beam currents can be used (ca. 1 nA or less) and thus the resolution is markedly better. This is illustrated in figure 3.23 for He at an  $E_0$  of 500 eV and 90 meV FWHM resolution.

#### 3.3.4.3 Variable Scattering Angle

Figure 3.24 demonstrates the variable angle capability of the instrument in the valence shell regime. Figure 3.24, recorded at 150 meV FWHM resolution, illustrates the enhancement of the dipole-forbidden ( $1s \rightarrow 2s$ ) transition at 20.6 eV relative to the dipole-allowed ( $1s \rightarrow 2p$ ) transition at 21.2 eV in He at increasing scattering angles (and thus increasing momentum transfer).

Figure 5.7 plots the relative GOS of the ( $1s \rightarrow \pi^*$ ) transition in  $N_2$  at 400.7 eV. The

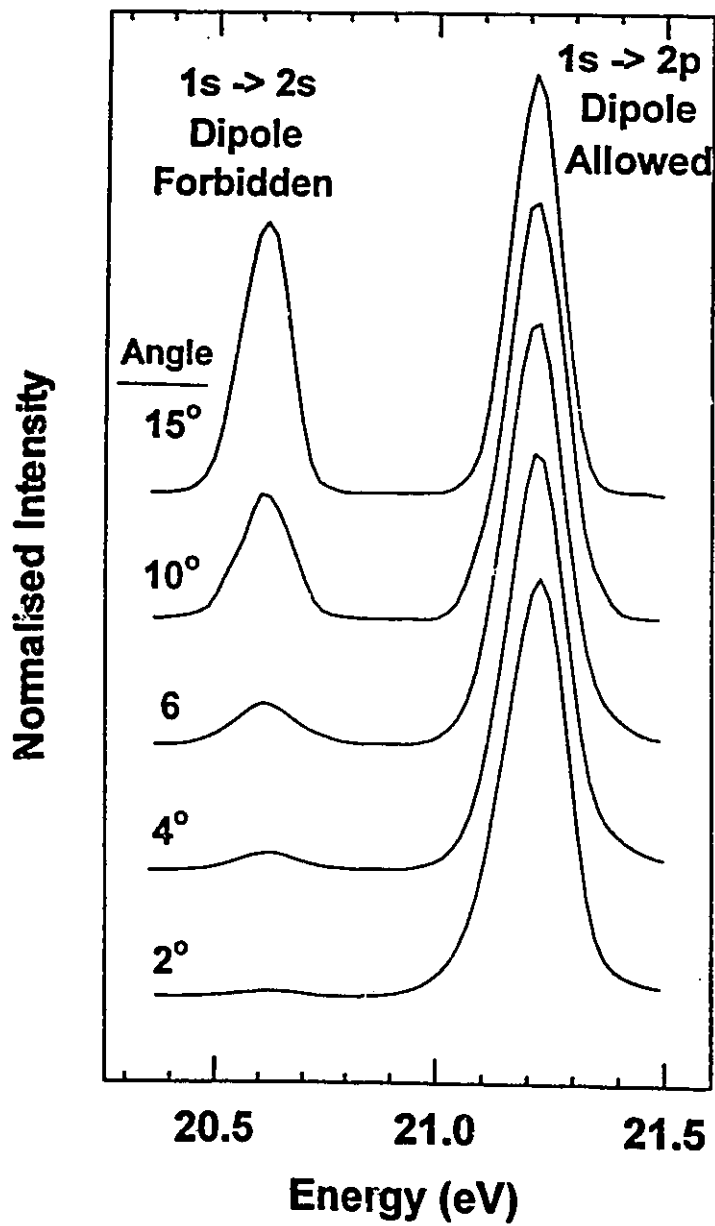


Fig. 3.24

Illustration of variable angle capability of McVAHRES in the valence regime using He. The dipole-forbidden  $1s \rightarrow 2s$  transition at 20.6 eV is enhanced at large scattering angles relative to the dipole-allowed  $1s \rightarrow 2p$  transition at 21.2 eV.

$\pi^*$  feature was scanned at a series of scattering angles up to  $30^\circ$  at an impact energy of 1430 eV. Using methods outlined in chapter 5, the relative GOS was determined as a function of  $K^2$ , and normalised to the data of Camilloni et al. [CF&87]. The agreement with the data of CF&87 is good, (within error bars) which provides confidence that the instrument can make meaningful measurements on new chemical systems for which no comparative literature result exists. Note that in general, large angle, inner shell excitation experiments are particularly a challenge, due to extremely low cross-sections that result in count rates less than 10 cps in some cases.

#### 3.3.4.4 Constant Momentum Transfer

Figure 5.1 presents S 2p spectra of SF<sub>6</sub> recorded under conditions of nearly constant momentum transfer. This type of experiment incorporates both the variable angle and variable impact energy aspects of the instrument to demonstrate the validity of the first Born approximation. It is hoped in the future to modify the scanning algorithm such that true constant momentum transfer spectra can be acquired. To achieve this, it is necessary to scan  $E_0$  (or the scattering angle) simultaneously with the energy loss, as discussed in part in section 3.2.6.1. With the present level of interfacing, accommodating this type of scan mode should require only minor modifications.

#### Summary

This chapter outlined a set of design objectives for, and practical implementation of, a new electron spectrometer capable of high resolution, variable scattering angle and

variable impact energy for studies of inner shell and valence dipole and spin forbidden electronic transitions. In addition, a sophisticated electronics system was incorporated, allowing enormous flexibility with respect to control and acquisition. The selection of results presented in the last section of this chapter and in chapters 4,5 and 6 effectively demonstrate that the performance of the instrument in practice corresponds favourably to the original design motives.

There are a host of improvements that have been identified to improve the present level of spectrometer performance. These include: addition of the second analyser (tandem geometry discussed in section 3.2.4.4) which should improve the resolution and significantly lower background at the  $0^\circ$  scattering angle; addition of the parallel detection unit, which should improve the throughput and thus allow improved resolution by enabling the use of lower pass energies; more flexible scanning to include the constant  $K^2$  and excitation modes and finally automated current monitoring with feedback to improve overall stability of the incident beam. It is envisaged that all or most of these suggestions will be incorporated into the present instrument by August 95.

**Chapter 4**  
**Triplet State Spectroscopy**



## Chapter 4 (a)

Studies of C 1s  $\rightarrow$   $\pi^*$  Triplet States of Carbon Monoxide,  
Benzene, Ethylene and Acetylene

The following work which documents spin forbidden core excited states observed at low impact energies has been published in the Canadian Journal of Physics (Can. J. Phys. 72 (1994) 879) and is presented here as the journal article, which is reprinted with permission (see page 202).

The author of this thesis performed all the experimental work and prepared the bulk of the paper in collaboration with Prof. A.P. Hitchcock. The calculations were performed and reported by C. Enkvist and S. Lunell of the Department of Quantum Chemistry, Uppsala University, Uppsala, Sweden.

As a co-author of the following journal article:

Can. J. Phys. 72, 1994, 879.

I hereby authorize James Francis to reprint this work as part of his Ph.D. thesis.

Date: March 16, 1993

Signature: Alex P. Hitchcock

Date: March 19, 1995

Signature: Sten Lunde

Date: March 19, 1995

Signature: Christin Enkvist

## Studies of $C 1s \rightarrow \pi^*$ triplet states of carbon monoxide, benzene, ethylene, and acetylene

J.T. FRANCIS

*Department of Chemistry, McMaster University, Hamilton ON L8S 4M1, Canada*

C. ENKVIST AND S. LUNELL

*Department of Quantum Chemistry, Uppsala University, Uppsala, Sweden, S-75120*

AND

A.P. HITCHCOCK<sup>1</sup>

*Department of Chemistry, McMaster University, Hamilton ON L8S 4M1, Canada*

Received March 29, 1994

Accepted June 1, 1994

This paper is dedicated to Dr. Gerhard Herzberg on the occasion of his 90th birthday

The ( $C 1s^{-1}, \pi^*$ ) triplet states of carbon monoxide, benzene, ethylene, and acetylene have been studied using electron energy loss spectroscopy with low-energy (near-threshold) excitation. The singlet-triplet splitting for the ( $C 1s^{-1}, \pi^*$ ) states of the hydrocarbon species were measured for the first time. Intermediate neglect of differential overlap (spectroscopic) (INDO/S) calculations within the equivalent cores approximation were used to calculate ( $1s^{-1}, \pi^*$ ) singlet-triplet splittings. The calculated values are in reasonable agreement with the experimental values for the hydrocarbon species but are significantly underestimated for CO. A strong correlation between singlet-triplet splittings and oscillator strengths for the  $1s \rightarrow \pi^*$  transitions was noted and rationalized in terms of the dependence of both factors on the spatial overlap of  $1s$  and  $\pi^*$  wave functions.

Les états triplets ( $C 1s^{-1}, \pi^*$ ) du monoxyde de carbone, du benzène, de l'éthylène ont été étudiés par spectroscopie de perte d'énergie des électrons, avec une énergie d'excitation voisine du seuil. La séparation singulet-triplet pour les états ( $C 1s^{-1}, \pi^*$ ) des hydrocarbures a été mesurée pour la première fois. Le calcul de ces séparations a été effectué par la méthode INDO/S (Intermediate neglect of differential overlap/spectroscopic), à l'approximation des coeurs équivalents. Les valeurs calculées sont raisonnablement en accord avec les valeurs expérimentales pour les hydrocarbures, mais elles sont nettement trop basses dans le cas de CO. On a noté une forte corrélation entre les séparations singulet-triplet et les forces d'oscillation pour les transitions  $1s \rightarrow \pi^*$ , ce qui peut s'expliquer par le fait que les deux facteurs dépendent de la superposition spatiale des fonctions d'ondes  $1s$  et  $\pi^*$ .

[Traduit par la rédaction]

Can. J. Phys. 72, 879 (1994) © National Research Council of Canada

### 1. Introduction

Inner shell excitation of both free and surface-adsorbed atoms and molecules using electron impact techniques [1, 2] has gained recognition in the last two decades as a valuable alternative to photoabsorption. Recently, developments in soft X-ray monochromators coupled with dedicated synchrotron radiation sources have led to major advances in high-resolution studies of electric dipole inner-shell excitation by photoabsorption and related techniques [3, 4]. Even so, the energy resolution provided by inner-shell electron energy loss spectroscopy (ISEELS) using monochromated electron beams remains competitive for studies above 200 eV. The majority of ISEELS studies have been carried out under conditions of small momentum transfer (impact energy,  $E_0 > 1$  keV; scattering angle,  $\theta < 2^\circ$ ) where electric dipole transitions dominate and the resulting spectra are essentially identical to photoabsorption. However, inelastic electron scattering can also be carried out under large momentum transfer conditions ( $E_0$  close to threshold and (or) large scattering angles) where dipole-forbidden transitions can make large contributions. These include excitations forbidden by either angular momentum and (or) spin conservation electric dipole selection rules. Since the 1960s, nondipole *valence* electronic excitations have been studied extensively [5–8]. However, nondipole *core* excitation studies [9, 10] have been studied much less extensively owing to their much smaller excitation cross-

section relative to that for valence transitions.

The first core-excited spin-forbidden transition, that for  $N 1s \rightarrow \pi^*$  excitation in  $N_2$ , was observed in 1982 by lowering the impact energy of the incident electron close to the threshold [10]. Simplistically, the excitation from the singlet ground state to the triplet core-excited state, which is forbidden under conditions of fast electron impact, becomes allowed because the matrix element corresponding to exchange between the incident and a target electron can be appreciable in slow collisions. The near-threshold conditions then result in the appearance of a "triplet partner" that increases in intensity as the impact energy approaches threshold and as the scattering angle increases (see Fig. 1). The ( $C 1s^{-1}, \pi^*$ )  $^3\Pi$  state of CO has been studied relatively extensively [11–13] since the singlet-triplet energy splitting ( $\Delta(1-3)$ ) in CO is relatively large (1.47 eV), which allows detection even with spectrometers of modest resolution. Harrison and King [13, 14] have used an unmonochromated energy-loss spectrometer with a fixed  $90^\circ$  scattering angle to carry out systematic studies of near-threshold ISEEL spectra of a number of molecules in order to map the chemical systematics of core excitation singlet-triplet splittings. These studies have contributed much to the understanding of the spectroscopy and chemical basis of core-state singlet-triplet splittings. In particular, they reveal a strong correlation of  $\Delta(1-3)$  and the degree of spatial overlap of the core and "optical" orbital (i.e., the orbital into which the core electron is excited); that is, significant singlet-triplet splittings are only found in intense

<sup>1</sup>Author to whom correspondence may be addressed.

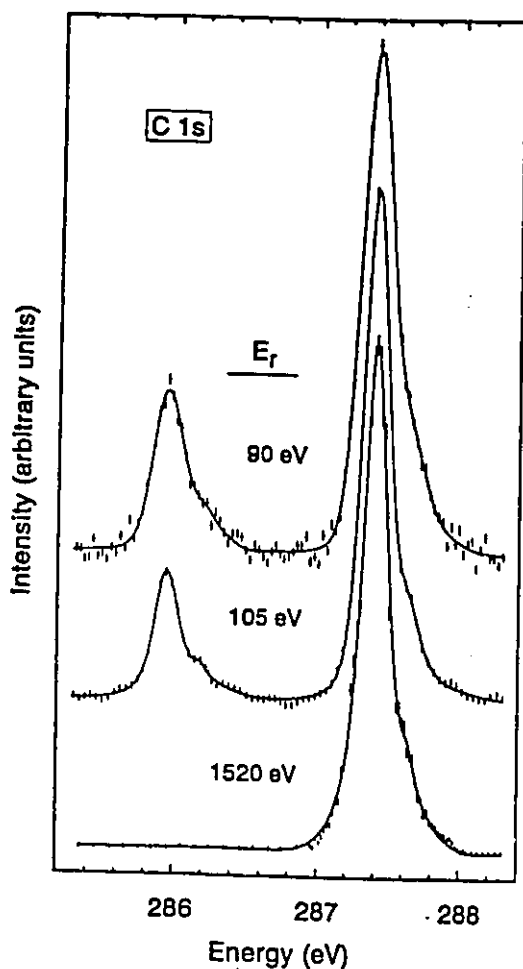


Fig. 1. Electron energy loss spectra of CO in the region of the C  $1s \rightarrow \pi^*$  transitions recorded at  $2^\circ$  scattering angle with 0.20 eV resolution and impact energies of  $\sim 376$ ,  $\sim 391$ , and  $\sim 1806$  eV, corresponding to the indicated  $E_r$ , the residual electron energy after the inelastic scattering. The experimental data are indicated by points and vertical error bars while the solid lines are the result of curve fits to Gaussian lines.

transitions corresponding to core excitations into compact virtual orbitals of a large valence character [13, 14]. However, because the resolution of their spectrometer was only 0.7 eV, the triplet states of a number of important species, notably hydrocarbons, could not be resolved. In this work we have used a newly developed, high-resolution, variable angle, variable impact energy spectrometer to study the near-threshold ISEEL spectra of benzene, ethylene, and acetylene, along with that of CO. The improved resolution has allowed the first detection of the singlet-triplet splitting of the (C  $1s^{-1}, \pi^*$ ) states of these hydrocarbon species. Our results are compared to INDO/S calculations.

The energy separation of the singlet and triplet (C  $1s^{-1}, \pi^*$ ) states arises from the exchange interaction of the unpaired electrons in the C  $1s$  and  $\pi^*$  orbitals. In the Hartree-Fock orbital approximation the exchange interaction,  $K(1s, \pi^*)$ , is related to the spatial overlap of the  $1s$  and  $\pi^*$  orbitals. Since the oscillator

strength for  $1s \rightarrow \pi^*$  electric dipole transitions also depends on the degree of spatial overlap (albeit with an  $r$  rather than an  $r^{-1}$  operator), species with large dipole ( $1s, \pi^*$ ) oscillator strengths are expected to have large singlet-triplet splittings [14]. The validity of this concept is explored both experimentally and theoretically in the present work. Previously, Lassetre and Dillon demonstrated that there is a relationship between transition intensity (although in their work the intensity was measured as the integrated generalized oscillator strength for the singlet ( $\pi, \pi^*$ ) transition) and singlet-triplet splittings for valence excitations [6].

Accurate experimental determinations of singlet-triplet splittings for core excitation provide a useful testing ground for quantum calculations of exchange interactions in core-excited states [15, 16]. The accuracy of such calculations has become an issue of considerable importance in the interpretation of the O  $1s$  spectrum of  $O_2$  (refs. 17-19 and A.P. Hitchcock, S.G. Urquhart, J.T. Francis, and N. Kosugi, unpublished). As Harrison and King have shown for COS and  $CS_2$  [14], the magnitude of singlet-triplet splittings can be used to evaluate the spatial extent of the optical orbital and thereby gain insight into the possible valence (small- $R$ ) versus Rydberg (large- $R$ ) character of core-excited states. Finally, the energies of triplet ( $1s^{-1}, \pi^*$ ) states are of interest in the context of the excitation and electronic/ionic decay of core states of molecular adsorbates on metal surfaces (studied by near-edge X-ray absorption fine structure and de-excitation electron spectroscopies). There is evidence that exchange with the electrons of the metal substrate converts the initially formed ( $1s^{-1}, \pi^*$ )  $^1\Pi$  singlet states into the corresponding, lower energy ( $1s^{-1}, \pi^*$ )  $^3\Pi$  triplet states prior to electronic decay (refs. 20, 21, and P. Bruhwiler, S. Svensson, S. Lunell et al., unpublished).

## 2. Experimental

The ISEELS spectra were recorded using a newly developed variable impact energy, variable angle, high-resolution electron spectrometer that will be described in detail in a future publication. Briefly, the incident electron beam is monochromated using an hemispherical electrostatic selector operated with pass energies between 10 and 25 eV for this study. The beam exiting from the monochromator is focused at the gas target using a five-element lens. Electrons inelastically scattered at the mechanically determined scattering angle ( $\sim 10^\circ$ - $110^\circ$ ) are transferred to a hemispherical electron energy analyzer by a seven-element lens. In this study spectra were recorded using both a jet formed by expansion through a capillary array (100:1 aspect ratio of the channels) and a gas cell. The jet source provided higher quality results because it avoided a background signal arising from secondary electron scattering in the gas cell. The near threshold spectra of the hydrocarbon species were recorded with 180 eV residual energy and a small scattering angle ( $0^\circ$  or  $2^\circ$ ; near-threshold spectra are independent of scattering angle up to  $10^\circ$ ). The C  $1s$  spectrum of CO was measured under a wide range of scattering conditions; a full report of these results will be presented elsewhere. The hydrocarbon species were challenging to study on account of a buildup of insulating films on the electron optical surfaces that occurred due to electron beam cracking of surface-adsorbed hydrocarbons. This limited the time available to measure spectra with adequate energy resolution. The lowest impact energy at which spectra could be successfully recorded was also limited due to surface charging effects to which low-energy electrons are

particularly sensitive. Individual spectra were signal averaged for several hours since the peak count rates were in the range of 10–30 cps. The spectra reported in this paper are sums of between 5 and 10 such spectra. The energy resolution was 0.20 eV FWHM for CO, 0.31 eV for benzene, 0.35 eV for ethylene, and 0.55 eV for acetylene.

### 3. Calculations

The calculations were performed using a localized core model. The remaining  $1s$  electron in the core-excited state was represented by a Slater-type orbital (STO) with exponent,  $\xi = 6.0$  for the C  $1s$  and  $\xi = 8.0$  for the O  $1s$  orbital, corresponding to an unscreened nuclear charge. The valence orbitals were calculated by means of the INDO/S method, using the  $Z + 1$  approximation to represent the atom with the core hole. The singlet–triplet splitting was obtained as twice the exchange integral  $K(1s, \pi^*)$ . Only one-centre contributions were retained. Exchange integrals involving two or more centres are known to be at least one order of magnitude smaller than one-centre integrals [22] and can therefore be neglected to a first approximation, giving the expression:

$$K(1s, \pi^*) \sim K(1s, 2p) \cdot |c_{2p}|^2 \quad (1)$$

where  $c_{2p}$  is the LCAO-MO coefficient of the C  $2p$  AO in the  $\pi^*$  orbital and  $K(1s, 2p)$  is a one-centre exchange integral. Relative oscillator strengths were calculated for the different  $1s \rightarrow \pi^*$  transitions, also using a one-centre approximation. Neglecting the small variations in excitation energy and assuming a constant value for the atomic transition integral  $\langle 1s | e r | 2p \rangle$ , this implies that the oscillator strengths are also proportional to the local  $2p$ -population of the  $\pi^*$  orbital on the core-excited atom; i.e.,

$$f_{\text{osc}}(1s^{-1}, \pi^*) \sim (\text{const}) \cdot |c_{2p}|^2 \cdot |\langle 1s | e r | 2p \rangle|^2 \quad (2)$$

### 4. Results and discussion

Figure 1 presents C  $1s$  spectra of CO in the region of excitations to the  $(C 1s^{-1}, \pi^*) {}^3\Pi$  and  $(C 1s^{-1}, \pi^*) {}^1\Pi$  states, recorded at  $2^\circ$  scattering angle and impact energies of  $\sim 376$ ,  $\sim 391$ , and  $\sim 1806$  eV (corresponding to residual energies ( $E_r$ ) of 90, 105, and 1520 eV). This series of spectra illustrates the "turning on" of the exchange between the incident and the target electron as the impact energy approaches that of the threshold for the  $(C 1s \rightarrow \pi^*) {}^3\Pi$  electronic excitation (286 eV). In addition, these spectra demonstrate the capability of the instrument to record ISEEL spectra at a resolution adequate to resolve vibrational band structure under low cross section conditions. The solid lines passing through the experimental data points in Fig. 1 are the results of curve fits using Voigt lineshapes for each vibrational component with a fixed Lorentzian width of 60 meV (the natural linewidth [3, 4]) and an optimized Gaussian width. The detailed lineshape analysis shows there is a significant difference in the Franck–Condon factors and thus potential energy curves of the  $(C 1s^{-1}, \pi^*) {}^3\Pi$  and  $(C 1s^{-1}, \pi^*) {}^1\Pi$  states. These results will be reported elsewhere. The analysis determines  $\Delta(1-3) = E({}^1\Pi, v=0) - E({}^3\Pi, v=0)$ , the separation of the adiabatic transitions, to be 1.47 (3) eV, in good agreement with values reported by others [11–13].

Figure 2 presents the C  $1s$  spectra of benzene, ethylene, and acetylene recorded at small scattering angle and 180 eV residual electron energy. Curve fitting to Gaussian lines has been used to

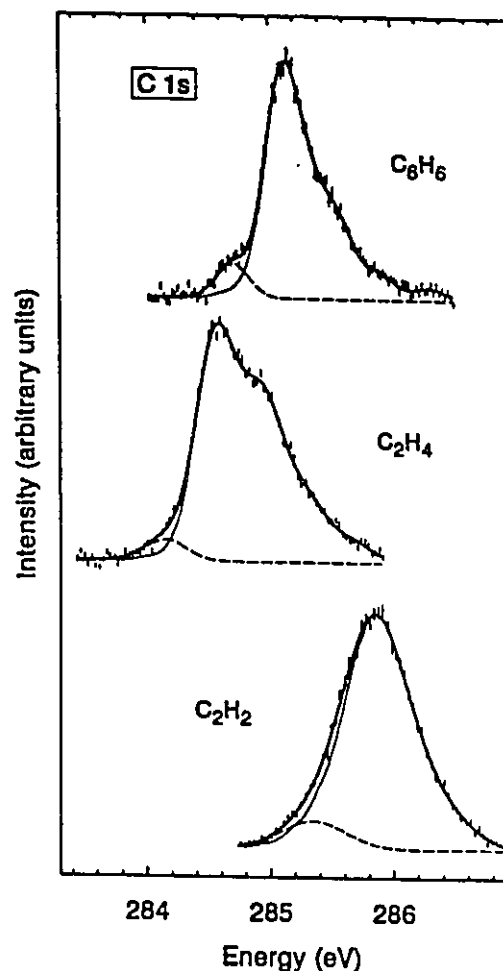


FIG. 2. Electron energy loss spectra of benzene, ethylene, and acetylene in the region of the C  $1s \rightarrow \pi^*$  transitions recorded with  $\sim 465$  eV impact energy and  $0^\circ$  or  $2^\circ$  scattering angle. The low impact energy experimental data are indicated by points and vertical error bars, the thick solid line passing through the data is the result of curve fits to Gaussian lines, and the broken lines indicate the triplet  $(C 1s^{-1}, \pi^*)$  component. The low-energy side of the singlet signal recorded at the same resolution with 1300 eV impact energy (near-dipole-regime), is also plotted (thin solid line) to experimentally demonstrate the existence of the triplet signal in the low impact energy spectrum.

accurately measure  $\Delta(1-3)$ . The thicker solid lines in Fig. 2 are the overall results of the curve fits while the broken lines indicate the fit line for the component corresponding to the triplet states. The thinner solid line superimposed on each C  $1s$  spectrum in Fig. 2 is the leading edge of the singlet  $(C 1s^{-1}, \pi^*)$  signal taken from a high impact energy spectrum where there is negligible triplet signal. Comparison with the corresponding low impact energy spectrum clearly reveals the contribution of the  $(1s^{-1}, \pi^*) {}^3\Pi$  state. The numerical results for all four molecules are presented in Table 1, along with the INDO/S results. For CO the  $\Delta(1-3)$  value corresponds to the difference in the adiabatic transition energies. However, since the vibrational structure of the  $(1s^{-1}, \pi^*)$  triplet states could not be resolved for the

TABLE 1. Energies and singlet-triplet splittings of  $C\ 1s \rightarrow \pi^*$  transitions in CO,  $C_6H_6$ ,  $C_2H_4$ , and  $C_2H_2$  derived from experimental measurements and INDO/S calculations

Species	Experimental				$\Delta(1-3)$ Calculation	
	$E(1s^{-1}, \pi^*)^1\Pi^a$	$E(1s^{-1}, \pi^*)^3\Pi^a$	$\Delta(1-3)$	Literature	This work	Literature
CO	284.7	283.2	1.47 (3)	1.45, <sup>b</sup> 1.45 <sup>c</sup>	0.98	1.29, <sup>d</sup> 1.4 <sup>e</sup>
$C_6H_6$	285.2	284.8	$0.41 \pm \frac{1}{2}$ <sup>0</sup>	—	0.34	—
$C_2H_4$	284.7	284.3	$0.43 \pm \frac{1}{2}$ <sup>2</sup>	—	0.43	—
$C_2H_2$	285.8	285.3	0.50 (3)	0.5 <sup>f</sup>	0.55	—

<sup>a</sup>The energy of the singlet ( $C\ 1s^{-1}, \pi^*$ ) state (and that of the triplet in CO) corresponds to the adiabatic ( $v = 0$ ) energy. All spectra were calibrated to literature values [3, 4, 18, 19] at this peak. The energies given for the triplet ( $C\ 1s^{-1}, \pi^*$ ) states are the vertical energies (peak position of a single Gaussian line).

<sup>b</sup>Reference 11.

<sup>c</sup>Reference 12.

<sup>d</sup>Reference 15.

<sup>e</sup>Reference 29.

<sup>f</sup>Reference 13.

TABLE 2. Oscillator strengths and singlet-triplet splittings for  $1s \rightarrow \pi^*$  transitions

Species	Experimental				Calc. - this work		Calc. - lit.
	$\Delta(1-3)$	$f(10^{-2})^a$	Divisor <sup>b</sup>	$f/trans.(10^{-2})$	$\Delta(1-3)$	$f(rel)^c(10^{-2})$	$f(10^{-2})$
CO C 1s	1.47 (3)	17 (2)	8	2.1 (3)	0.98	2.00	
CO O 1s	0.3 (1) <sup>d</sup>	7 (1)	8	0.9 (2)	0.18	0.21 <sup>e</sup>	
$C_6H_6$	$0.41 \pm \frac{1}{2}$ <sup>0</sup>	24 (3)	16	1.5 (2)	0.34	0.70	
$C_2H_4$	$0.43 \pm \frac{1}{2}$ <sup>2</sup>	6 (1)	4	1.5 (2)	0.43	0.85	2.4 <sup>f</sup>
$C_2H_2$	0.55 (3)	12 (2)	8	1.5 (2)	0.55	1.10	2.2 <sup>f</sup>

<sup>a</sup>Oscillator strengths (peak areas) derived from dipole-regime ISEELS spectra converted according to procedure outlined in ref. 2. Note these spectra are available by Internet from the Uppsala Dept. of Physics computer (see ref. 2 for details on access).

<sup>b</sup>This number is the number of individual dipole-allowed  $1s \rightarrow \pi^*$  transitions (i.e., accounting for the number of C 1s electrons and  $\pi^*$  orbital degeneracy that contribute to the lowest energy C 1s  $\rightarrow \pi^*$  dipole-allowed transition).

<sup>c</sup>Relative oscillator strengths estimated as  $c_{2p}^2$  values (except for O 1s of CO, see footnote e). The calculated values have been scaled by 3.1, the average ratio of  $f_{exp}/f_{calc.,rel}$ .

<sup>d</sup>Estimated from an increased linewidth observed in the near-threshold O 1s ISEELS of CO [11].

<sup>e</sup>The calculated value of  $c_{2p}^2$  for the (O  $1s^{-1}, \pi^*$ ) state of CO (0.14) has been divided by 2.05, which is the ratio  $|\langle C\ 1s|e|C\ 2p\rangle|^2/|\langle O\ 1s|e|O\ 2p\rangle|^2$  [26], in order to have a valid comparison between our estimation of the C 1s and O 1s relative oscillator strengths from LCAO-MO coefficients. The result has then been scaled by the 3.1 factor used to match all calculated  $c_{2p}^2$  values to experiment.

<sup>f</sup>From ref. 30, with the divisor correction applied (the calculated values reported were 0.087 for  $C_2H_4$  and 0.173 for  $C_2H_2$ ).

hydrocarbon species,  $\Delta(1-3)$  is the difference in the vertical excitation energy of the triplet and the adiabatic excitation energy of the singlet. The reported uncertainty in the  $\Delta(1-3)$  values includes an estimate of the difference in the adiabatic and vertical transitions to the ( $1s^{-1}, \pi^*$ ) triplet state, as outlined below.

Low-resolution ISEELS [23] places the vertical transition to the [ $C\ 1s(e_{2g}), \pi^*(e_{2u})$ ]  $^1A_{2u}$  state in benzene at 285.2 eV. In our higher resolution spectrum the singlet component is asymmetric because of incompletely resolved vibrational structure. The singlet lineshape has been fit using several Gaussians, whose initial energy positions were set to the values reported in high-resolution photoabsorption studies [3, 4]. Although the transition to the  $^1A_{2u}$  state is expected to exhibit vibrational structure, the small  $\Delta(1-3)$  value and the limited statistical precision prevented its detection. Thus the [ $C\ 1s(e_{2g}), \pi^*(e_{2u})$ ]  $^1A_{2u}$  signal peaking at 284.8 eV was fit using a single Gaussian line, and the derived  $\Delta(1-3)$  value for  $C_6H_6$  (0.41 eV) is the difference between  $v = 0$  for the  $^1A_{2u}$  transition and the maximum of the single Gaussian fit to the  $^1A_{2u}$  signal. The error associated with the fit is only  $\pm 0.03$  eV. However, our value for  $\Delta(1-3)$  of benzene could be underestimated by the difference in the adiabatic and vertical  $^1A_{2u}$  energy which is likely to be similar

to that of 0.10 eV for the [ $C\ 1s(e_{2g}), \pi^*(e_{2u})$ ]  $^1A_{2u}$  state. Thus we report the  $\Delta(1-3)$  value for benzene to be  $0.41 \pm \frac{1}{2}$  (i.e., between 0.38 and 0.51 eV).

The excitation to the [ $C\ 1s^{-1}(b_{1u}), \pi^*(b_{2g})$ ]  $^1B_{3u}$  state in ethylene has a strong vibrational progression in  $\nu_{C-H}$  (appearing as a high-energy shoulder in our spectrum) with the adiabatic  $v = 0$  band at 284.7 eV [3, 4, 19]. The partially resolved signal corresponding to excitation to the [ $C\ 1s^{-1}(b_{1u}), \pi^*(b_{2g})$ ]  $^1B_{3u}$  state is centred at 284.3 eV. It is not as well resolved as that in benzene, in part due to a slightly lower experimental resolution and in part because the leading edge of the singlet transition in  $C_2H_4$  is inherently broader than that in  $C_6H_6$ , perhaps because of extensive excitation of low-frequency torsion modes and (or) hot bands, which are unresolved even in the higher resolution dipole spectra [3, 4, 24]. As in benzene, the singlet signal is fit by several Gaussians whose initial positions are set according to literature [4] while the triplet signal was fit using only a single Gaussian line. The resulting  $\Delta(1-3)$  value is 0.43 eV, which could be an underestimate of the adiabatic-adiabatic separation by as much as 0.12 eV, the adiabatic-vertical separation for the singlet  $\pi^*$  transition.

The excitation to the [ $C\ 1s^{-1}(\sigma_g), \pi^*(\pi_g)$ ]  $^1\Pi_g$  state in acetylene

also possesses vibrational structure with the  $\nu = 0$  band at 285.8 eV [24]. Due to the lower instrumental resolution (0.55 eV FWHM, necessitated due to charging and surface contamination problems) the triplet state in acetylene is not resolved. However, the high impact energy ISEEL spectrum measured at the same energy resolution clearly exhibits a sharper rise on the low-energy side than the low impact energy spectrum (Fig. 2). A similar observation has been reported by Harrison and King [14]. The region between 284.7 and 287 eV in the low impact energy spectrum of acetylene requires three Gaussian lines for an adequate fit. The two higher energy lines have positions and intensities consistent with the vibrational components of the  ${}^1\Pi_u$  state previously identified in optical [3, 4] and dipole regime ISEEL [24] spectra. The third, lowest energy Gaussian line, indicated by the broken line in Fig. 2, is attributed to excitation to the  $(C\ 1s^{-1}(\sigma_u), \pi^*(\pi_g))\ {}^3\Pi_u$  state. The curve fit yields a  $\Delta(1-3)$  value of 0.50 (3) eV. This is in excellent agreement with the value of "approximately 0.5 eV" estimated by Harrison and King [14].

In addition to the experimental results, Table 1 also includes the  $\Delta(1-3)$  values for each molecule predicted by INDO/S calculation. For CO the calculated value (0.98 eV) is one third below the experimental value. The calculated values for the  $C_2H_4$  and  $C_2H_2$  agree with experiment within 10% while that for  $C_6H_6$  is low by 25%. The INDO/S results reproduce the large difference in  $\Delta(1-3)$  between CO and hydrocarbons but it exaggerates the variation among the three hydrocarbon species. Without further theoretical study it is not possible to determine if this mainly reflects limitations of the one-centre model, the minimal STO basis or the INDO method. Given the primitive nature of the semiempirical INDO/S scheme, the agreement with experiment is considered reasonable.

The theoretical and experimental relationship between  $\Delta(1-3)$  and  $f_{opt}(1s^{-1}, \pi^*)$ , the optical oscillator strength for the  $(1s^{-1}, \pi^*)\ {}^1\Pi$  state, is explored in Table 2 and Fig. 3. To account for intrinsic differences in the intensities of these  $C\ 1s \rightarrow \pi^*$  transitions, the experimentally derived  $f_{opt}(1s^{-1}, \pi^*)$  has been divided by a "degeneracy factor," corresponding to the product of the number of  $1s$  electrons and  $\pi^*$  orbitals associated with dipole-allowed contributions to the observed signal. These degeneracy factors are 8, 4, 8, and 16 for CO,  $C_2H_4$ ,  $C_2H_2$ , and  $C_6H_6$ , respectively. The  $C\ 1s$  absolute oscillator strength data given in Table 2 were derived from energy loss spectra recorded in the dipole regime [1, 25]. The experimental  $\Delta(1-3)$  value quoted for the  $O\ 1s \rightarrow \pi^*$  state in CO is that estimated by Ungier and Thomas [11] based on a slight broadening on the low-energy side of the  $\pi^*$  peak in their near-threshold spectrum that they attribute to transitions to the  $(O\ 1s^{-1}, \pi^*)\ {}^3\Pi$  state. The calculated (relative) oscillator strengths (i.e.,  $c_{2p}^2$ , see (2)) and the calculated and experimental  $\Delta(1-3)$  values are also summarized in Table 2. The calculated oscillator strength for the  $O\ 1s \rightarrow \pi^*$  transition in CO has been divided by 2.05 ( $|\langle C\ 1s | e r | C\ 2p \rangle|^2 / |\langle O\ 1s | e r | O\ 2p \rangle|^2$  [26]) in order to have a valid comparison between the  $C\ 1s$  and  $O\ 1s$  data.

As shown in Fig. 3, the experimental  $\Delta(1-3)$  increases systematically with increasing oscillator strength. A perfect linear correlation is observed between the INDO/S values of  $\Delta(1-3)$  and  $f_{opt}(1s^{-1}, \pi^*)$ . This is easily rationalized in terms of the one-centre approximation described in Sect. 3. Within this approximation, both quantities are proportional to the  $2p$  population of the  $\pi^*$  orbital on the core-hole atom. Hence, for a given atomic type (e.g., carbon), the model predicts a linear relationship between  $\Delta(1-3)$  and  $f = (f_{opt} 1s^{-1}, \pi^*)$ :

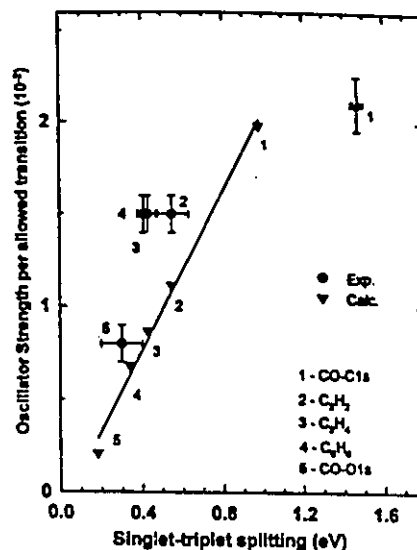


Fig. 3. Plot of the experimental and calculated singlet-triplet splitting ( $(E(1s, \pi^*)\ {}^1\Pi - E(1s, \pi^*)\ {}^3\Pi) = \Delta(1-3)$ ) versus experimental absolute and INDO/S calculated relative oscillator strengths ( $\times 10^{-2}$ ) for electric dipole excitation to the  ${}^1\Pi$  state. See Table 2 for numerical values and details on sources of the oscillator strength data.

$$\begin{aligned} \Delta(1-3) &= E({}^1\Pi) - E({}^3\Pi) \\ &= (\text{const}) \cdot f \cdot K(1s, 2p) / |\langle 1s | e r | 2p \rangle|^2 \\ &= (\text{const}') \cdot f \end{aligned} \quad (3)$$

The simple one-centre treatment qualitatively explains the experimental trends. However, quantitative agreement is not found. Although the quality of the experimental correlation is low due to the limited accuracy of the oscillator strengths, it does not appear to be a simple linear relationship as predicted by the one-centre treatment. In principle, deviations from the predicted linear relationship of  $\Delta(1-3)$  and  $f_{opt}(1s^{-1}, \pi^*)$  could give insight into how the one-centre approximation fails in specific cases. In practice, a larger range of more accurate  $\Delta(1-3)$  and  $f_{opt}(1s^{-1}, \pi^*)$  values is required before this can be explored in any detail.

It is noted that the oscillator strengths (per allowed transition) and singlet-triplet splittings for the three unsaturated hydrocarbons are very similar. As supported by the correlation of these quantities, this can be rationalized by similarities among all three molecules in the spatial extent of the  $C\ 1s$  orbital and the  $2p$  density of the  $\pi^*$  orbital in the region of the  $C\ 1s$  orbital at the core excited carbon atom. The similarity of the  $C\ 1s$  orbitals is consistent with the absence of any chemical shift with extent of unsaturation in hydrocarbons [27]. The situation for singlet-triplet splittings of states arising from valence shell  $\pi \rightarrow \pi^*$  excitations is very different than that for  $C\ 1s \rightarrow \pi^*$  excitation. In particular, the adiabatic singlet-triplet energy splittings [28] are 0.9, 2.4, and  $\geq 1.4$  eV for the lowest energy states associated with  $\pi \rightarrow \pi^*$  transitions in  $C_2H_2$  [8],  $C_6H_6$  [31-33], and  $C_2H_4$  [34, 35], respectively. In fact the singlet-triplet splitting for the lowest energy ( $\pi^{-1}, \pi^*$ ) excited state of  $C_6H_6$  is larger than that for CO [6] (2.4 eV versus 2.1 eV) whereas  $\Delta(1-3)$  for the  $(C\ 1s^{-1}, \pi^*)$  state of CO is more than three

times as large as that for  $C_2H_2$ . The large difference in the chemical systematics for singlet-triplet separations for ( $C\ 1s^{-1}, \pi^*$ ) and ( $\pi^{-1}, \pi^*$ ) states probably is associated with the delocalized nature of the valence-excited states which makes them much more sensitive to differences in the chemical bonding.

### 5. Summary

The inner-shell excitation spectra of carbon monoxide, benzene, ethylene, and acetylene have been recorded in the region of the  $C\ 1s \rightarrow \pi^*$  transitions using low impact energy ISEELS. This study has provided the first accurate measurements of the singlet-triplet splittings for the ( $C\ 1s^{-1}, \pi^*$ ) states in the hydrocarbon species. A strong correlation of singlet-triplet splitting and optical oscillator strengths for singlet excitation has been documented and rationalized in terms of a common dependence on spatial overlap of the  $1s$  and  $\pi^*$  wave functions. The results have been interpreted with the aid of INDO/S calculations.

### Acknowledgements

Financial support for this research has been provided by the Natural Sciences and Engineering Research Council of Canada (NSERC). J.T.F. gratefully acknowledges the support of an NSERC postgraduate scholarship. Dr. T. Tylliszczak is thanked for assistance in spectrometer construction and support of data acquisition and analysis software.

1. A.P. Hitchcock. *Phys. Scr.* T31, 159 (1990); *Jpn. J. Appl. Phys. Part 2*: 32, 176 (1993).
2. A.P. Hitchcock and D.C. Mancini. *J. Electron Spectrosc.* 67, 1 (1994).
3. Y. Ma, F. Sette, G. Meigs, S. Modesti, and C.T. Chen. *Phys. Rev. Lett.* 63, 2044 (1989).
4. Y. Ma, F. Sette, G. Meigs, S. Modesti, and C.T. Chen. *Phys. Scr.* 41, 833 (1990); Y. Ma, C.T. Chen, G. Meigs, K. Randall, and F. Sette. *Phys. Rev. A: Gen. Phys.* 44, 1848 (1991).
5. E.N. Lassetre and A. Skerbele. *Methods Exp. Phys.* 3B, 868 (1974).
6. E.N. Lassetre and M.A. Dillon. *J. Chem. Phys.* 59, 4778 (1973).
7. A. Chutjian, R.I. Hall, and S. Trajmar. *J. Chem. Phys.* 63, 892 (1975).
8. D.G. Wilden, P.J. Hicks, and J. Cohmer. *J. Phys. B: At. Mol. Phys.* 10, L403 (1977).
9. G.C. King, M. Tronc, F.H. Read, and R.C. Bradford. *J. Phys. B: At. Mol. Phys.* 10, 2479 (1977).
10. D.A. Shaw, G.C. King, F.H. Read, and D. Cvejanovi. *J. Phys. B: At. Mol. Phys.* 15, 1785 (1982).
11. L. Ungier and T.D. Thomas. *Chem. Phys. Lett.* 96, 247 (1983).
12. D. A. Shaw, G.C. King, D. Cvejanovi, and F.H. Read. *J. Phys. B: At. Mol. Phys.* 17, 2091 (1984).
13. I. Harrison and G.C. King. *J. Phys. B: At. Mol. Phys.* 19, L447 (1986).
14. I. Harrison. Ph.D. Thesis, University of Manchester, 1986; I. Harrison and G.C. King. *J. Electron Spectrosc.* 43, 155 (1987).
15. W.H.E. Schwarz and R.J. Buenker. *Chem. Phys.* 13, 153 (1976).
16. A. Barth and J. Schirmer. *J. Phys. B: At. Mol. Phys.* 18, 867 (1985).
17. W. Wurth, J. Stöhr, P. Feulner, X. Pan, K.R. Bauschspiess, E. Hudel, G. Roeker, and D. Menzel. *Phys. Rev. Lett.* 65, 2426 (1990).
18. M.W. Ruckman, J. Chen, S.L. Qui, P. Kuiper, M. Strongin, and B.I. Dunlap. *Phys. Rev. Lett.* 67, 2533 (1991).
19. A. Yagashita, E. Shigemasa, and N. Kosugi. *Phys. Rev. Lett.* 72(25), 3961 (1994).
20. W. Eberhardt, C.T. Chen, W.K. Ford, E.W. Plummer, and H.R. Moser. *In DIET II. Edited by W. Brenig and D. Menzel.* Springer, Berlin, 1985.
21. W. Wurth, C. Schneider, R. Treichler, D. Menzel, and E. Umbach. *Phys. Rev. B: Condens. Matter*, 37, 8725 (1988).
22. D.B. Cook. Structures and approximations for electrons in molecules. Ellis Horwood Ltd., Chichester, England, 1978.
23. A.P. Hitchcock and C.E. Brion. *J. Electron Spectrosc.* 10, 317 (1977).
24. M. Tronc, G.C. King, and F.H. Read. *J. Phys. B: At. Mol. Phys.* 12, 137 (1979).
25. R. McLaren, S.A.C. Clark, I. Ishii, and A.P. Hitchcock. *Phys. Rev. A: Gen. Phys.* 36, 1683 (1987).
26. S.P. McGlynn, L.G. Vanquickenborne, M. Kinshita, and D.G. Carroll. Introduction to applied quantum chemistry. Holt, Rinehart and Winston, New York, 1972. p. 237.
27. W.L. Jolly, D. Bomben, and C.J. Eyermann. *At. Data Nucl. Data Tables*, 31, 433 (1984).
28. G. Herzberg. Electronic structure of polyatomic molecules. Van Nostrand Reinhold Co., New York, 1966.
29. P.S. Bagus and M. Seel. *Phys. Rev. B: Condens. Matter*, 23, 2065 (1981).
30. A. Barth, S.D. Peyerimhoff, and W. Butscher. *Chem. Phys.* 46, 149 (1980).
31. J.P. Doering. *J. Chem. Phys.* 51(7), 2866 (1969).
32. R. Azria and G.J. Shulz. *J. Chem. Phys.* 62(2), 573 (1974).
33. J.P. Doering. *J. Chem. Phys.* 67(9), 4065 (1977).
34. E.H. Van Veen. *Chem. Phys. Lett.* 41(3), 540 (1976).
35. G.J. Verhaart and H.H. Brongersma. *Chem. Phys.* 52, 431 (1980).

## Chapter 4(b)

Experimental and Theoretical Studies of the ( $C\ 1s^{-1}, \pi^*$ )  $^3\Pi$ 

## State of CO: Momentum Transfer Dependence and

## Vibrational Structure

The following work which documents the momentum transfer dependence and vibrational structure of a core excited triplet state of carbon monoxide has been published in the Journal of Chemical Physics (J. Chem. Phys. 101(12) (1994) 10429) and is presented here as the journal article. It has been reprinted with the permission of the American Institute of Physics (see page 203).

The experimental work has been performed by the author of this thesis, in addition to the bulk of the paper preparation in collaboration with Prof. A. P. Hitchcock. The calculations were performed and reported by N. Kosugi of the Institute for Molecular Science, Myodaiji, Okazaki, Japan.

**As a co-author of the following journal article:**

J. Chem. Phys. 101(12), 1994, 10429.

I hereby authorize James Francis to reprint this work as part of his Ph.D. thesis.

Date:

March 16, 1995

Signature:

Alex P. Hitchcock

Date:

March 15, 1995

Signature:

Nobuhiro Kosugi

Nobuhiro Kosugi



# Experimental and theoretical studies of the $(C\ 1s^{-1}, \pi^*)^3\Pi$ state of CO: Momentum transfer dependence and vibrational structure

J. T. Francis

Department of Chemistry, McMaster University, Hamilton, Ontario L8S 4M1, Canada

N. Kosugi

Institute for Molecular Science, Myodaiji, Okazaki 444, Japan

A. P. Hitchcock

Department of Chemistry, McMaster University, Hamilton, Ontario L8S 4M1, Canada

(Received 26 July 1994; accepted 29 August 1994)

The intensity of the  $X\ ^1\Sigma^+ \rightarrow (C\ 1s^{-1}, \pi^*)^3\Pi$  transition of CO has been measured by electron energy loss spectroscopy using a range of scattering angles ( $0^\circ$ – $45^\circ$ ) and impact energies (376 to 1806 eV) in order to investigate the momentum transfer dependence of a spin forbidden inner-shell excitation. A Franck–Condon factor analysis of the vibrational structure of the singlet and triplet  $(C\ 1s^{-1}, \pi^*)$  states was used to quantify differences in the potential energy curves of these states. *Ab initio* self-consistent field configuration interaction (SCF-CI) calculations were carried out to generate the potential curves of the  $^1\Pi$  and  $^3\Pi(C\ 1s^{-1}, \pi^*)$  states. The electronic and vibrational energies and Franck–Condon factors are in good agreement with the experimental results. The calculations indicate that the difference in the  $^1\Pi$  and  $^3\Pi$  potential curves are related to differences in relaxation of both the (active)  $\pi^*$  and other (passive) valence electrons. © 1994 American Institute of Physics.

## I. INTRODUCTION

The vast majority of all work in the field of inner shell excitation via electron impact techniques has been conducted under conditions of small momentum transfer, which effectively simulates photoabsorption. (A bibliography of atomic and inner shell excitation studies has been published recently.<sup>1</sup>) Such conditions are achieved experimentally by employing small scattering angles ( $\theta < 2^\circ$ ) and “fast” electrons, typically using impact energies of more than five times the excitation energy of the core level transition. As the momentum transfer becomes significant (large  $\theta$  and/or small impact energy), the probability of nondipole transitions increases. The ability to excite electric dipole forbidden processes represents a distinct advantage of electron impact techniques, specifically electron energy loss spectroscopy (EELS), over photoabsorption.

Dipole forbidden spin exchange excitations to inner shell excited states are difficult to study on account of their intrinsically small cross sections. The first reported observation was that of Shaw *et al.* in 1982 who detected the vibrationally resolved  $X\ ^1\Sigma_g^+ \rightarrow (1\sigma_g^{-1}, \pi_u^1)^3\Pi_u$  transition in  $N_2$ .<sup>2</sup> Such spin forbidden transitions are induced by lowering the impact energy close to the energy of excitation. Under these slow collision conditions the probability of exchange of incident and target electrons becomes appreciable. The  $(C\ 1s^{-1}, \pi^*)^3\Pi$  state of CO has been studied previously by Ungier and Thomas,<sup>3</sup> Shaw *et al.*,<sup>4</sup> and Harrison and King.<sup>5</sup> Recently we have investigated the  $(C\ 1s^{-1}, \pi^*)$  triplet state spectroscopy of CO, benzene, ethylene and acetylene.<sup>6</sup>

To date there has been no systematic study of the angular dependence of inelastic cross sections for a spin-forbidden inner-shell excitation. Harrison and King investigated the impact energy dependence of the singlet–triplet intensity ratio of CO but mainly using a fixed  $90^\circ$  scattering angle and

impact energies less than 40 eV above threshold.<sup>5,7</sup> In order to explore more fully the spin exchange scattering mechanism we have measured the energy loss spectrum of CO in the region of the  $(C\ 1s^{-1}, \pi^*)^3\Pi$  and  $^1\Pi$  states using a wide range of angles ( $2^\circ$ – $45^\circ$ ) and impact energies (376–1806 eV). These results have been analyzed to examine the momentum transfer dependence of the triplet/singlet intensity ratios.

In addition, the vibrational band structure of both the  $^1\Pi$  and  $^3\Pi(C\ 1s^{-1}, \pi^*)$  states has been measured and analyzed. High quality *ab initio* calculations have been carried out to determine the potential curves and thus Franck–Condon overlap factors for the  $(C\ 1s^{-1}, \pi^*)^3\Pi$  and  $^1\Pi$  states. The theoretical calculations are in good agreement with the present experimental results, with high resolution photoabsorption studies of the  $C\ 1s \rightarrow ^1\Pi$  transition,<sup>8–12</sup> and with an earlier EELS experimental study of the  $C\ 1s \rightarrow ^3\Pi$  transition<sup>4</sup> in CO. Small differences in the potential curves of the  $^1\Pi$  and  $^3\Pi(C\ 1s^{-1}, \pi^*)$  states are explained in terms of differences in the relaxation of both the active  $\pi^*$  and passive valence electrons in the core excited states.

## II. EXPERIMENT

The inner shell electron energy loss spectra (ISEELS) were recorded using a newly developed, variable impact energy, variable angle, high-resolution electron spectrometer which will be described in detail in a future publication. Briefly, a monochromated electron beam impinges on the gas target. Electrons inelastically scattered at a mechanically determined scattering angle ( $-10^\circ$  to  $110^\circ$ ) are dispersed using a lens system and a hemispherical electron energy analyzer. The signal is detected using a channel electron multiplier and standard pulse counting electronics. In this study, spectra were recorded using a jet formed by expansion through a

capillary array (100:1 aspect ratio of the channels). The jet was found to eliminate background contributions from secondary electron scattering which had been a problem when a gas cell was used.

Constant residual energy (90 to 1520 eV above threshold) scanning was used which is advantageous since it eliminates chromatic aberrations at the analyzer exit lens as the spectrum is scanned. A resolution of 0.18 eV was used to study the vibrational band structure. The resolution was degraded to 0.40 eV to study the angle and impact energy dependence of the  $^3\Pi$  and  $^1\Pi$  intensity in order to improve signal statistics. Count rates were as little as 2 cps at higher scattering angles ( $45^\circ$ ) which necessitated long acquisition times (24–48 h).

### III. CALCULATIONS

The calculations were carried out using the GSCF3 code<sup>13,14</sup> on a MIPS RS3330 UNIX workstation. The core-ionized and core-excited self-consistent field Hartree-Fock (SCF-HF) solutions were obtained with explicit consideration of the core hole. Potential energy curves for the  $^1\Sigma^+$  ground state, the  $^2\Sigma^+(C\ 1s^{-1}, \pi^*)$  ionized state, and the  $^1\Pi$  and  $^3\Pi(C\ 1s, \pi^*)$  core excited states were obtained with the configuration interaction (CI) method using the SCF orbitals as in Ref. 15. The vibrational states and the Franck-Condon factors were obtained from numerical solutions of the nuclear Schrödinger equation.<sup>16</sup> Cooley's method<sup>17</sup> was used in the numerical integration.

The CI calculations allow double substitution to the virtual-orbital space from the valence-orbital space ( $C\ 2s$ ,  $C\ 2p$ ,  $O\ 2s$ , and  $O\ 2p$ ). The valence space is described with single substitution within the  $\pi$ -electron subspace and the core space is frozen. The virtual and vacant valence orbitals were obtained with the hole ( $V^{N-1}$ ) potential method.<sup>18</sup> Primitive basis functions were taken from (73/6) contracted Gaussian-type functions of Huzinaga *et al.*<sup>19</sup> They were augmented with single polarization functions ( $\zeta_d=0.600$  for C, 1.154 for O). The contraction schemes were (51121/411/1\*) and (721/51/1\*) for carbon and oxygen atoms, respectively.

### IV. RESULTS AND DISCUSSION

#### A. Momentum transfer dependence of the triplet-singlet intensity ratio

Figure 1 presents  $C\ 1s$  spectra of CO in the region of excitation to the  $(C\ 1s^{-1}, \pi^*)^3\Pi$  and  $(C\ 1s^{-1}, \pi^*)^1\Pi$  states, recorded at small scattering angles ( $<4^\circ$ ) and residual electron energies of 90, 105, and 1520 eV, corresponding to impact energies at the  $^3\Pi$  excitation of 376, 391, and 1806 eV. The solid lines passing through the experimental data points in Fig. 1 are the results of curve fits using Voigt lineshapes for each of the vibrational components. The Lorentzian width was set to 60 meV (the natural linewidth<sup>11,12</sup>) while the Gaussian width was optimized, yielding a value of 180 meV which was the same as the experimental resolution determined from the fwhm of the  $^1S_0 \rightarrow ^1P_1$  transition in He at 21.22 eV. Figure 1 also plots the ratio of the triplet to the singlet intensity, determined from spectra recorded at angles

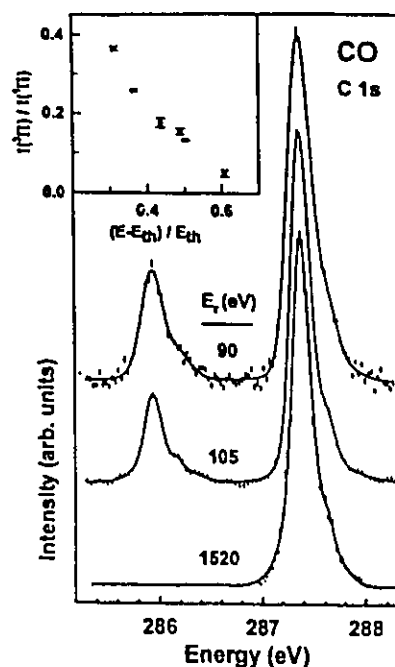


FIG. 1. Electron energy loss spectra of CO in the region of the  $(C\ 1s^{-1}, \pi^*)^3\Pi$  and  $^1\Pi$  states recorded at residual energies of 90, 105, and 1520 eV and scattering angles of  $4^\circ$ ,  $4^\circ$ , and  $2^\circ$ , respectively. The resolution was 0.18 eV (FWHM). The inset plots the ratio of the triplet/singlet intensities as a function of fractional energy above threshold  $[(E - E_{th})/E_{th}]$ .

below  $5^\circ$ , as a function of fractional energy above threshold,  $(E - E_{th})/E_{th}$ , where  $E$  is the impact energy and  $E_{th}$  is the threshold energy. Figure 1 illustrates the "turning on" of the exchange between the incident and the target electron and thus excitation of the  $^3\Pi$  state as the impact energy approaches threshold.

Figure 2 plots  $C\ 1s$  spectra of CO recorded with 140 eV residual energy at scattering angles of  $4^\circ$ ,  $26^\circ$ , and  $45^\circ$ . The insert to Fig. 2 presents a larger sampling of the variation of the triplet-singlet intensity ratio as a function of scattering angle. The peak areas used to evaluate the intensity ratios plotted in Figs. 1 and 2 were obtained from the curve fit procedure described above. The error bars were estimated from the counting statistics.

While the relative probability of triplet state excitation increases relatively rapidly above  $10^\circ$ , there is very little variation in the triplet/singlet intensity ratio at small angles ( $2^\circ$  to  $10^\circ$ ), at the impact energy used (426 eV). This behavior contrasts that found for many valence excited states, where large variations in the inelastic cross sections often occur in the  $2^\circ$ – $10^\circ$  range of scattering angles. The angle independence of the core excitation spectrum in the small angle regime is associated with the fact that  $K^2$  is almost independent of angle whenever  $\theta < \theta_E$  (where  $\theta_E = \Delta E/2E$ , in radians).  $\theta_E$  is  $20^\circ$  for  $E=400$  eV and  $\Delta E=286$  eV. Thus it is not surprising that  $K^2$  increases by only a small amount for angles between  $2^\circ$ – $10^\circ$  (6.4 to 6.9 a.u.<sup>-2</sup>) but by a much

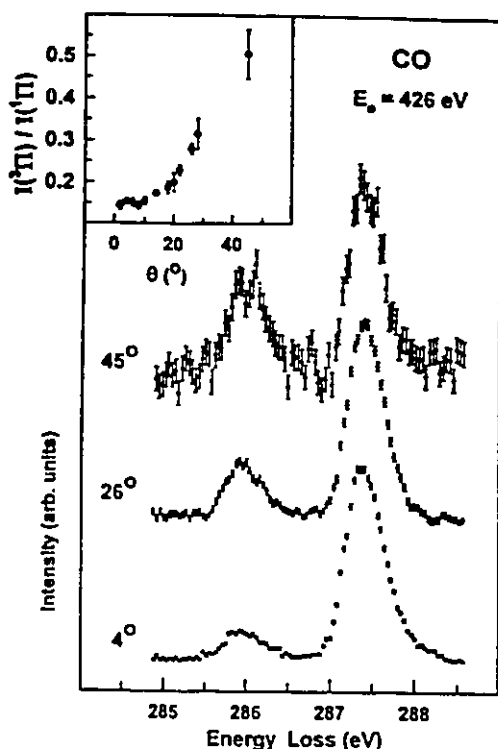


FIG. 2. Electron energy loss spectra of CO recorded using 140 eV residual energy and the indicated scattering angles. The insert plots the ratio of the ( $C\ 1s^{-1}, \pi^*$ ) triplet/singlet intensities over  $2^\circ$ – $45^\circ$  scattering angle.

larger amount for a similar variation in angle at a larger average angle—for example,  $K^2$  varies from 7.3 to 10.6  $\text{a.u.}^{-2}$  between  $20^\circ$ – $30^\circ$  at 400 eV impact energy.

Figure 3 combines the angle and impact energy dependence of the singlet–triplet intensity ratio by plotting this ratio as a function of momentum transfer. In addition to our data, results from Harrison and King<sup>5</sup> and Ungier and Thomas<sup>3</sup> are also plotted. Note that the four sets of results do not form a single smooth curve. Of particular note is the systematic deviation in the  $K^2$  variation of the triplet–singlet intensity ratio when  $K^2$  is changed by varying the impact energy rather than varying the scattering angle.

At impact energies near threshold the interaction between the incident electron and the target is large. Under these conditions the weak interaction assumption that is the basis of the first Born approximation<sup>20,21</sup> is likely to fail. A standard experimental test for the validity of the Born approximation is to measure the dependence on impact energy of the spectral intensities or intensity ratios at a fixed  $K^2$ . A necessary condition for applicability of the Born approximation is that the result is independent of impact energy. The data shown in Fig. 3 indicates that the transition intensity at a given  $K^2$  does depend on the impact energy in the near threshold regime. Thus we conclude that the generalized oscillator strength concept<sup>20,21</sup> is inapplicable under near-threshold electron scattering conditions.

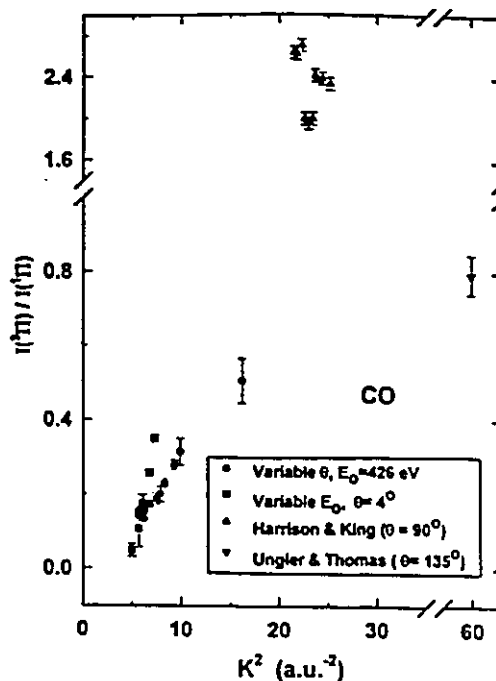


FIG. 3. Momentum transfer dependence of the ( $C\ 1s^{-1}, \pi^*$ ) triplet/singlet intensity ratio derived from both variable impact energy and variable angle measurements. Literature data from Ungier and Thomas (Ref. 3) and Harrison and King (Ref. 5) are also included.

The intensity of the  $^3\Pi$  signal, and thus the exchange probability, increases rather dramatically as the impact energy approaches the excitation threshold (see Fig. 1). Harrison and King have determined triplet–singlet intensity ratios of greater than 2 for impact energies less than 40 eV above threshold.<sup>7</sup> The measurements of Ungier and Thomas were carried out at an even larger  $K^2$  (60  $\text{a.u.}^{-2}$ ) but, even at this very large momentum transfer, the triplet–singlet intensity ratio is only 0.80. Clearly, it is extremely low impact energies and not large scattering angles which are most important in spin forbidden excitations.

A naive view of the origin of the triplet spin-exchange signal is that at low energies the incident or outgoing electron can physically exchange with one of the target electrons. If this exchange is a completely random event with equal probability for exchanging electrons of the same or opposite spin, then the largest possible triplet–singlet intensity ratio would be 1.0. The observation of low impact energy spectra with a  $^3\Pi/^1\Pi$  intensity ratio much greater than 1 (Ref. 7) clearly rules out this picture. The exchange process involved in the triplet excitation cannot be described by a simple 1:1 statistical exchange. Rather there must be selectivity in the interaction which favors exchange of unlike electrons when low energy electrons are involved. Alternatively, if one adopts a more state-oriented viewpoint, the limiting  $^3\Pi/^1\Pi$  intensity ratio might be expected to be 3, reflecting the inherent state degeneracies. The Harrison and King results do not rule out this situation.

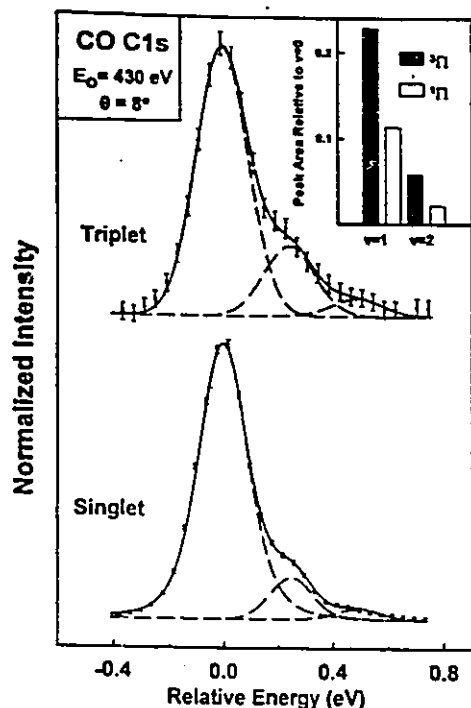


FIG. 4. Curve fit analysis of the vibrational band structure of the  $X^1\Sigma^+-(C\ 1s^{-1},\pi^*)\ ^3\Pi$  and  $X^1\Sigma^+-(C\ 1s^{-1},\pi^*)\ ^1\Pi$  transitions recorded at 140 eV residual energy,  $8^\circ$  scattering angle and 0.18 eV FWHM resolution. Details of the curve fit procedure are given in the text.

#### B. Vibrational structure of the $(C\ 1s^{-1},\pi^*)$ singlet and triplet states

Figure 4 presents a detailed lineshape analysis of the vibrational structure of the singlet and triplet features recorded at 0.18 eV FWHM energy resolution. The insert plots the intensities of the  $v=1$  and  $v=2$  components ratioed to that of the  $v=0$  component. The peak intensities and positions derived from curve fitting are summarized in Table I in comparison to the results of the *ab initio* calculations.

Figure 5 presents the calculated anharmonic potential curve, in comparison to that derived from the experimental energies and Franck-Condon factors in a harmonic approximation. (Note that each of the theoretical curves have been shifted 0.5 eV to lower energy). The bond length of the core excited states are assumed to be longer than that in the ground state since the character of these transitions is essentially nonbonding to antibonding. Relative to the ground state, the shift in the equilibrium bond length derived from the Franck-Condon factors is 0.036 Å for the  $^3\Pi$  state and 0.024 Å for the  $^1\Pi$  state.

The separation of the adiabatic ( $v=0$ ) transitions is 1.47(3) eV, in good agreement with the values reported by others.<sup>3-6</sup> Analysis of the areas of the vibrational features reveals a difference in the Franck-Condon factors between the triplet and singlet states. This difference was also found in the high resolution study of Shaw *et al.*<sup>2</sup> The Franck-Condon factors and vibrational spacings for the  $^3\Pi$  and  $^1\Pi$

states are summarized in Table I, in comparison with the theoretical results. These results probe the differences in the potential energy surfaces of the triplet and singlet ( $C\ 1s^{-1},\pi^*$ ) excited states. The calculated equilibrium bond length of 1.1539 Å for the  $^1\Pi$  state is similar to the value of 1.1527 Å estimated from our experimental Franck-Condon factor and the value of 1.153 Å reported by Domke *et al.*<sup>8</sup> Shaw *et al.* analyzed their results<sup>4</sup> to indicate a reduction of 0.024 Å in the equilibrium bond length of the  $^1\Pi$  state relative to that of the  $X^1\Sigma^+$  ground state. We believe this is not consistent with the antibonding character of the  $\pi^*$  orbital.

The triplet state is predicted by the calculation to be slightly elongated at 1.1595 Å, somewhat less than the experimental estimate of 1.1639 Å. The calculated vibrational spacings are 268 meV (2162  $\text{cm}^{-1}$ ) and 245 meV (1980  $\text{cm}^{-1}$ ) for the singlet and triplet states, respectively, in reasonable agreement with experiment (250 and 242 meV). Experimentally, there are not enough resolved vibrational bands to make a reliable estimate of the anharmonicity of the potential curve of either state. Thus, the experimental observations have been represented in Fig. 5 by harmonic estimations of the true potential curves. The favorable agreement with theory supports our assumption that the bond length in the  $^1\Pi$  and  $^3\Pi$  states is larger than in the ground state as was also concluded by Domke *et al.*<sup>8</sup> for the  $^1\Pi$  state.

The situation for the lowest valence  $A^1\Pi$  and  $a^3\Pi$  states is different than that just described for the core excited states. *Ab initio* SCF-CI calculations of the potential curves for the  $A^1\Pi$  and  $a^3\Pi$  states reported by Cooper and Langhoff<sup>22</sup> predict a slight contraction of the triplet state bond length (by ca. 0.03 Å) relative to the singlet state. The difference in the valence excitation energies ( $T_{0,0}$ ), from both theory and experiment<sup>22-25</sup> is ca. 2.1 eV compared to 1.47(3) eV for the core excited states. The larger triplet-singlet splitting in the valence  $\pi\rightarrow\pi^*$  excitation may be associated with better overlap between the initial and final states in the valence transition matrix element relative to that for the  $1s\rightarrow\pi^*$  core excitation matrix element.

The general trends in the experimental observations are reproduced by the theoretical calculations although there are quantitative differences between experiment and theory. The equilibrium bond length and harmonic vibrational frequency calculated for the ground state are in agreement with the experimental results<sup>25</sup> within the errors in the doubly excited CI calculations using the double  $\zeta$  plus polarization basis set. However they are worse than the result of a sophisticated calculation based on the complete active space (CAS) multiconfigurational SCF and contracted CI methods (1.129 Å, 273 meV).<sup>26</sup> The calculated  $1s\rightarrow\pi^*$  excitation energies are about 0.45 eV larger than the experimental values, but the singlet-triplet separation and the calculated ionization energy are in good agreement with the experimental values. The equilibrium bond length of the  $(C\ 1s^{-1})$  ionized state calculated in the present work (1.0906 Å) is slightly larger than the experimental estimate from  $(C\ 1s^{-1})$  Rydberg photoabsorption [1.073–1.083 Å (Ref. 8)];  $(C\ 1s^{-1})$  photoionization [1.077 Å (Ref. 9)]; and the theoretical result by Correia *et al.* [1.073 Å (Ref. 26)]. Ågren *et al.*<sup>27</sup> calculated the potential energy curve of the  $(C\ 1s^{-1})$  ionized state based on

TABLE I. Experimental and theoretical results for potential curves and vibrational parameters.

$X^1\Sigma^+$ (ground) state	Theory	Experiment	Expt. (Ref. 25)	
Bond length ( $r_e$ , Å)	1.1362	1.1283 <sup>a</sup>	1.1283	
$\omega_e$ (eV)	0.281	0.269 <sup>a</sup>	0.269	
(C $1s^{-1}, \pi^*$ ) $^3\Pi$ state	Theory	Experiment <sup>b</sup>	Expt. (Ref. 4)	
$T_{00}$ (eV)	286.37	285.95 (5)	285.945 (5)	
$\omega_e$ (eV)	0.245	0.242 (6)	0.249(10)	
$R_e$ (Å)	1.1595	1.1639	...	
$\Delta(v_0-v_1)$ (eV)	0.2549	0.242 (6) <sup>c</sup>	0.249(10)	
$\Delta(v_0-v_2)$ (eV)	0.5191	0.474(16)	...	
$\Delta(v_0-v_3)$ (eV)	0.7714	...	...	
Franck-Condon factors:				
$v_0$	0.726	0.778(16)	0.80	
$v_1$	0.218	0.177(16)	0.20	
$v_2$	0.047	0.045 (6)	...	
$v_3$	0.009	...	...	
(C $1s^{-1}, \pi^*$ ) $^1\Pi$ state	Theory	Experiment <sup>b</sup>	Expt. (Ref. 4)	Expt. (Ref. 8)
$T_{00}$ (eV)	287.87	287.40 <sup>d</sup>	287.40 (3)	287.400(2)
$\omega_e$ (eV)	0.268	0.248 (7)	0.258 (4)	0.256(2)
$R_e$ (Å)	1.1539	1.1527	1.104 (2)	1.153
$\Delta(v_0-v_1)$ (eV)	0.2700	0.248 (7)	0.258	0.256(4)
$\Delta(v_0-v_2)$ (eV)	0.5418	0.500(19)	0.510	0.512(4)
$\Delta(v_0-v_3)$ (eV)	0.8068	...	...	0.768
Franck-Condon factors:				
$v_0$	0.850	0.881	0.875	
$v_1$	0.128	0.100 (3)	0.111 (3)	
$v_2$	0.020	0.019 (9)	0.014 (1)	
$v_3$	0.003	...	...	
(C $1s^{-1}$ ) $^2\Sigma^+$ ion state	Theory	Experiment	Expt. (Ref. 9)	
$T_{00}$ (eV)	296.21	296.24 <sup>e</sup>	296.13 (3)	
$\omega_e$ (eV)	0.292	...	0.309(17)	
$R_e$ (Å)	1.0906	...	1.077 (5)	
$\Delta(v_0-v_1)$ (eV)	0.3084	...	0.320 (6)	
$\Delta(v_0-v_2)$ (eV)	0.6335	...	0.670 (6)	
$\Delta(v_0-v_3)$ (eV)	0.9490	...	0.940 (6)	
Franck-Condon factors:				
$v_0$	0.601	...	0.535	
$v_1$	0.316	...	0.337	
$v_2$	0.073	...	0.112	
$v_3$	0.010	...	0.016	

<sup>a</sup>Reference 25.<sup>b</sup>This work.<sup>c</sup>Errors estimated from the results of several fits with different starting parameters.<sup>d</sup>Assumed for calibration.<sup>e</sup>Reference 25.

the equivalent-core and SCF (Hartree-Fock) approximations, but did not report the Franck-Condon factors. Gelius *et al.*<sup>24</sup> calculated the Franck-Condon factors of the ionized state using the empirical potential energy curves of ground state CO and NO<sup>+</sup>, where the closed-shell NO<sup>+</sup> species is core equivalent to the (C  $1s^{-1}$ ) ionized state of CO. However there is poor agreement with results from vibrationally resolved C  $1s$  photoelectron spectra.<sup>9,10</sup> On the other hand, the present Franck-Condon factors for the (C  $1s^{-1}$ ) ionized state based on the CI potential energy are in good agreement with the recent experimental analysis.<sup>9</sup> The calculated vibrational spacing of 308 meV between the  $v'=0$  and  $v'=1$  states is also in good agreement with the photoelectron spectra [309 meV (Ref. 9), 301 meV (Ref. 10)] and the (C  $1s^{-1}$ ,

Rydberg) photoabsorption spectra [292-307 meV (Ref. 8)]. It is marginally better than the result of the CASSCF and subsequent contracted CI calculations (322 meV)<sup>25</sup> and significantly better than the value of 330 meV based on the equivalent-core and SCF approximations.<sup>29</sup>

The difference in the singlet and triplet (C  $1s^{-1}, \pi^*$ ) states arises from the exchange interaction of the unpaired electrons in the C  $1s$  and  $\pi^*$  orbitals. Why should this give rise to a difference in potential curves? The smaller vibrational spacing in the  $^3\Pi$  state implies a less tightly bound potential, consistent with the larger equilibrium bond distance and the larger Franck-Condon factors for the higher vibrational states. In CO, the  $\pi^*$  orbital is relatively strongly localized on the carbon atom. The greater ability of the trip-

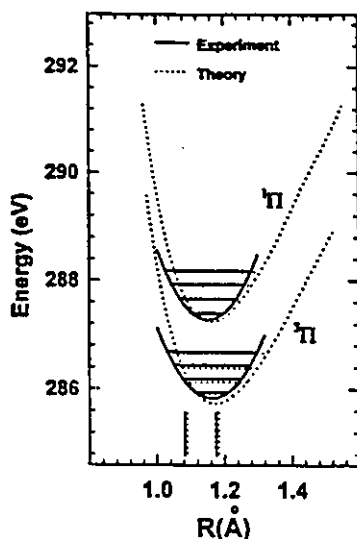


FIG. 5. Calculated anharmonic potential curves for the ( $C 1s^{-1}, \pi^*$ )  ${}^3\Pi$  and  ${}^1\Pi$  states compared to those estimated from the experimental results using an harmonic approximation. Each of the theoretical curves have been shifted 0.50 eV to lower energy. The vertical bars indicate the limits of the Franck-Condon region (the turning points of the  $v=0$  level of the  $X {}^1\Sigma^+$  ground state) according to calculation (this work) and experiment (Ref. 25).

let electron configuration to allow the  $\pi^*$  and  $C 1s$  electron to share the same region of space could lead to relatively greater  $\pi^*$  electron density at the carbon atom.

While it is dangerous to discuss bond length differences of 0.01 Å solely within a one-electron picture, in this case the Mulliken population and orbital contour analyses carried out in the one-electron (SCF) approximation which are summarized in Table II do give results consistent with the above. In particular they emphasize the importance of orbital relaxation in establishing the properties of the core excited states. While a more sophisticated CI analysis would likely make quantitative changes, the qualitative picture from the one-

TABLE II. Mulliken population analysis of charge and charge transfer calculated using the SCF orbitals for  $R=1.160$  Å. The orbital relaxation is analyzed in the passive (closed-shell) and active ( $\pi^*$ ) parts.

State/charge transfer	Mulliken population	
	C	O
Ground state	5.727	8.273
$\pi^*$ orbital	0.809	0.191
Triplet state	5.894	8.106
$\pi^*$ electron (active)	0.777	0.223
relaxation (passive)	+0.390	-0.390
total change	(+1.167-1.0)	-0.167
Singlet state	5.978	8.022
$\pi^*$ electron (active)	0.604	0.396
relaxation (passive)	+0.648	-0.648
total change	(+1.251-1.0)	-0.251
Ionized state	5.327	7.673
relaxation (passive)	(+0.600-1.0)	-0.600
(total change)		

electron analysis appears reasonable. In the triplet state the "active charge transfer" (i.e., charge transfer to the core excited carbon atom involving the  $\pi^*$  electron) is twice as large as the "passive charge transfer" (i.e., rearrangement of the closed shell  $\pi$  and  $\sigma$  electrons) (see Table II). On the other hand, the active charge transfer by the  $\pi^*$  electron is smaller in the singlet state than in the triplet state so that the passive reorganization is relatively more important for the singlet state. Overall the relative effect of relaxation is that the unpaired  $\pi^*$  electron has more probability to be located at the carbon atom in the triplet state than in the singlet state. The ionized state has a shorter bond length because of greater Coulomb attraction between the C and O atoms relative to the ground state. The singlet excited state has nearly the same passive charge transfer as the ionized state. It is only the antibonding nature of the  $\pi^*$  orbital that elongates the bond in the singlet excited state. On the other hand, even though the antibonding nature of the  $\pi^*$  orbital is weaker in the triplet than the singlet excited state, the passive charge transfer is smaller in the triplet state (0.390) than in the ionized and singlet states (0.600, 0.648 respectively) and the Coulomb attraction arising in the passive charge transfer is weaker. This difference in relaxation is critical to establishing the difference between the potential energy curves in the singlet and triplet excited states.

## V. SUMMARY

In this work we have documented for the first time the angular dependence of a spin-forbidden core excitation. In addition, we have greatly extended the variable impact energy results of Harrison and King.<sup>5,7</sup> This study has given additional insight into the scattering mechanism and it has illustrated the breakdown of the Bethe-Born theory for slow collisional processes. High quality *ab initio* SCF-CI theoretical results have been reported and found to be in good agreement with the potential energy curves for the singlet and triplet ( $C 1s^{-1}, \pi^*$ ) states derived from the experimental vibrational structure. The calculations illustrate the importance of orbital relaxation in establishing the details of core excited state potential curves.

## ACKNOWLEDGMENTS

One of us (J.T.F.) acknowledges the Natural Science and Engineering Research Council (NSERC) for a research scholarship. We are deeply grateful to Dr. T. Tylliszczak for his assistance in the design and construction of the spectrometer and the data acquisition and analysis software, and to Dr. Shinkoh Nanbu for his advice and discussion of the molecular vibration and its numerical calculation.

<sup>1</sup>A. P. Hitchcock and D. C. Mancini, *J. Electron Spectrosc.* **67**, 1 (1994).

<sup>2</sup>D. A. Shaw, G. C. King, F. H. Read, and D. Cvejanović, *J. Phys. B* **15**, 1785 (1982).

<sup>3</sup>L. Ungier and T. D. Thomas, *Chem. Phys. Lett.* **96**, 247 (1983).

<sup>4</sup>D. A. Shaw, G. C. King, D. Cvejanović, and F. H. Read, *J. Phys. B* **17**, 2091 (1984).

<sup>5</sup>I. Harrison and G. C. King, *J. Phys. B* **19**, L447 (1986).

<sup>6</sup>J. T. Francis, C. Enkvist, S. Lunell, and A. P. Hitchcock, *Can. J. Phys.* (in press).

- <sup>7</sup>I. Harrison, Ph. D. Thesis, University of Manchester, 1986; I. Harrison and G. C. King, *J. Electron Spectrosc.* **43**, 155 (1987).
- <sup>8</sup>M. Domke, C. Xue, A. Puschmann, T. Mandel, E. Hudson, D. A. Shirley, and G. Kaindl, *Chem. Phys. Lett.* **174**, 668 (1990); **173**, 122 (1990).
- <sup>9</sup>L. J. Medhurst, P. A. Heinmann, M. R. F. Siggel, D. A. Shirley, C. T. Chen, Y. Ma, S. Modesti, and F. Sette, *Chem. Phys. Lett.* **193**, 493 (1992).
- <sup>10</sup>K. J. Randall, A. L. D. Kilcoyne, H. M. Koppa, J. Feldhaus, A. M. Bradshaw, J. E. Rubensson, W. Eberhardt, Z. Xu, P. D. Johnson, and Y. Ma, *Phys. Rev. Lett.* **71**, 1156 (1993).
- <sup>11</sup>Y. Ma, F. Sette, G. Meigs, S. Modesti, and C. T. Chen, *Phys. Rev. Lett.* **63**, 2044 (1989).
- <sup>12</sup>Y. Ma, F. Sette, G. Meigs, S. Modesti, and C. T. Chen, *Phys. Scr.* **41**, 833 (1990); Y. Ma, C. T. Chen, G. Meigs, K. Randall and F. Sette, *Phys. Rev. A* **44**, 1848 (1991).
- <sup>13</sup>N. Kosugi and H. Kuroda, *Chem. Phys. Lett.* **74**, 490 (1980).
- <sup>14</sup>N. Kosugi, *Theor. Chim. Acta* **72**, 149 (1987).
- <sup>15</sup>Y. Yagishita, E. Shigemasa, and N. Kosugi, *Phys. Rev. Lett.* **72**, 3961 (1994).
- <sup>16</sup>S. Iwata and N. Sato, *J. Chem. Phys.* **82**, 2346 (1985).
- <sup>17</sup>J. W. Cooley, *Math. Comput.* **15**, 363 (1961).
- <sup>18</sup>S. Iwata, N. Kosugi, and O. Nomura, *Jpn. J. Appl. Phys.* **17**, Suppl. 2, 109 (1978).
- <sup>19</sup>S. Huzinaga, J. Andzelm, M. Klobukowski, E. Radzio-Andzelm, Y. Sakai, and H. Tachwaki, *Gaussian Basis Sets for Molecular Calculations* (Elsevier, Amsterdam, 1984).
- <sup>20</sup>E. N. Lassette and A. Skerbele, in *Methods of Experimental Physics*, edited by D. Williams, Vol. 3 (Part B), Chap. 7.2, 868 (Academic, New York, 1974).
- <sup>21</sup>M. Inokuti, *Rev. Mod. Phys.* **43**, 297 (1971).
- <sup>22</sup>D. M. Cooper and S. R. Langhoff, *J. Chem. Phys.* **74**, 1200 (1981).
- <sup>23</sup>E. N. Lassette and M. A. Dillon, *J. Chem. Phys.* **59**, 4778 (1973).
- <sup>24</sup>M. A. A. Clyne and M. C. Heaven, *J. Chem. Soc. Faraday Trans. 2* **77**, 1375 (1981).
- <sup>25</sup>G. Herzberg and K. P. Huber, *Constants of Diatomic Molecules* (Van Nostrand Reinhold, New York, 1979).
- <sup>26</sup>N. Correia, A. Flores-Riveros, H. Ågren, K. Helenelund, L. Asplund, and U. Gelius, *J. Chem. Phys.* **83**, 2035 (1985).
- <sup>27</sup>H. Ågren, L. Selander, J. Nordgren, C. Nordling, K. Siegbahn, and J. Müller, *Chem. Phys.* **37**, 161 (1979).
- <sup>28</sup>U. Gelius, S. Svensson, H. Siegbahn, E. Basilier, Å. Faxälv, and K. Siegbahn, *Chem. Phys. Lett.* **28**, 1 (1974).
- <sup>29</sup>T. D. Clark and J. Müller, *Theor. Chim. Acta* **41**, 193 (1976).

## Chapter 5

# EXPERIMENTAL METHODOLOGY FOR THE DETERMINATION OF GENERALISED OSCILLATOR STRENGTHS

### 5.1 Introduction

This section outlines the experimental procedures developed for McVAHRES to allow the determination of generalised oscillator strengths for electronic excitation and ionisation as a function of momentum transfer. A systematic procedure was developed with the primary intention of mapping out the GOS for species previously undocumented in the literature. The relative merits of the procedure were evaluated using He and N<sub>2</sub>, two well-characterised species for which experimental and theoretical GOS have been reported in the literature [SL64, LSD64, LSD70, KI68, CF&87, RO78, BB92, BNH92] for specific energy loss ranges. These two species were also chosen because the adopted GOS determination procedure could be evaluated in both the valence and inner shell energy regimes. The results of these preliminary studies were used as a basis for experiments on the S 2p edge of SF<sub>6</sub> over a large K<sup>2</sup> range. This work on SF<sub>6</sub> considerably extends that already documented in the literature [YML93], and will be discussed in detail in chapter six.

There are many instrumental factors that must be considered before meaningful measurements can be carried out. Some of the major considerations are now briefly



outlined here. The scattering angle and impact energy must be well-defined in order to correctly determine the magnitude of  $K^2$ . Provision must be made to account for signal arising from gas in the vacuum chamber outside of the collision region, which can lead to an overestimation of the GOS, particularly at small scattering angles. Systematic monitoring of the gas pressure, beam current, etc. is necessary with respect to spectral normalisation procedures. Such considerations enable spectra collected as independent data sets under different experimental conditions to be combined. In addition to these instrumental considerations, specialised acquisition and data analysis software are required to collect and process the spectral data into GOS values. Finally, a systematic treatment of the errors associated with the GOS values is required in order to make meaningful comparisons to the work (past or future) of others.

## 5.2 Spectral Acquisition Strategy

This section describes the preliminary considerations involved in actually setting up a typical GOS experiment using the McVAHRES instrument.

### 5.2.1 Consideration of the First Born Approximation

It is always possible to define  $K^2$  using equation (2.2), as it is a well-defined vector parameter representing conservation of momentum. However, in order to use the Bethe-Born relation in determining the GOS as a function of  $K^2$  (equation 2.21), the experimental conditions used must satisfy the first Born approximation. Although it is difficult to predict beforehand whether a set of experimental conditions will satisfy this

criterion, it is in general advantageous to use the largest possible impact energy within the physical limitations imposed by factors such as electrical isolation and maximum power supply output. With this approach, the magnitude of the scattering angles needed to achieve a particular range of  $K^2$  values is reduced with larger  $E_0$ , as is the minimum  $K^2$  value that can be obtained. The decrease in the excitation cross-section accompanying larger  $K^2$  values places a practical limit on the maximum  $K^2$  value that can be achieved in a reasonable acquisition time.

In general, deviations from the first Born approximation are greatest at large scattering angles and near-threshold impact energies. In addition, Lassette has shown that deviations from the first Born approximation are more pronounced for transitions between states of the same symmetry, relative to transitions between states of different symmetry [L70]. It is possible to experimentally verify the applicability of the first Born approximation for a particular set of scattering conditions using a combination of variable  $E_0$  and scattering angles at constant  $K^2$ . Figure 5.1 demonstrates an experimental check of the validity of a particular choice of impact energy for the GOS work on  $SF_6$  at a  $K^2$  value of 8 a.u.<sup>2</sup>. The selected  $E_0$  was 1400 eV, which dictates a scattering angle of 16° for  $K^2 = 8$  a.u.<sup>2</sup> according to the simple cosine relation for  $K^2$  (chapter 2, equation 2.2). If the first Born approximation is satisfied, then using additional impact energies of 1000 eV and 1700 eV and corresponding angles of 18.9° and 14.6°, the S 2p energy loss spectra obtained under these three different sets of conditions should be identical. To evaluate quantitatively the level of similarity between the three spectra, a linear least squares analysis was performed on each of the three possible intensity (y axis)

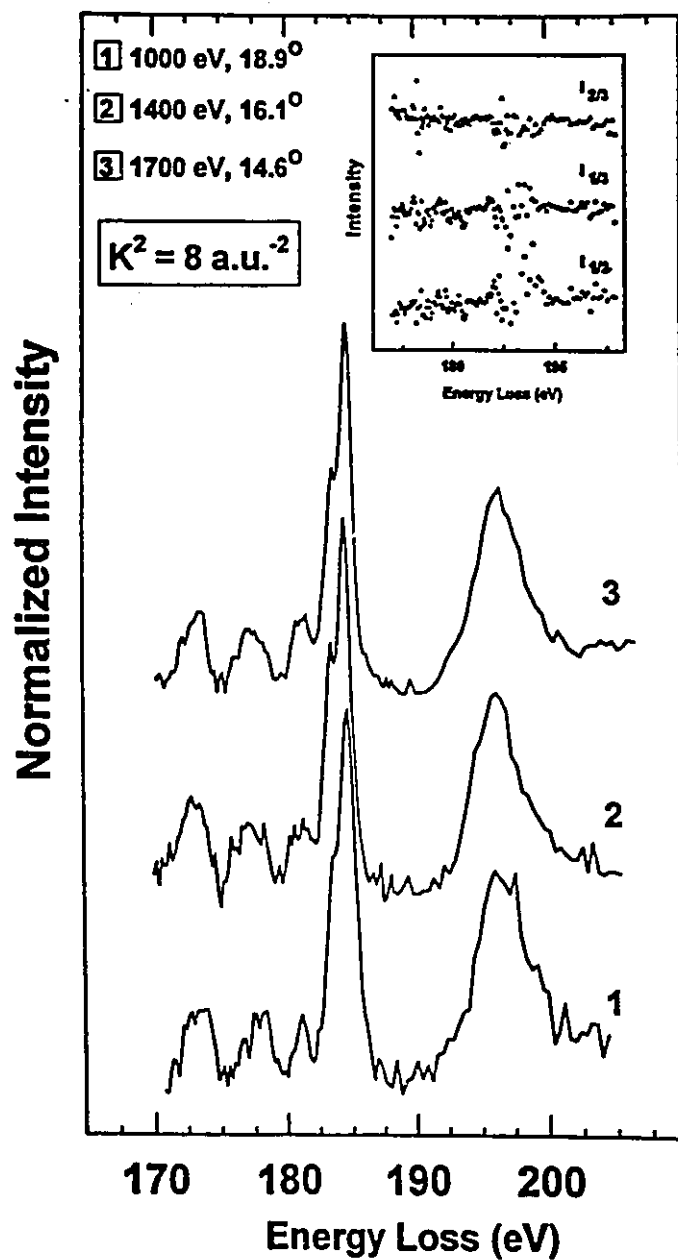


Fig. 5.1 Experimental test of the validity of the Born approximation for a set of scattering conditions using the S 2P edge of  $\text{SF}_6$ . The momentum transfer corresponds to  $8 \text{ a.u.}^{-2}$  in each case. Inset depicts the ratios of the spectral intensities for the three sets of conditions.

combinations, using a common energy scale. Labelling the spectra by their impact energies, it was found that the intensity ratios 1000/1400, 1000/1700 and 1400/1700 had correlation coefficients of 0.91, 0.95 and 0.90, respectively. This is considered reasonable agreement, given that the signal to background ratio is less than 2:1 under these conditions. In addition, there is an overall spread of 700 eV in the impact energies and small variations in the optics behaviour could contribute to the discrepancy as well.

### 5.2.2 Acquisition Procedures

In this section, two different methods of acquiring the spectral data necessary to compute GOS curves are discussed and the relative merits of each method are examined. Both of these methods are accommodated by the scanning algorithm presented in figure 3.18 and discussed in chapter 3.

In both methods, it is possible to either collect energy spectra as a function of the scattering angle  $\theta$  in linear angle increments, or use a constant  $K^2$  spacing instead, where  $K^2$  and  $\theta$  are related by equation 2.2.

#### 5.2.2.1 Acquisition Method 1: Scanning Full Energy Loss Spectra at a Series of Angles

In this approach, entire energy loss spectra, covering an energy range of up to 100 eV, are acquired and signal averaged until a fixed number of spectra have been collected. The number of energy loss spectra actually collected is pre-determined by either fixing numerically the number of scans, or by defining an average counts per point criterion. The average counts per point criterion ensures that comparable statistics will be obtained

at all scattering angles scanned. The angle is then incremented to the next one in the series, and the full set of energy scans repeated. In turn, the entire angle scanning process is cycled, with one pass through the angular series constituting one cycle. The cyclic nature of this method helps average out the effects of decaying beam current, pressure fluctuations, etc. The final result is written as a multicolumn file, with each column containing the signal-averaged, raw inelastic cross section as a function of energy loss for a particular  $K^2$  value.

It is desirable to have data quality with the maximum statistical precision possible (ideally, better than 1% based on a Poisson distribution) in order to obtain optimum results from the subsequent fitting procedures. Thus, depending on the signal-to-background ratio and count rates (which can be less than 10 cps at larger angles) several hundred complete energy spectra may have to be averaged at an individual scattering angle. In addition, this number will increase non-linearly as the scattering angle increases. As a practical example of how the rapid fall-off in cross section with increasing scattering angle affects the acquisition time using this method, larger angle acquisition cycles (16 to 22°) often took a factor of 10 times longer than small angle cycles (4 to 16°) in the case of the S 2p edge of SF<sub>6</sub> (165-212 eV).

In addition to the time spent acquiring energy spectra, there is the time spent changing angles, and removing backlash (5°) whenever the rotation direction is changed. In practice, this can represent up to 10% of the total acquisition time. Overall then, in the case where the number of points in energy is large (150 or more), this method is relatively time consuming and depends on long-term instrument stability. The addition of

the parallel detector in the future should drastically reduce the acquisition time for this method.

#### 5.2.2.2 Acquisition Method 2: Scan Few Fixed Energy Points at Several Angles

In an effort to reduce the long acquisition times associated with method one, an alternative approach was devised to provide the same quantitative information in less time. In this method, a single (or small number of) selected energy point(s), typically corresponding to peak maxima are sampled repeatedly at a given scattering angle, for a range of angles. As in method one, the procedure is cycled over the angular series. In this manner, it is possible to accumulate better than 1% counting statistics for each selected energy point in a fraction of the time necessary for method one. Figure 5.2 compares the sampling of the S 2p spectrum of SF<sub>6</sub> using methods one and two. In method two, in addition to the peak maxima, points on the low and high energy sides of each peak are also sampled and four background points are included to allow background subtraction in subsequent data processing procedures.

In terms of acquisition time, it was found in practice that method two can sample the same K<sup>2</sup> range with comparable statistics in a fraction of the time required by method one. Alternatively, method two can provide several times the number of K<sup>2</sup> points obtainable using method one, with comparable statistics, in the same acquisition period. However, because method one provides full spectra (typically including a sampling of the background), one has better control over subsequent data processing procedures, such as background subtraction and fitting. In addition, method one allows extraction of peak

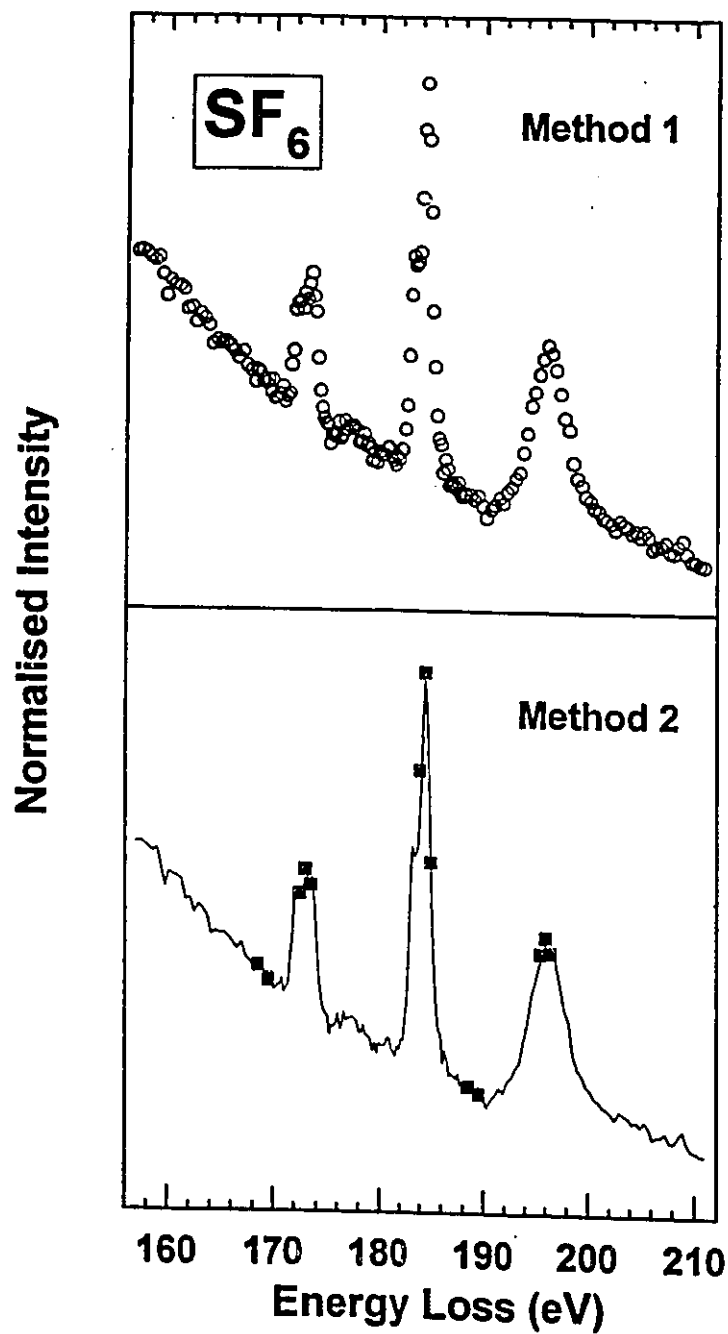


Fig. 5.2 Comparison of the energy spectrum sampling for acquisition methods one and two. Method one acquires complete spectra including background using a dense energy spacing. Method two samples selected peak intensities only, including a few background points.

areas, whereas method two provides only single point intensities for each feature. As illustrated in figure 5.10 (p. 143) for the  $t_{2g}$  and  $a_{1g}$  features in the S 2p spectrum of  $SF_6$ , for comparable statistics between the two methods, method two has a larger degree of scatter in the resulting GOS values than is found from method one. Presumably this scatter can be reduced by improved statistical precision in the intensities, which requires longer acquisition times. Method one has so far been the procedure of choice for all the variable  $K^2$  work done with this instrument.

### 5.2.3 Correction Factors for Spectral Normalisation

The goal of a GOS experiment is to investigate the change in excitation cross section with momentum transfer. Ideally, this means that all other factors such as pressure, incident beam current etc. that can influence the excitation cross section are held constant. In practice, however, over the period of acquisition which can take several days and involve interruptions for instrument maintenance, such factors do not remain perfectly constant. It is thus necessary to develop methods, which are discussed in this section, to monitor and correct for changes in pressure, beam current and position, geometrical overlap, etc. during the acquisition period. Such procedures enable spectra acquired under different conditions to be combined and provide better statistics.

This section also outlines the consideration of a geometrical overlap factor that plays an important part in correctly determining GOS's.



### 5.2.3.1 Gas Pressure

For typical GOS experiments, the chamber pressures (measured via the nude ionisation gauge) range from  $1.0 \times 10^{-5}$  Torr to  $4.0 \times 10^{-5}$  Torr. The relative pressure could be read from the analog gauge with a precision of 5%.<sup>1</sup> In general, the pressure is kept as high as possible in order to maximize signal count rates. Above  $6.0 \times 10^{-5}$  Torr, the possibility of electrical breakdown exists. At the collision region, the pressure of the gas jet exiting the capillary array is typically half an order of magnitude higher than the chamber pressure. This is based upon a comparison of the inelastic signal intensity obtained by introducing the sample gas first through the capillary array and subsequently through the auxiliary inlet far from the collision region (see figure 3.2).

During the course of an acquisition period (i.e. using method one), the pressure is monitored and logged manually at regular intervals, typically at least twice every hour depending upon instrument stability and type of gas. Sets of spectra to be used for GOS determination are then normalised relative to one another by dividing by the pressure values.

### 5.2.3.2 Incident Beam Current

It is important not only to monitor the incident current intensity, but also the

---

<sup>1</sup> Since the Varian Ratiomatic ion gauge controller used with this instrument has no absolute reference, it is necessary to calibrate it using a controller capable of providing absolute measurements.

position of the beam and (as much as possible) its profile. The beam current intensity is measured at two points A and B (see figure 3.1), corresponding to the first aperture of the analyser lens after the collision region and the first aperture of the monochromator exit lens after the monochromator exit plane, respectively. The current measured at point A is used for spectral normalisation, and repeat measurements are made and logged at each scattering angle during the acquisition period. Since the collision cell is operated at ground potential, it has a large intrinsic bias with respect to the incident beam. The incident beam current measured with and without the application of a + 22 V bias were essentially identical within the precision of the analog ammeter. Thus, for most of the GOS experiments done to date, a bias voltage was not applied. However, for additional confidence in the current readings, it is desirable to apply a small bias voltage (+22 V) at this point in order to capture low energy secondary electrons that may escape the collection surface, and to reduce any sensitivity to changes in the work function of this surface. It is thus possible that there is an error introduced by failure to bias the incident current readings which must be acknowledged, though it is difficult to estimate its magnitude.

At the beginning of each acquisition cycle, the position of the beam is set at the zero scattering angle. This can be verified using He as illustrated in chapter three, figure 3.5 and/or using the following procedure. The analyzer is set to the mechanical zero angle position, and the X, Y deflectors at the exit of the monochromator exit lens adjusted so that the incident beam enters aperture A of the analyser lens. By adjusting  $V_4$  of the monochromator exit lens, the beam current on aperture A could be minimised, thus

focusing the incident beam. Scanning the beam across the 1 mm opening of aperture A in both the X and Y directions using the monochromator exit lens deflectors typically results in 95-99% of the beam entering the aperture, which implies that the beam diameter (FWHM) at this point is  $\leq 1$  mm. Setting maximum transmission of the incident beam through aperture A at the mechanical zero angle thus sets the experimental zero scattering angle, and all incremental  $K^2$  measurements are referenced to it by the scanning algorithm. This condition is monitored manually 'on the fly' and logged each time the analyser rotation changes direction and passes through the zero degree scattering angle during the backlash removal routine that occurs at the end of each angle cycle. Systematic monitoring of the incident beam is important due to the fact that if the beam position drifts significantly during the acquisition period, the accuracy of the momentum transfer values determined from the scattering geometry will be affected, which leads to subsequent inaccuracies in the GOS values. With this in mind, it is estimated that the zero scattering angle is known within  $\pm 0.25^\circ$ , and thus all subsequent scattering angle measurements (for same direction scanning) will have an associated error of this magnitude. This error is in turn propagated to the determination of  $K^2$  values.

As in the case of the pressure measurements, sets of spectra are normalised relative to each other by dividing the spectral intensity by the magnitude of the incident beam current. In this manner, spectra that differ only in the magnitude of the incident beam current used can be combined to improve statistics. In the future, the incident beam monitoring will be done automatically by the acquisition computer using an ADC interface.

### 5.2.3.3 Geometrical Overlap Correction

In addition to accounting for variations in the beam current, gas pressure, etc. there is also a variation in the collision path length at the gas cell with scattering angle that must be considered. Figure 5.3 depicts a simple two-dimensional representation of the collision region defined by the area of intersection of the incident electron beam and the view cone of the analyser lens. For simplicity, the incident beam and analyser view cone are approximated as cross-sections of cylinders over the short range (approximately 0.5 cm) of the collision region. It can be seen from figure 5.3 that at small scattering angles, the interaction volume is markedly greater than at large scattering angles.

As depicted by the differential shading in figure 5.3, the gaseous sample within the boundaries defined by the interaction volume can be separated into two components: a well-collimated gas jet with circular cross-section arising from the capillary array (the dark circle in figure 5.3) and a more diffuse component arising from the background chamber gas (light shading in figure 5.3). Assuming that the capillary jet component is constant, this simple model implies that in order to correctly determine the excitation cross-section over a series of scattering angles (GOS), the angle-dependent contribution to the interaction region from the background chamber gas must be accounted for.

The first approach to implementing the overlap correction in practice involved deriving a mathematical correction factor based on the geometry in figure 5.3 (see Appendix A). It has the following form:

$$\frac{xy}{a \sin \theta} + c \quad (5.1)$$

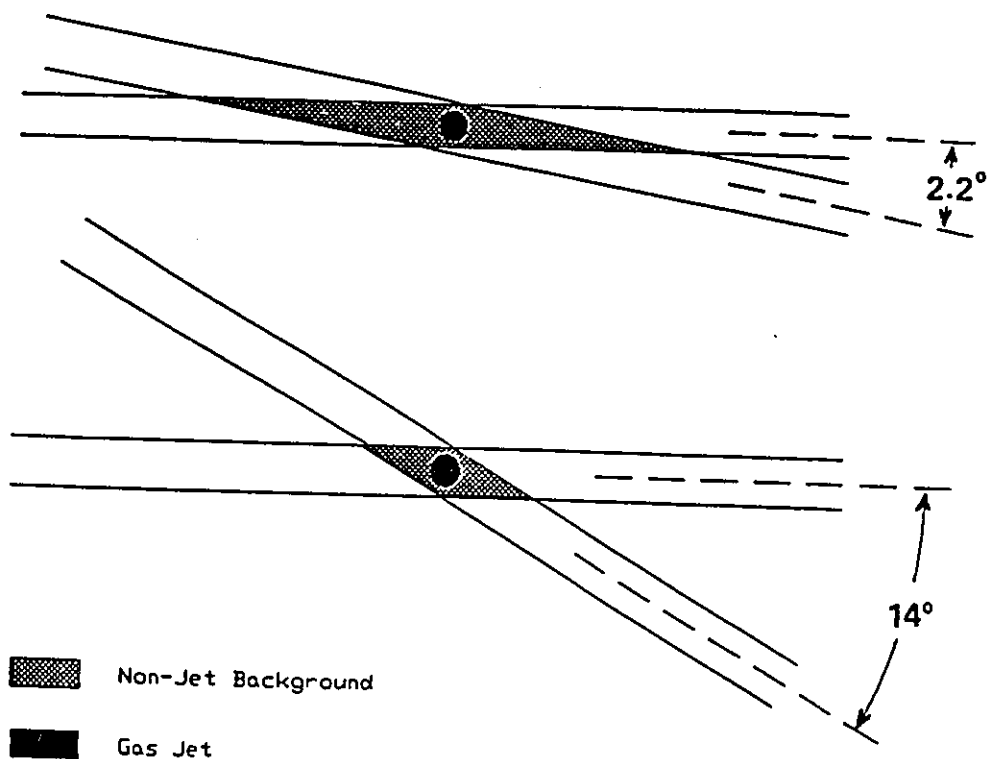


Fig. 5.3 Illustration of the geometrical change in the interaction region with scattering angle. The collision path length is longer at small angles due to the contribution from the background chamber gas in the region intersected by the incident beam and analyser view cone.

where  $x$  and  $y$  are the diameters of the incident beam and analyzer view cylinders,  $\theta$  is the scattering angle,  $a$  is the ratio of the gas jet and background chamber pressures and  $c$  is the area of the gas jet. An inverse  $\sin\theta$  relationship in the scattering geometry has also been noted by Lasettre and co-workers [LSD68] and Bromberg [B68].

Using physically reasonable estimates of the parameters  $\{x, y, a \text{ and } c\}$ , the correction factor was then applied to a set of angle dependent, helium elastic cross section data (denoted as  $\sigma_{\text{elastic}}$ ). These were derived from spectra collected on McVAHRES using acquisition method one for a series of scattering angles. Parameters  $x$  and  $y$  were estimated to be 1 mm each, based on practical experience with the beam behaviour at the 1 mm diameter apertures at points A and B in figure 3.1.  $a$  was estimated to be 5 by taking the ratio of signal intensities observed when the sample gas is admitted either through the capillary array or through the auxiliary leak valve.  $c$  was estimated to be between 0.5 and 1 mm<sup>2</sup> in area, based on the physical diameter of the capillary array. By comparison to  $\sigma_{\text{elastic}}$  values from the literature [B68] and adjusting the initial estimates of the parameters  $x, y$  and  $c$  in equation 5.1, it was found that division by a correction factor of  $(1/[5\sin\theta] + 0.78)$  yielded favourable results, which are presented below in Table 5.1.

To illustrate the importance of this type of geometrical correction, the GOS for the <sup>1</sup>P and <sup>1</sup>S features at 21.2 eV and 20.6 eV respectively in He were determined with and without the application of the overlap correction. The inelastic cross sections ( $\sigma_{\text{inelastic}}$ ) at a series of scattering angles were derived from data collected using acquisition method one (corrected for pressure and incident beam current) as the integrated areas of the gaussian peak profiles at 21.22 eV. Application of the kinematic correction,

$(k_0/k_1)(K^2)(E/2)$ , to the set of  $\sigma_{\text{inelastic}}$  at each  $K^2$  value yielded the relative GOS function which were then single-point normalised for comparison to theoretical and literature values. Figures 5.4 (a) and 5.4 (b) plot the experimentally determined He  $^1P$  and  $^1S$  GOS functions as a function of  $K^2$  before and after application of the overlap correction. In addition, theoretical and experimental curves from the literature [LSD64, SL64, KI68 and LSD70] are plotted for comparison. It is apparent from the uncorrected experimental GOS curves shown in the insets of figures 5.4 (a) and (b) that the non-gas jet background leads to a significant overestimation of the GOS that is most pronounced at small scattering angles. The overlap corrected curve agrees favourably with the literature experimental and theoretical curves and thus provides confidence in this methodology.

To test the applicability of the overlap correction factor derived for He to other species, the same relative GOS experiment described above was performed using a set of angle-dependent  $\sigma_{\text{inelastic}}$  for the N  $1s \rightarrow \pi^*$  transition at 400.1 eV in  $N_2$  measured using McVAHRES. Figure 5.5 plots the relative GOS curves obtained using two different correction factors, along with the GOS curve obtained without any correction applied to the set of raw  $\sigma_{\text{inelastic}}$ . These curves are in turn single point normalised to the data of Camilloni *et al.* [CF&87] at a value of  $\ln(K^2) = 3.1$  for comparison.

It can be seen from figure 5.5 that the GOS curve derived using equation 5.1 as a correction with the parameters for helium does not agree with the curve digitised from [CF&87]. This is in all likelihood due to the fact that the experimental conditions used to derive the  $N_2$   $\sigma_{\text{inelastic}}$  were very different than those for He. Assuming that the parameter  $c$  was unchanged, parameters  $x$ ,  $y$  and  $a$  were adjusted to account for a smaller

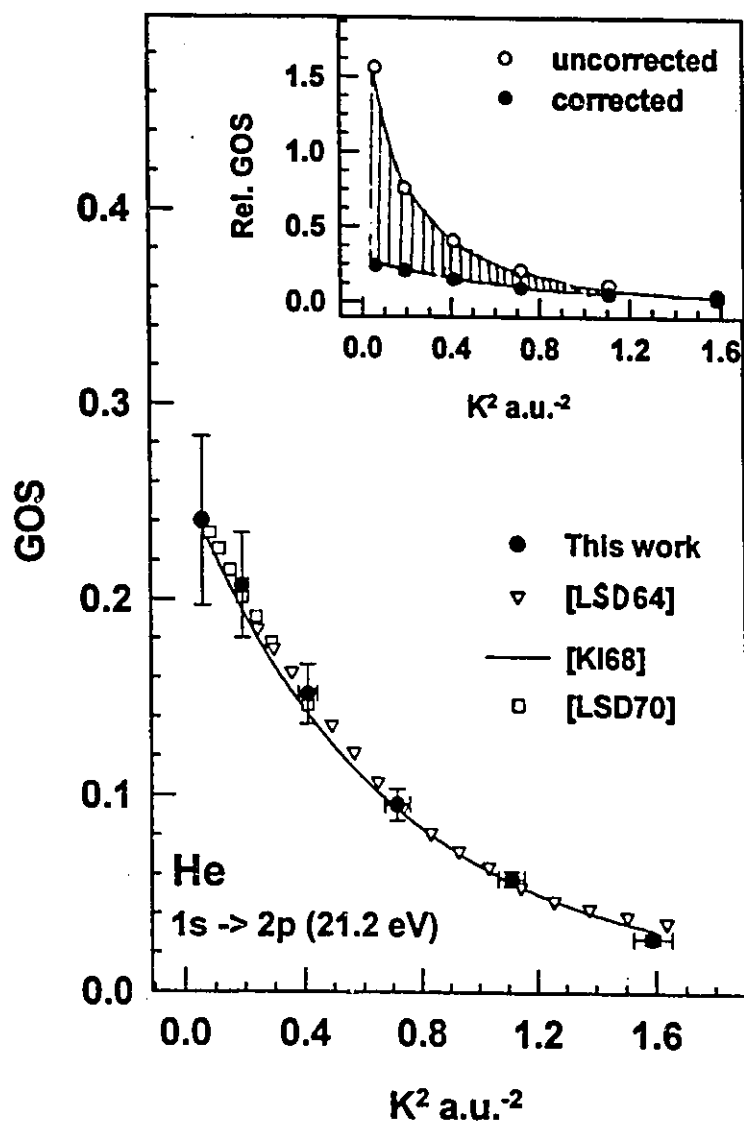


Fig. 5.4(a) Normalised relative GOS curve for the He  $1s \rightarrow 2p$  dipole-allowed electronic transition at 21.22 eV derived from McVAHRES using the mathematical overlap correction factor in comparison to literature results. Inset shows the GOS functions before and after overlap correction. Error bar estimation discussed in text.



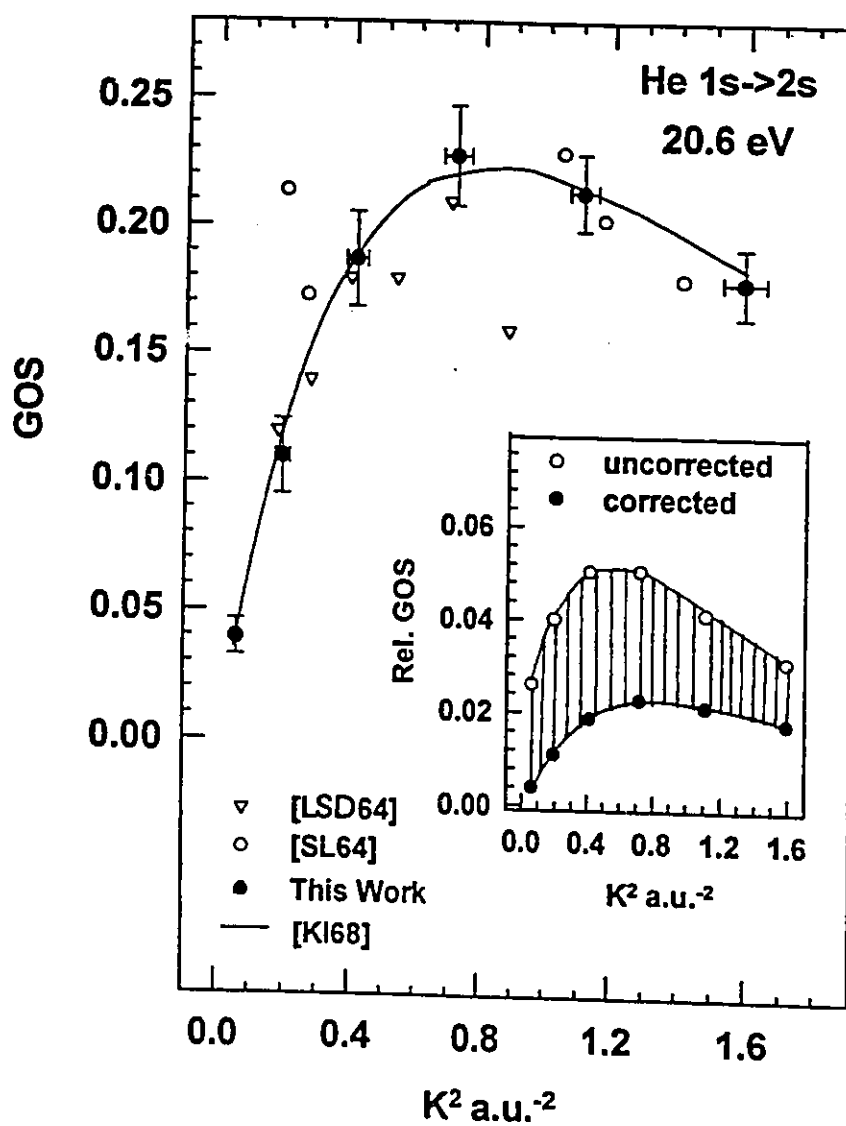


Fig. 5.4(b) Normalised relative GOS curve for the He 1s → 2s dipole-forbidden transition at 20.6 eV derived from McVAHRES using the mathematical overlap correction factor in comparison to literature results. Inset shows the GOS functions before and after overlap correction.

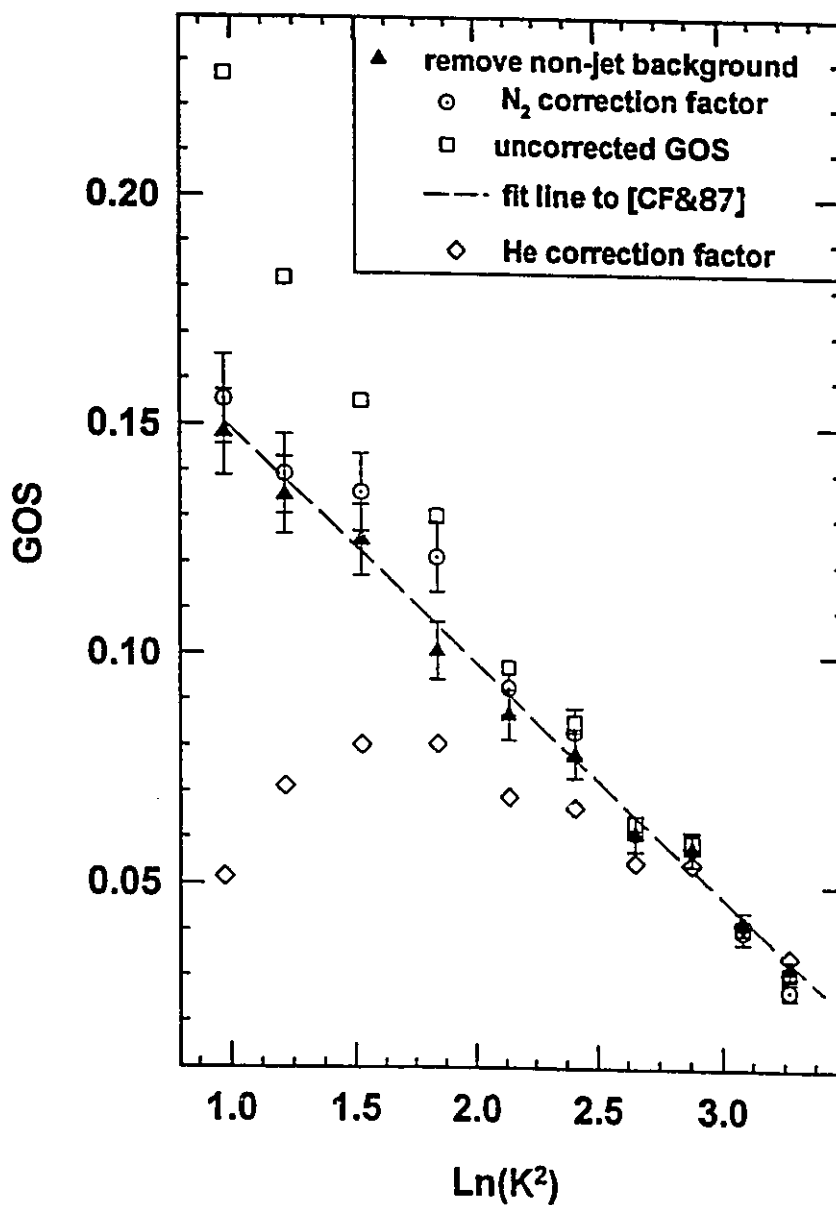


Fig. 5.5 Graphical evaluation of the mathematical approach to overlap correction using the normalised relative GOS for the N  $1s \rightarrow \pi^*$  electronic transition in  $N_2$ , in comparison to the results of Camilloni et al. [CF&87] and the non-gas jet background subtraction method.

Table 5.1 Comparison of overlap-corrected experimental He elastic cross-sections with literature values.

Angle	$\sigma_{\text{elastic}}$ (expt.) <sup>a</sup>	correction factor <sup>b</sup>	corrected $\sigma_{\text{elastic}}$	$\sigma$ ratio: <sup>c</sup> expt./lit.
2	9.45	6.50	1.45	0.97
4	3.56	3.65	0.98	0.90
6	2.26	2.69	0.84	0.97
8	1.56	2.22	0.70	1.00
10	1.17	1.93	0.61	1.03
12	0.87	1.74	0.50	1.04

- (a) Determined as the integrated area of the gaussian elastic peak profile.
- (b) Determined using equation 5.1 with  $x = y = 1$  mm,  $a = 5$  and  $c = 0.78$  mm<sup>2</sup> and the indicated scattering angles.
- (c) Literature values from [B68].

beam size and higher pressure differential. This is because the  $E_0$  for  $N_2$  was 1400 eV vs. 500 eV for He, and a higher  $E_0$  typically results in better focussing of the beam even though the incident current was much greater (x1000) in the case of  $N_2$ . The chamber pressure during the  $N_2$  experiment was ca.  $3 \times 10^{-5}$  Torr higher than for the He experiment, which could necessitate a larger value of  $a$  in equation 5.1. The best values of the product  $xy$  and the parameter  $c$  in equation 5.1 for  $N_2$  were obtained by fitting to the data of Camilloni *et al.* [CF&87]. In this manner, it was found that a correction factor of  $(0.4/9\sin\theta + 0.78)$  yielded a GOS function that agrees reasonably well with the data of [CF&87], as shown in figure 5.5.

In spite of the simplicity of the geometrical model used, this approach appears to be a viable means of overlap correction. However, it becomes apparent that in order to ensure reliability, a new correction factor must be derived for each different molecule and/or set of experimental conditions. Furthermore, this requires literature and/or theoretical data for correct determination. Since the main objective is to provide new GOS functions for previously unstudied species, this approach is at a disadvantage without further modification of the mathematical model to allow reliable overlap correction independent of literature data.

Using the simple picture shown in figure 5.3, an alternative approach was devised which is simple to execute and does not require normalisation to literature data. If one admits the sample gas through the auxiliary inlet far from the collision region and acquires data using the identical conditions and scan parameters as for sample gas admitted through the capillary array, the signal intensity so derived at each  $K^2$  value is

the contribution to the total intensity arising from the background chamber gas. This is shown as the lightly shaded area in figure 5.3. It is then possible to subtract this non-gas jet background component at each  $K^2$  value (scattering angle) from the total intensity, effectively isolating the pure gas jet component of the total intensity which is then used for GOS determination. A very similar approach has been reported by Boechat-Roberty *et al.* for GOS determination [BBS91]. The one disadvantage of this procedure is that it is necessary to perform the acquisition routine twice. This adds significantly to the total acquisition time as the count rates for the non-jet background gas are several times lower than those corresponding to gas admitted through the capillary array. Figure 5.6 illustrates the magnitudes of the background signal intensity relative to the total uncorrected intensity for scattering angles of  $2.2^\circ$  and  $14^\circ$  degrees in the case of  $SF_6$ .

The measured non-jet background correction procedure was applied to the same  $N_2$  data set (gas jet + background signal). As illustrated in figures 5.5 and 5.7, the resulting GOS function agrees within the estimated error bars with the literature GOS function of Camilloni *et al.* [CF&87]. The McVAHRES curve was single-point normalised to the corresponding value of [CF&87] at  $\ln K^2 = 1$ . The theoretical GOS functions of Rescigno *et al.* [RO79] and Bielschowsky *et al.* [BNH92] and the experimental GOS curve of Barbieri *et al.* [BB92] are also plotted in figure 5.7 for comparison. Neglecting considerations of absolute normalisation, the McVAHRES GOS curve is somewhat at variance with the curves of [BB92] and [BNH92] in regards to overall curvature. The curvature of the McVAHRES GOS function matches reasonably well with the curve of [RO79], although this is difficult to evaluate due to the limited  $K^2$

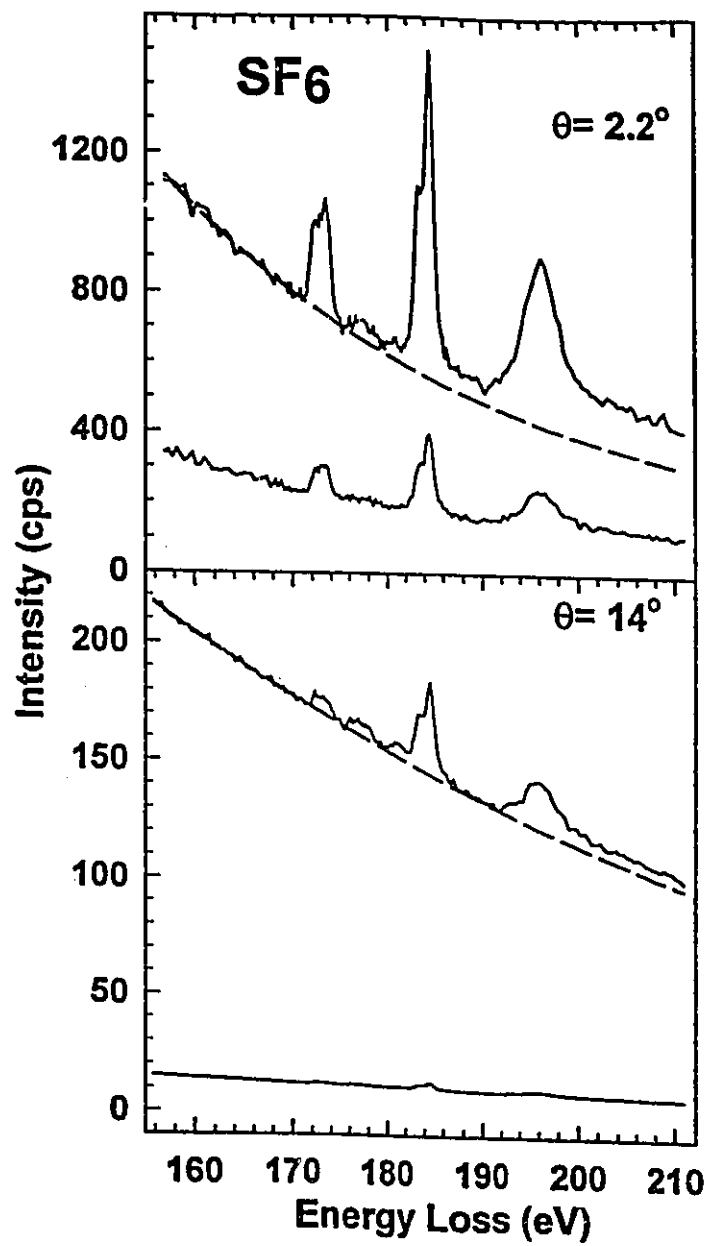


Fig. 5.6 Illustration of the magnitudes of the background signal intensity relative to the total uncorrected signal intensity for the S 2p edge of SF<sub>6</sub>, at scattering angles of 2.2° and 14.1°.

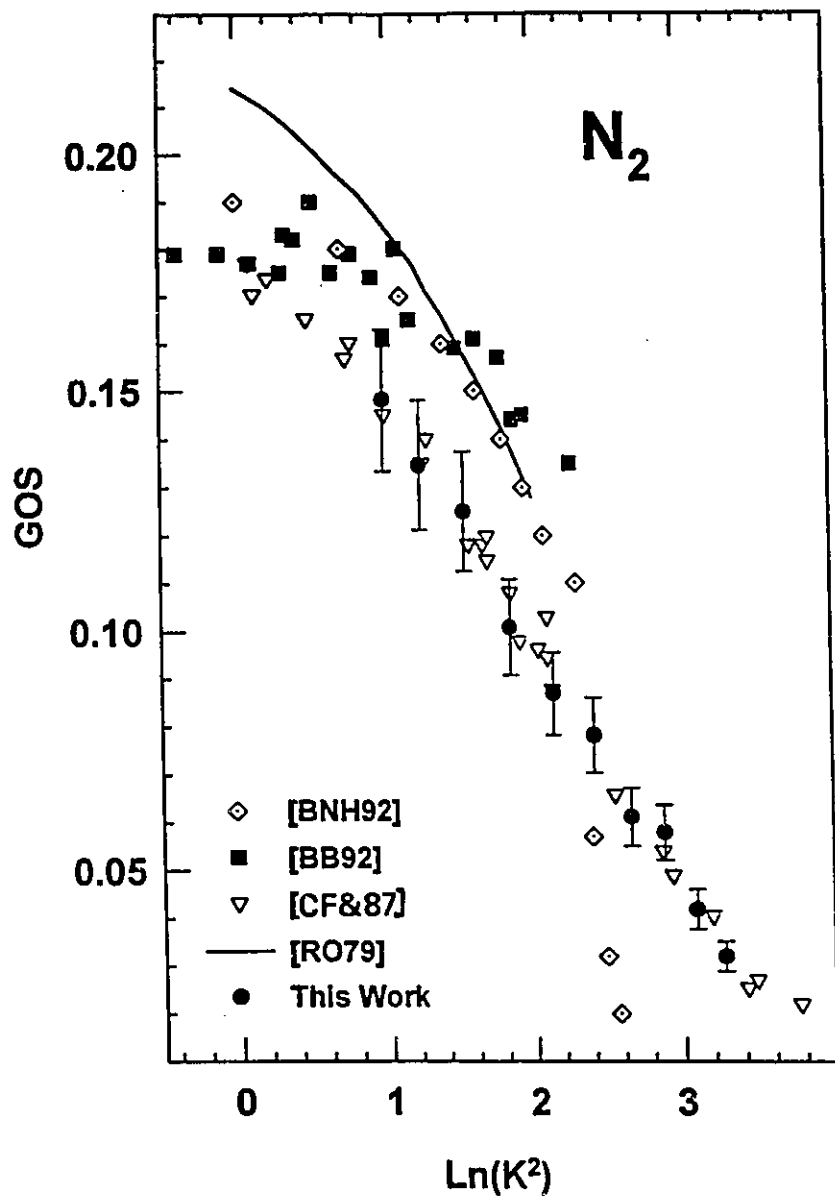


Fig. 5.7 GOS for the N  $1s \rightarrow \pi^*$  transition at 400.7 eV in  $N_2$  derived from McVAHRES using the non-gas jet background subtraction method and area determination procedures discussed in text. This work is compared to several other results, both experimental and theoretical, from the literature. McVAHRES curve is single point normalised to the results of [CF&87].

range of the [RO79] data set. As in the case of He, the effect of the overlap correction is largest at small scattering angles, with the uncorrected and corrected GOS curves converging at higher  $K^2$ . Typically after a scattering angle of  $16^\circ$  the overlap correction becomes constant and comparatively negligible.

These results provided confidence in this approach and it was thus used in all subsequent GOS measurements, including the  $SF_6$  study presented in chapter 6.

### 5.3 Data Processing for Quantitative GOS Determination

This section discusses the procedures used to process the raw spectral data obtained using acquisition method one into relative GOS functions that can be single-point normalised and thus made absolute. In general, these procedures are somewhat molecule dependent, in that the complexity of the energy loss spectrum determines the sophistication of the background subtraction and curve fit methods used. The algorithms used were designed in house by Tolmar Instruments [TK94] and a list of each program and brief description of its capabilities is presented in Appendix B. In addition, the treatment of errors is also discussed.

#### 5.3.1 Procedures for Extracting Inelastic Peak Areas

After applying the overlap correction to the raw data, as described in section 5.2.3.3, the task remains to determine the areas of the inelastic peak profiles at each scattering angle. These areas correspond to the integrated differential cross sections,  $d\sigma/d\Omega$ , ( $d^2\sigma/d\Omega dE$  for continuum states) in the Bethe-Born equation for the GOS (chapter



2, equation 2.21) as a function of  $K^2$ . They will be denoted as  $\sigma_{\text{inelastic}}$  in the following discussion, as in the case of He.

The BAN data analysis program (see Appendix B) is used to prepare each overlap corrected,  $K^2$  dependent, energy spectrum for fitting. The energy scale of the spectrum is calibrated, using accepted literature energy loss values for the transition of interest. Next, the inelastic peak of interest is isolated by removal of the scattered electron and valence ionisation background. Depending on the species and experimental conditions, the background removal may only require a simple linear subtraction. However, other cases can require more complex background manipulation, such as spline, exponential, power law or non-linear least squares fitting and subsequent subtraction. Figure 5.8 illustrates graphically the steps outlined above in preparing the energy spectrum for fitting using the S 2p edge of  $\text{SF}_6$ .

Determination of the inelastic peak areas was accomplished by fitting the inelastic peak profiles using the BGAUSS or MGAUSS algorithms (see Appendix B). Depending upon the natural linewidth of the excitation of interest and the instrumental resolution Gaussian, Voigt and/or Lorentzian lineshapes can be used. The fit routine requires the input of the width, energy position and amplitude of each line comprising the overall fit. In addition, it is possible to fix at a constant value and/or correlate any of these parameters during the fitting routine. Ionisation edges can be accommodated using arctan functions. The output of the routine lists the widths, energy positions, amplitudes and in the case of Gaussian lines, the area.

As an illustrative example, figure 5.9 presents two  $\text{SF}_6$  S 2p spectra corresponding

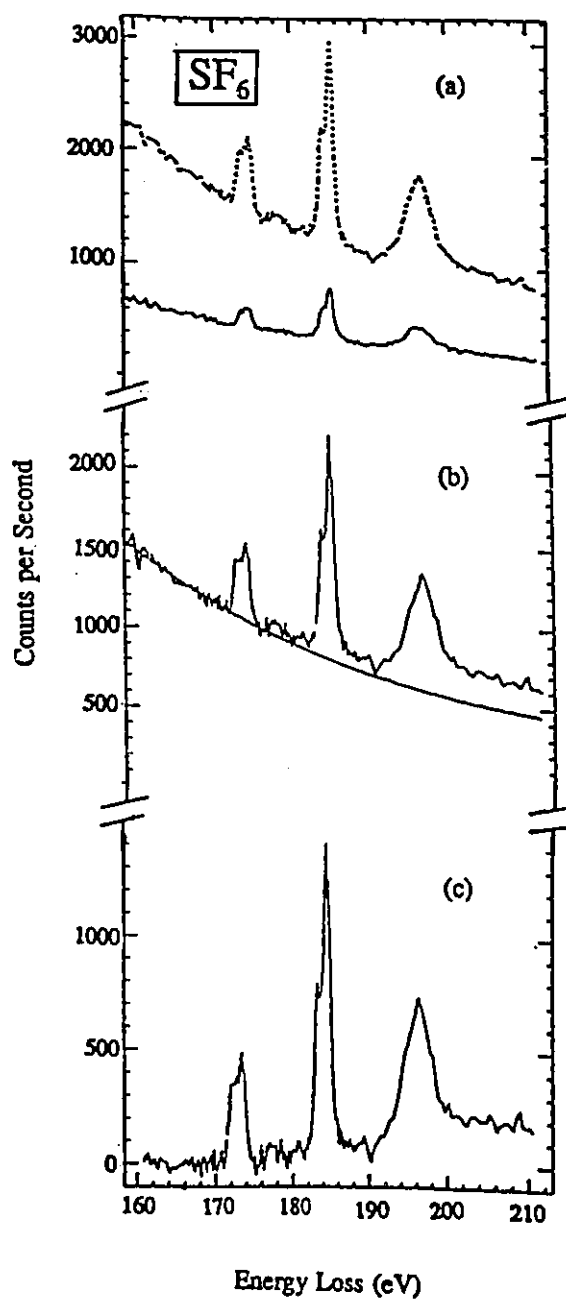


Fig. 5.8 Graphical representation of the steps involved in preparing raw energy spectrum for curve fitting and area determination. In (a), the non-gas jet background is subtracted. (b) shows subtraction of the valence ionisation background. (c) is the resultant spectrum ready for the fitting procedures discussed in the text.

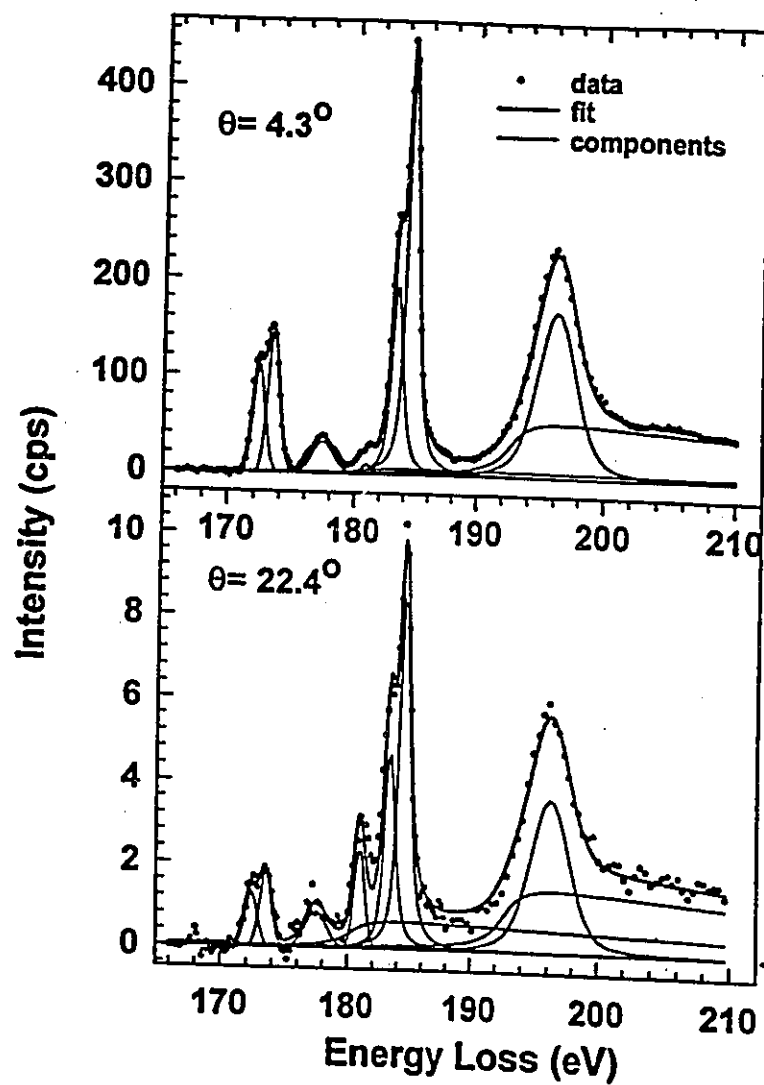


Fig. 5.9 Demonstration of the MGAUSS fitting algorithm. Energy spectra acquired at several different scattering angles can be fit simultaneously using a common set of fit parameters. See text for details.

to scattering angles of  $4.3^\circ$  and  $22.4^\circ$  that were fit simultaneously using common energy position, linetype and linewidth parameters with the MGAUSS algorithm. (The spectroscopic model is discussed further in chapter 6). This example illustrates the flexibility of the algorithm in accommodating relatively complicated spectral profiles. The  $a_{1g}$  resonance doublet at 170-175 eV was fit using two Gaussian lines each of widths 0.96 eV and 1.18 eV (FWHM). These were required to be separated in energy by an amount equal to the spin orbit splitting (1.14 eV). The  $t_{2g}$  resonance doublet at 182-188 eV required two Voigt lines, each with 0.60 eV FWHM Gaussian component lines. The two Lorentzian components had widths of 0.71 eV and 0.93 eV, respectively. These were also required to be separated in energy according to the spin orbit splitting (1.18 eV). The  $t_{1u}$  feature at 175-180 eV and the feature at 180-182 eV were not spin-orbit resolved experimentally, and thus they were fit using single Gaussian profiles of widths 2.03 eV and 1.14 eV respectively. The remaining  $e_g$  resonance was fit using a Voigt function with Gaussian and Lorentzian widths of 3.03 eV and 1.31 eV FWHM, respectively.

For Gaussian lineshapes, MGAUSS and BGAUSS provide the areas in the output file at the conclusion of the fit routine. Lorentzian and Voigt lineshapes can be integrated using BAN. The quality of a particular fit depends upon the validity of the spectroscopic model used, with regards to the number of lines and lineshapes used to model a particular energy spectrum. This is considered in section 5.3.3, which deals with error treatment.

### 5.3.2 Calculation of the GOS as a Function of $K^2$

Once the overlap-corrected inelastic scattering cross sections,  $\sigma_{\text{inelastic}}$ , are

determined for each  $K^2$ , it is a simple matter to convert them to their corresponding relative GOS values. Multiplication of the set of  $\sigma_{\text{inelastic}}$  by the kinematic correction factor,  $(k_f/k_i)K^2 (E/2)$ , yields the corresponding relative GOS as a function of  $K^2$ . It should be noted that this approach assumes that  $K^2$  is constant over the energy range of the electronic transition(s) of interest. While this is a good approximation over energy ranges of only a few eV (e.g. the N 1s  $\rightarrow \pi^*$  feature at 400.1 eV), longer range energy loss spectra require the individual determination of  $K^2$  for features separated by several eV.

It is possible to render the relative GOS functions absolute by extrapolating them to  $K^2 = 0$ . The value at zero momentum transfer is then matched to the corresponding optical oscillator strength (OOS), which is available from the photoabsorption literature, the results of theoretical calculations and more recently, from electron impact measurements made under conditions of extremely small momentum transfer [CCB91, CC&92]. As will be seen in chapter 6 however, there is often some disagreement between the OOS values reported in the literature from different sources. In such cases, the average of as many literature OOS values as can be found is taken, with the standard deviation being a measure of the error in normalisation. Alternatively, it is possible to use a sum rule normalisation procedure to render the GOS absolute (refer to chapter 2, section 2.4). The error in the absolute GOS determination thus depends upon the reliability of the extrapolation to  $K^2 = 0$ , and the accuracy of the optical value chosen for normalisation.

### 5.3.3 Treatment of Errors

The method used to estimate the errors in the relative GOS values is now discussed. It is possible to express the GOS in the following form:

$$GOS = N \left[ K^2 \frac{k_0 E_n}{k_1 2} \right] \cdot \frac{d^2 \sigma}{dE d\Omega} \quad (5.2)$$

Assuming constant  $E_n$ , for relative GOS determination this expression can be simplified to:

$$GOS = c \cdot K^2 \cdot Area \quad (5.3)$$

where  $c = NE_n k_0 / 2k_1$  and Area corresponds to the overlap corrected inelastic peak areas determined from the fitting procedures of section 5.3.1. The absolute error in the GOS can thus be written as:

$$\Delta GOS = \frac{\partial GOS}{\partial (K^2)} \Delta K^2 + \frac{\partial GOS}{\partial Area} \Delta Area + \frac{\partial GOS}{\partial N} \Delta N + \dots \quad (5.4)$$

Assuming that the error associated in determining  $E_n$  is negligible compared to the errors involved in  $K^2$  and Area, and letting  $N=i$  for relative GOS determination, (5.4) reduces to:

$$\frac{\Delta GOS}{GOS} = \frac{\Delta K^2}{K^2} + \frac{\Delta Area}{Area} \quad (5.5)$$

The error associated with  $K^2$  is determined by estimating that the scattering angles are correct to within  $\pm 0.25^\circ$ . This reflects the uncertainty in the zero scattering angle position, to which all other scattering angles are referenced for same direction scanning.

For each angle  $\theta$ , the corresponding  $K^2$  value is calculated for  $\theta$ ,  $(\theta + 0.25^\circ)$  and  $(\theta - 0.25^\circ)$ . The error in  $K^2$  is thus taken as the smallest difference between these three values. For small  $E_0$  and small scattering angles, such as in the case of the He data presented in this chapter ( $E_0 = 500$  eV), the error in  $K^2$  can approach 30% or more at small angles. As such, it is typically the major source of error in the GOS values. In addition, the error in  $K^2$  is expressed in the horizontal error bars for figures 5.4 (a) and (b).

The error associated with the area determinations,  $\Delta Area$ , includes contributions from normalisation factors such as the gas pressure and beam current. In addition, there are contributions from the statistical precision of the data (which is provided by the BGAUSS algorithm), and the validity of the spectroscopic model used to determine the number and type of lines used in the fit procedure. These are treated as uncorrelated quantities and are added in quadrature to give  $\Delta Area$ . As an example, taking the relative uncertainties in the pressure, current, counting statistics and fit model to be 5%, 5%, 1% and 0.5%, one finds that:

$$\frac{\Delta Area}{Area} = \sqrt{(5^2 + 5^2 + 1^2 + 0.5^2)} = 7\%$$

This procedure for error estimation was used to determine the error bars for figures 5.4 (a) and (b) and 5.7 in this chapter and for the GOS work on  $SF_6$  presented in chapter 6.

#### 5.4 Further Examples

To compliment the He and  $N_2$  data presented in this chapter, for which both theoretical and experimental data exists in the literature, this section presents the first

determination of the GOS for the C 1s  $\rightarrow \pi^*$  transition at 287.4 eV in CO. In addition, a pseudo-Bethe surface is constructed to illustrate the type of future experiments planned for this instrument, now that the methodology outlined in this chapter has been established.

#### 5.4.1 Relative GOS for the C 1s $\rightarrow \pi^*$ transition in CO

Figure 5.11 presents the relative GOS derived from a set of angle-dependent,  $\sigma_{\text{inelastic}}$  measurements in the C 1s region of CO using the procedures outlined in this chapter. The impact energy was 1357 eV. The relative GOS function has been rendered absolute by extrapolation to  $K^2 = 0$  and single point normalisation to the OOS for the 1s  $\rightarrow \pi^*$  transition ( $f_{\text{opt}} = 0.17$ , [HM94]). This result is the first GOS determination for this species in this energy region.

#### 5.4.2 Pseudo-Bethe Surface for the C 1s Region of CO.

Figure 5.12 illustrates a 'pseudo' Bethe surface representation for the CO data used to derive figure 5.11. This energy region includes the prominent  $\pi^*$  feature at 287.4 eV, in addition to Rydberg structure and part of the ionisation continuum. In order to have a true Bethe surface, the momentum transfer must be constant for each energy spectrum cross-section. Experimentally, this means scanning the impact energy simultaneously with the energy loss, as discussed in chapter 3, section 3.2.6.1. Once the instrument is capable of such a scan mode, this type of constant  $K^2$  experiment is considered a primary goal for future studies with McVAHRES. Examples of true Bethe



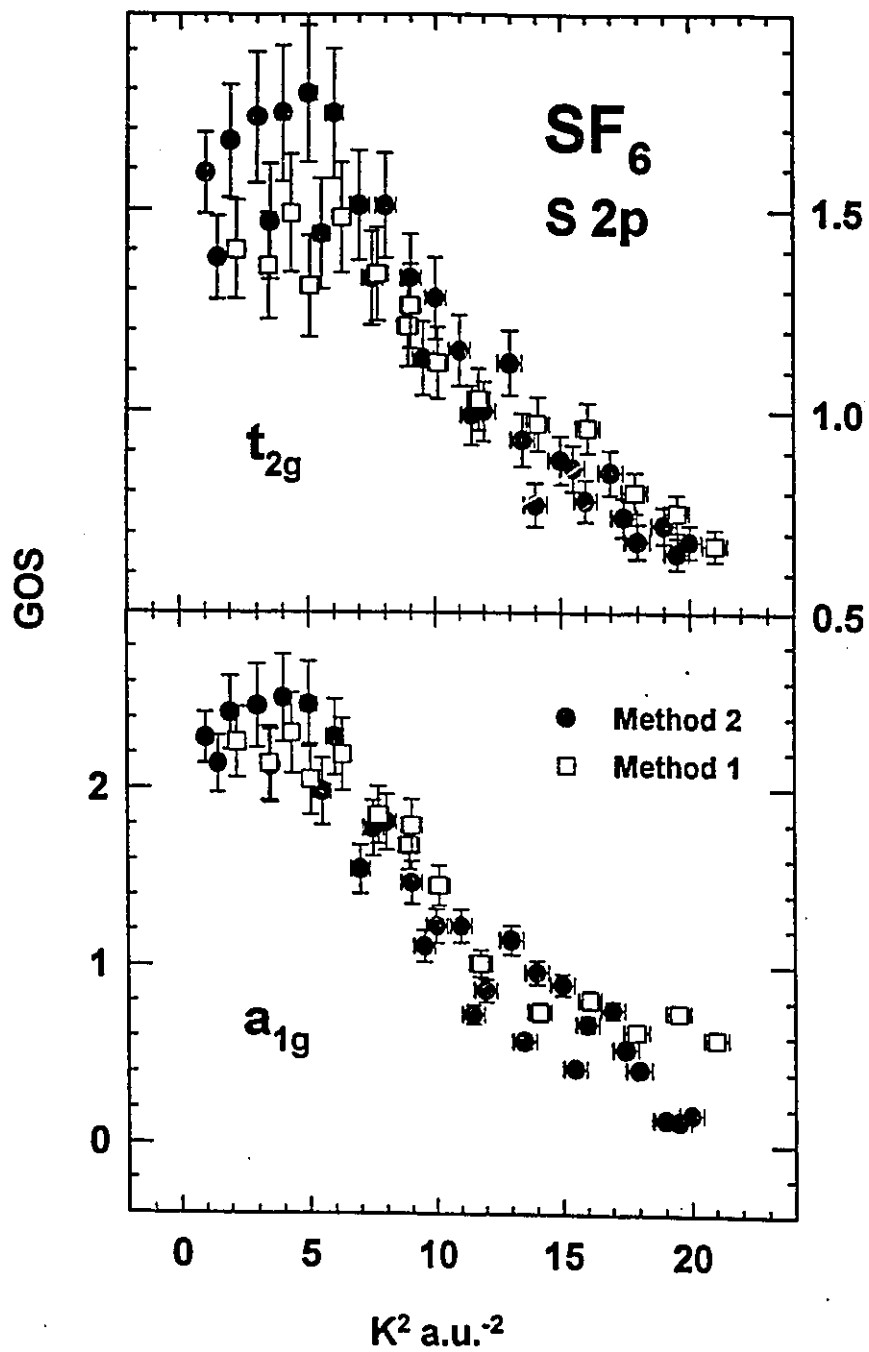


Fig. 5.10 Comparison of the GOS curves determined using acquisition method one (empty squares) vs. acquisition method two (dark circles). Method one uses peak areas, while method two utilizes selected peak intensities.

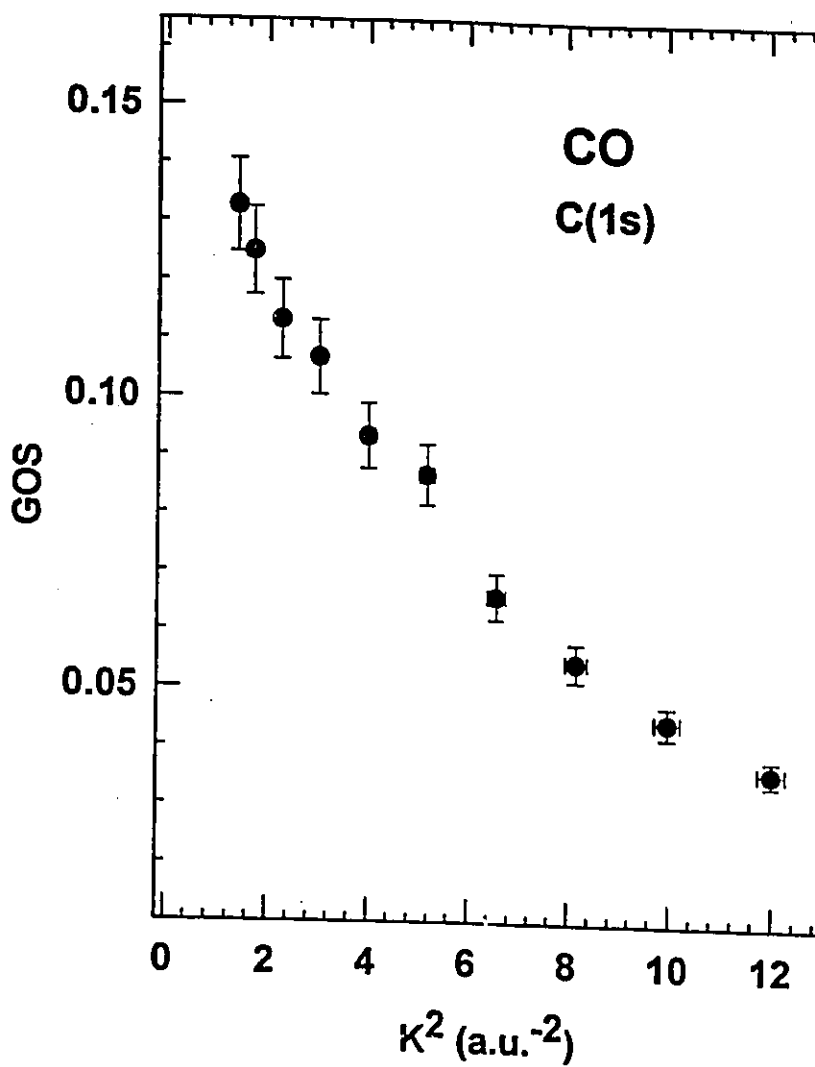


Fig. 5.11 First determination of the relative GOS function for the C  $1s \rightarrow \pi^*$  transition in CO at 287.4 eV using the procedures outlined in this chapter. The curve was single-point normalised by extrapolation to zero momentum transfer and matching to the OOS for this transition. The error bar determination is discussed in the text.

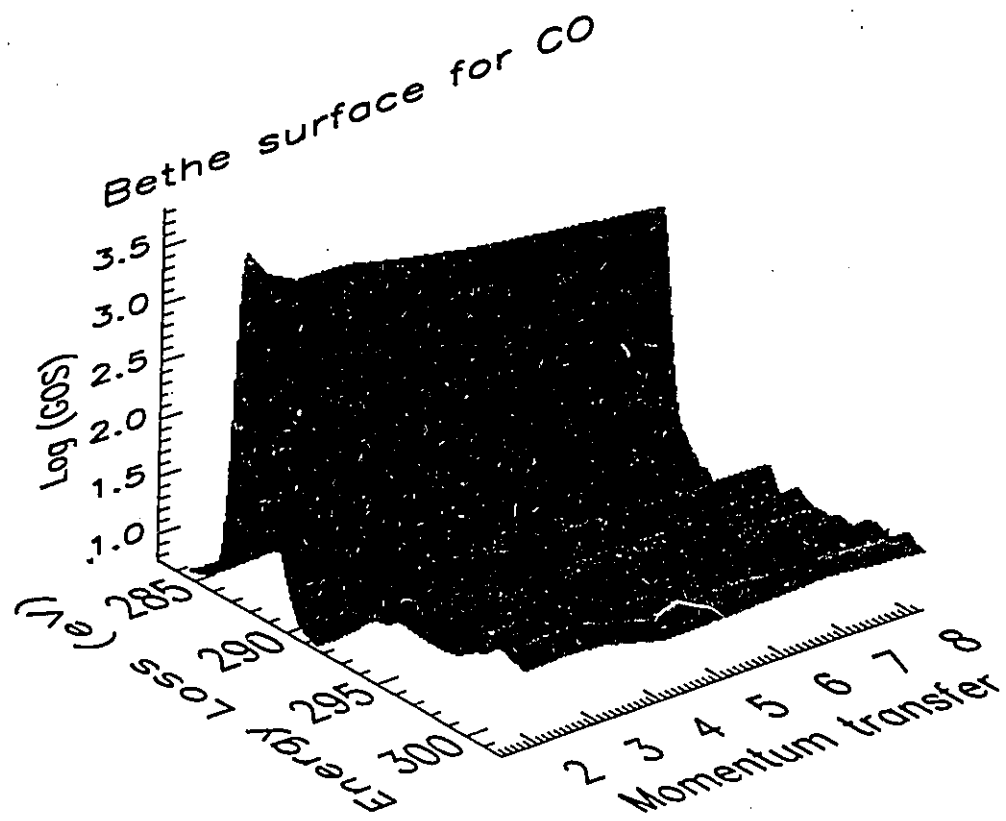


Fig. 5.12 "Pseudo" Bethe surface for a portion of the C 1s energy loss spectrum of CO.

surfaces from the literature include that of Lahmam-Bennani *et al.* [LDW79, LD&80] for CO<sub>2</sub> and NH<sub>3</sub> at E<sub>0</sub> = 35 keV and the theoretical surfaces of Inokuti [IIT71].

### Summary

This chapter outlined two acquisition methods used to acquire momentum-transfer dependent, inelastic cross sections. At present, acquisition method one has been the method of choice. The problem of spectral normalisation and geometric overlap correction was examined and a procedure that was independent of literature data was developed. These overlap correction procedures were evaluated using He and N<sub>2</sub> by comparison to experimental and theoretical results in the literature. The fit procedures used to derive the inelastic cross section as integrated areas of peak profiles were discussed, using a relatively sophisticated example derived from SF<sub>6</sub>. The problem of estimating errors in both the relative GOS and K<sup>2</sup> values was examined in detail. Finally, these procedures were used to derive the GOS for the C 1s → π\* transition at 287.4 eV for the first time, and to construct a Bethe surface.

## Chapter 6

### NON-DIPOLE S 2p AND S 2s STATES AND GENERALISED OSCILLATOR STRENGTHS FOR THE S 2p STATES OF SF<sub>6</sub>

#### 6.1 Introduction

Having developed the instrumentation and methodology to derive generalised oscillator strengths (chapters 3 and 5), one of the goals of this work was to determine the GOS functions for the S 2p states of SF<sub>6</sub>. In addition, a question arose based upon some preliminary data acquired during the instrument development stage as to whether or not there existed a dipole-forbidden feature at 181 eV in the S 2p spectrum. This chapter presents the results of experiments on SF<sub>6</sub> performed using McVAHRES with these motives in mind.

Section 6.2 presents electron energy-loss spectra of SF<sub>6</sub> recorded using McVAHRES in the region of S 2p and S 2s excitation, using both dipole and non-dipole electron scattering conditions. In addition, F 1s spectra of SF<sub>6</sub> are presented. They were recorded under both dipole and non-dipole conditions using an older, lower resolution spectrometer (which will be referred to in future as McFALRES, for McMaster Fixed Angle, Low Resolution Electron Spectrometer). Relative to dipole-EELS or photoabsorption, there are large intensity redistributions in both the S 2p and S 2s spectra under non-dipole conditions, which are not observed in the F 1s spectra. A spectral

feature was observed at 181 eV which is tentatively assigned as an electric quadrupole excitation to the  $(S2p (t_{1u})^{-1}, t_{1u}) ^1E_g$  state. Section 6.3 presents the generalised oscillator strengths (GOS) for discrete and continuum S 2p excitations which were derived in the momentum transfer range ( $K^2$ ) of 1 - 26 a.u.<sup>-2</sup> from the angular variation of the relative differential cross section for inelastic electron scattering.

### 6.2 Non-Dipole S 2p, S 2s and F 1s States of SF<sub>6</sub>

The electronic structure of sulfur hexafluoride has been a subject of much interest both because of its technological importance [AF81, CW88, PRB87, UK87] and because of its unusual spectroscopy. Photoelectron [AT&86, AT&89, BH&72, D72, FM&67, N70, VZ72], photoionization [CH&68, DW66, FL&88, HS&92, HS&93] and inelastic electron scattering [HB78, SB90, SS&89, YML93] measurements have been performed. The core excitation spectroscopy of SF<sub>6</sub> has been studied intensively over the past years because it is a prototype of a number of species in which a central atom is surrounded by a "cage" of electronegative atoms. Its unusual core excitation spectral features are often described to be the consequence of a "potential barrier".

Nefedov [N70] and Dehmer [D72] proposed the potential barrier concept to explain the "anomalous" intensity distributions observed in the inner-shell electron excitation spectra of "cage molecules" containing highly electronegative ligands such as SF<sub>6</sub>, SO<sub>2</sub>, SiF<sub>4</sub>. These unusual intensity redistributions consist of the suppression of direct ionisation and the enhancement of a selected features, both above and below the inner-shell ionisation limit (IP). The latter features are attributed to excitations of core electrons

into unoccupied molecular orbitals (UMO) to form states spatially localised inside a potential barrier.

In the potential barrier model, excited states are localised by a potential barrier into either the inner-well or outer-well region of the potential space. Fig. 6.1 depicts a one-dimensional model of this phenomenon. The compact virtual valence orbitals are spatially localised in the inner-well and thus there is strong spatial overlap with the compact core orbital. If the symmetry is correct, this results in very intense core  $\rightarrow$  valence excitations in dipole-EELS and X-ray photoabsorption (XAS) spectra. For  $\text{SF}_6$  excitations to  $t_{1u}$  in the S 1s and S 2s spectra and excitations to  $a_{1g}$ ,  $t_{2g}$  and  $e_g$  in the S 2p spectrum are of this type. In contrast, spatially extended Rydberg and continuum orbitals are excluded from the inner well and 'localised' in the outer-well region. This results in poor overlap with the core orbital and thus low spectral intensities for core  $\rightarrow$  Rydberg excitations [HS&92] and for near threshold core ionisation. Although core  $\rightarrow$  Rydberg transitions are suppressed, they are still observed in the core spectra of most 'potential barrier' species, either because of 'tunnelling' through the barrier, or because of Rydberg-valence mixing in which the final state wavefunction obtains some 'inner-well' character [BMN90, BNM86, BT&87, R85, KL86, TL&89].

Potential barrier effects have also been observed [HB80, WBV72] and predicted [D76, DD75] in the inner-shell spectra of a wide range of molecules, particularly unsaturated species such as  $\text{N}_2$  and  $\text{CO}$ , which are not "cage molecules". For these species, the enhanced intensity of the core  $\rightarrow$   $\sigma^*$  feature has been attributed to shape resonances which occur at energies where the outgoing core-ionised electron is

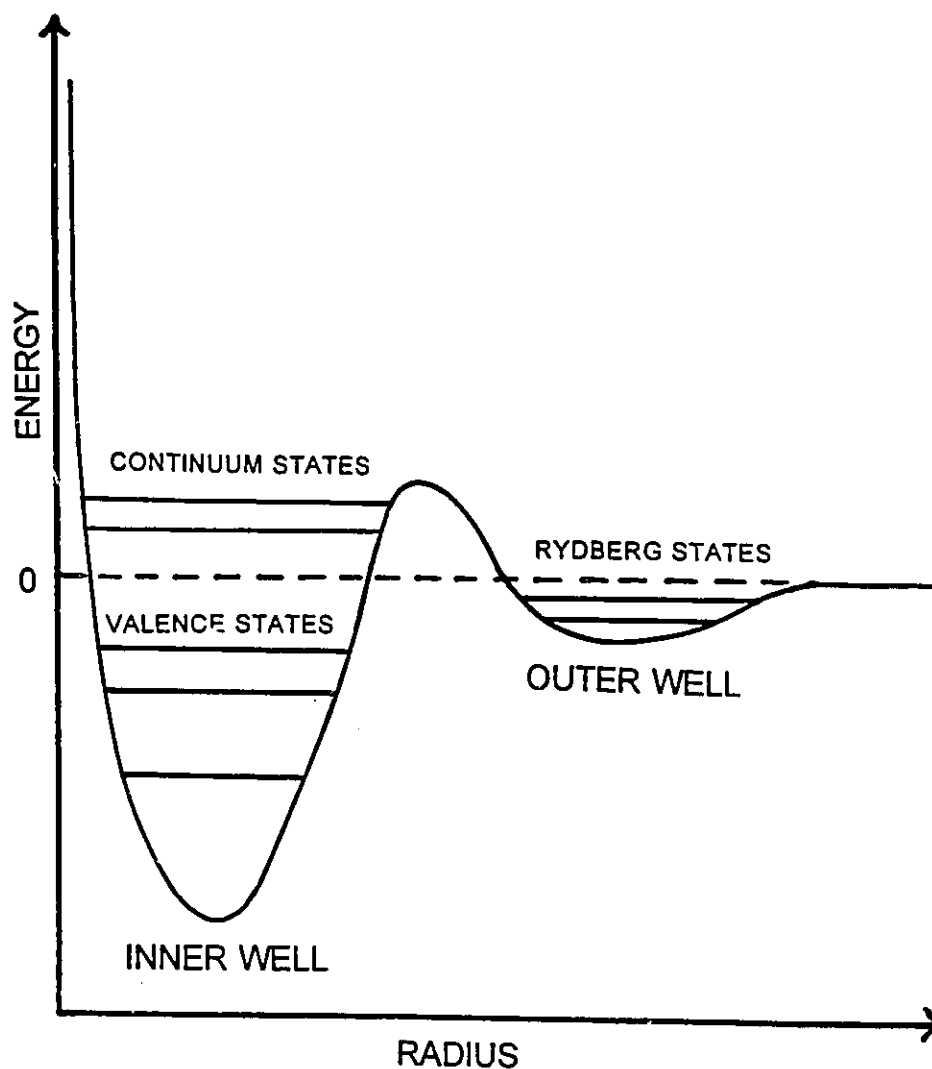


Fig. 6.1 Graphical representation of a double well potential. The centrifugal component of the effective molecular potential gives rise to a barrier that divides the potential into inner well and outer well regions. The valence orbitals are located mainly in the inner well, along with a few low energy Rydberg orbitals. The Rydberg orbitals are located mainly in the outer well region. Due to the height of the barrier, some continuum states are 'quasibound', and give rise to intense resonances in the EELS and photoabsorption spectra. The electron can then rapidly tunnel through the barrier and escape the molecule.



temporarily trapped by multiple intramolecular scattering by the anisotropic molecular field. The nature of the potential barrier in both "cage" and "non-cage" species has been the subject of considerable debate [D72, D76, DD75, N70, SG&89]. MS-X $\alpha$  calculations [D76, DD75, GGL72, GN&83, SP&74, TC86, VK&74 VK76] suggest that the dominant effect is a centrifugal barrier associated with large angular momentum of the ejected photoelectron since the continuum resonances appear at specific energies in selected angular momentum partial waves of the outgoing electron in the final state.

However, MO calculations also predict continuum intensity enhancements associated with transitions to core excited states which are quasi-bound in the continuum [SG&89]. In many cases a one-to-one correspondence can be made between the MO and the shape resonance picture. Stöhr [S92] has presented a detailed discussion of the relationships among various models for intensity-enhanced core excitation spectral features. It is debatable whether there is such a correspondence for SF<sub>6</sub>. Traditionally [D72,N70] the intensity enhanced t<sub>2g</sub> and e<sub>g</sub> resonances in the S 2p continuum are associated with the t<sub>2g</sub> and e<sub>g</sub> orbitals arising from crystal field splitting of the S 3d orbitals. However Addison *et al.* [AT&89] have used MS-X $\alpha$  calculations to show that the same continuum resonances can be found in a hypothetical octahedral "F<sub>6</sub>" species which does not even contain a S atom!

While the electric dipole core excitation spectroscopy of SF<sub>6</sub> has been very extensively studied, there has been relatively few investigations of non-dipole excitations [YML93]. Variable momentum transfer electron energy loss spectroscopy (EELS) is particularly advantageous for this since the nature of the excitation mechanism can be

probed experimentally. The characteristic transition time increases in small impact parameter, large momentum transfer electron-molecule collisions [SC&87]. Thus it is possible that, in addition to turning on non-dipole electronic excitations, there could be large changes to the potential barrier phenomena, such as increased intensity of Rydberg and near-continuum transitions. In order to investigate this aspect we have carried out a systematic investigation of the inner shell electron energy loss spectra (ISEELS) in both dipole and non-dipole regimes. This section reports our spectroscopic findings, the most significant of which is the observation of a non-dipole electronic state, which is tentatively assigned as being quadrupolar coupled to the ground state.

### 6.2.1 Experimental Details

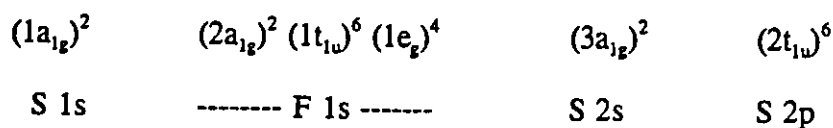
The sulfur hexafluoride (99.99% purity) used in these experiments was purchased from Matheson and was used without further purification. The overall energy resolution, determined by the monochromator and analyzer pass energies of 70 eV each, was 0.5 eV full width at half maximum (FWHM) for all experiments with an impact energy of 1400 eV on McVAHRES. For the F 1s experiments recorded on McFALRES, the resolution was 0.7 eV FWHM. McFALRES has been described in detail in the literature [H90]. The scattering conditions for the S 2p and S 2s experiments (using McVAHRES) involved incident energies between 700 and 1500 eV and scattering angles between 0° and 30°. The F 1s spectra were recorded using incident energies of 3200 eV (dipole conditions) and 1500 eV (non-dipole conditions), with scattering angles between 2° and 10°.

## 6.2.2 Results and Discussion

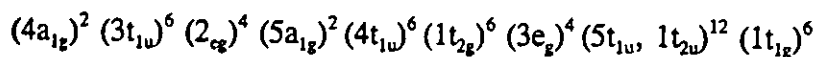
### 6.2.2.1 Orbital and State Descriptions

The ground state electron configuration of SF<sub>6</sub> can be written as follows [GK83, RSW74]:

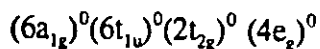
#### Core orbitals



#### Valence orbitals



#### Virtual Valence Orbitals



Note that, while the ordering of the occupied valence orbitals, in particular the closely spaced 5t<sub>1u</sub>, 1t<sub>2u</sub> and 3e<sub>g</sub> orbitals, is still a subject of debate, the energy ordering of the virtual valence orbitals is well established, as is the independence of this ordering on the remainder of the electronic configuration.

States corresponding to the possible configurations arising from excitations of S 2p, 2s and F 1s core electrons to the four virtual valence orbitals are summarised in Table 6.1, along with an indication of the order of electric multipole transition (monopole, dipole, quadrupole, etc.) which can couple each state to the <sup>1</sup>A<sub>1g</sub> electronic ground state.

It is noted that this analysis ignores spin-orbit coupling. A more complete analysis encompassing spin-orbit coupling requires the use of double groups.

#### 6.2.2.2 S 2p: Spectral presentation and analysis

Fig. 6.2 compares ISEEL spectra of the S 2p region of SF<sub>6</sub>, recorded using dipole (E<sub>0</sub>=1400 eV, θ=2.2°) and strongly non-dipole (E<sub>0</sub>=1400 eV, θ=16.1°) conditions. Tables 6.2 and 6.5 present the energies, term values and spectral assignments. The absolute energy scale was calibrated using the energy of the S 2p<sub>1/2</sub> → t<sub>2g</sub> transition (184.54 eV) reported by Sodhi and Brion [SB84]. Both as-recorded and background subtracted spectra are presented. The estimated underlying valence shell background used to obtain the background subtracted spectrum was generated by extrapolating a least-squares fit of the signal between 155-170 eV to a function, a(E-b)<sup>c</sup>.

Studies including both synchrotron radiation photoabsorption spectroscopy [BH&72, FL&88] and small-angle EELS [HB78, SB90] have indicated that the dipole-regime S 2p spectrum is dominated by three bands, corresponding to dipole-allowed excitations to the a<sub>1g</sub>, t<sub>2g</sub> and e<sub>g</sub> virtual valence orbitals. As the group theory analysis indicates (Table 6.1), for each of these (S 2p<sup>-1</sup>, UMO) configurations, there is only a single state which is dipole coupled to the ground state. The S 2p photoabsorption spectrum of SF<sub>6</sub> is identical for both gas and solid phases [BH&72] consistent with a large, spatially-compact, valence character to the excited electron in each of the resonance states. By contrast the weak Rydberg excitations (seen in higher resolution ISEELS [HB78, SB90] and photoabsorption [HS&93] S 2p spectra) are absent in the solid state

**Table 6.1 S 2p, 2s and F 1s Core Excited States of SF<sub>6</sub>**

Upper Orbital	S 2p excitation		S 2s excitation		F 1s excitation	
	Electronic State(s)	Selection rules	Electronic State(s)	Selection rules	Electronic State(s)	Selection rules
a <sub>1g</sub>	T <sub>1u</sub>	D	A <sub>1g</sub>	M	A <sub>1g</sub> T <sub>1u</sub> E <sub>g</sub>	M D Q
t <sub>1u</sub>	A <sub>1g</sub> E <sub>g</sub> T <sub>1g</sub> T <sub>2g</sub>	M Q H Q	T <sub>1u</sub>	D	T <sub>1u</sub> (2) T <sub>1g</sub> T <sub>2u</sub> A <sub>1g</sub> T <sub>2g</sub> E <sub>g</sub>	D H O M Q Q
t <sub>2g</sub>	A <sub>1u</sub> E <sub>u</sub> T <sub>1u</sub> T <sub>2u</sub>	? ? D O	T <sub>2g</sub>	Q	T <sub>2g</sub> (2) T <sub>1g</sub> T <sub>1u</sub> A <sub>1u</sub> T <sub>2u</sub> E <sub>u</sub>	Q H D ? O ?
e <sub>g</sub>	T <sub>2u</sub> T <sub>1u</sub>	O D	E <sub>g</sub>	Q	E <sub>g</sub> (2) A <sub>2g</sub> A <sub>1g</sub> T <sub>2u</sub> T <sub>1u</sub>	Q ? M O D

M - monopole, D - dipole, Q - quadrupole, O - octupole, H - hexadecapole  
 ? = higher order multipole,  $\Delta J > 4$

**Table 6.2 Energies (eV), term values and assignments of features in the S 2p electron energy-loss spectrum of SF<sub>6</sub>**

Feature <sup>a)</sup>	Energy loss ( $\pm 0.1$ eV)		Term Value (eV)		Assignment
	2p <sub>3/2</sub>	2p <sub>1/2</sub>	2p <sub>3/2</sub>	2p <sub>1/2</sub>	
1,2	172.4	173.5	8.0	8.1	(t <sub>1u</sub> <sup>-1</sup> , 6a <sub>1g</sub> ) <sup>1</sup> T <sub>1u</sub>
3,4	(177.4) <sup>b)</sup>		(3.6)		(t <sub>1u</sub> <sup>-1</sup> , 6t <sub>1u</sub> ) <sup>1</sup> E <sub>2g</sub>
5	(180.9)		(0.1)		(t <sub>1u</sub> <sup>-1</sup> , 6t <sub>1u</sub> ) <sup>1</sup> T <sub>2g</sub>
IP <sup>c)</sup>	180.4	181.6			
6,7	183.4	184.5	-3.0	-3.4	(t <sub>1u</sub> <sup>-1</sup> , 2t <sub>2g</sub> ) <sup>1</sup> T <sub>1u</sub>
8	(196.2)		(-16.2)		(t <sub>1u</sub> <sup>-1</sup> , 4e <sub>g</sub> ) <sup>1</sup> T <sub>1u</sub>

a) From Fig. 6.2

b) Average of 3/2 and 1/2 - spin-orbit splitting not observed; term values expressed relative to average IP

c) The S 2p IP's are from XPS measurements [JBE84]

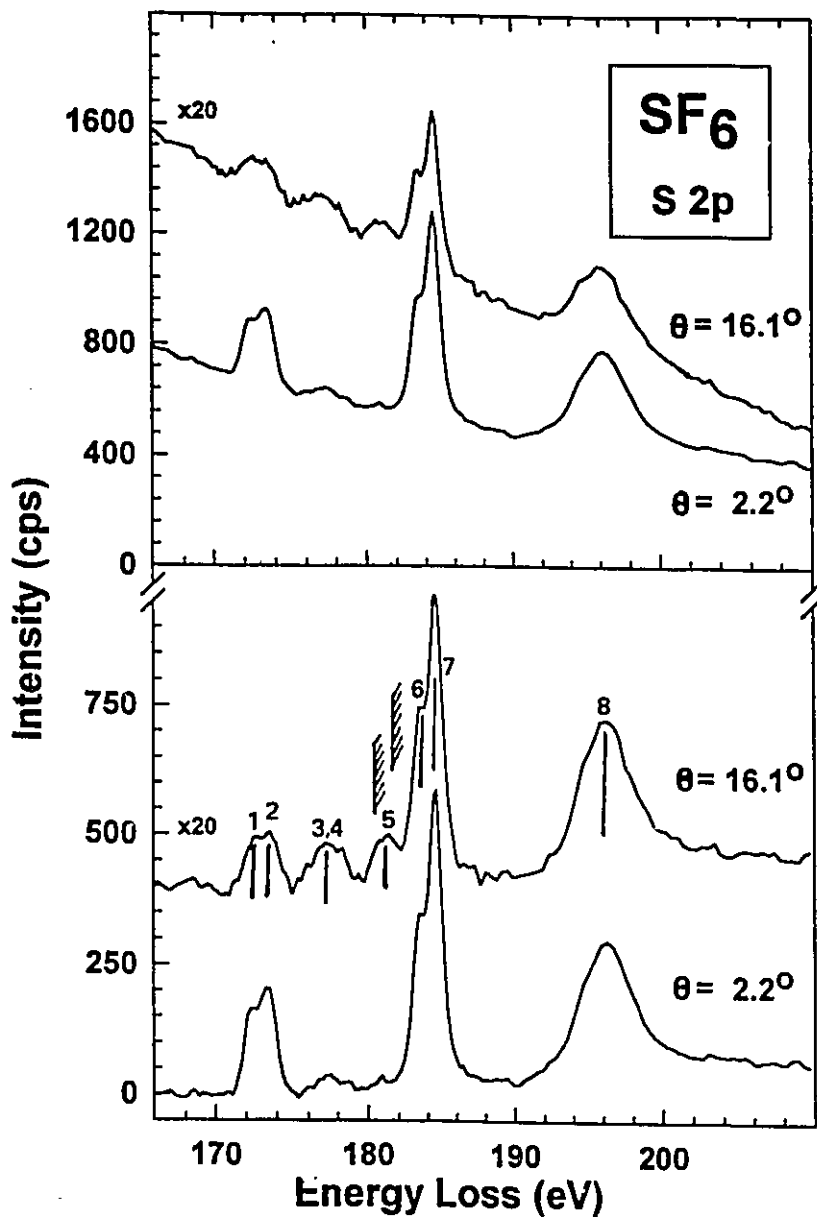


Fig. 6.2 S 2p EELS spectra of  $\text{SF}_6$  recorded with 1400 eV impact energy, the indicated scattering angles ( $\theta$ ) and 0.5 eV fwhm instrumental resolution. The upper two spectra are as-recorded data. The S 2p component, isolated by subtraction of an extrapolation of the underlying valence continuum is plotted on the bottom. The  $16^\circ$  spectrum has been multiplied by 20 and offset for clarity. The numbered features are tabulated in Table 6.2. Hatched lines represent onset of the ionisation continuum.

spectrum [TL91]. In addition, even at relatively small momentum transfer there is a broad underlying signal in the 175-178 eV region of the EELS spectrum which is not generally observed in photoabsorption [HB78, GKM77]. However, evidence of this feature has been observed in S 2p photoabsorption spectra [HS&93] which suggests that vibronic coupling is involved. This signal has been associated with the quadrupole-allowed, dipole-forbidden S 2p  $\rightarrow$   $t_{1u}$  excitation. Simultaneous excitation of either a  $t_{1u}$  or  $t_{2u}$  vibrational mode in the octahedral complex would break the centre of symmetry and render this excitation weakly dipole allowed.

The present dipole-regime spectra are consistent with all earlier EELS results [HB78, SB90]. The  $a_{1g}$  and  $t_{2g}$  features display a doublet structure with a splitting of 1.15(2) eV which is associated with the spin-orbit interaction of the S 2p<sup>5</sup> configuration. While variations of up to 0.03 eV are found in these values, the spin-orbit splitting does not vary systematically with momentum transfer (K) and thus these variations are attributed to statistical imprecision. The value obtained in this work for the spin-orbit splitting in these states is in agreement with that obtained by photoionization [SCT73] and photoabsorption studies [AT&86].

At large scattering angles where the momentum transfer becomes large and non-dipole excitations are expected to contribute more strongly, there are dramatic changes in the relative intensities of the core  $\rightarrow$  valence excitations. In particular the intensity of the feature at 177 eV ascribed to S 2p  $\rightarrow$   $t_{1u}$  excitations, increases considerably with respect to the three dipole-allowed bands. This is consistent with the dipole-forbidden, quadrupole-allowed character of the assigned transition [HB78]. The intensity of the  $a_{1g}$

resonance decreases relative to that of the two continuum resonances. In addition to these intensity redistributions, the large scattering angle spectrum clearly exhibits a non-dipole feature at 181 eV, which has also been observed by Harrison *et al.* [H86]. On close examination there are also hints of this signal in lower momentum transfer EELS spectra, but the existence of a state at this energy has not previously been claimed. The enhancement of the 181 eV signal with increasing momentum transfer is characteristic of a quadrupole transition.

This 'fifth state' is a rather surprising observation. According to the accepted minimal basis set *orbital* description, only four S 2p excitations to virtual valence levels are expected. However, when the S 2p spectrum is considered from a *state* perspective there are possible candidate states for which spectral signatures have not been identified. As outlined in Table 6.1 there are eleven states which arise from S 2p excitation to the four virtual valence orbitals. Among these, there are only TWO states which could be coupled to the ground state via a dipole-forbidden, quadrupole-allowed transition. A possible explanation is that the features at 177 and 181 eV correspond to these two states. Before adopting this interpretation, a number of alternative assignments must be considered. These alternatives, along with reasons for rejecting them are outlined in the remainder of this section.

#### Re-assignment of the $(t_{1u}(S\ 2p)^{-1}, t_{1u})$ State

One possibility is that the earlier assignments of the quadrupole S 2p  $\rightarrow$   $t_{1u}$  excitation to the 177 eV feature is incorrect and that the 181 eV signal is in fact this one-



electron excitation. The 177 eV feature could then be explained in terms of a quadrupole S 2p  $\rightarrow$  Rydberg transition, such as one of 2p  $\rightarrow$  4p character. However, one can argue rather strongly against this proposal in that the term value of the 177 eV signal traditionally assigned as the S 2p  $\rightarrow$   $t_{1u}$  excitation matches well to that of the dominant electric-dipole allowed signal in the S 2s spectra [HB78] (see Table 6.5).

Negative ion resonances, such as electron transmission spectroscopy (ETS), provide a probe of unoccupied electronic structure which complements core excitation. ETS for SF<sub>6</sub> [KBM79] supports the accepted assignments of the three dipole and one quadrupole S 2p spectral features. In particular, the relative energy spacing of the four ETS features matches reasonably well to those of dipole regime core excitation (EELS or XAS) spectra.

#### Triplet partner to the ( $t_{1u}(S\ 2p)^{-1}, t_{2g}$ ) State

The 181 eV signal is about 2 eV below that of the main  $t_{2g}$  resonance. This separation is a plausible magnitude for a singlet-triplet exchange splitting especially since large singlet-triplet splittings are generally associated with intense spin-conserving singlet excitations [FE&94, FKH94].

In order to investigate this possibility, S 2p spectrum was recorded with an impact energy of only 700 eV. Lowering the impact energy is more effective than increasing the scattering angle for enhancing spin-exchange excitations [FE&94, FKH94]. This was illustrated in the triplet state work presented in chapter four. As shown in Fig. 6.3, relative to the  $t_{2g}$  peak, the intensity of the 181 eV signal is the same or smaller at 700

eV, as compared to 1400 eV impact energy and approximately the same  $K^2$  value. This is rather strong evidence against the spin exchange transition hypothesis. On the other hand, the systematic increase in intensity with increasing momentum transfer is fully consistent with a spin-conserving electric quadrupole allowed transition.

#### Quadrupole transition to a double excitation state

While two-electron (core→valence plus valence→valence) excitations are generally rather weak, the inner-well localized character of the S 2p excited states could make it possible that a quadrupole-allowed double excitation could have considerable intensity. Plausible candidates would need to combine the HOMO → LUMO ( $t_{1g} \rightarrow a_{1g}$ ) excitation with the S 2p →  $a_{1g}$  excitation. Since the lowest energy electronic excited state of SF<sub>6</sub> is 9.6 eV, and the corresponding double excitation energy is generally somewhat larger, this places the lowest likely double excitation at (173 eV + 9.6 eV) or 182.6 eV. This is 1.6 eV above the 181 eV signal.

#### Enhanced threshold ionisation signal at large momentum transfer

When two gaussian lines are used to fit the 181 eV signal (see fig. 6.3), the lines lie remarkably close to the S 2p IPs of 180.4 and 181.6 eV determined by X-ray photoelectron spectroscopy [JBE84]. This, along with a suggestion of a high energy tail to the 181 eV signals, could suggest some type of enhanced tunnelling of very low energy electrons into the direct ionisation channel. Since the *time* for a large momentum transfer scattering event is much larger than that of a grazing, low momentum transfer collision

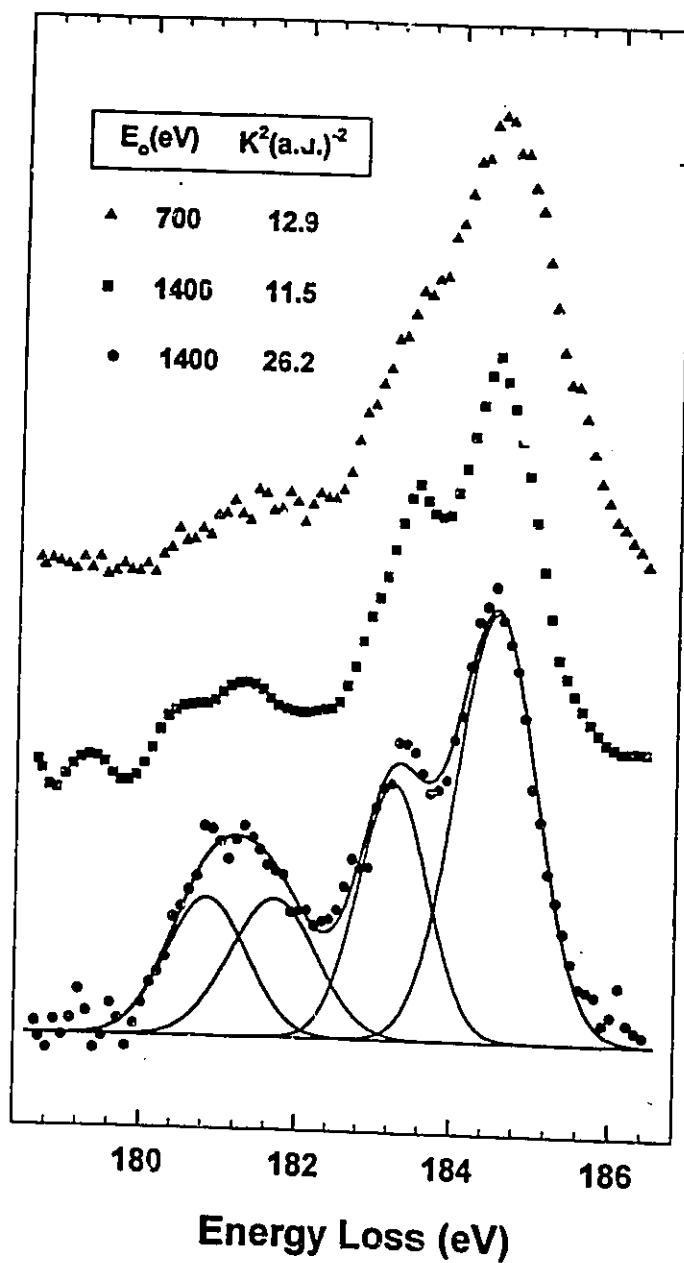


Fig. 6.3 Comparison of S 2p spectra of SF<sub>6</sub> in the region of the 181 eV feature, recorded at 1400 and 700 eV impact energy and  $K^2$  values of 12.9, 11.5 and 26.2 a.u.<sup>-2</sup>. A fit of four Gaussian lines to the 26 a.u.<sup>-2</sup> data is shown.

[SC&87], the probability for tunnelling should plausibly increase. However, if this was the case at threshold, it is difficult to understand why the continuum intensity would not be enhanced at all energies up to the top of the barrier. While the near continuum (180.4 - 190 eV) intensity does increase at increasing momentum transfer, there is a larger difference between the momentum transfer dependence for the 181 eV peak and the underlying 180-190 eV continuum signal. It is possible that the 181 eV signal corresponds to a component of the direct ionisation which is additionally enhanced at-threshold through a combination of post-collision interaction (PCI) effects [N77] and increased interaction time. Photoemission or electron-electron coincidence spectroscopy close to threshold might reveal direct evidence for a PCI like effect, in terms of shifts in the photoelectron energies. In the absence of more direct evidence, such a speculative interpretation cannot be supported.

Based on the above considerations, it appears that the 181 eV feature is most likely a quadrupole-allowed transition to one of the two quadrupole-coupled states associated with the  $(S\ 2p(t_{1u})^{-1}, t_{1u})$  configuration. It is then a matter of deciding whether the 177 and 181 eV states should be assigned as  $(E_g < T_{2g})$  or  $(T_{2g} < E_g)$ . If one considers the expected splittings for an electron in a 3d orbital in  $O_h$  symmetry then  $T_{2g}$  should fall below  $E_g$  and the 181 eV feature should be assigned as the  $E_g$  state. Ab initio calculations would be useful in confirming this tentative assignment.

#### 6.2.2.3 S 2s: Spectral presentation and analysis

Figure 6.4 compares ISEEL spectra of  $SF_6$  in the S 2s region, recorded using both dipole ( $E_0=1500$  eV,  $\theta=0^\circ$ ) and strongly non-dipole ( $E_0=1500$  eV,  $\theta=15^\circ$ ) conditions.

The energies, term values and spectral assignments are presented in Tables 6.3 and 6.5. For each spectrum, both as-recorded and background subtracted data is presented. Since the S 2s signal is relatively weak and the underlying S 2p continuum intensity quite strong, very good quality data is required to allow examination of the S 2s spectra with adequate statistics.

As outlined in Table 6.1 and noted in many previous discussions of the core spectroscopy of SF<sub>6</sub>, there is a complementarity between the selection rules for S 2p and S 2s excitation. Excitation to levels which are dipole allowed from S 2p are dipole forbidden from S 2s and vice-versa. Thus the only electric-dipole allowed transition is that to the (S 2s<sup>-1</sup>, t<sub>1u</sub>) <sup>1</sup>T<sub>1u</sub> state. Photoabsorption spectra [L72] detect only this feature. In contrast, even in the dipole scattering regime, EELS spectra exhibit relatively strong contributions from dipole-forbidden, quadrupole-allowed S 2s excitations to the t<sub>2g</sub> and e<sub>g</sub>. Very careful examination of the 0° spectrum in Fig. 6.4 even reveals a weak shoulder at 237 eV, which, after comparison to the dipole spectrum, can be associated with a weak S 2s → a<sub>1g</sub> excitation.

At large momentum transfer conditions the intensity of all S 2s features declines relative to the underlying S 2p ionisation continuum. This makes it difficult to detect the weak signal on a strong background, but a good quality spectrum at 15° scattering angle was achieved after 150 hours of signal averaging. This spectrum exhibits a great increase in intensity of the quadrupole excitations to the a<sub>1g</sub>, t<sub>2g</sub> and e<sub>g</sub> orbitals, with the most dramatic change being the clear detection of the a<sub>1g</sub> feature at 237 eV. Since the S 2s orbital is non-degenerate, only a single excited state is associated with each (S 2s<sup>-1</sup>, UMO)

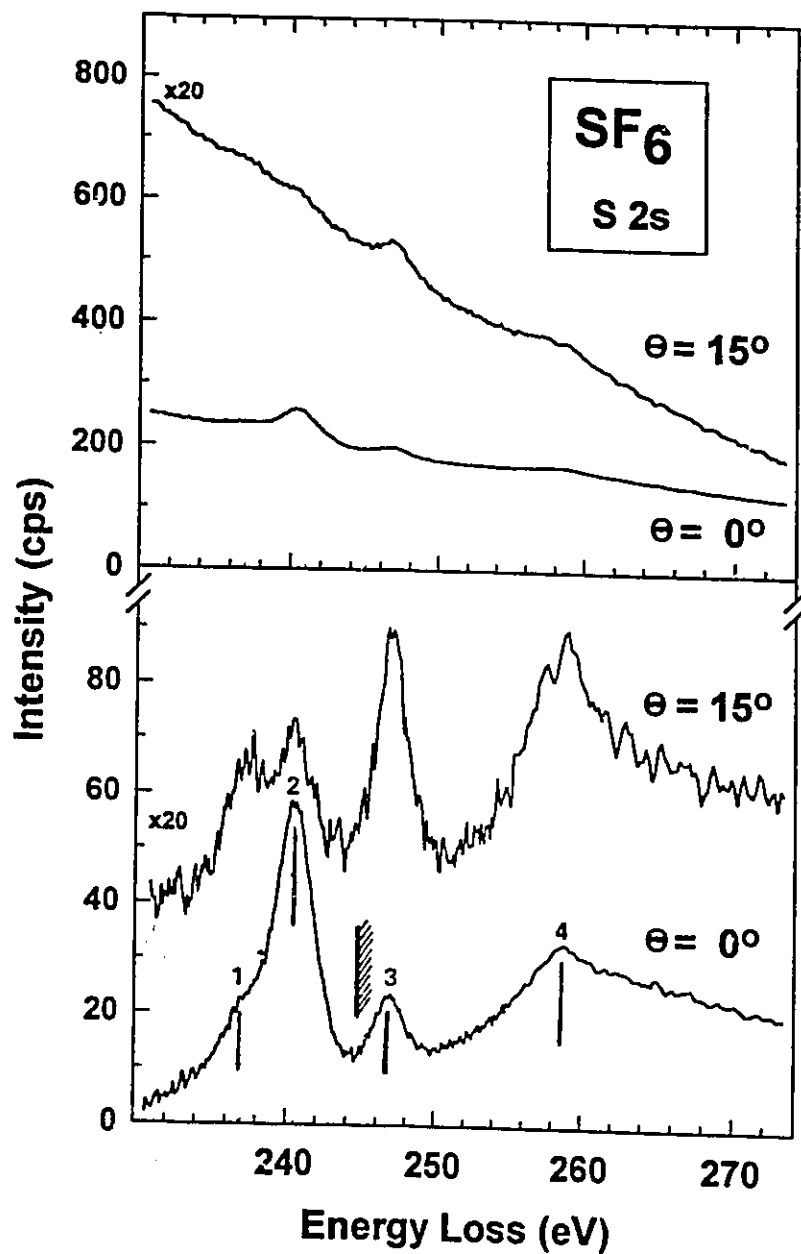


Fig. 6.4 S 2s EELS spectra of  $\text{SF}_6$  recorded with 1500 eV impact energy and the indicated angles. The upper spectra are as-recorded data. The S 2s component, isolated by subtraction of an extrapolation of the underlying S 2p continuum, is displayed on the bottom. The  $15^\circ$  spectrum has been multiplied by 20 and offset for clarity. The numbered features are tabulated in Table 6.3. Hatched lines represent onset of the ionisation continuum.

**Table 6.3** Energies (eV), term values and assignments of features in the S 2s electron energy-loss spectrum of SF<sub>6</sub>

Feature <sup>a)</sup>	Energy loss ( $\pm 0.1$ eV)	Term Value (eV)	Assignment
1	236.9	7.8	(S 2s <sup>-1</sup> , 6a <sub>1g</sub> ) <sup>1</sup> A <sub>1g</sub>
2	240.5	4.2	(S 2s <sup>-1</sup> , 6t <sub>1u</sub> ) <sup>1</sup> T <sub>1u</sub>
IP <sup>b)</sup>	244.7		
3	246.7	-2.0	(S 2s <sup>-1</sup> , 2t <sub>2g</sub> ) <sup>1</sup> T <sub>2g</sub>
4	259.0	-14.3	(S 2s <sup>-1</sup> , 4e <sub>g</sub> ) <sup>1</sup> E <sub>g</sub>

a) From Fig. 6.4

b) From XPS [JBE84]

**Table 6.4** Energies (eV), term values and assignments of features in the F 1s electron energy-loss spectrum of SF<sub>6</sub>

Feature <sup>a)</sup>	Energy loss ( $\pm 0.2$ eV)	Term Value (eV)	Assignment
1	688.0	(6.6)	6 a <sub>1g</sub>
2	692.6 (sh)	(2.0)	
3	694.6	0	6t <sub>1u</sub>
IP <sup>b)</sup>	694.6	0	
4	699.1	(-4.5)	2t <sub>2g</sub>
5	712.2	(-17.6)	4e <sub>g</sub>

a) From Fig. 6.5

b) From XPS [JBE84]

configuration. Thus, there can be no relationship between the 237 eV S 2s feature and the new 181 eV S 2p feature, even though the 3.6 eV separation from the 240.5 eV ( $S\ 2s^{-1}, t_{1u}$ ) state is similar to that of 3.5 eV between the  $E_g$  and  $T_{2g}$  states associated with the ( $S\ 2p^{-1}, t_{1u}$ ) configuration. Based on its term value and quadrupole character we attribute this feature to the  $S\ 2s \rightarrow a_{1g}$  excitation.

The term values for these non-dipole S 2s features are in reasonable agreement with those reported for the S 1s spectrum and with the term values for their dipole counterparts in the S 2p spectrum (see table 6.5). Poorer agreement is found with the F 1s term values, consistent with differing core hole relaxation effects when the site of the core hole changes.

#### 6.2.2.4 F 1s Spectra Presentation and Analysis

Fig. 6.5 compares ISEEL spectra of the F 1s region of  $SF_6$  recorded using McFALRES under dipole ( $E_0=3200\text{ eV}$ ,  $\theta \approx 2^\circ$ ) and non-dipole ( $E_0=1500\text{ eV}$ ,  $\theta \approx 10^\circ$ ) conditions. The momentum transfer in each case corresponds to  $\approx 4\text{ a.u.}^{-2}$  and  $\approx 9\text{ a.u.}^{-2}$ , respectively. It must be noted that these are best estimates only as it is difficult to accurately determine the scattering angle for McFALRES used to acquire the F 1s spectra. The energies, term values and spectral assignments are presented in Table 6.4. The absolute energy scale was calibrated using the energy of the  $F\ 1s \rightarrow a_{1g}$  transition at 688.0 eV reported by [HB78]. A linear background has been subtracted from both spectra for presentation.

In contrast to the S 2p and S 2s edges where there are dipole forbidden states,



Table 6.5 Comparison of Term Values for S 2p, S 2s, S 1s and F 1s core excitations

upper orbital	S 2p <sup>a</sup>	S 2s	S 1s <sup>b</sup>	F 1s <sup>c</sup>
a <sub>1g</sub>	8.0	7.8	8.1	6.6
t <sub>1u</sub>	1.8 <sup>d</sup>	4.2	4.1	2.0
t <sub>2g</sub>	-3.2	-2.0	? <sup>e</sup>	-4.5
e <sub>g</sub>	-16.2	-14.3	? <sup>e</sup>	-17.6

a. Average of S 2p<sub>3/2</sub> and S<sub>1/2</sub> values

b. from [RB&92]

c. from [HB78], these from [VZF72]

d. average of the features assigned to the T<sub>2g</sub> and E<sub>g</sub> states. Note that the term value for the lower energy (177 eV) t<sub>1u</sub> feature is 3.6 eV, in better agreement with the term values for the t<sub>1u</sub> feature in the S 2s and S 1s spectra.

e. Features were attributed to S 1s excitations to these orbitals in early work but photoemission partial cross-section studies [FL&86] suggest the continuum features so-assigned are actually shake-up features. No non-dipole ISEELS has been carried out in the S 1s region .

Table 6.6 Energies, widths and line shapes for the curve fit analysis of the S 2p spectra

State	E (eV)	width (eV)	Line-type
<sup>1</sup> T <sub>1u</sub> (a <sub>1g</sub> ) - 3/2	172.29	0.96	Gaussian
<sup>1</sup> T <sub>1u</sub> (a <sub>1g</sub> ) - 1/2	173.43	1.18	Gaussian
<sup>1</sup> T <sub>2g</sub> (t <sub>1u</sub> )	180.95	1.14	Gaussian
continuum-1	180.26	-	Arctangent
<sup>1</sup> E <sub>g</sub> (t <sub>1u</sub> )	177.43	2.03	Gaussian
<sup>1</sup> T <sub>1u</sub> (t <sub>2g</sub> ) - 3/2	183.34	0.60 (Gaussian) 0.71 (Lorentzian)	Voigt
<sup>1</sup> T <sub>1u</sub> (t <sub>2g</sub> ) - 1/2	184.52	0.60 (Gaussian) 0.93 (Lorentzian)	Voigt
continuum -2	192.71	-	Arctangent
<sup>1</sup> T <sub>1u</sub> (e <sub>g</sub> )	196.21	3.03 (Gaussian) 1.31 (Lorentzian)	Voigt

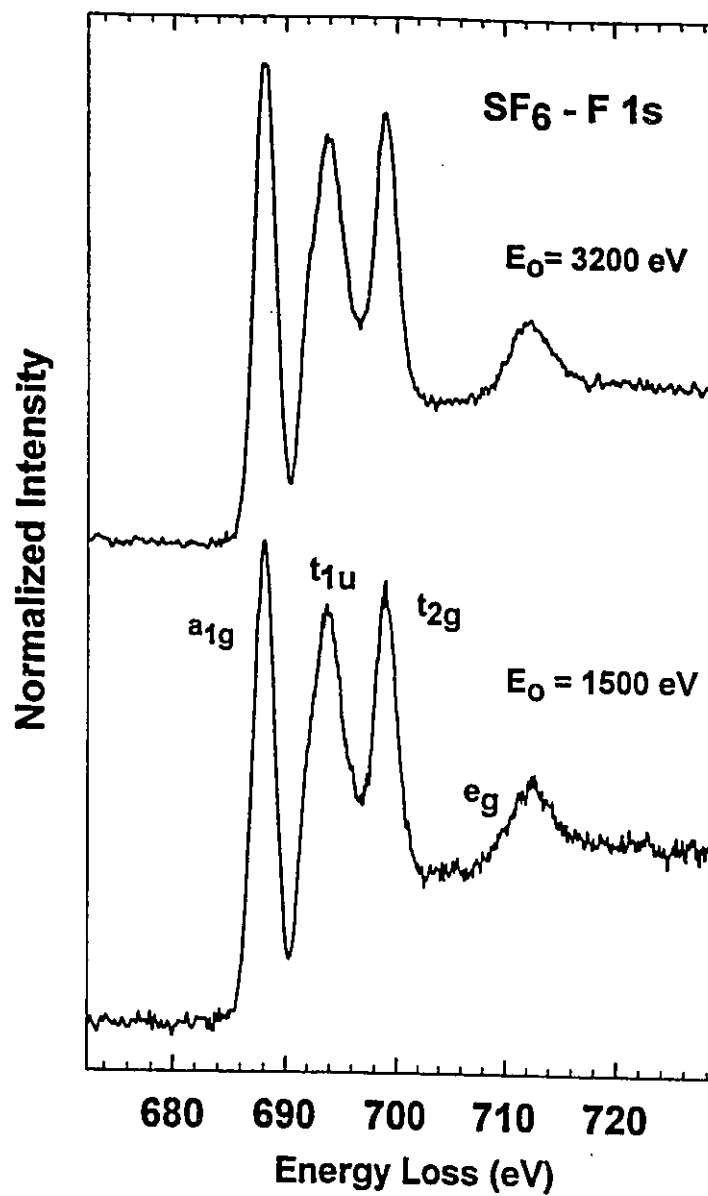


Fig. 6.5 F 1s EELS spectra of SF<sub>6</sub> recorded with 1500 eV impact energy ( $\theta \approx 10^\circ$ ) and 3500 eV impact energy ( $\theta \approx 2^\circ$ ).

there are electric-dipole excitations from F 1s orbitals to all four virtual valence orbitals. This is due to the fact that the initial F 1s orbitals include both gerade ( $2a_{1g}$ ,  $1e_g$ ) and ungerade ( $1t_{1u}$ ) symmetries. There will thus be a dipole allowed transition to each final orbital. Further, at large momentum transfer it is reasonable to suppose that these dipole allowed components will dominate over the non-dipole components in intensity. Thus one does not expect to see as dramatic changes between dipole and non-dipole ISEELS.

### 6.3 Generalised Oscillator Strengths for the S 2p States of SF<sub>6</sub>

Though the potential of EELS to provide additional spectroscopic information has been known for years, there have been very few systematic measurements of the GOS for inner-shell excitation. Inner shell GOS determinations reported in the literature include those for CO<sub>2</sub>, N<sub>2</sub>, NO, N<sub>2</sub>O, NH<sub>3</sub> and some chlorofluoromethanes [CF&87, BBS91, MB&94, SK&82, YL94b]. Ying *et al.* [YML93] have recently reported GOS curves for specific S 2p excited states of SF<sub>6</sub> over a limited K<sup>2</sup> range (up to 6 a.u.<sup>2</sup>). Their results were derived using peak intensities, as opposed to peak areas, however. Treatment of the McVAHRES data using the procedures of Ying *et al.* should allow a valid comparison of the S 2p GOS results in the future.

In this section, GOS determinations for specific S 2p excited states are presented, based on angle-resolved measurements for SF<sub>6</sub> acquired using McVAHRES. Experimental tests have been carried out to ensure that the impact energy used (1400 eV) is sufficiently high that the Bethe-Born approximation is valid.

### 6.3.1 Experimental Details

The spectra were acquired using acquisition method one which is discussed in detail in chapter 5. The S 2p spectra were acquired in six multi-angle measurement blocks, each of which covered a number of different scattering angles in the range  $1^\circ$  -  $25^\circ$ . An impact energy ( $E_0$ ) of 1400 eV was used. The angles within the measurement blocks were chosen with overlap to allow cross-referencing. The chamber pressure was typically  $2 \times 10^{-5}$  torr during measurements with an estimated ten-fold enhancement of the gas density in the region of the jet.

The spectra reported in this section are sums of a number of individual spectra each of which had been signal averaged in both energy loss and angle for a period of several hours. The common average counts per point criterion was employed, as discussed on chapters 3 and 5, to provide similar statistical precision in spite of decreasing cross sections at increasing scattering angle. The angles for measurement were chosen to give a suitable spacing of points in  $K^2$  space.

The instrumental energy resolution at the chosen monochromator and analyzer pass energies of 70 eV, was 0.5 eV full width at half maximum (FWHM). Based on the reproducibility of the spin-orbit split lineshapes for the  $a_{1g}$  and  $t_{2g}$  resonances, the experimental resolution did not change by more than 5% over the whole series of measurements using 1400 eV impact energy.

### 6.3.2 Validity of the first Born approximation

In order to make a valid GOS measurement it is important that the impact energy is sufficiently large that the first Born approximation (and thus the Bethe-Born GOS analysis) is valid. These considerations were discussed in chapter 5, section 5.2.1 using as an example three S 2p spectra of SF<sub>6</sub> for which the scattering conditions corresponded to  $K^2 = 8 \text{ au}^2$ . The (E<sub>0</sub>, θ) values, specific to this experiment, were (1000 eV, 18.9°), (1400 eV, 16.1°) and (1700 eV, 14.6°). The constancy of the spectral shape among these three spectra (within the limitations imposed by statistical precision - refer to chapter 5, section 5.2.1) was taken as direct evidence that the first Born approximation [LSD69] and thus the GOS concept is valid at the 1400 eV impact energy used for these measurements.

### 6.3.3 Data Processing for Quantitative GOS Determination

The procedures involved in deriving relative GOS functions from the raw spectral data have been discussed in detail in chapter 5, section 5.3 using as an example the SF<sub>6</sub> data pertinent to this discussion. For the SF<sub>6</sub> work described in this chapter, these procedures were performed most competently by Mrs. Cassia Turci with the aid of Dr. T. Tyliczszak. Re-iterating the important steps, the non-gas jet background signal was determined for all scattering angles sampled up to 16° (see figures 5.6 and 5.8) and subtracted from the total signal. The contribution from the underlying valence-shell ionisation continuum was removed by subtracting a smooth curve determined from a curve fit of the function  $a(E-b)^c$  to the signal between 154 and 170 eV, below the S 2p → a<sub>1g</sub> peak (see figure 5.8). This is an important step since the relative amounts of

underlying valence continuum change greatly with changing scattering angle, due to the fact that the valence Compton peak [LCS89] passes through the S 2p region, with a maximum intensity around  $K^2 = 13 \text{ a.u.}^{-2}$

After removal of the non-jet background and the valence ionisation signal, the isolated S 2p spectra were then subjected to an extensive curve fit analysis (see figure 5.9), the details of which were presented in detail in chapter 5, section 5.3.1. The model for the S 2p spectrum consisted of a combination of Gaussian and Lorentzian peak shapes and two arc tangent edge functions, chosen to match the spectral interpretation. A multi-file analysis procedure (the MGAUSS algorithm, see Appendix B and [AT&94]) was used to ensure that all spectra were fit with the same model. While all parameters were optimised over a set of up to 15 energy loss spectra, only the peak and continuum amplitudes were allowed to vary independently from spectrum to spectrum. The specific width, energy, etc. parameters were discussed in chapter 5, section 5.3.1 and summarised in Table 6.6. Accounting for differences in resolution, the linewidth and energy position parameters obtained from the fit procedure performed using the spectral model described above are in good agreement with those of Hudson *et al.* [HS&93] who used a similar spectral model to fit their S 2p photoabsorption spectrum of SF<sub>6</sub>.

#### 6.3.4 Absolute GOS and Error Treatment

The method used for error estimation has been discussed in chapter 5, section 5.3.3. In this section, however, the error associated with absolute normalisation of the relative GOS curves is explicitly considered. Since the relative GOS functions are single

point normalised to the corresponding OOS after extrapolation to  $K^2 = 0$ , discrepancies in the OOS values will result in an uncertainty in the resulting absolute GOS. As can be seen from Table 6.7, there are discrepancies in the literature OOS values [D72, VZ72]. This is compounded in some cases by the fact that the S 2p-isolated OOS were not reported and thus had to be derived by digitization and integration. For each of the  $a_{1g}$  and  $t_{2g}$  features, all possible literature OOS values that could be found were used to determine a set of normalisation factors, N (chapter 5, equation 5.4). These were obtained by dividing the extrapolated relative GOS value at  $K^2 = 0$  by each available OOS optical value. The extrapolation procedure involved extending the best fit GOS curve (derived using the BAN algorithm, see Appendix B) to  $K^2 = 0$ . To a good approximation, the GOS was nearly linear over the extrapolation range and thus a straight line could be used to obtain the  $K^2 = 0$ , relative GOS value. The error in the extrapolation method was estimated from several trials and its magnitude ranged between 2% and 30% (in the case of the  ${}^1T_{2g}$  state). The standard deviation of the mean normalisation factor N was taken as a measure of uncertainty (i.e.  $\Delta N$ ) with a range between 3% and 10%.

The average value of the two mean N values derived from extrapolation of the  $a_{1g}$  and  $t_{2g}$  GOS curves was used to normalise the relative GOS curves of all five S 2p features. The two mean normalisation factors determined separately for the  $a_{1g}$  and  $t_{2g}$  features agree to within 1% (the values were 6536, 6462 respectively) when the continuum underlying the  $t_{2g}$  feature is accounted for in the curve fitting and peak area determination procedures. Failure to account for the underlying continuum contribution when determining the GOS (extrapolated to  $K^2 = 0$ ) for the  $t_{2g}$  feature results in a mean

Table 6.7 Optical Oscillator Strengths

State	this work	Ying et al <sup>(a)</sup>	Optical <sup>(b,c)</sup>
${}^1T_{1u}(a_{1g})$	$3.9 \pm 0.2$	3.7	3.8 <sup>(b)</sup> 3.9 <sup>(c)</sup>
${}^1T_{2g}(t_{1u})$	$0.3 \pm 0.1$		
${}^1E_g(t_{1u})$	0(1)	$0.50 \pm 0.06$	0.35
${}^1T_{1u}(t_{2g})$	$10.6 \pm 0.5$	11.5	10.4 <sup>(b)</sup> 10.8 <sup>(c)</sup>
${}^1T_{1u}(e_g)$	$9.2 \pm 0.9$	7.8	7.7 <sup>(b)</sup> 9.0 <sup>(c)</sup>

a. [YML93]

b [D72]

c [VZ72] these from [ZF66]



normalisation factor  $N$  that is 30% greater than that determined for the  $a_{1g}$  feature.

The optical values obtained by single point normalisation of the extrapolated relative GOS functions (from McVAHRES) using the mean factor  $N$  discussed above are listed in Table 6.7. The overall error in the absolute normalisation was taken from the error in  $N$  and the extrapolation method discussed above added in quadrature. For the three dipole allowed features, this error amounted to 5% for the  $a_{1g}$  and  $t_{2g}$  features and 10% for the  $e_g$  feature. Owing to the difficulty of the extrapolation procedure for the two dipole forbidden features, the uncertainty in the normalisation was of the order of 30%.

The uncertainties in the pressure, incident current, statistics and fit model, which are treated as uncorrelated quantities in determining the error associated with peak area determination ( $\Delta\text{Area}$  in chapter 5, equation 5.4), were taken to be 2%, 1%, 1% and between 1 and 30% respectively for the experiments in this chapter. The error associated with the fit model was feature-dependent, and ranged from 1% for  $t_{2g}$  to a maximum of 30% for the new feature (at low  $K^2$  values). The error in  $K^2$  was based on an uncertainty in the scattering angle of  $\pm 0.25^\circ$  degrees.

### 6.3.5 GOS curves for the 5 S 2p features and the continua

The GOS in the  $K^2$  range from 0.6 to 19 a.u.<sup>-2</sup> for the three dipole-allowed transitions are presented in Fig. 6.6. Fig. 6.7 presents the GOS results for the two quadrupole states, while Fig. 6.8 presents the integrated areas for the lower energy (180.3 - 190.3 eV) and higher energy (192.7 - 202.7 eV) regions of the S 2p ionisation continuum. While not strictly correct, a plausible interpretation of these signals would

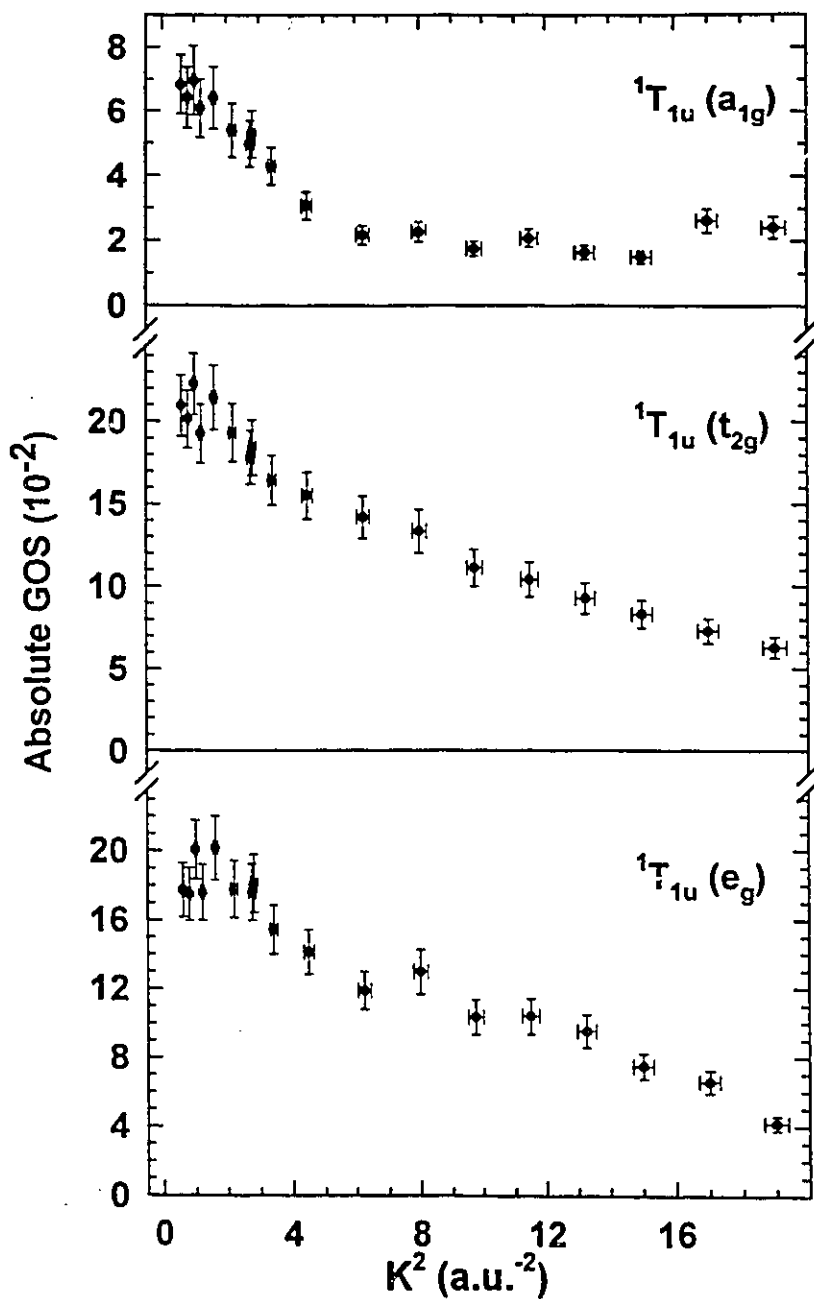


Fig. 6.6 GOS curves for the  ${}^1T_{1u}(a_{1g})$ ,  ${}^1T_{1u}(t_{2g})$ , and  ${}^1T_{1u}(e_g)$  dipole-coupled S 2p excited states derived from the experimental data as described in the text.

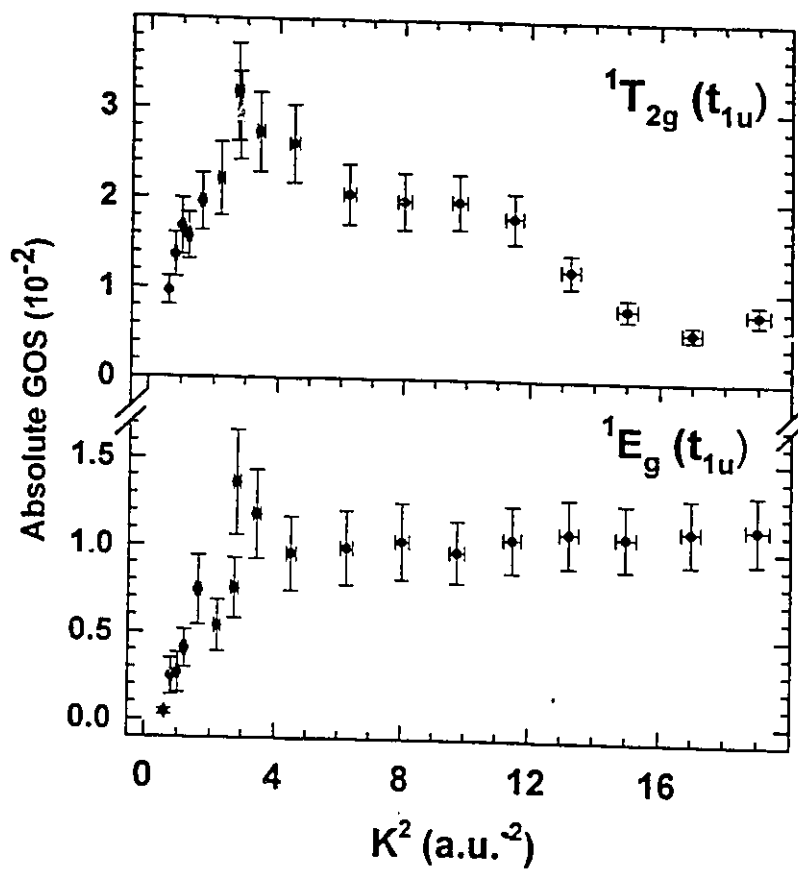


Fig. 6.7 GOS curves for the  ${}^1T_{2g}(t_{1u})$  (177 eV) and  ${}^1E_g(t_{1u})$  (181 eV) quadrupole-coupled S 2p excited states.

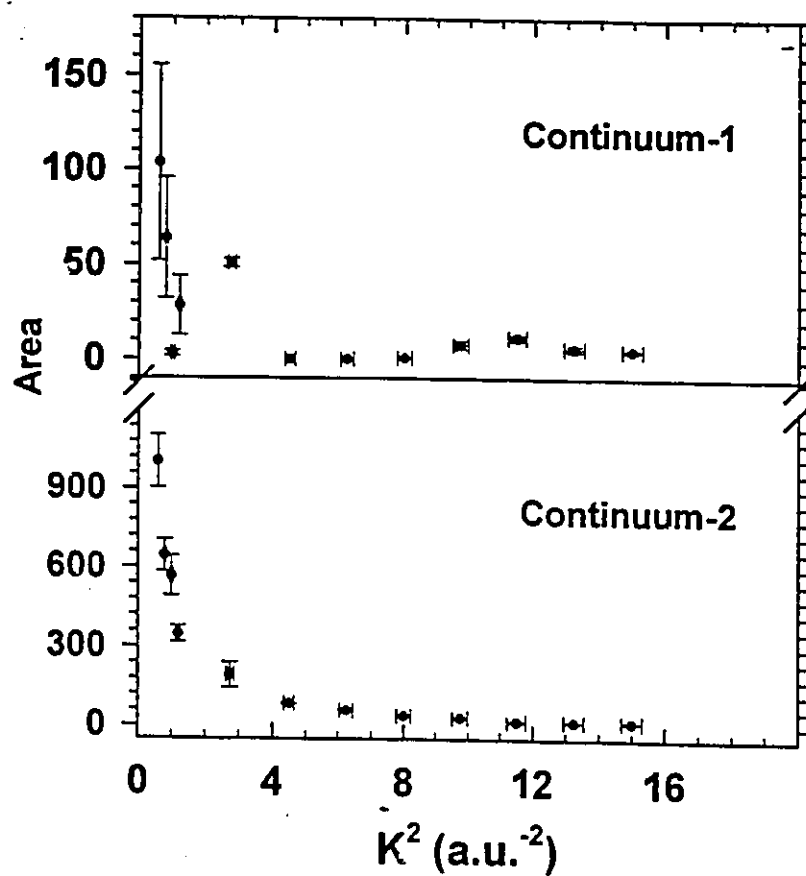


Fig. 6.8 Integrated areas for two arctangent components used to represent the low energy (180.3 - 190.3 eV) and higher energy (192.7 - 202.7 eV) portions of the S 2p continuum.

assign continuum 1 as the "tunnelled", below-barrier ionization while continuum 2 corresponds to the direct, above-barrier ionization (see Fig. 6.1).

Figs. 6.6 and 6.7 demonstrate that dipole-allowed and dipole forbidden transitions have qualitatively different GOS curves. In particular, the GOS for the dipole-allowed transitions [S 2p(2t<sub>1u</sub>)→6a<sub>1g</sub>, S 2p(2t<sub>1u</sub>)→2t<sub>2g</sub> and S 2p(2t<sub>1u</sub>)→4e<sub>g</sub>] decrease relatively smoothly from a maximum at  $K^2 = 0$  (see Table 6.7 for optical values). In contrast, the GOS curves for the dipole-forbidden transitions [S 2p(2t<sub>1u</sub>)→6t<sub>1u</sub>] increase with increasing momentum transfer and extrapolate to a minimum value at zero momentum transfer, as expected for electronically-dipole forbidden transitions. The GOS for the 177 eV state appears to be non-zero in the limit of zero momentum transfer, as evidenced by the non-zero OOS value in Table 6.7 for this state and the OOS attributed to vibronic coupling. This was noted in the S 2p photoabsorption spectrum of Hudson *et al.* [HS&93].

### Summary

Energy loss spectra of SF<sub>6</sub> recorded under dipole and strongly non-dipole conditions in the region of S 2p, S 2s and F 1s excitation have been obtained. In section 6.2, a non-dipole S 2p electronic excited state of SF<sub>6</sub> was observed at 181 eV and the non-dipole S 2s states more clearly identified than in earlier work. The F 1s spectra showed no significant intensity re-distribution when recorded under both dipole and non-dipole conditions.

In section 6.3, the generalised oscillator strengths (GOS) for  $0 < K^2 < 20 \text{ a.u.}^{-2}$

were derived for S 2p excitations in SF<sub>6</sub>. The procedures used to obtain these results have been presented in detail.

## Chapter 7

### Concluding Remarks

A new electron spectrometer (McVAHRES), which incorporates both variable impact energy and variable scattering angle, has been constructed and commissioned. The flexibility of the instrument design allowed spectroscopic measurements of both inner shell and valence shell electronic transitions under both dipole and non-dipole conditions.

The complex electron optics system was designed with the aid of computer simulations. The in-house built, sophisticated electronics system is highly computer-interfaced. This allowed a high degree of flexibility and stability with regards to control and acquisition. In addition, this enabled the use of simplex optimisation routines to lend a degree of automated tuning.

The performance evaluation and characterisation of McVAHRES was carried out using well-known gas phase species, namely  $N_2$ , CO, He and  $SF_6$ , whose energy loss and photoabsorption spectra are widely reported in the literature. Comparing the operational mode(s) used in practice (i.e. lens voltages), the agreement with the mode predicted by computer simulations was poor. This was attributed to the discovery of alternate operating modes during experimental optimisation routines that were not investigated theoretically. This is due to the difficulty of exploring all possible operating modes via computer simulations. In terms of resolution, transmission and angle-dependent and impact energy-

dependent scanning, the instrument in practice approached our original ambitious expectations most satisfactorily.

Having developed confidence in the instrument's capabilities through the characterisation and performance evaluation procedures, a series of new spectroscopic investigations were carried out. Two fundamentally different types of experiments were performed which were aimed at furthering the understanding of dipole and spin forbidden electronic transitions which accompany scattering conditions involving significant momentum transfer.

Focussing on spin forbidden transitions, near-threshold impact energy experiments were carried out in order to investigate C 1s core excited triplet states of CO, C<sub>2</sub>H<sub>4</sub>, C<sub>2</sub>H<sub>2</sub> and C<sub>6</sub>H<sub>6</sub> (discussed in chapter 4 (a)). The singlet-triplet splittings of the hydrocarbon species were documented for the first time. A strong correlation between singlet-triplet splittings and oscillator strengths for the 1s → π\* transitions was noted and rationalised in terms of the dependence of both factors on the spatial overlap of 1s and π\* wavefunctions.

An extension of this theme led to the investigation of the momentum transfer dependence and vibrational structure of the (C 1s, π\*) <sup>3</sup>Π state of CO (discussed in chapter 4 (b)). A difference in the Franck-Condon factors between the singlet and triplet states indicated that the two states have different potential curves. This was supported by the results of high level ab initio SCF-CI calculations. The breakdown of the Bethe-Born theory under low impact energy conditions was also illustrated. These results also serve as a useful gauge for evaluating quantum mechanical calculations.



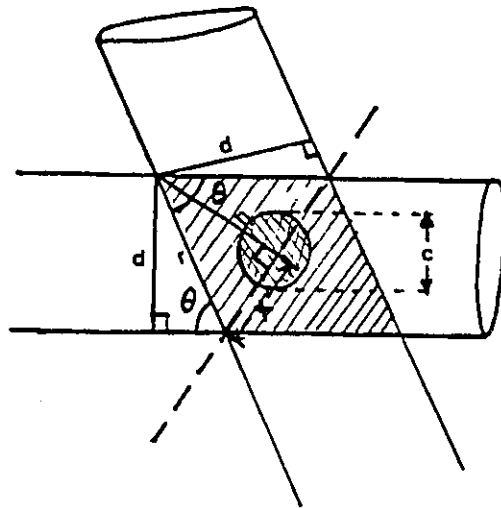
In the second major set of experiments, a systematic procedure was developed for the determination of GOS as a function of momentum transfer. This method was then applied in the determination of the GOS for the S 2p edge of SF<sub>6</sub> in the K<sup>2</sup> range 1 - 26 a.u.<sup>-2</sup>. These results extend considerably the work of Ying *et al.* reported in the literature [YML93].

In addition to the GOS profiles, a non-dipole feature at 181 eV in the S 2p spectrum was observed which displayed characteristic quadrupolar momentum transfer behaviour. It has been assigned to the (S 2p (t<sub>1u</sub>)<sup>-1</sup>, t<sub>1u</sub>) <sup>1</sup>E<sub>g</sub> state. It was also observed in this work that the S 2p and 2s spectra displayed large intensity re-distributions upon going from dipole to non-dipole experimental conditions. In contrast, the F 1s spectrum showed a constancy of spectral shape and intensity under both dipole and non-dipole conditions. This was rationalised in terms of selection rules based upon the symmetries of the initial and final states at each edge. Perhaps the most interesting aspect of this work is that additional spectroscopic information was derived from a system (SF<sub>6</sub>) that has been very well characterised over the years. This serves in part as a demonstration of the success of the new instrument, and the procedures developed here will be used in all future momentum transfer studies using McVAHRES.

In closing, it is noted that three major instrumental improvements will be made in the future that should dramatically enhance the capability of this instrument. These are: parallel detection, a tandem hemispherical analyser system and differential pumping of the vacuum chamber. There are a host of interesting experiments that can be envisaged in the near the future. One appropriate experiment would be derivation of the GOS (and

Bethe surfaces) profiles for features in the S 2s spectrum of SF<sub>6</sub> (which would compliment the work in chapter six) and other highly symmetric gas phase species. Highly symmetric species would be most favourable in terms of illustrating the violation of optical selection rules at increasing momentum transfer. Another challenging experiment would be investigation of the dipole forbidden (N1s  $\sigma_g^{-1}$ , 2p  $\pi_g$ )  $^1\Pi_g$  state in N<sub>2</sub>, which would demand large K<sup>2</sup> conditions, good transmission and < 100 meV resolution. Such work could provide insight into the question of core hole localisation.

Appendix A: Derivation of the Geometrical Overlap Correction Factor



From the above diagram, one can derive the area of the parallelogram as a function of  $\theta$  (assuming that the diameters of the cylinders,  $d$ , are equal).

- 1)  $d/r = \sin\theta$ , and thus  $r = d/\sin\theta$
- 2)  $x/r = \sin(\theta/2)$  and  $h/r = \cos(\theta/2)$ , and thus substitution for  $r$  yields:  

$$x = \{d\sin(\theta/2)\}/\sin\theta \quad \text{and} \quad h = \{d\cos(\theta/2)\}/\sin\theta$$
- 3) The area of the parallelogram is  $4 ( \frac{1}{2}hx ) = 2hx$ , and thus substitution for  $x$  and  $h$  yields:

$$\begin{aligned} \text{Area} &= \{2d\sin(\theta/2) \times (d\cos(\theta/2))\}/\{\sin\theta\}^2 \\ &= \{2d^2\sin(\theta/2)\cos(\theta/2)\}/\{\sin\theta\}^2 \end{aligned}$$

- 4) Using the familiar half angle formula, this expression reduces to:

$$\text{Area} = d^2/\sin\theta$$

- 5) For unequal diameters of the incident beam ( $d_1$ ) and analyser view cone ( $d_2$ ), it is a simple matter to show that the above expression becomes:

$$\text{Area} = d_1 d_2 / \sin\theta$$

- 6) Assuming: (i) a pressure differential  $a$  between the gas jet and surrounding interaction volume defined by the parallelogram above; and (ii) that the area of the gas jet component is  $C = \pi c^2$ , the final form of the correction factor,  $F$ , can be expressed as:

$$F = d_1 d_2 / a \sin\theta + C$$

## Appendix B

### Brief Description of Algorithms

All programs listed here are produced and distributed by:

Tolmar Instruments

397 East 25th St. Hamilton, Ont. L8V 3A9

Fax/Tel (905) 574-6887

#### 1) BAN - Data Analysis Program:

BAN is an interactive data analysis program oriented towards analysis of X-ray absorption spectra (near-edge and EXAFS), but applicable to a wide range of graphics oriented spectral analysis tasks. It operates on 640 K AT/386 (or better) systems with a math co-processor running DOS with a graphics card, graphics printer and a mouse. (NB PC/XT and non-coprocessor versions are possible by compilation with different compiler options). It is written in Microsoft Fortran (ver. 4.0) with all graphics performed with subroutines from the HALO-88 package (agent: Media Cybernetics, 8484 Georgia Ave., Silver Spring, MD 20910; Tel: (301) 495-3305).

The package, as it stands, can be configured for a range of graphics devices (Hercules mono, CGA, EGA, VGA), printers (a variety of Epson-compatible, 9- and 24-pin printers; HP LASER-jet; : see copies of HALO device driver descriptions) and

mice (2- and 3-button mice) through modifications to an ASCII file called BAN.SET which defines the HALO drivers to be used by BAN (see below). All of the FORTRAN source code for BAN is enclosed.

Data input is in the form of (x,y) pairs in either an ASCII or Binary file format, or in a format of up to 50 columns with one or more comment lines. The presence or absence of a first card with an integer indicating the number of points is also accommodated. The program can read directly files written by acquisition programs running at most synchrotron radiation beam lines. Output files are written as (x,y) pairs in either Binary or ASCII. All data manipulation routines are designed to work with variable x-data point spacing.

The program has 8 permanent and one working buffer, each capable of holding a 1024-point spectrum. Most operations that change a spectrum place the result in the working buffer No. 9.

### Data Manipulations

A wide range of data manipulations are supported:

#### **A. EXAFS analysis**

- background subtraction (spline, multi-smooth, exponential or power law nonlinear least square fits, linear)
- $E \leftrightarrow k$  transfer
- Fourier transform, back-transform with flexible apodisation
- single shell R, CN and DW analysis based on ratio method using (FEFF,

McKale and/or experimental phase shift and amplitude functions)

- simulation of EXAFS spectrum using theoretical tabulated functions.

#### **B. Restricted range analyses**

- multi-line Gaussian fit
- linear least-square fit
- polynomial spline fit

#### **C. Spectral manipulation**

- all math functions with 2 files and/or constants (+, -, \*, /)
- 1- and 2-point x-axis calibration
- log or exp conversion of x or y axis
- delete, truncate, append - region or single point
- integration and differentiation
- smoothing, running average, binning
- trigonometric conversion (sin, asin, tan, atan, cos)
- histogram of data
- sorting

#### **D. Presentation**

- comparison plotting of up to 9 files with very flexible rescaling:
- no rescale, auto rescale
- user-defined numerical limits
- graphics-defined window

- Cursor with continuous readout; areas

## II BGAUSS - Lineshape and Edge shape Fitting Program

BGAUSS is an interactive line fitting program. It can fit gaussian, lorentzian, true Voigt and Doniach-Sunjic line shapes as well as multiple arctan or error function edge shapes. Up to 40 parameters can be fit. The current version does not utilise the errors of individual experimental points during the fit procedure. The program can operate on AT/386/486 systems with a math co-processor running DOS, a graphics card, graphics printer and a mouse. It requires 400 Kb of free memory. (PC/XT and non-coprocessor versions are possible by compilation with different compiler options). It is written in Microsoft Fortran (ver. 4.01) with all graphics performed using subroutines from the HALO-88 package (agent: Media Cybernetics, 8484 Georgia Ave., Silver Spring, MD 20910; Tel: (301) 495-3305).

The package, as it stands, can be configured for a range of graphics devices (Hercules mono, CGA, EGA, VGA), printers (a variety of Epson-compatible, 9- and 24-pin printers; HP LASER-jet; : see copies of HALO device driver descriptions) and mice (2- and 3-button mice) through modifications to an ASCII file called BGAUSS.SET which defines the HALO drivers to be used by BGAUSS. All of the FORTRAN source code for BGAUSS is enclosed.

Data input is in the form of (x,y) pairs in either an ASCII or Binary file format or in a format of up to 40 columns with one or more comment lines. Output files are written as (x,y) pairs in either Binary or ASCII. An optional ASCII parameters file allows



many files to be fit with similar parameters. It is also possible to use the same fitting parameter for different lines. For example, one can fit the same lines with the same width or fit a gaussian line and lorentzian line using the same position and width for a Voigt line shape simulation.

### Available Line Shapes

The following line shapes are available for fitting:

- gaussian:  $f(E) = A \cdot \exp[-\ln 2 \cdot (E - E_0)^2 / (W/2)^2]$

- lorentzian:  $f(E) = A / (1 + (E - E_0)^2 / (W/2)^2)$

- voigt:  $f(E) = A \cdot \int_{-\infty}^{\infty} G(E, W_G, E_0) L(x, W_L, E_0) dx$

- Doniach-Sunjic:

$$f(E) = A \cdot \cos \left[ \pi \cdot a / 2 + (1 - a) \cdot \arctan((E - E_0) / (W/2)) / ((E - E_0)^2 + (W/2)^2)^{(1-a)/2} \right]$$

- error function edge:

$$f(E) = 1/2 \cdot A \cdot (1 + \operatorname{erf}(235.48 \cdot (E - E_0) / (W/2))) \cdot \exp(-1 \cdot \text{dec} \cdot (E - E_0))$$

- arctan function edge:

$$f(E) = A \cdot (1/2 + 1/\pi \cdot \arctan(2.3548 \cdot (E - E_0) / (W/2))) \cdot \exp(-1 \cdot \text{dec} \cdot (E - E_0))$$

### III) MGAUSS - Multiple File Lineshape and Edge shape Fitting Program

MGAUSS is similar to BGAUSS; the major difference is that it allows one to fit several data files simultaneously using a common fit parameters file.

## References

- A71 E.E. Anderson, Modern Physics and Quantum Mechanics, Toronto: Saunders Publishing Co., 1971.
- AF81 R. d' Agostino and D. L. Flamm, *J. Appl. Phys.* 52 (1981) 162.
- AM73 L.H. Auer and D. Mihalas, *Astrophys. J.* 184 (1973) 151.
- AT&86 B. M. Addison, K. H. Tan, G. M. Bancroft and F. Cerrina, *Chem. Phys. Lett.* 129 (1986) 468.
- AT&89 B. M. Addison, K. H. Tan, B. W. Yates, J. N. Cutler, G. M. Bancroft and J. S. Tse, *J. of Electron Spec. and Rel. Phen.* 48 (1989) 155.
- AT&94 A.P.Hitchcock, T. Tyliczszak, P. Aebi, X.H. Feng, Z.H. Lu, J.M. Baribeau and T.E. Jackman, *Surface Science* 301 (1994) 260.
- B13 N. Bohr, *Phil. Mag.* 25 (1913) 10.
- B15 N. Bohr, *Phil. Mag.* 30 (1915) 581.
- B30 H. Bethe, *Ann. Physik* 5 (1930) 325.
- B68 J.P. Bromberg, *J. Chem. Phys.* 50 (1968) 3906.
- BB92 R.S. Barbieri and R.A. Bonham, *Phys. Rev. A* 45 (1992) 7929.
- BBS91 H. M. Boechat Roberty, C. E. Bielschowsky and G. G. B. de Souza, *Physical Rev. A* 44 (1991) 1694.
- BD94 A. Baraldi and V.R. Dhanak, *J. Elec. Spec. Relat. Phenom.* 67 (1994) 211.

- BDK92 A. Baraldi, V.R. Dhanak and G.C. King, *Meas. Sci. Technol.* 3 (1992) 778.
- BH&72 B. D. Blechschmidt, R. Haensel, E. E. Koch, U. Nielsen and T. Sagawa, *Chem. Phys. Letters* 14 (1972) 33.
- BH81 C.E. Brion and A. Hamnett, offprints from The Excited State in Chemical Physics, Part 2, J.W. McGowan, editor. J. Wiley and Sons, 1981.
- BMN90 S. Bodeur, P. Millie, and I. Nenner, *Phys. Rev. A* 41 (1990) 252.
- BNH92 C.E. Bielschowsky, M.A.C. Nascimento and E. Hollauer, *Phys. Rev. A* 45 (1992) 7942.
- BNM86 S. Bodeur, I. Nenner and P. Millie, *Phys. Rev. A* 34 (1986) 2986.
- BT&87 J.D. Bozek, K. H. Tan, G. M. Bancroft and J. S. Tse, *Chem. Phys. Lett.* 138 (1987) 33.
- CC&92 W.F. Chan, G. Cooper, X. Guo and C.E. Brion, *Phys. Rev. A* 45 (1992) 1420 and W.F. Chan, G. Cooper, X. Guo, G.R. Burton and C.E. Brion, *Phys. Rev. A* 46 (1992) 149.
- CCB91 W.F. Chan, G. Cooper and C.E. Brion, *Phys. Rev. A* 44 (1991) 186.
- CF&87 R. Camilloni, E. Fainelli, G. Petrocelli and G. Stefani, *J. Phys. B: At. Mol. Phys.* 20 (1987) 1839.
- CH&68 R. N. Compton, R. H. Huebner, P. W. Reinhardt and L. G. Christophorou, *J. Chem. Phys.* 48 (1968) 901.
- CNK74 D.di Chio, S.V. Natali and C.E. Kuyatt, *Rev. Sci. Inst.* 45 (1974) 559.
- CS90 C.T. Chen and F. Sette, *Physica Scripta* T31 (1990).

- CW88 F. A. Cotton and G. Wilkinson, *Advanced Inorganic Chemistry*, 5th ed. (Interscience, Toronto, 1988) p. 509.
- D72 J. L. Dehmer, *J. Chem. Phys.* 56 (1972) 4496.
- D76 D. Dill, *J. Chem. Phys.* 65 (1976) 5327.
- DBH84 S. Daviel, C.E. Brion and A.P. Hitchcock, *Rev. Sci. Instr.* 55 (1984) 182.
- DD75 J. L. Dehmer and D. Dill, *Phys. Rev. Letters*, 35 (1975) 213.
- DD77 D.A. Dahl and J.E. Delmore, SIMION PC/2 Version 3.1, Idaho National Laboratory, EG&G Idaho Inc., Idaho Falls, ID 83415.
- DL74 M.A. Dillon and E.N. Lassette, *J. Chem. Phys.* 62 (1975) 2373.
- DW66 V. H. Dibeler and J. A. Walker, *J. Chem. Phys.* 44 (1966) 4405.
- E90 R.C. Elton, X-Ray Lasers, Orlando: Academic Press, 1990.
- F54 U. Fano, *Phys. Rev.* 95 (1954) 1198.
- F63 U. Fano, *Ann. Rev. Nucl. Sci.* 13 (1963) 1.
- FC68 U. Fano and J.W. Cooper, *Rev. Mod. Phys.* 40 (1968) 441.
- FE&94 J.T. Francis, C. Enkvist, S. Lunell and A.P. Hitchcock, *Can. J. Phys.* 72 (1994) 879.
- FH14 J. Franck and G. Hertz, *Verhandl. Deut. Phys. Ges.* (1914) 457
- FKH94 J.T. Francis, N. Kosugi and A.P. Hitchcock, *J. Chem. Phys.* 101 (1994) 10429.
- FL&86 T.A. Ferret, D.W. Lindle, P.A. Heimann, H.G. Kerkhoff, U.E. Becker and D.A. Shirley, *Phys. Rev. A* 34 (1986) 1916.

- FL&88 T.A. Ferret, D.W. Lindle, P.A. Heimann, M.N. Piancastelli, P.H. Kobrin, H.G. Kerkhoff, U. Becker, W.D. Brewer and D. A. Shirley, J. Chem.Phys. 89 (1988) 4726.
- FM&67 D. C. Frost, C. A. McDowell, J. S. Sandhu and D. A. Vroom, J. Chem. Phys. 46 (1967) 2008.
- G64 J. Geiger, Z. Phys. 1981 (1964) 413.
- GGL72 F.A. Gianturco, C. Guidotti and U. Lamanna, J. Chem. Phys. 57 (1972) 840.
- GK83 G. L. Gutsev and A. P. Klyagina, Chem. Phys. 75 (1983) 243.
- GKM77 E.S. Gluskin, A.A. Krasnoperova and L.N. Mazalov, J. Struct. Chem. 18 (1977) 156.
- GN&83 M.M. Gofman, V.I. Nefedov, V.L. Kraizman and R.V. Vedrinski, J. Electron Spectrosc. 32 (1983) 59.
- H71 D.W.O. Heddle, J. Phys. E. 4 (1971) 589.
- H90 A.P. Hitchcock, Physica Scripta T31 (1990) 159.
- HB78 A. P. Hitchcock and C. E. Brion, Chem. Phys. 33 (1978) 55.
- HB80 A. P. Hitchcock and C. E. Brion, J. Electron Spectrosc. 18 (1980) 1.
- HK86 I. Harrison and G.C. King, J. Phys., B 19 (1986) L447.
- HK87 I. Harrison and G.C. King, J. Elec. Spec. Relat. Phenom., 43 (1987) 155.
- HM94 A.P. Hitchcock and D. C. Mancini, J. Elec. Spec, Relat. Phenom. 67 (1994) 1.

- HP84 D.W.O. Heddle and N. Papadovassilakis, *J. Phys. E: Sci. Inst.* 17 (1984) 599.
- HR76 E.Harting and F.H. Read, Electrostatic Lenses, Elsevier Scientific Pub. Co., Amsterdam, 1976.
- HS&92 D. M. P. Holland, D. A. Shaw, A. Hopkirk, M. A. MacDonald and S. M. McSweeney, *J. Phys. B: At. Mol. Opt. Phys.* 25 (1992) 4823.
- HS&93 E. Hudson, D. A. Shirley, M. Domke, G. Remmers, A. Puschmann, T. Mandel, C. Xue and G. Kaindl, *Phys. Review A* 47 (1993) 361.
- HSL71 W.R. Harshbarger, A. Skerbele and E.N. Lassetre, *J. Chem. Phys.* 54 (1971) 3784.
- HU&92 A.P. Hitchcock, S.G. Urquhart and E.G. Rightor, *J. Phys. Chem.* 96 (1992) 8736.
- IIT71 Inokuti, M., Itikawa, Y. and Turner, *J. Rev. Mod. Phys.* 43 (1971) 297.
- JBE84 W.L. Jolly, K. D. Bomben and C. J. Eyermann, *At. Data Nucl. Data Tables* 31 (1984) 433.
- K67 C.E. Kuyatt, *Electron Optics Lectures*, April-June 1967.
- K72 Y.-K. Kim, *Phys. Rev.*, A6 (1972) 666.
- KBM79 R. E. Kennerly, R. A. Bonham and M. McMillan, *J. Chem. Phys.* 70 (1979) 2039.
- KI68 Y. Kim and M. Inokuti, *Phys. Rev.* 175 (1968) 176.
- KL86 F. Keller and H. Lefebvre-Brion, *Z. Phys. D* 4 (1986) 15.
- KMR77 G.C. King, J.W. McConkey and F.H. Read, *J. Phys. B* 10 (1977) L541.

- L70 E.N. Lassette, J. Chem. Phys. 53 (1970) 3801.
- L72 R.E. LaVilla, J. Chem. Phys. 57 (1972) 899.
- LCS89 P. Letardi, R. Camilloni and G. Stefani, Phys. Rev. B 40 (1989) 3311.
- LDW79 A. Lahmam-Bennani, A. Duguet and H.F. Wellenstein, Chem. Phys. Lett. 60 (1979) 405.
- LD&80 A. Lahmam-Bennani, A. Duguet, H.F. Wellenstein and M. Rouault, J. Chem. Phys. 72 (1980) 6398.
- LS&68 E.N. Lassette, A. Skerbele, M. Dillon and K.J. Ross, J. Chem. Phys. 48 (1968) 5066.
- LS71 E.N. Lassette and A. Skerbele J. Chem. Phys. 54 (1971).
- LS74 E.N. Lassette and A. Skerbele, Meth. Exp. Phys. 3B (1974) 868
- LSD64 E.N. Lassette, A. Skerbele and M.A. Dillon, J. Chem. Phys. 40 (1964) 1242.
- LSD69 E.N. Lassette, A. Skerbele and M.A. Dillon, J. Chem. Phys. 50 (1969) 1829.
- LSD70 E.N. Lassette, A. Skerbele and M.A. Dillon, J. Chem. Phys. 52 (1970) 2797.
- M58 A. Messiah, *Quantum Mechanics*, Vol. 12., Amsterdam: North Holland, 1958.
- MB&94 M. P. de Miranda, C. E. Bielschowsky, H. M. Boechat Roberly and G. G. B. de Souza, Phys. Rev. A 49 (1994) 2399.
- ML94 A. Mann and F. Linder, J. Phys.E. 21 (1994) 805.

- N70 V.I. Nefedov, J. Struct. Chem. 11 (1970) 272.
- N77 A. Niehaus, J. Phys. B. 10 (1977) 1845.
- P38 E.M. Purcell, Phys. Rev. 54 (1938) 818.
- P49 J.R. Pierce, Theory and Design of Electron Beams, Van Nostrand, New York. 1949.
- PF&88 W.H. Press, B.P. Flannery, S.A. Teukolsky and W.T. Vetterling, Numerical Recipes in C: The Art of Scientific Computing, Cambridge University Press, Cambridge, 1988, 309.
- PRB87 R. Pinto, K. V. Ramanathan and R. S. Babu, J. Electrochem. Soc. 134 (1987) 165.
- R74 M.B. Robin, Higher Excited States of Polyatomic Molecules, Vols. I,II (1974); Vol. III, (1986).
- R85 M.B. Robin, Chem. Phys. Lett. 119 (1985) 33.
- RB&92 C. Reynaud, S. Bodeur, J. L. Marechal, D. Bazin, P. Millie, I. Nenner, U. Rockland and H. Baumgartel, Chem. Phys. 166 (1992) 411.
- RBD91 H.M. Boechat Roberty, C.E. Bielschowsky and G.G.B. De Souza, Phys. Rev. A 44 (1991) 1694.
- RC&74 F.H. Read, J. Comer, R.E. Imhof, J.N.H. Brunt and E. Harting, J. Elec. Spec. Relat. Phenom. 4 (1974) 293.
- RO79 Rescigno, T.N. and Orel, A.E., J.Chem. Phys. 70 (1979) 3390.
- RSW74 N. Kösch, V.H. Smith Jr. and M.H. Whangbo, J. Am. Chem. Soc. 96 (1974) 5984.



- S48 K. Spangenberg, Vacuum Tubes, McGraw-Hill, New York, 1948.
- S81 S. Daviel, PhD. Thesis, University of Manchester, 1981.
- S92 J. Stöhr, NEXAFS Spectroscopy, Spr. Ser. Surf. Sci. Vol. 25 (Heidelberg, 1992).
- SB84 R. N. S. Sodhi and C. E. Brion, *J. Electron Spectrosc.*, 34 (1984) 363.
- SB90 K. H. Sze and C. E. Brion, *Chem. Phys.* 140 (1990) 439.
- SC&87 W.H.E. Schwarz, T.C. Chang, U. Seeger and K.H. Hwang, *Chem. Phys.* 117 (1987) 73.
- SCT73 R.W. Shaw Jr., T.X. Carroll and T.D. Thomas, *J. Am. Chem. Soc.* 95 (1973) 5870.
- SG&89 J.A. Sheehy, T.J. Gil, C.L. Winstead, R.E. Farren and P.W. Langhoff, *J. Chem. Phys.* 91 (1989) 1796.
- SK&82 D.A. Shaw, G.C. King, F.H. Read and D. Cvejanovic, *J. Phys. B* 15 (1982) 1785.
- SL64 S.M. Silverman and E.N. Lassette, *J. Chem. Phys.* 40 (1964) 1265.
- SP&74 V.P. Sachenko, E.V. Polozhentsev, A.P. Kovtun, Yu. F. Migal, R.V. Vedrinski and V.V. Kolesnikov, *Phys. Lett. A* 48 (1974) 169.
- SS&89 T. Sakae, S. Sumiyoshi, E. Murakami, Y. Matsumoto, K. Ishibashi and A. Katase, *J. Phys. B: At. Mol. Opt. Phys.* 22 (1989) 1385.
- T78 Turro, N.J., Modern Molecular Photochemistry, Benjamin/Cummings Pub. Co., 1978.
- T82 M. Tronc, private communication.

- TC86 R. Tang and J. Callaway, *J. Chem. Phys.* 84 (1986) 6854.
- TH76 H. Tanaka and R.H. Huebner, Argonne National Laboratory Report, 1976. 14-34.
- TK94 T. Tyliczszak and M. Kiela, Tolmar Instruments, Hamilton, Ontario. L8S 4M1
- TL&89 J.S. Tse, Z.F. Liu, J. D. Bozek, and G. M. Bancroft, *Phys. Rev. A* 39 (1989) 1791.
- TL91 J.S. Tse and Z.F.Liu, *Phys. Rev. A* 44 (1991) 7838.
- UK87 T. Urisi and H. Kyuragi, *J. Vac. Sci. Technol.* B5 (1987) 1436.
- UT83 L. Ungier and T.D. Thomas, *Chem. Phys. Lett.* 96 (1983) 247.
- VK&74 R.V. Vedrinskii, A.P. Kovtun, V.V. Kolesnikov, Yu. F. Migal, E.V. Polozhentsev and V.P. Sachenko, *Bull. Acad. Sci. USSR Phys. Ser.* 38 (1974) 8 .
- VK76 R.V. Vedrinskii and V.L. Kraizman, *Bull. Acad. Sci. USSR Phys. Ser.* 40 (1976) 114.
- VZ72 A. S. Vinogradov and T. M. Zimkina, *Opt. Spectrosc.* 32 (1972) 17.
- VZF71 A. S. Vinogradov, T. M. Zimkina and V. A. Fomichev, *J. Struct. Chem.* 12 (1971) 823.
- W74 G.R. Wight, PhD Thesis, UBC, 1974.
- W92 A.T. Wen, Ph. D. Thesis, McMaster University, 1992.
- WBV72 G.R. Wight, C.E. Brion and M.J. Van der Wiel, *J. Electron Spectrosc.* 1 (1972/1973) 457.

- WS&75 H.F. Wellenstein, H. Schmoranzler, R.A. Bonham, T.C. Wong and J.S. Lee, *Rev. Sci. Inst.* 46 (1975) 92.
- YD&93 J.F. Ying, T.A. Daniels, C.P. Mathers, H. Zhu and K.T. Leung, *J. Chem. Phys.* 99 (1993) 3390.
- YL94 J.F. Ying and K.T. Leung, *J. Chem. Phys.* 100 (1994) 7120; J.F. Ying and K.T. Leung, *J. Chem. Phys.* 100 (1994) 1011 and J.F. Ying and K.T. Leung, *J. Chem. Phys.* 101 (1994) 8333.
- YL94b J.F. Ying and K.T. Leung, *J. Chem. Phys.* 101 (1994) 7311.
- YM&93 J.F. Ying, C.P. Mathers, K.T. Leung, H.P. Pritchard, C. Winstead and V. McKoy, *Chem. Phys. Lett.* 212 (1993) 289.
- YML93 J.F. Ying, C.P. Mathers and K.T. Leung, *Phys. Rev. A* 47 (1993) R5.
- ZF66 T. M. Zimkina and V. A. Fomichev, *Sov. Phys. Doklady* 11 (1967) 726 and *Dokl. Akad. Nauk. SSSR* 169 (1966) 1304.


**McMASTER UNIVERSITY**

Institute for Materials Research

1200 Main Street West, Hamilton, Ontario, L8S 4M1

Telephone: (905) 525-9140, Ext. 24683

Telex: 091-8347 FAX: (905) 521-2773

**March 13, 1995**
**Research/Journals Division  
National Research Council of Canada  
Ottawa, Ontario, Canada**

Dear Sir/Madame,

For my PhD thesis, entitled "Non-dipole and Dipole Core Electronic Excitation", I would like your permission to reprint the following journal article (of which I am principal author):

Can. J. Phys. 72, 1994, 872.

I am also requesting that you grant an irrevocable, non-exclusive licence to McMaster University (and the National Library of Canada) to reproduce this material as a part of the thesis. Proper acknowledgement of your copyright of the reprinted material will be given in the thesis.

If these arrangements meet with your approval, please sign where indicated below and Fax me this letter at (905)-521-2773 Your attention is much appreciated in this matter.

Sincerely,

James T. Francis

 .....  
**PERMISSION GRANTED FOR THE USE REQUESTED ABOVE**

**Company Name:** National Research Council of Canada  
**Authorized By:** Paul McClymont  
**Title:** Business Manager  
**Date:** March 15, 1995  
**Signature:** Paul McClymont

THE JOURNAL OF CHEMICAL PHYSICS  
PUBLISHED BY THE  
AMERICAN INSTITUTE OF PHYSICS

J.C. LIGHT  
EDITOR  
D.H. LEVY  
ASSOCIATE EDITOR

DEPARTMENT OF CHEMISTRY  
5735 S. ELLIS AVENUE  
UNIVERSITY OF CHICAGO  
CHICAGO, ILLINOIS 60637  
(312) 702-7067 / FAX: (312) 702-8314  
e-mail editor@jcp.uchicago.edu

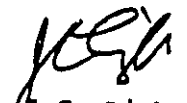
Dr. James T. Francis  
Institute for Materials Research  
McMaster University  
1280 Main Street West  
Hamilton, Ontario  
CANADA L8S 4M1

Dear Dr. Francis:

Thank you for your letter of March 13, 1995 requesting permission to reproduce material which has been submitted for publication in the Journal of Chemical Physics.

Permission to reproduce the material cited in your letter is granted provided that you have obtained the permission of all authors and that acknowledgement of the authors and the Journal of Chemical Physics is made.

Sincerely yours,



J.C. Light  
D.H. Levy

JCL:mc  
cc: DeLorenzo/AIP

Article [J. Chem. Phys. 101(12), 10429 (1994)].